UNIVERSITÉ DE STRASBOURG

ÉCOLE DOCTORALE 182

Institut de Physique et Chimie des Matériaux de Strasbourg

THÈSE présentée par :

Steve Dave WANSI WENDJI

soutenue le : **20 Septembre 2024**

pour obtenir le grade de : **Docteur de l'université de Strasbourg**

Discipline/ Spécialité : Physique – Chimie Physique

TITRE de la thèse

Français **: Modélisation à l'échelle atomique de premiers principes et d'apprentissage automatique des systèmes désordonnés pour les applications énergétiques**

Anglais **: First-principles and machine learning atomistic modeling of disordered systems for energy applications**

THÈSE dirigée par :

Mr **Carlo MASSOBRIO**	Directeur de Recherche, ICUBE – Université de Strasbourg
Mr **Guido ORI**	Chargé de Recherche, IPCMS – Université de Strasbourg

RAPPORTEURS :

Mme **Marie-Vanessa COULET**	Directrice de Recherche, MADIREL – Aix-Marseille Université
Mr **Fabrizio CLERI**	Professeur des Universités, IEMN – Université de Lille

---

AUTRES MEMBRES DU JURY :

Mme **Evelyne MARTIN**	Directrice de Recherche, ICUBE – Université de Strasbourg
Mme **Anne HEMERYCK**	Chargée de Recherche, LAAS – Université de Toulouse

Abstract

Polyanionic glasses and glass-ceramics are a rapidly growing family of innovative materials with broad potential applications in next-generation solid-state batteries, offering enhanced safety, environmental sustainability, and simplified design. Within this family, sodium-vanadium-phosphate (NVP) systems are particularly promising due to their high structural stability and facilitated by strong covalent bonding. The abundance, widespread distribution, and low cost of sodium resources further enhance the appeal of NVP materials for technological implementation, especially for applications not limited by volumetric energy density. However, practical applications have been restricted by a limited understanding of both their complex structures and the underlying ion dynamics.

This thesis focuses on the design of NVP glasses for cathode materials through atomic-scale modeling methodologies. By combining classical and first-principles molecular dynamics (MD) simulations, we provide unprecedented insights into the structural, magnetic, electronic, and dynamical properties of this intricate class of materials. Initially, we evaluated the performance of available empirical force fields (FF) by comparing their predictions to experimental data. We then proposed a hybrid approach that involves performing full classical MD (CMD) simulations with the most accurate FF, followed by a short equilibration using Born-Oppenheimer MD (BOMD). This hybrid scheme demonstrates unparalleled agreement with experimental measurements for the binary VP50 [1, 2] and ternary NVP25 and NVP43 glasses [3] (numbers 50, 25 and 43 indicate vanadium oxide concentrations), surpassing the accuracy of any single FF tested. To further validate this approach, we conducted full ab initio modeling of two NVP glass compositions and compared the resulting structures with those obtained using the hybrid method. Our findings indicate that full BOMD yields superior accuracy compared to experimental data, but the hybrid scheme captures all the essential structural details observed in pure BOMD simulations.

To extend our investigation and address the computational demands of pure BOMD modeling to assess statistical errors across multiple uncorrelated replicas with FPMD accuracy, we developed, tested, and validated a machine learning interatomic potentials (MLIP) based on first-principles MD data. This novel approach was initially tested and validated on other oxide and chalcogenide [4, 5] systems. Using the newly developed potentials, we investigated the structural and dynamical properties of VP50 and four NVP glass compositions. The MLIPs consistently demonstrate accuracy comparable to full first-principles MD simulations and, in some cases, such as VP50, even outperform the hybrid approach [6].

Keywords : Polyanionic, glass, glass-ceramic, NVP, chalcogenides, MD, first-principles, CMD, BOMD, MLIP, FF

Résumé

Les verres et vitrocéramiques polyanioniques constituent une famille en pleine expansion de matériaux innovants aux vastes applications dans les batteries solides de nouvelle génération. Ils offrent une sécurité accrue, une durabilité environnementale et une conception simplifiée. Au sein de cette famille, les systèmes sodium-vanadium-phosphate (NVP) sont particulièrement prometteurs en raison de leur grande stabilité structurale et facilitée par de fortes liaisons covalentes. L'abondance, la large distribution et le faible coût des ressources en sodium renforcent encore l'attrait des matériaux NVP pour la mise en œuvre technologique en particulier pour les applications qui ne sont pas restreintes par la densité d'énergie volumétrique. Cependant, les applications pratiques restent limitées par une compréhension restreinte de leurs structures complexes et de la dynamique ionique sous-jacente.

Cette thèse se concentre sur la conception des verres NVP pour les matériaux cathodiques par la modélisation à l'échelle atomique. En combinant des simulations de dynamique moléculaire (MD) classique et ab initio (FPMD), nous fournissons des informations sans précédent sur les propriétés structurelles, magnétiques, électroniques et dynamiques de cette classe complexe de matériaux. Dans un premier temps, nous avons évalué les performances des champs de force (FF) empiriques disponibles en comparant leurs prédictions aux données expérimentales. Nous avons ensuite proposé une approche hybride qui consiste à effectuer des simulations MD classique (CMD) avec le FF le plus précis, suivies d'une courte équilibration en utilisant la MD de Born-Oppenheimer (BOMD). Ce schéma hybride démontre un accord sans précédent avec les mesures expérimentales pour les verres binaires VP50 [1, 2] et ternaires NVP25 et NVP43 [3] (les nombres 50, 25 et 43 indiquent la teneur en oxyde de vanadium), surpassant la précision de tous les FF testés. Pour valider davantage cette approche, nous avons mené des simulations complète BOMD sur deux compositions de verre NVP et comparé les structures résultantes à celles obtenues avec l'approche hybride. Nos résultats indiquent que la BOMD complète donne une précision supérieure par rapport aux données expérimentales, néamoins le schéma hybride capture tous les détails structurels essentiels observés dans les simulations pures BOMD.

Pour étendre notre investigation et contourner le coût de calcul élevé de la BOMD afin d'évaluer les erreurs statistiques sur plusieurs répliques non corrélées avec une précision FPMD, nous avons développé, testé et validé un potentiel interatomique d'apprentissage automatique (MLIP) basé sur des données BOMD. Cette nouvelle approche a d'abord été testée et validée sur d'autres systèmes d'oxydes et de chalcogénures [4, 5]. En utilisant le potentiel nouvellement développé, nous avons étudié les propriétés structurelles et dynamiques de quatre systèmes des verres NVP ainsi que le binaire VP50. Le MLIP démontrent systématiquement une précision comparable à celle de la BOMD et, dans certains cas, comme pour le VP50, surpassent même l'approche hybride [6].

Mots clés : Polyanionique, verres, vitroceramique, NVP, chalcogenures, MD, FPMD, BOMD, MLIP

Publications[1] **:**

[1] **S.D. Wansi Wendji**, C. Massobrio, M. Boero, C. Tugène, E. Levchenko, F. Shuaib, R. Piotrowski, D. Hamani, G. Delaizir, P.-M. Geffroy, P. Thomas. O. Masson, A. Bouzid, G. Ori 'Quantitative Assessment of the Structure and Bonding Properties of $50V_xO_y$-$50P_2O_5$ Glass by Classical and Born-Oppenheimer Molecular Dynamics' *J. Non-Cryst. Solids*, **(2024)**. DOI: 10.1016/j.jnoncrysol.2024.122967.

[2] C. Massobrio, I.A. Essomba, M. Boero, C. Diarra, M. Guerboub, K. Ishisone, A. Lambrecht, E. Martin, I. Morrot-Woisard, G. Ori, C. Tugène, **S.D. Wansi Wendji** 'On the actual difference between the Nosé and the Nosé-Hoover thermostats: a critical review of canonical temperature control by molecular dynamics' *Phys. Status Solidi B Basic Res.* **(2023)**. DOI: 10.1002/pssb.202300209; HAL: hal-04280276v1.

[3] **S.D. Wansi Wendji**, R. Piotrowski, C. Massobrio, M. Boero, C. Tugène, F. Shuaib, D. Hamani, P.-M. Geffroy, P. Thomas, A. Bouzid, O. Masson, G. Delaizir, G. Ori 'Enhanced structural description of sodium vanadium phosphate glasses: A combined experimental and molecular dynamics study', *J. Non-Cryst. Solids*, 655, 123420, **(2025)**. DOI: 10.1016/j.jnoncrysol.2025.123420

[4] T.-L. Pham, M. Guerboub, **S.D. Wansi Wendji**, A. Bouzid, C. Tugène, M. Boero, C. Massobrio, Y.-H. Shin and G. Ori 'Structural properties of amorphous Na_3OCl electrolyte by first-principles and machine learning potential molecular dynamics' *arXiv preprint*, **(2024)**. DOI: arXiv:2404.11442.

[5] M. Guerboub, **S.D. Wansi Wendji**, C. Massobrio, A. Bouzid, M. Boero, G. Ori, and E. Martin. 'Impact of the local atomic structure on the thermal conductivity of amorphous $Ge_2Sb_2Te_5$.' *J. Chem. Phys.* 158, 084504 **(2023)**. DOI: 10.1063/5.0139590; HAL: hal-04014339.

[6] **S.D. Wansi Wendji**, R. Piotrowski, A. Familiari, C. Massobrio, M. Boero, C. Tugène, F. Shuaib, D. Hamani, P.-M. Geffroy, P. Thomas, A. Pedone, A. Bouzid, O. Masson, G. Delaizir, G. Ori 'Structure, bonding and ionic mobility in Na-VPO glasses for energy storage applications', *Chem. Commun.*, **(2025)**.
DOI: 10.1039/D5CC00443H

[1] A complete list of scientific contributions, including published articles, preprints, and works in preparation, is available at the end of this thesis on page 162

Contents

List of Figures

List of Tables

Acknowledgement

This thesis was conducted at the *Institut de Physique et Chimie des Matériaux de Strasbourg* (IPCMS – UMR 7504, CNRS) of the University of Strasbourg, France, under the direction of Carlo MASSOBRIO (*Laboratoire des Sciences de l'Ingénieur, Informatique et Imagerie*, Icube – UMR 7357) and in co-supervision with Guido ORI (IPCMS) from October 1, 2021 to September 30, 2024.

These three years of research have been made possible thanks to a wealth of human and material resources, a conducive and healthy work environment, and the grace of God. I would like to express my sincere gratitude to all those who contributed.

First and foremost, I would like to express my deepest gratitude to my supervisory team, who have accompanied me every step of the way throughout this thesis.
To my thesis supervisor, Carlo MASSOBRIO, for the confidence he showed in me by entrusting me at the helm of a timely and promising project. He allowed me to join a dynamic team and instilled in me the scientific and human values required for exemplary scientific production, while encouraging me to always give my best.
To my co-advisor, Guido ORI, who was also my master's internship supervisor and who has remained very close to me since then, following me every day in every detail of this work. His courtesy, accessibility, and constant availability have been fundamental to my scientific growth and above all to the realization of this thesis.
Carlo and Guido have trained me in the use of computational methods from the basic to the most advanced, as well as in the rigor of scientific production, which has allowed me to complete my thesis successfully and under good conditions.

I would like to thank Mauro BOERO, another distinguished member of the group, for our many fruitful discussions on electronic structure calculations and his numerous presentations for the benefit of doctoral students and master's interns in the group.
I express my gratitude to all my colleagues and members of the ADYNMAT consortium for all the discussions during our traditional monthly seminar, as well as the convivial moments shared. Each of them, in their own way, has helped to solidify my knowledge on various aspects of this project.

I also thank :
M. GUERBOUB, K. ISHISHONE and I. B. A. ESSOMBA, previous PhD students who welcomed me into the team and facilitated my integration. I had many enriching discussions with them, both at the office and during our convivial moments outside of work.
A. FAMILIARI, an ERASMUS+ intern with whom I shared the office during my writing phase. Through our exchanges on science and culture, he brought me a great deal of energy.

This research was funded by the French National Research Agency (ANR) as part of the Advanced Modelling as a Strategy to design glass and glass-ceramic materials for Energy Storage applications (AMSES) project. The numerical computations in this work

were made possible thanks to the high-performance computing resources of the *Grand Equipement National de Calcul Intensif* (GENCI) at IDRIS and TGCC, as well as the *Centre de Calcul de l'Université de Strasbourg* (CCUS), to which I express my sincere gratitude.
I would like to express my sincere gratitude to the computational group led by Assil Bouzid, the experimental team led by Olivier MASSON from IRCER Limoges, and all members of the AMSES project, for their invaluable discussions and data sharing during our meetings. Their contributions have been instrumental in shaping and illuminating this thesis. I warmly thank them all.

Finally, I dedicate this work to my family in Cameroon, France, Belgium, Germany, and United States.
To my parents in Cameroon, who have always supported and guided me throughout my journey, their love and prayers have given me the determination necessary for this project.
To my brothers and sisters, uncles, aunts, cousins, and nephews/nieces each of them has contributed energy in their own way. In particular, my brother Dorian and his wife Irène (who sadly passed away on September 12, 2023, may her soul rest in peace) who braved the weather every week to have lunch with me, discuss my progress, and offer advice from his experience.
To my life partner, Chanelle DJOUMBISSI, and our unborn child. Her daily presence, support, discussions about my work, and her playful interviews about my research have always brought me good humor and energy to move forward. These moments have always been an inexhaustible source of motivation and fulfillment. They are both my greatest sources of motivation.
My heartfelt thanks to all of them.

List of Acronyms

BLYP	Becke, Lee, Yang and Parr
BOMD	Born-Oppenheimer Molecular Dynamic at 300 K after full CMD
CMD	Classical Molecular Dynamics
CPMD	Car-Parrinello Molecular Dynamics
CPU	Central Processing Unit
CDFT	Constrained Density Functional Theory
DFT	Density Functional Theory
DOS	Density Of State
***f*BOMD**	full Born-Oppenheimer Molecular Dynamic thermal cycle
FFs	Force Fields
FPMD	First-Principles Molecular Dynamics
FSDP	First Sharp Diffraction Peak
GAP	Gaussian Approximation Potential
GGA	Generalized Gradient Approximation
GPR	Gaussian Process Regression
GTH	Goedecker, Teter, and Hutter
HF	Hartree-Fock
HDNNP	High Dimensional Neural Network Potential
KS	Khon-Sham
LAMMPS	Large-scale Atomic/Molecular Massively Parallel Simulator
LDA	Local Density Approximation
LSD	Local Spin Density Approximation
MAE	Mean Absolute Error
MD	Molecular Dynamics
ML	Machine Learning
MLIP	Machine Learning Inter-atomic Potential
MLWF	Maximally-localized Wannier Functions
MSD	Mean-Square Displacement
NIBs	Sodium Ion Batteries
NN	Neural Network
NVP	Sodium Vanadium Phosphate
PBCs	Periodic Boundary Conditions
PBE	Perdew-Burke-Ernzerhof
PBE0	Hybrid 0.75 PBE exchange + 0.25 Hartree-Fock exchange
PCFs	Pair Correlation Functions
PDFs	Pair Distribution Functions
PES	Potential Energy Surface
PP	Pseudo-Potentials
PW	Plane Waves
SOAP	Smooth Overlap of Atomic Positions
TM	Troullier and Martins
XC	Exchange-Correlation

Chapter 1

General Introduction

Summary

The opening chapter of this thesis is devoted to the role that materials play in energy applications, with a special focus on polyanionic materials along with glasses (G) and glass-ceramic (GC) systems. The idea is to underscore the significance of atomic-scale simulation methods within computational materials science to gain an in-depth understanding of the properties and behaviors of G and GC materials. This chapter features an overview of the latest advancements in the modeling of these materials, spotlighting both the achievements and the existing challenges. It wraps up by clearly stating the primary motivation behind this research, which is fostered by the recognition of knowledge gaps, and outlines the thesis in an organized manner.

1.1 Materials for energy storage systems

The global demand for energy has experienced a rapid increase over the years, driven by its pivotal role in human activities. Fossil fuels, the primary source of energy, contribute significantly to environmental degradation and global warming due to their high CO_2 emissions. These issues underscore the urgency of addressing energy concerns and make a transition towards alternative, renewable, and environmentally-friendly energy sources such as solar, wind, and hydroelectric power. Nevertheless, the widespread adoption of these renewable sources faces limitations due to their intermittent nature, characterized by significant variability over time and location. In this context, energy storage systems (ESSs) are a highly appropriate green energy source, meeting various demands from portable electronics to large-scale grid storage. Diverse sectors take advantage of it, such as electric vehicles, industrial and commercial activities, as well as applications in aviation, shipping, and medicine [1].

Various technologies exist for large-scale ESSs, and while mechanical energy storage are currently the most prevalent [2], batteries, classified as electrochemical ESSs, have garnered growing attention. Notably, the significant progress in this field was acknowledged by the 2019 Nobel Prize in Chemistry, awarded to J.B. Goodenough, M.S. Whittingham, and A. Yoshino for their pioneering contributions to lithium-ion batteries [3].
In the context of battery technology, alkali-ion batteries (AIBs) and, particularly, lithium-ion batteries (LIBs), have gained significant prominence due to their high-energy density, conversion efficiency, and long life-time. However, the growing demand for Li and its non-uniform global distribution, along with soaring market prices, necessitates exploration of alternatives like Na-ion batteries (NIBs), among the others.
This is because sodium is an abundant and uniformly distributed resource (Fig. 1.1). NIBs share similar components and operational mechanisms with LIBs. However, notable differences exist between the two materials. The ionic radius of Na^+ ions is 102 *pm* with a mass of 22.99 g mol^{-1}, substantially larger than Li^+'s radius of 76 *pm* and mass of 6.94 g mol^{-1}. This variance can significantly influence transport properties, interface formation, and stability. Additionally, sodium exhibits a higher standard electrode potential (-2.71 V vs. -3.02 V for Li), theoretically resulting in NIBs having a lower specific energy density than LIBs [4]. Nevertheless, studies have revealed that the energy barriers for Na^+

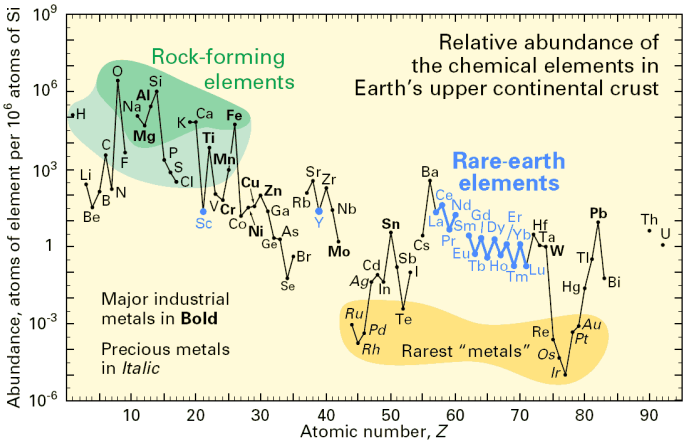

Figure 1.1. Abundance (atom fraction) of the chemical elements in Earth's upper continental crust as a function of atomic number. Many of the elements are classified into (partially overlapping) categories: rock-forming elements, rare earth elements, major industrial metals, precious metals, and the nine rarest "metals" [5].

migration can potentially be lower than those for Li^+ migration in open structures, which

better accommodate the larger Na^+ ion [6]. This means that Na-ion systems have the potential to be competitive with Li-ion ones, especially for large-scale grid storage systems [7, 8]. Recent advances in materials science have stimulated the emergence of increasingly promising materials with enhanced electrochemical performance and longevity. Despite these significant advances, it is essential to emphasize that NIBs still face considerable challenges, requiring further improvements in electrochemical and structural properties before large-scale commercialization of NIBs can be successfully achieved.
This thesis will mainly study **disordered materials for their potential use in NIBs**, with a special focus as cathode materials. For clarity and to ensure the comprehension of certain definitions, we will briefly outline the principal components and key definitions related to battery technology in the subsequent section. Fig. 1.2 elucidates the primary components and the operational process of a NIBs battery during both charging and discharging phases, with sodium ions migrating in the electrolyte between the positive electrode (cathode) and negative electrode (anode).

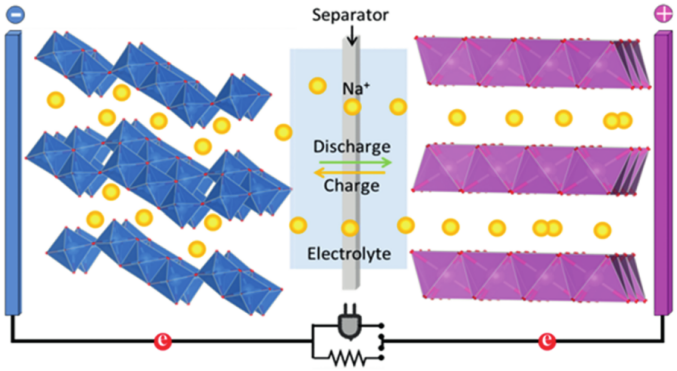

Figure 1.2. Working principle of NIBs illustrating the movement of Na^+ ions within the electrolyte between the negative and positive electrodes during both discharge and charge cycles. The voltage across the electrodes determines the battery's voltage [2].

The choice of materials for the three main components (electrolyte and the two electrodes) plays a crucial role in determining the performance, safety, cost and environmental impact of batteries. For example, in optimal scenarios, the theoretical voltage of a battery is dictated by the chemical potential disparity between the positive and negative electrodes. Below, we provide a concise overview of the key components and definitions pertinent to battery technology.

The **electrolyte** component plays an important role in battery technology, facilitating the ions diffusion between the electrodes during charge and discharge cycles. Generally, electrolytes in batteries can be liquid, solid, or gel types ionic conducting medium. Liquid state electrolytes (LSEs) represent the most common type of electrolytes found in rechargeable batteries, often, consisting of lithium/sodium salts dissolved in organic solvents. LSEs offers high ionic conductivity, allowing for efficient ion transport between the electrodes. However, they can be flammable and prone to leakage, which poses safety concerns. Gel electrolytes combine the properties of liquid and solid electrolytes and consist of a polymer matrix that immobilizes a LSEs solution, forming a gel-like substance.
Gel electrolytes offer improved safety compared to liquid electrolytes due to their reduced risk of leakage. They also exhibit some degree of flexibility, which can be advantageous in certain battery designs. However, they may have lower ionic conductivity compared to liquid electrolytes.
Solid state electrolytes (SSEs) are gaining attention as potential alternatives to LSEs, particularly in next-generation all solid-state batteries technologies. SSEs are the core component of SSBs, typically they are composed of solid-state materials such as ceramics,

glasses, sulfide and polymers facilitating Li^+/Na^+ ion transport between electrodes without the volatility and combustibility risks associated with liquid electrolytes [9, 10]. By replacing LSEs with SSEs, energy density, durability and battery safety can be considerably improved [11]. As illustrated in the Fig. 1.3, the properties of SSEs, such as ionic conductivity, mechanical durability, interface compatibility, and chemical/electrochemical behavior, are significantly shaped by the constituent materials [9].

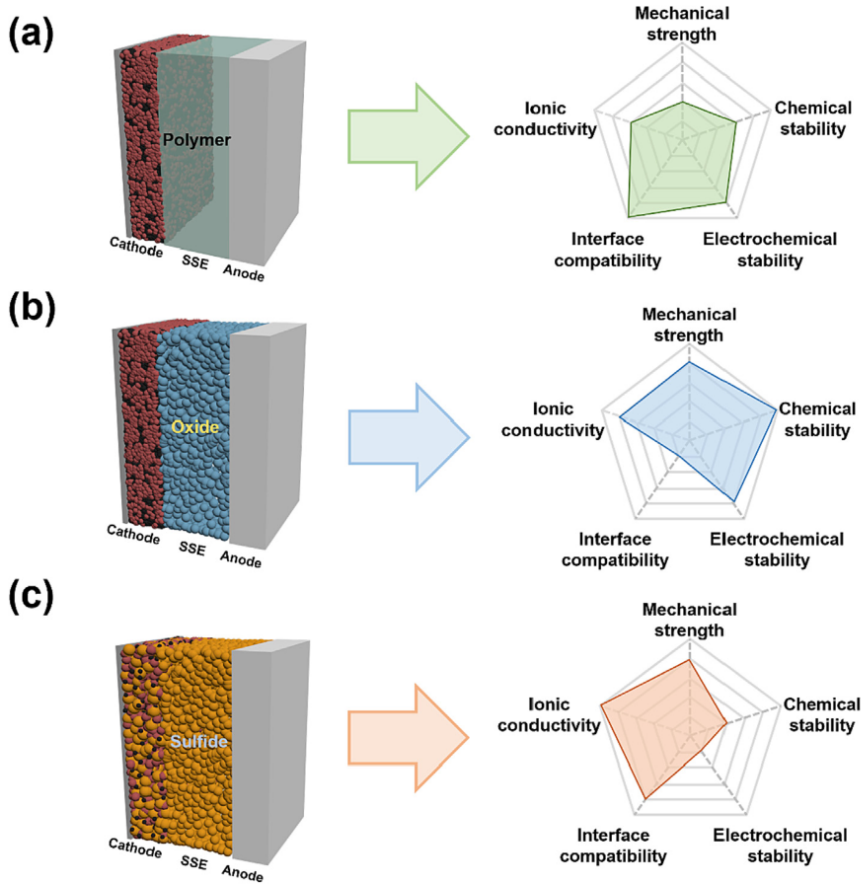

Figure 1.3. Solid-state batteries made with polymer (a), oxide (b) and sulfide (c) [9].

The **anode** component is the electrode where oxidation takes place. The choice of anode electrode material depends on the type of electrolyte and is crucial for achieving optimal performance and stability. For LSEs, metals like zinc (Zn), lead (Pb), or iron (Fe) are commonly used as anodes. These type of materials are stable in aqueous environments and can undergo reversible redox reactions. In SSBs, the anode materials need to possess several key characteristics. Firstly, they should have a high theoretical capacity to allow for greater energy storage per unit mass. Additionally, they should exhibit a low electrochemical potential compared to Li/Na to maintain a high cell voltage. For these materials it is crucial to demonstrate excellent electronic conductivity to facilitate efficient electron transfer within the battery, thus enhancing throughput capacity. Moreover, structural stability is of paramount importance as the anode material has to endure volume changes resulting from the intercalation/extracalation processes of Li/Na without experiencing significant degradation [10]. To address these criteria, significant resources are being invested in the study of materials such as graphitic carbons, silicon, selenides, sulfides, low potential transition metal oxides and alloys (bismuth, tin, antimony, phosphorus), which exhibit favorable characteristics such as high capacity and compatibility with solid electrolytes [2, 12]. Nevertheless, challenges such as volume expansion and the

creation of an unstable solid electrolyte interphase (SEI) persist, calling for advancements in materials science and engineering. The establishment of a durable SEI holds particular significance in SSB technology as it can mitigate dendrite formation, thereby enhancing safety. Careful material selection and optimization are imperative to ensure compatibility with the solid electrolyte and establish a stable interface [10].

Over the past decade, a large family of materials have been considered as **cathode** (positive) electrode for AIBs as shown in Fig 1.4. The first AIBs with Lithium was commercialized in the late 1970s by Exxon with an energy density of 130 $Wh.kg^{-1}$. The cathode of this battery was made of metal dichalcogenides (TiS_2) designed by M.S. Whittingham [13]. Despite TiS_2's high Li^+ ion intercalation capacity about 240 $mAh.g^{-1}$ and high durability [14], handling under ambient conditions was difficult due to the spontaneous release of toxic H_2S gas on contact with moisture [15]. A decade after the TiS_2 battery came onto the market, a step forward has been made towards the use of a high-voltage layered crystalline structures as metal oxide cathodes like $Li_xMn_2O_4$, $Li_xV_2O_5$, $Li_xV_3O_8$, A_xTmO_2 (with A being alkali ion (Li, Na) and Tm transition metal such as Co, Ni, Fe, Mn, V) for rechargeable AIBs [16]. These oxides are reasonably good ionic and electronic conductors, and have the advantage of good stability at ambient conditions [15]. Among these oxides, $LiCoO_2$, first designed by J.B Goodenough et al. [17] remains the most widely used cathode employed in Li-ion batteries [16]. Selecting an optimal battery cathode material is far from straightforward. Facilitating the mass production of energy storage systems and avoiding deterioration throughout charge/discharge cycles requires meeting multiple prerequisites. These include high energy density, robust moisture resistance, reasonable cost, high voltage and theoretical capacity, electrochemical reversibility, environmental sustainability, compatibility with other cell components (anode, electrolyte), structural robustness, presence of reducing and oxidizing ions, proficient ionic insertion/extraction rate, and effective electronic conductivity [1, 18].

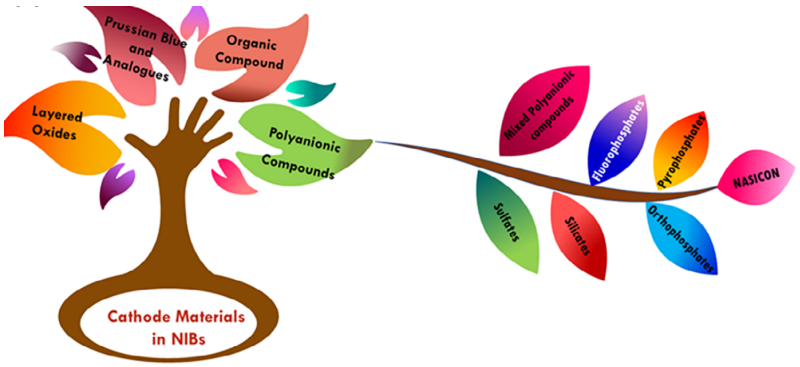

Figure 1.4. Varieties of cathode materials for NIBs with sub-branches of polyanionic compounds [1].

Extensive research into promising cathode materials for the next generation of NIBs has revealed that layered transition metal oxides, Prussian blue analogues (PBAs) and polyanionic materials are the main candidates for cathode materials among the various explored cathode materials. PBAs are gaining interest because of their high theoretical capacity and open 3D crystal structure. However, the synthesis process of PBA cathodes typically results in the formation of significant coordination water and lattice vacancies, leading to the deterioration of electrochemical performance. Additionally, the ultrafine grains produced contribute to a low volumetric energy density, thereby limiting their practical utility [19]. Regarding layered transition metal oxides, they exhibit a high discharge capacity but are plagued by a sloping voltage profile across a broad potential range, yielding

a relatively low average voltage, typically not exceeding 3.4 V [20]. Complex phase transitions further exacerbate structural instability. Additionally, the dense lattice structures hinder the rapid migration kinetics of Na^+ ions. Moreover, the possible release of oxygen from the cathode poses a significant safety concern.

To enhance the electrochemical performance of current NIBs, research has proved the benefits of cathode materials with high specific capacitance, operating voltage, cyclic stability, and optimal flow capacity. Among the various investigated cathode materials, **polyanionic compounds** emerge as one of the most promising class of candidates for NIBs' cathodes offering numerous advantages including favorable ion diffusion pathways, high safety standards, and exceptional structural stability [15, 16, 21, 22].
The next section is devoted to recent developments in polyanionic materials used as cathodes in NIBs and current challenges.

1.2 Brief review on polyanionic compounds as electrode materials for NIBs

In contrast to pure transition metal oxides, crystalline polyanionic compounds with general formula $A_xTm_yMO_z$ (A=Li or Na; Tm=transition metal (V, Fe); M= P, S, B or Si) offer many potential advantages. The strong M-O covalent bonding in tetrahedral polyanion MO_4^{n-} due to the high electronegativity of M specie gives rise to open channels for Li^+/Na^+ ion diffusion, high thermal stability, superior safety properties, as well as higher voltages (inductive effects). In addition, multi-electronic redox reactions between Tm sites with different oxidation states enable very high capacities to be achieved [1]. A plethora class of polyanionic compounds have been investigated as positive electrode for NIBs among which sodium super ionic conductor (NASICON); ortho-, pyro-, or flurophosphates; sulfates, silicates, and mixed polyanionic compounds.

Based on the crystalline arrangement of the materials, polyanionics can be categorized

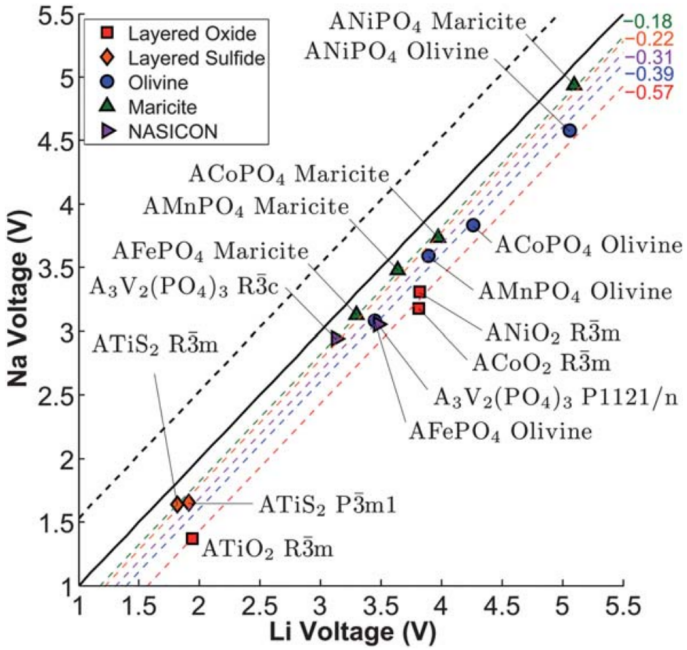

Figure 1.5. Comparison of calculated voltage for sodium and lithium over various cathode material structures. Colored dashed lines represent the fitted average voltage difference (V_{Na^+} - V_{Li^+}). From [6].

into olivine, maricite, alluaudite, tavorite, or NASICON type structure. Fig. 1.5 presents a comparison of calculated voltages for Na and Li in various cathode material structures, highlighting the substantial impact of structural characteristics on battery performance. S.P. Ong et al. have demonstrated that open NASICON-type structures offer a stable pathway for Na^+ migration, in contrast to oviline structures which are more suitable for Li^+ [6]. NASICON type polyanionic compounds take the general formula $A_nM_2(XO_4)_3$ (where A represents alkali ions, M represents transition metals, and X can be S, P, Si, or As) and were first identified in 1976 by J.B. Goodenough et al. [23]. They are the most widely developed class of potential cathodes for NIBs [12]. The first polyanionic compounds identified as cathode materials with suitable hosting potential for second-generation batteries included $LiFePO_4$ in oviline and NASICON structure [24].

1.2.1 Phosphate based polyanionics

Phosphates are at the top of the most representative polyanionic compounds for NIBs. The P–O bond in polyanionic phosphates provides good structural stability essential for long-term cycling and improved safety. Also, the thermal properties of phosphate materials are directly related to the stability of the phosphate-metal bonds, which limits the possibility of oxygen release from the structure. In addition, the high presence of interstitial sites in the structure limits volumetric expansion during Na^+ ion intercalation/extracalation, thus promoting stability while the inductive effect of the PO_4^{3-} group allows for higher redox potential values compared to Na^+/Na [24]. Among others, two main phosphates polyanionic compounds are more attractive for NIBs due to their good electrochemical properties, the oviline structure $NaTmPO_4$ with TM=Fe or Mn and NASICON structure $Na_xTm_2(PO_4)_3$ with Tm = V or Ti.
NASICON-type Vanadium-based phosphates $Na_3V_2(PO_4)_3$ are widely investigated as cathode materials for NIBs [6, 16, 19, 25, 26]. The stability provided by this structure favors the migration of Na^+. However, its low electronic conductivity leads to lower capacity rates and cycling stability. Recently, it has been reported that carbon coating processes have achieved a theoretical reversible capacity of 118 mAh g^{-1} and increased the $Na_3V_2(PO_4)_3$ cathode performance so as to challenge the $LiCoO_2$ and $LiFePO_4$ cathodes of LIBs [27].

1.2.2 Other polyanionic materials

- Sulfate based polyanionic $Na_xTm_y(SO_4)_z$ (Tm =Fe, Mn, Co, Ni) are another valuable alternative since transition metal sulfates have strong electronegativity allowing high redox potential. Among all Fe-based NIBs cathode materials, $Na_2Fe_2(SO_4)_3$ have shown a higher operating potential of 3.8 V based on the Fe^{3+}/Fe^{2+} redox couple with a theoretical capacity of 120 mAh g^{-1} based on one electron transfer. The $NaFe_2(SO_4)_2$ layered cathode has a reversible reaction with Fe^{3+}/Fe^{2+} redox couple at a voltage of 3.2 V vs Na^+/Na with reported theoretical capacity of 99 mAh/g [24]. Another research on NASICON $Fe_2(SO_4)_3$ was reported as Na^+ ions intercalation host but, in contrary to Lithium, only one mole of Na^+ ion per unit mol of $Fe_2(SO_4)_3$ can be stored compared to 2 mole [24]. Unfortunately, the obtained practical electrochemical performance of $NaFe_2(SO_4)_2$ and $Fe_2(SO_4)_3$ were not higher compared to other cathodes materials. For this class of transition metal sulfates cathodes, precise understanding of electrochemical processes is essential to further improve the performances.

- Fluorine based polyanionic $NaTmMO_4F$ (Tm=V, Fe, Co, Mn; M= P, S) have an

heightened electronegativity of the F^- anion, coupled with the inductive effect of the MO_4^{3-} group, significantly contributing to enhance the operational potential and energy density of NIBs. Fluorophosphates and fluorosulfates persist as top contenders for high-potential cathode materials [24]. Among various fluorosulfate compounds, $NaFeSO_4F$ has emerged as electrochemically active, exhibiting a Fe^{3+}/Fe^{2+} redox couple voltage of 3.6 V vs Li^+/Li. Investigations into Na^+ ion migration within this material have also been conducted through atomic scale modeling [28].

Polyanionic cathodes for NIBs continually face numerous limitations, including low electronic conductivity and low operating voltage (2.6–3.5 V). The electrochemical performance of crystalline host materials depends on factors that hamper their performance, such as crystal orientation, grain boundaries, structural stability, phase transition, spatial dimension of ion migration, defects in the crystal and stochiometric limitation of ion insertion [29].

To conclude this section, one can observe that, in contrast to crystalline materials, **glassy materials** feature several advantages: the lack of grain boundaries facilitates sodium ion transport, while the specific capacitance can be controlled by adjusting the glass composition. Additionally, the softening point enhances interfacial contact between the electrode material and the solid electrolyte, thereby improving the efficiency of sodium ion transport [29, 30].

1.2.3 Glassy (G) and glass-ceramic (GC) materials as AIBs' electrodes

Glass-based systems are at the forefront of developing solid-state devices, with the integration of transition metal oxides (TMOs) as dopants or primary constituents playing a pivotal role in tailoring specific functionalities. Fig. 1.6 shows general trade-offs between voltage, capacity, and various practical considerations for different sodium-ion battery cathode materials, highlighting the potential advantages of glass and glass-ceramic compositions. Transition metals like V, Fe, and Cu have been incorporated into various glass matrices to enhance their semi-conductive capabilities and functional properties. Particularly, glasses and glass-ceramics enriched with V_2O_5 are under investigation for their potential as cathode materials in secondary batteries [32, 33]. The incorporation of Vanadium ions, which exist in multiple oxidation states (such as +3, +4, and +5), makes

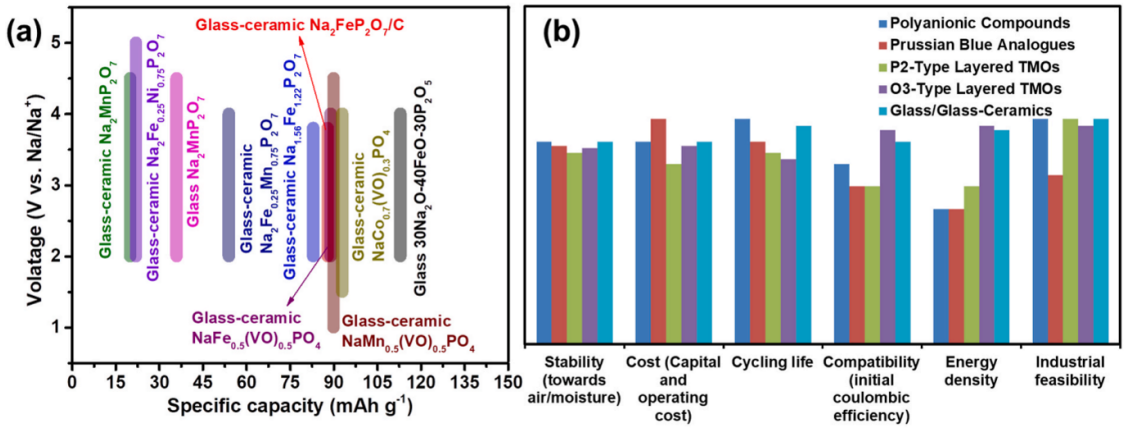

Figure 1.6. Comparison of SIB cathode materials. a) Voltage *vs* specific capacity for various glass, glass-ceramic, and ceramic cathode materials. The materials are color-coded and labeled with their compositions. b) Performance metrics for different classes of cathode materials, including polyanionic compounds, Prussian blue analogues, P2-type layered transition metal oxides (TMOs), O3-type layered TMOs, and glass/glass-ceramics. The metrics cover stability, cost, cycling life, compatibility, energy density, and industrial feasibility. Each material class is represented by a different color, allowing for easy comparison across multiple performance criteria. Figure adapted from [31].

easier electronic conductivity through small polaron hopping mechanisms carrying our transitions between vanadium's low and high valence states [34, 35]. This characteristic makes them highly valuable for applications in solid-state physics and chemistry.

The multiplicity of V oxidation states not only contributes to electronic conductivity but also leads to a diversity of geometric configurations and local structural environments within the glass matrices. This significantly impedes the understanding and characterization of these materials. In vanado-based glasses, the prevalent oxidation states of vanadium (+4 and +5) result in a wide range of vanadium-oxygen coordination geometries, including tetrahedral, trigonal pyramidal, square pyramidal, and distorted octahedral structures. This variability in coordination and structure is heavily dependent on the glass composition and contributes to the material's complexity. Despite extensive experimental investigation into vanado-based glasses, the detailed mechanisms and structures underpinning their properties remain elusive, highlighting the need for further research in this domain.
The growing interest in using G and GC as solid electrolytes and electrodes containing TMOs such as V for LIBs and NIBs is driven by advances in optimizing their crystalline structure to ease rapid Li^+ and Na^+ ion diffusion, improve cycling performance, guarantee superior thermal stability and promote high electronic and ionic conductivity [31]. The increasing study of Na-based G [36–38] and GC [38–45] cathodes underlines the plethora of advantages inherent in this class of materials. By increasing the operating voltage of cathode materials while maintaining specific capacity, battery performance and energy density can be significantly improved. This is illustrated by the use of high-voltage redox couples such as Mn^{4+}/Mn^{3+}, Co^{4+}/Co^{3+}, Ni^{4+}/Ni^{2+}, Fe^{3+}/Fe^{3+}, and $V^{5+}/V^{4+}/V^{3+}$. Various classes of G and GC have been studied as cathode materials for LIBs and NIBs, including Li(Na) iron phosphate G, Li(Na) iron pyrophosphate GC, Li(Na) manganese pyrophosphate G and GC ($Na_2MnP_2O_7$), Li(Na) iron-manganese pyrophosphate GC ($Na_2Fe_xMn_{1-x}P_2O_7$), Li(Na) iron-nickel pyrophosphate GC ($Na_2Fe_xNi_{1-x}P_2O_7$), and mixed polyanion G and GC ($Li/NaM_{1-x}(VO)_xPO_4$ with M = Fe, Mn and Co). Table 1.1 summarizes G and GC systems developed in recent years as cathodes in LIBs and NIBs, detailing crystalline phases, electrochemical properties, and thermal stability (often expressed as $\Delta T = T_c$ - T_g, with T_c being the crystalline temperature and T_g the glass transition temperature).

The intricate structure of polyanionic Li- and Na-VPG, also referred to as vanadophosphate in the literature, has been somewhat overlooked, particularly the sodium-based variants, which have garnered minimal focus. The inclusion of V_2O_5 introduces a variety of structural configurations, depending on whether it acts as a glass former or modifier, particularly evident when PO_4 tetrahedra are fully polymerized, or as a glass modifier, especially when present at low concentrations [36]. Vanado-phosphate glasses (VPGs) are renowned for their semi-conductive properties, attributed to polaron hopping mechanisms made possible by the presence of vanadium ions in mixed valence states (V^{4+} and $^{5+}$) [35, 46]. The electronic transport in VPGs hinges on the mobility of small polarons[34, 35], with the degree of conductivity closely linked to the V^{4+}/V^{tot} ratio. This is due to the distinct electronic configurations of V^{4+} and V^{5+} ions, which form interconnected polyhedral pathways conducive to polaron movement [46, 47]. The stability of VPGs and their electronic properties are significantly influenced by the vanadium concentration within the glass matrix. An increase in vanadium content stabilizes the glass structure, decreasing the likelihood of vanadium reduction and altering the V^{4+}/V^{tot} ratio. This ratio is also sensitive to processing conditions, such as the cooling rate post-melt, where a loss of oxygen can result in the reduction of V^{5+} to V^{4+} ions [47].
Key structural determinants of VPGs' electronic behavior include the prevalence of V^{4+}–

O –V^{5+} linkages, the coordination number of vanadium, and the inter-vanadium distances. Despite extensive research, a definitive structural model for VPGs is not available yet, with various studies proposing different configurations that impact polaron hopping efficiency [48]. Alkaline ion doping introduces additional complexity to the conductivity mechanisms within VPGs. The incorporation of ions like Li^+, Na^+, or K^+ contributes to the total conductivity by providing an ionic mechanism alongside electronic polaron hopping. This duality of conduction pathways enables the use of alkali-doped VPGs as cathode materials in solid-state batteries. The precise balance between electronic and ionic conductivity, however, is highly dependent on the glass composition, specifically the alkali content and type, which can influence the network structure and, consequently, the dominant conductivity mechanism [48, 49]. In essence, the semi-conductive behavior of VPGs arises from a complex interplay of structural features and compositional variables, making them a subject of ongoing technical inquiry for their potential in advanced electronic and energy storage applications.

Lithium-vanadophosphates (LVP) glasses have been studied as parental glass for the synthesis of GC such a β-$LiVOPO_4$ [50] and $Li_3V_2(PO_4)_3$ [51, 52]. These studies have demonstrated the feasibility of producing relatively high-performing LVP glass-ceramics cathode materials starting from parent LVP glasses via a comparatively straightforward synthetic process (see Section 1.8) [51]. The wide range of applications of Li/Na VPG qnd VPGC has motivated numerous experimental studies, employing techniques such as X-rays and Neutrons diffraction [53–55], Raman Spectroscopy [56], Nuclear Magnetic Resonance (NMR) [57, 58], X-ray Photoelectron Spectroscopy (XPS) [59], Infrared Spectroscopy (IR) [60], Extended X-ray Absorption Fine Structure (EXAFS) [61, 62], and X-ray Absorption Near-Edge Structure (XANES) [59, 62, 63]. Nevertheless, the determination of the local coordination environment of V sites remains a major challenge. One of the key issues is related to the identity of the coordination state of V ions, in relationship with V sites other than V^{5+} (V^{4+} and V^{3+}) conferring a (para)magnetic character to the system and preventing the use of some experimental techniques [58].
An additional source of debate stems from the existence of V^{4+} in four-fold coordination in silicate and phosphate glasses [59, 64, 65]. For instance, XPS and XANES measurements provided evidence for the presence of V^{4+} in four-fold coordination in aluminoborosilicate glasses containing high vanadium content [59]. Similarly, in VP glasses, 1D/2D $^{31}P/^{31}V$ magic angle spinning NMR techniques and advanced pulsed electron paramagnetic resonance (EPR) [57] pointed toward V^{4+} ions in four-fold coordination. However, in amorphous Na_2O-V_xO_y-P_2O_5 [66] and crystalline vanadium oxides and VP systems [63, 67–69], V^{4+} four-fold coordination is not found, and only V^{5+} is widely reported to be able to accommodate the tetrahedral coordination. Therefore, it appears that the lack of agreement between experiments and theory calls for further work improving our knowledge of the coordination state of V in vanadophosphate glasses.
Prior to stepping into the current state-of-the-art challenges in Li/Na VPG and VPGC, the subsequent section will outline essential definitions, fundamental concepts, and principal preparation methods for glass and glass-ceramic materials, as detailed in Section 1.3.

Table 1.1. Overview of G and GC materials employed as cathodes for LIB and NIBs. In part, adapted from [31].

Glass composition	Crystalline phase	Active system	Voltage range (V)	ΔT (K)	Electrical conductivity (G/GC) at 300K (S/cm)	Capacity (theo. / discharge) (mAh/g)
$33.3Li_2O$–$33.3V_2O_5$-$33.3P_2O_5$ [50]	β-$LiVOPO_4$	G/GC	3.0–4.3	348-388	5×10^{-10} / 1.7×10^{-7}	–
$37.5Li_2O$–$25V_2O_5$ - $37.5P_2O_5$ [51]	$Li_3V_2(PO_4)_3$	G/GC	3.0–4.3	433	7.7×10^{-9}	132 / 117–126
$25Li_2O$–$50V_2O_5$-$25P_2O_5$ [70]	–	G	1.5–4.5	373	5×10^{-8}	75
$30Na_2O$–$40FeO$–$30P_2O_5$ [37]	$Na_2FeP_2O_7$	G	2.0–4.0	343	10^{-12}–10^{-10}	–/ 115
$Na_2MnP_2O_7$ [38]	$\beta Na_2MnP_2O_7$	G/GC	2.0–4.5	348	–	80 / 36
$Na_2MnP_2O_7$ [38]	$Na_2MnP_2O_7$ (layer)	GC	2.0–4.5	–	–	– / 20
$Na_2FeP_2O_7$ [39]	$Na_2FeP_2O_7$	GC	2.0–3.8	402	–	97 / 88
$Na_{1.56}Fe_{1.22}P_2O_7$ [40]	$Na_2FeP_2O_7$ (P $\bar{1}$ type)	GC	2.0–3.8	350	–	– / 83
$Na_2Fe_{0.25}Mn_{0.75}P_2O_7$ [42]	β-$Na_2MnP_2O_7$ (layer)	GC	2.0–4.0	331	$\sim 10^{-13}$	– / 54
$Na_2Fe_{0.25}Ni_{0.75}P_2O_7$ [43]	$Na_2NiP_2O_7$	GC	2.0–5.0	364	–	– / 21.8
$NaFe_{0.5}(VO)_{0.5}PO_4$ [44]	$Na_2FeP_2O_7$	GC	2.0–4.0	387	5.14×10^{-7}	149.42 / 89
$NaMn_{0.5}(VO)_{0.5}PO_4$ [45]	$Na_2MnP_2O_7$	GC	1.0–4.5	456	5.92×10^{-7}	152 / 90
$NaCo_{0.7}(VO)_{0.3}PO_4$ [41]	$Na_2CoP_2O_7$	GC	1.5–4.0	437	6.41×10^{-7}	– / 93

1.3 The glassy state of matter and glass-ceramic materials

1.3.1 The glass state of matter

Glasses, also referred to as vitreous materials, have a non-crystalline structure similar to that of amorphous materials (materials lacking long-range periodic order). However, unlike glass, amorphous materials do not undergo a glass transition under thermal conditions. One of the most detailed definitions of the nature of glasses can be found in the work by E. D. Zanotto et al. in 2017: *Glass is a nonequilibrium, non-crystalline condensed state of matter that exhibits a glass transition. The structure of glasses is similar to that of their parent supercooled liquids (SCL), and they spontaneously relax toward the SCL state. Their ultimate fate, in the limit of infinite time, is to crystallize* [71]. The conventional enthalpy versus temperature diagram (see Fig. 1.7, left) delineates the key phases involved in the process of glass formation. It encompasses four primary stages: firstly, the thermodynamically stable liquid phase existing above the melting point (at temperature Tm), which is incapable of undergoing crystallization; secondly, the metastable supercooled liquid (SCL) phase existing between Tm and the glass transition temperature (Tg), wherein crystallization becomes feasible over time upon surpassing a thermodynamic barrier; thirdly, the unstable glass phase below Tg, which exhibits spontaneous relaxation to the SCL phase at non-zero temperatures (gray arrow in Fig. 1.7 left). The glass transition occurs precisely at Tg, a temperature where the experimental time aligns with the average structural relaxation time of SCL [71].

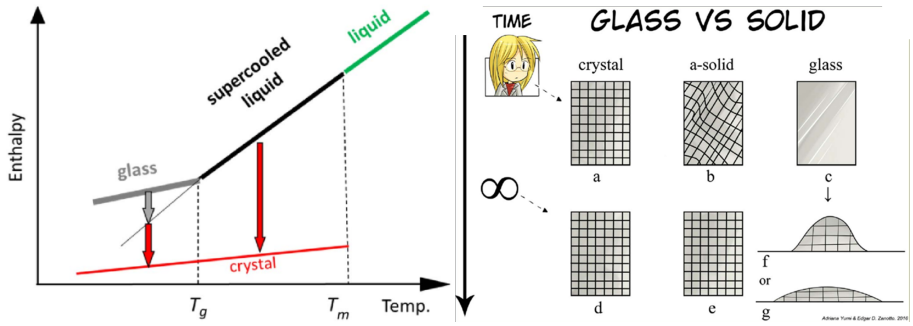

Figure 1.7. Left: Enthalpy as function of temperature graph illustrating the thermal behavior of a glass-forming material in four discernible states (liquid, supercooled liquid, glass, and crystal). Right: Structural evolution of a crystalline solid, an amorphous solid, and a glass over both human and infinite time scales. Adapted from [71].

Conversely, glass experiences a temperature-dependent transition back to SCL at Tg. Similar to SCL, glass can ultimately crystallize (red arrow in Fig. 1.7, left) following an extended period, specifically, an observation time considerably longer than the relaxation time. Ultimately, below Tm temperatures, the crystalline phase emerges with a well-ordered atomic structure at both short- and long-range, signifying stability.
Fig. 1.7 (right) presents the morphology of a crystal, amorphous solid (a-solid), and glass at a human scale, along with their transformations over an infinite duration. While crystalline solids typically maintain their structure and form under environmental pressures indefinitely, a-solid and glass possess the potential to crystallize. a-solids may undergo recrystallization through atomic diffusion given a sufficiently extended time. In the case of glass, they exhibit spontaneous relaxation, flow, and deformation in response to gravitational forces, eventually culminating in crystallization upon continuous heating or over an infinitely protracted period at any positive temperature. By combining the properties of crystalline and glass materials, a new family of materials called glass-ceramic materials

can be produced.

1.3.2 Glass-ceramic materials

First introduced in 1957 by Stanley Donald Stookey, the term GC was used to describe a new family of materials made from special glasses containing nucleating agents, which then undergo controlled crystallization of the glass particles [72]. The definition of GC has since evolved significantly over the last few decades with the development of new and more advanced glass and ceramic processing techniques (co-firing, additive manufacturing, laser patterning), as well as new compositions of nano and micro structures, amplifying the applications and performance of GCs. J. Deubener et al. proposed the following updated and comprehensive definition of GC in 2018, *Glass-ceramics are inorganic, non-metallic materials prepared by controlled crystallization of glasses via different processing methods. They contain at least one type of functional crystalline phase and a residual glass. The volume fraction crystallized may vary from part per million (ppm) to almost 100 %* [73]. In the field of GC production, it is crucial to acknowledge that not all glasses are amenable to crystallization. Certain glasses exhibit a level of "stability" that impedes crystallization, making them challenging to transform into GC. Conversely, some glasses crystallize with excessive ease, often resulting in an uncontrolled crystallization process and the development of an undesirable microstructure [74]. Thus, the composition of the base glass emerges as a pivotal factor in the creation of a GC material of acceptable quality. The GC manufacturing procedure can be summarized in two main phases described in Fig. 1.8: preparation of optically homogeneous glass by different techniques (sol-gel, deposition, melt-quenching) followed by internal crystallization through controlled heat treatments to achieve a pore-free and good shape product with the desired functionality.

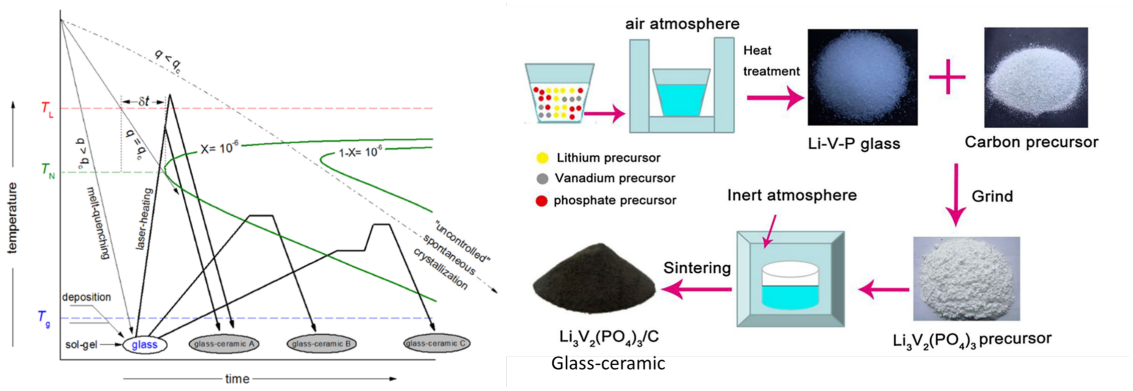

Figure 1.8. Left: Schematic illustration of glass-ceramic (GC) production from glass. Glass formation through melt quenching is observed for $q \geq q_c$, while spontaneous "uncontrolled" crystallization initiates for $q < q_c$. q_c represents the critical cooling rate, T_L, T_N and T_g are liquidus temperature also called melting temperature (Tm), nose temperature and glass transition temperature respectively, X is the crystal fraction and δt the minimum time required to achieve X=10^{-6} crystal fraction. Glass-ceramics A are achieved through cooling, while glass-ceramics B and C are transformed via heat treatment in one or two stages, respectively [73]. Right: Schematic illustration of the microcrystalline glass–ceramic synthesis process of $Li_3V_2(PO_4)_3$ starting from the parental glass 37.5Li_2O-25V_2O_5-37.5P_2O_5 [51, 75].

1.4 Brief state of the art and open challenges in modeling G and GC materials

The field of materials science is evolving due to the contribution of atomic-scale modeling, which is improving our understanding of complex materials. Atomic-scale modelling emerges as a powerful tool, providing unprecedented insights into microscopic behaviors.

The pursuit of accuracy in this kind of simulations has been crucial, enabling us to explore a wide range of materials, revealing properties, structures, and phenomena often beyond experimental reach. Different computational modeling schemes, depicted in Fig. 1.9, cater to diverse time and size scales, offering varying scales of observation and levels of accuracy. Density Functional Theory (DFT) and First-Principles Molecular Dynamics (FPMD) play fundamental roles in the meticulous modeling of materials behavior, albeit with inherent constraints. Machine learning (ML) has surged across scientific disciplines, accelerating computational schemes for understanding material phenomena. One growing field where ML schemes have been important is the so-called class of Machine Learning Interatomic Potentials (MLIP). MLIP are a promising approach to solve challenging (and often, unaffordable) problems in materials sciences that were previously neither accessible to classical force fields nor to costly DFT and FPMD methods (Fig. 1.9).

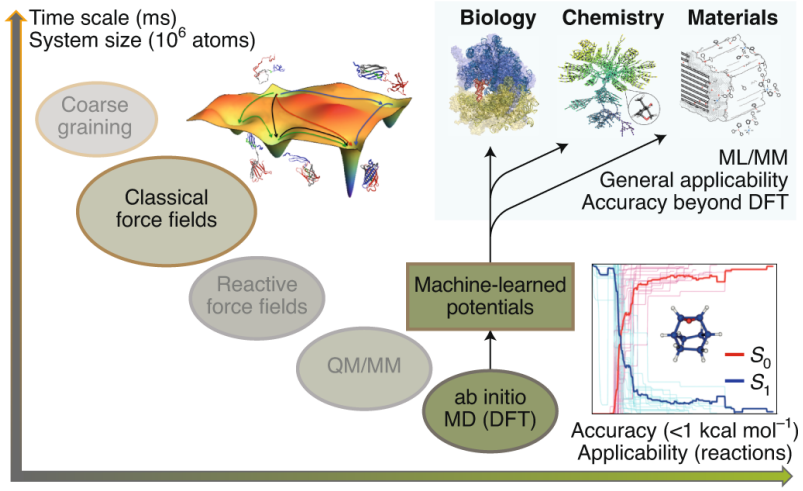

Figure 1.9. Overview of computational methods in materials science, showcasing the trade-off between system size/time scales and accuracy/applicability in dynamical approaches. The plot on the right depicts a simulation illustrating the dynamics of an excited state transition from S_1 to S_0, necessitating the use of ab initio methods to determine the properties of the excited state [76].

Recently, it has become evident that research efforts take advantage of atomistic simulations exploiting MLIP as a class of CMD tools. The accuracy and performance of any MLIP hinge on the quality of databases from DFT and FPMD calculations. Recent MLIP advancements have bridged the accuracy gap between classical MD and FPMD, opening new frontiers in materials research. This breakthrough allows classical MD simulations to approach the precision of FPMD, allowing to bypass limits to size and time scales.
In the context of polyanionic compounds, first-principles simulations have played a crucial role in elucidating structural, dynamical, and electronic properties of such materials. Meng and Domablo have highlighted how first-principles calculations can accelerate the search for energy storage electrode materials for LIBs by predicting relevant properties such as crystal structure, electronic structure, conductivity, hopping rate, thermal stability and ionic diffusion, and elucidating their link to the material's structural components [77]. Nevertheless, despite these abilities, the authors acknowledge that several challenges cannot be met when predicting new mechanisms beyond intercalation and, more generally, nanoscale material properties as those pertaining to surfaces and interphases, currently beyond the reach of first-principles calculations.
As an example worth quoting, Zhang and colleagues conducted an investigation into the mechanism of Na^+ ion migration within the Na_2MnSiO_4 structure, as well as in $Na_xLi_{2-x}MnSiO_4$ (with x values of 2, 1, and 0) using first-principles calculations. Their

computational findings revealed that the diffusion pathways observed in Na_2MnSiO_4 closely resembled those found in Li_2MnSiO_4. Additionally, it was observed that the diffusion of Na^+ ions within the Na_2MnSiO_4 structure occurred even more rapidly than the diffusion of Li^+ ions within the lithium analogue [78]. Recently, H. M. You et al. conducted a study on electron transport between the anode surface and the electrolyte in LIBs by modeling the anode/SEI/electrolyte interface using various methods such as CMD and FPMD [79]. The authors highlighted the difficulty of fully capturing the complex interactions between the multiple components of the anode/electrolyte system due to the high computational cost and limited time and length scale of AIMD simulation. In addition, they highlighted the limited accuracy of classical results correlated to the quality of the force field. To overcome these limitations in time and length scales while preserving accuracy, the authors proposed the use of techniques parameterized by ab initio-based computations such as deep neural networks (NN) with is a subset in the domain of artificial intelligence.
In the emerging field of artificial intelligence for materials science, machine learning-driven interatomic potentials are increasingly recognized as highly promising tools for the study of atomistic and nanoscale materials such as batteries components. This advance offers quantum-mechanical level accuracy at a remarkable speed, outperforming current modelling techniques by several orders of magnitude. In the second chapter of this thesis further information on this powerful tool can be found.

Experimental studies dominate the literature concerning polyanionic glasses and glass-ceramics based on sodium phosphate and vanadium materials. However, the complex compositions and resulting structures pose challenges for the experimental elucidation of the properties of these materials. FPMD realizations are currently lacking in this respect. Existing research relies mainly on the empirical methods of classical molecular dynamics, where the accuracy of the results depends on the efficiency of the force field used. Classical molecular dynamics (CMD) [32, 59, 80–84], non-constant force field MD (ncMD) [60] and reverse Monte Carlo (RMC) simulations [53–55, 85] have been predominantly employed on alkali-ion-containing VP glasses. Also, CMD has been increasingly used for modeling VP glasses, by complementing the experimental findings and offering qualitative insights into their structural properties. However, a quantitative assessment of the structural properties and the underlying electronic structure is still missing.

Previous CMD works by Ori[80], Broglia[48, 81], and Deng[86] et al. investigated the structure and diffusion behavior of Li/Na ions in Li/Na vanado-phosphate glasses using CMD simulations. For instance, Broglia et al. and Montorsi et al. reported that Li/Na ion self-diffusion coefficients are highly influenced by alkali ion content, while activation energy appears to be independent of Li/Na concentration and the number of V^{4+}–O–V^{5+} linkages promoting electron conductivity was linearly related to the V_2O_5/P_2O_5 ratio [81]. In 2021, L. Deng et al. conducted a study using CMD to examine the structure and bonding characteristics of sodium vanadate phosphate glass with a composition of $20Na_2$–$51.66V_2O_5$–$8.34VO_2$–$20P_2O_5$. Their findings revealed that the concentration of vanadium significantly impacts its local environment within the glass matrix. At lower vanadium concentrations, vanadium tends to exhibit weak coordination (4 or 5), while higher concentrations can result in a shift to a higher coordination environment, such as trigonal or octahedral bipyramidal units [86]. In Table 1.2, we present the glass compositions for LVPG and NVPG that have been simulated using classical molecular dynamics (CMD).

Table 1.2. Summary of different NVP and LVP glass compositions simulated by classical MD from the literature.

Composition	FF	Ref.
$20.0Na_2O$–$51.67V_2O_5$-$8.33V_2O_4$-$20P_2O_5$	[80, 86, 87]	[80, 86, 87]
$44.9Na_2O$–$7.2V_2O_5$-$2.9V_2O_4$-$44.9P_2O_5$	[80, 87]	[48]
$40Na_2O$–$14.9V_2O_5$-$5.2V_2O_4$-$40P_2O_5$	[80, 87]	[48]
$33Na_2O$–$29.6V_2O_5$-$5.2V_2O_4$-$33P_2O_5$	[80, 87]	[48]
$20Na_2O$–$55.5V_2O_5$-$4.5V_2O_4$-$20P_2O_5$	[80, 87]	[48]
$10Na_2O$–$75.1V_2O_5$-$4.9V_2O_4$-$10P_2O_5$	[80, 87]	[48]
$23.3Na_2O$–$26.4CaO$-$5.3V_2O_5$-$42.9SiO_4$-$2.1P_2O_5$	[84]	[88]
xNa_2O–$(90\text{-}x)V_xO_y$–$10P_2O_5$	[89]	[90]
$45Li_2O$–$7.5V_2O_5$-$2.5V_2O_4$-$45P_2O_5$	[80, 87]	[81]
$10Li_2O$–$18V_2O_5$-$12V_2O_4$-$60P_2O_5$	[80, 87]	[81]
$10Li_2O$–$34.5V_2O_5$-$15.5V_2O_4$-$40P_2O_5$	[80, 87]	[81]
$33.3Li_2O$–$24.7V_2O_5$-$8.7V_2O_4$-$33.3P_2O_5$	[80, 87]	[48]
$33.3Li_2O$–$17.4V_2O_5$-$16.0V_2O_4$-$33.3P_2O_5$	[80, 87]	[48]

1.5 Overall motivation, project's positioning and objectives, and organization of this thesis

As we have briefly seen in this chapter, the search for innovative solutions for cleaner and sustainable energy is a current priority in energy research. In light of this, glasses and glass-ceramic materials are promising prospects for the advancement of next-generation solid-state batteries. Particularly as electrode materials, they stand out for enhancing safety and performance, higher environmental sustainability, and simplifying synthesis and design processes. However, there are still a number of limitations to be surmounted for G and GC electrodes in order to achieve controlled ionic and electronic conductivity, structural and electrochemical stability, long cycle times and suitable properties at the electrolyte-electrode interface. This is mainly due to a lack of fundamental understanding of their atomic-scale structure, chemical bonding and the mechanisms underlying ion dynamics prevents their full potential from being exploited, thus limiting practical applications.

In this Ph.D. thesis, atomic-scale modeling is employed to enrich our understanding of a particularly promising category of potential electrode materials: polyanionic sodium vanado-phosphate glasses within the αNa_2O-βV_xO_y-γP_2O_5 (NVP) system. This is motivated by the current performance of similar Li-based systems as cathode materials, while Na-based systems have only been minimally explored. Interest in Na-based materials stems from the abundance and cost-effectiveness of Na resources compared to Li. However, the lack of information on NVP glass-based systems hinders the design of high-performance cathode materials for this compound class. NVPs are abundant, cost-effective, and environmentally friendly materials. Some glass systems, such as V_2O_5-P_2O_5, B_2O_3-V_2O_5, or MoO_3-P_2O_5, have shown promise as cathode electrode materials [91]. The addition of Li_2O or Na_2O enhances ionic conductivity alongside electronic conductivity through transition metal oxidation states [92]. Research on Li_2O- or Na_2O-based glasses has been extended to glass ceramics, benefiting from nanocrystals like V_2O_5 or metastable phases for enhanced conductivity. Despite limited studies, NVP G and GC hold potential, with only a few compositions explored [36, 57, 86, 93].

The main objective of this research project is the modeling of disordered NVP materials of interest as electrode materials for energy storage systems. More specifically, this means applying atomic-scale modeling techniques, such as DFT-FPMD, in conjunction

with machine learning techniques to study and design NVP materials with superior structural, chemical and electrochemical characteristics, suitable for energy storage systems. The idea is to establish solid benchmarks for NVP materials and disseminate these results to the wider scientific community. In addition, the project also aims at exploiting the trajectory data obtained from accurate DFT-FPMD calculations to build a comprehensive database. This database will serve as an input for machine learning algorithms to develop a machine learning interatomic potential, making possible the rapid and efficient exploration of large, realistic models of NVP G and GC materials.
The structure of this thesis is as follows: beginning with an introductory chapter 1, which elucidates the fundamental concepts relating to energy storage systems and outlines the scope and objectives of this study, the subsequent chapters follow systematically by describing the main objectives and results obtained in this thesis:

- Chapter 2 is devoted to the various computational methodologies employed in this research work.
- In Chapter 3, we focus on a case study (liquid $GeSe_2$) intended to guide, as a specific, benchmark example, the development of a machine learning potential using FPMD data. The availability of in-house FPMD data on this particular system and related chalcogenide disordered network has allowed capturing the subtleties inherent in the conjugate use of artificial intelligence and atomic-scale modelling,
- Chapter 4 takes a close look at the local atomic attributes as well as the structural and electronic characteristics of binary $50V_xO_y$-$50P_2O_5$ (VP50) glass.
- Chapter 5 features an in-depth analysis of various ternary systems within the framework of NVP glass models, encompassing discussions of their structural, electronic and dynamic properties;
- Chapter 6 describes the genesis and the realization of interatomic potential machine learning techniques suitable for NVP glasses exploiting information gleaned from previous FPMD data;

Finally, Chapter 7 contains concluding remarks, offering a unique perspective that integrates preliminary findings with a forward-looking discussion on the electronic conductivity properties of NVP glasses and the potential of NVP glass-ceramic materials. This chapter considers the implications of atomistic modeling for future research in this field.

Chapter 2

Computational Methods

Summary

This chapter offers an insight into the computational methodologies employed in this thesis. It briefly presents atomic-scale modeling techniques based on classical molecular dynamics, first-principles molecular dynamics and machine learning interatomic potentials employed within classical molecular dynamics to extent the temporal and spatial scales of atomic-scale modelling.

2.1 Introduction

The primary aim of this chapter is to elucidate the underlying physical principles of each computational method employed and examine their strengths and current limitations. First, classical molecular dynamics (CMD) is introduced together with some generic concepts of statistical mechanics and thermodynamics. The main issue about CMD is its inherent limited power in describing quantitatively the subtleties of chemical bonding. This requires the account of quantum mechanics in the calculation of energies and forces and, as a consequence, the introduction of its first-principles counterpart, i.e. first-principles molecular dynamics (FPMD). Two approaches of FPMD are recalled: Bohr Oppenheimer Molecular Dynamics (BOMD) and Car-Parrinello Molecular Dynamics (CPMD). At this point it is important to underline a very special and important feature of FPMD calculations, quite often overlooked when presenting the technique at the beginner and/or introductory level. FPMD is based on the classical equations of motion (Newtonian dynamics) as much as CMD and, in this respect, one cannot invoke any quantum mechanics concepts to underscore the differences between the two approaches. The quantum character of FPMD lies entirely in the account of quantum mechanics in the calculation of the energy and forces through the explicit account of the electronic structure described via density functional theory. Needless to day, this means a much higher computational cost, since, in principle, one needs a full electronic structure calculation for each atomic (ionic) configuration.

Having established the main differences between CMD and FPMD and referring to the content of this chapter for further details, it remains true that FPMD is characterized by a very high computational demand, somewhat limiting the size of the systems under investigation and the length of the temporal trajectories needed to take statistical averages. In this context, the integration of artificial intelligence into atomic modeling has made possible the development of self-learning interatomic potentials. The final section of this chapter looks at applications of these powerful machine learning tools in materials science, with a particular focus on glass and glass-ceramic modeling. Some final considerations on the comparative performances of FPMD, CMD and CMD based on MLIP end this chapter.

2.2 Classical molecular dynamics

Molecular dynamics is a powerful computational technique to study the properties (structure, dynamics, transport) of condensed matter systems at atomic level by solving the Newton equation of motion [94]. The idea is to connect statistical mechanics to thermodynamics by taking time averages on extended intervals of time at the equilibrium. Also, processes and mechanisms can be followed in real time, by granting to molecular dynamics the well known definition of "thought experiments". This method was first introduce by Alder and Wainwright in 1957 to study the phase diagram of hard-sphere system [95]. The first simulation employing a realistic potential (specifically, a truncated Lennard-Jones potential) was carried out in 1964 by A. Rahman to investigate the correlations in the motion of atoms in liquid argon [96]. Ten years later, F. Stillinger and A. Rahman studied liquid water using MD simulations [97]. This method was subsequently extended to a variety of other systems, in part due to the development of computational resources allowing for significant averages being taken on equilibrium trajectories. Nowadays, MD simulations has become a widely adopted tool in the field of materials science, medicine, chemistry and biophysics to elucidate any sort of macroscopic properties that can be expressed in terms of a microscopic variable acting as an atomic-scale counterpart. Typically, on very general

terms, and for a system of N atoms, the Hamiltonian employed for a classical molecular dynamics run is given by:

$$\mathcal{H}(\mathbf{R}^N, \mathbf{P}^N) = \sum_i^N \frac{\mathbf{p}_i^2}{2m_i} + V(\mathbf{R}^N), \tag{2.1}$$

where $\mathbf{R}^N = (\mathbf{r}_1, \mathbf{r}_2, \ldots, \mathbf{r}_N)$ and $\mathbf{P}^N = (\mathbf{p}_1, \mathbf{p}_2, \ldots, \mathbf{p}_N)$ are the position and momentum vectors of the N atoms, m_i is the mass of the i^{th} particle and $V(\mathbf{R}^N)$ is the potential energy function of the system. Since we are considering here CMD, the potential energy function depends on the coordinates only, with strictly no explicit dependence on the electronic structure of the system (no explicit dependence on whatsoever orbitals or eigenfunctions or any functional form referring to the electronic density).
The same is true for the force acting on each particle that can be calculated from the gradient of the potential energy function (Eq. (2.2))

$$\mathbf{F}_i(\mathbf{R}^N) = -\frac{\partial V(\mathbf{R}^N)}{\partial \mathbf{r}_i}, \tag{2.2}$$

and the motion of a single particle is describe by the Newton's equation of motion (second law):

$$m_i \frac{\partial^2 \mathbf{r}_i}{\partial t^2} = \mathbf{F}_i(\mathbf{R}^N) \tag{2.3}$$

The general procedure for classical MD simulations follows the flowchart illustrated in Fig. 2.1 in which the MD technique can be understood as an iterative numerical scheme for solving Newton's equation of motion (EOM). In step 4 of Fig. 2.1, the atomic position and velocity are updated by integrating the EOM using algorithms such as Euler [98] or Verlet algorithms [99–101]. The Verlet Leap-frog [102, 103] and velocity Verlet [104–106] are the most commonly used variants of Verlet's algorithm.
Care should be exercised when applying the Verlet algorithm in its original version since

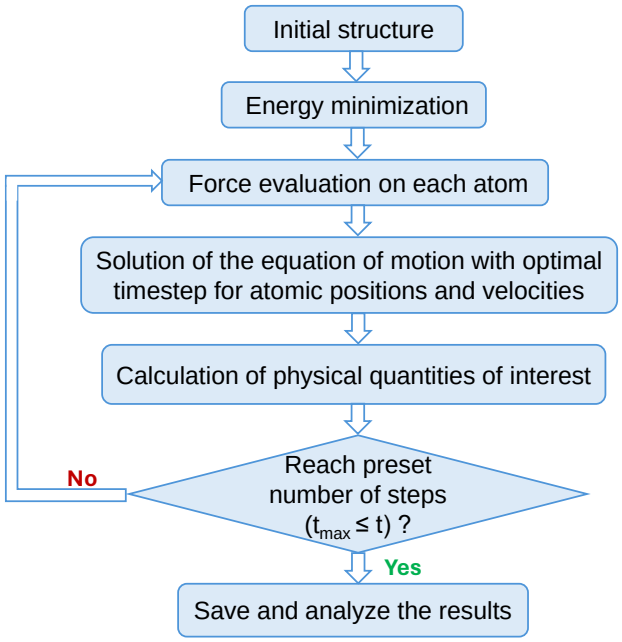

Figure 2.1. Step-by-step procedure for conducting MD simulations.

the velocities of the atoms are not directly integrated into the equations of motion. At first sight, this cannot be taken as a serious problem, since the kinetic energy leading to

the temperature of the system is not sensitive to changes occurring on the time scale of a single time step. In other words, ordinary Newton equations of motions do not depend on velocities. However, the situation changes, for instance, when some form of temperature control is introduced, as explained in one of the next sections devoted to thermostat. In that case, one needs to have positions and velocities at the same time to ensure proper integration of the equations of motion. This difficulty requiring additional effort for their determination. This difficulty has been circumvented by the velocity Verlet algorithm, used in all molecular dynamics simulations in this study, which updates atomic positions and velocities based on second- and first-order Taylor expansions of position ($\mathbf{r}_i$(t+Δt)) and velocity ($\mathbf{v}_i$(t+Δt)) at time t+Δt, respectively. More details on the implementation of the velocity Verlet algorithm are available in the literature and do not need to be recalled here since they are routinely used in any current version of available molecular dynamics codes, both classical or first-principles.

2.2.1 Potential energy functions/Interatomic potentials/ Force Fields: different terminologies for the same notion

There are various terminologies to define the interatomic potentials acting between the atoms in the framework of a classical molecular dynamics calculation. A consistent number of practitioners prefer to name these potentials Force Fields (FF). Throughout this manuscript we shall use either the notion of "interatomic potentials" or the one of "force fields" equivalently. These tools typically consist of terms representing bonded interactions (such as bonds and various kinds of angles) and non-bonded interactions (such as van der Waals and electrostatic interactions). They are used to calculate forces acting on atoms, which are then employed to update atomic positions and velocities according to Newton's equations of motion. In this thesis, we have selected and tested distinct empirical FF schemes for our CMD simulations combining short-range and long-range interactions, detailed as follows:

- The Morse [107] type interatomic potential named BMP-shrm in ref. [108] which combines the long-range Coulumb interaction, the short-range Morse function and a repulsive term (from the original PMMCS potential [87], Eq. (2.4)) with the harmonic three-body raster functional (Eq. (2.5)). The two-body potential parameters for V^{5+}–O and V^{4+}–O are taken from ref. [80]. The three-body potential parameter for the triad P–O–P, P–O–V^{5+}, and V^{5+}–O–V^{5+}, taken from ref. [84, 88, 108].

$$U_{ij} = \frac{Z_i Z_j e^2}{r_{ij}} + D_{ij}\left(\left\{1 - \exp\left[-a_{ij}(r_{ij} - r_{ij}^0)\right]\right\}^2 - 1\right) + \frac{B_{ij}}{r_{ij}^{12}}, \tag{2.4}$$

$$U'_{ijk} = \frac{K_{ijk}}{2}\left(\theta_{ijk} - \theta_{ijk}^0\right)^2 \exp\left[-\left(\frac{r_{ij}}{\rho} + \frac{r_{jk}}{\rho}\right)\right] \tag{2.5}$$

  Here, D_{ij}, a_{ij} and r_{ij}^0 are the Morse function parameters for the atomic pair $i-j$, B_{ij} is the parameter of a repulsive term acting to prevent atoms collapse at short distances, Z_i is the partial charges of ion i, r_{ij} is the interatomic distance of atoms i and j, K_{ijk} is the force constant parameter and θ_{ijk}^0 the reference angle connected to the $i-j-k$ triplet.

- The Buckingham [109] type pair potential (Eq. (2.6)) from ref. [32, 59] which is a combination of the long-range Coulomb interaction, the short-range Buckingham function and a correction term (Eq. (2.7)) necessary at high temperature when the atoms can move close at unphysically short distances.

$$U_{ij} = \frac{Z_i Z_j e^2}{r_{ij}} + A_{ij}\exp\left(-\frac{r_{ij}}{\rho_{ij}}\right) - \frac{C_{ij}}{r_{ij}^6}, \tag{2.6}$$

$$U'_{ij} = \frac{B_{ij}}{r_{ij}^{n_{ij}}} + D_{ij} r_{ij}^2 \tag{2.7}$$

In these equations ((2.6) and (2.7)), in addition to the others parameters defined previously, A_{ij}, ρ_{ij} and C_{ij} are empirical Buckingham parameters associated to $i-j$ pair. U'_{ij} is the repulsive term used when $r_{ij} \leq r_{ij}^s$ (splice distance), parameters B_{ij}, n_{ij} and D_{ij} are determined at the point where the second derivative of the potential approaches 0 [59].

2.2.2 Periodic boundaries conditions

The use of periodic boundary conditions (PBCs) in MD consists in mimicking the behavior of an infinite system (bulk materials) by reproducing the simulation box in all three dimensions. This approach ensures that only a relatively small number of particles are treated in order to obtain reasonable results that can accurately account for the corresponding experimental data. PBCs assume that the simulated system is surrounded by identical copies of itself in all directions. When a particle exits from one side of the simulation box (unit cell), it re-enters from the opposite side, thus maintaining the continuity of the system. However, in practice, the atomic coordinates are not modified to account for this virtual exit from the central box, since this operation is ensured by an appropriate programmable instructions that automatically search for the shortest distance between pairs of atoms. The same holds true for any part of the first-principles Hamiltonian (see below) that are intrinsically periodic due to the use of a basis set (plane waves) made to have the periodicity of the cell and its replicas.

2.2.3 Thermodynamic ensembles

In MD simulations, different thermodynamic ensembles are used to describe the statistical behavior of a system. These ensembles are a framework to understand the properties of the system under various conditions such as fixed energy (E), temperature (T), pressure (P) or chemical potential (μ). Considering a system of N particles in a unit cell of volume V, we provide in the following a short review of the conceptual framework to capture the differences between the ensembles. However, it should be kept in mind that molecular dynamics produces **temporal** trajectories in the microcanonical (NVE) and canonical (NVT) ensembles (the isothermal-isobar ensemble being an extension of the NVT one in which the volume is allowed to fluctuate to achieve the required average pressure). Therefore, the expressions employed in what follows are given with a purely informative scope and **do not correspond to any actual implementation carried out in this thesis**. In fact, they are based on "probabilities", while within **molecular dynamics one follows the evolution of the system along temporal trajectories instead of sampling the phase space according to a specific probability law**. This is exactly the essence of Boltzmann ergodic hypothesis stating that "the temporal averages and ensemble averages must coincide in the limit of very long time".

i) **Microcanonical Ensemble (NVE):** This ensemble describes an isolated system with a fixed number of particles, volume, and energy. It corresponds to the idea that an isolated system in equilibrium has equal probability (Eq. (2.8)) of being found in all accessible microstates. Ω is the total number of microstates accessible to the system at energy E. It is interesting to note that for the total energy, due to its strict conservation in time in the absence of dissipation, the notions of instantaneous and average quantities are equivalent, making this thermodynamic variable easily accessible within molecular dynamics.

$$p_i = \frac{1}{\Omega} \tag{2.8}$$

ii) **Canonical Ensemble (NVT):** In this ensemble, the system is in thermal equilibrium with a heat bath at constant temperature, fixed number of particles, and volume. The probability to find the system in a given microstate i is related to its energy by the following Eq. (2.9) in which k_B is the Boltzmann constant. The practical realization of the canonical ensemble for molecular dynamics is not straightforward and has required a conceptual breakthrough that will be considered in the next section. On a purely intuitive basis, talking of a "constant temperature" makes little sense for a finite system, since the temperature, as any average quantity (in this case of the kinetic energy) is bound to fluctuate in time. This apparent paradox can be circumvented by noting that the temperature is strictly constant in the thermodynamic limit only (infinite number of particles and infinitely extended trajectory).

$$p_i(E_i) = \frac{\exp(-\frac{E_i}{k_B T})}{\sum_i \exp(-\frac{E_i}{k_B T})} \tag{2.9}$$

iii) **Isothermal-Isobaric Ensemble (NPT):** It describes a system in thermal and mechanical equilibrium with a thermostat at temperature T and a barostat at pressure P. The system not only exchanges heat with the thermostat, but also work/volume with the barostat. The total number of particles remains fixed while the total energy and volume fluctuate. The probability (Eq. (2.10)) of finding the system in a microstate i depends on its internal energy E_i and its volume V_i.

$$p_i(E_i, V_i) = \frac{\exp\left(-\frac{E_i + PV_i}{k_B T}\right)}{\sum_i \exp\left(-\frac{E_i + PV_i}{k_B T}\right)} \tag{2.10}$$

iv) **Grand Canonical Ensemble (μVT):** This ensemble describes a system in equilibrium with a reservoir of particles, allowing for exchange of both particles and energy with the reservoir, while keeping the chemical potential μ, temperature, and volume constant. Eq. (2.11) provides the probability of finding the system in a specific microstate i, which depends on both its energy E_i and the number of particles N_i. The practical realization of this ensemble is quite hard to implement within molecular dynamics and, in any case, goes well beyond all schemes and methodologies employed in this thesis.

$$p_i(E_i, N_i) = \frac{\exp\left(-\frac{E_i - \mu N_i}{k_B T}\right)}{\sum_i \exp\left(-\frac{E_i - \mu N_i}{k_B T}\right)} \tag{2.11}$$

2.2.4 Temperature control: Nosé-Hoover thermostat

One of the most challenging issues faced in the early days of molecular dynamics was the control of temperature (and its instantaneous counterpart, the kinetic energy) to create temporal trajectories compatible with the notion of canonical ensemble. Looking back at the various attempts put forth since the eighties we can mention the approaches by Berendsen [110], Andersen [111] as the most valuable realisations. They were both aimed at introducing of a temperature control rooted into the monitoring of the kinetic energy and its average. However, the most rigorous scheme for a thermostat, fully compatible with statistical mechanics, is due to Nosé, together with a later derivation due to W. G. Hoover. Overall, this technique has been labelled as the Nosé-Hoover [112, 113] thermostat. In what follows, attention will focus mainly on the Nosé-Hoover thermostat, which is the one used in the all the NVT simulations of this thesis.

The Nosé-Hoover thermostat is a rigorous method widely used to control the temperature of a system based on extended Hamiltonian dynamics (see [112, 114] and [113]). In the original idea, Nosé demonstrated that a trajectory compatible with the canonical ensemble (NVT) can be obtained via an additional degree of freedom s coupled with the kinetic energy of a system. This new variable is given a fictitious mass η and velocity $\dot{s}$. Accordingly, the Nosé Hamiltonian is given by:

$$\mathcal{H}_{\text{Nosé}} = \sum_{i=1}^{N} \frac{\mathbf{p}_i^2}{2s^2 m_i} + \sum_{i=1}^{N} U_i(\mathbf{r}_i) + \frac{\mathbf{p}_s^2}{2\eta} + (N_{\text{ind}} + 1) k_b T^{\text{TG}} \ln s \tag{2.12}$$

where $\mathbf{p}_i$ and $\mathbf{p}_s$ are the momentum of atom i and the artificial variable s respectively, T^{TG} is the target temperature of the system. The virtual time t_v governing the Eq. (2.12) is link to the real time t_r by the following relation: $t_v = st_r$.
The Nosé equations of motion that can be obtained from Eq. (2.12) due to their Hamiltonian (Lagrangian) were derived by W. G. Hoover in 1985 by taking advantage of the same formalism but expressed in real time t_r [115]:

$$\dot{\mathbf{r}}_i = \frac{\partial \mathbf{r}_i}{\partial t_r} = s \frac{\partial \mathbf{r}_i}{\partial t_v} \tag{2.13}$$

$$\dot{\mathbf{r}}_i = \frac{\mathbf{p}_i}{sm}; \qquad \dot{\mathbf{p}}_i = s\mathbf{F}_i; \qquad \dot{s} = \frac{sp_s}{\eta}; \qquad \dot{p}_s = \sum_{i=1}^{N} \frac{\mathbf{p}_i^2}{s^2 m} - (N_{\text{ind}} + 1) k_b T^{\text{TG}} \tag{2.14}$$

with $\mathbf{F}_i$ the force acting on atom i.
It is worth noting that the real-time equation of motion (2.14) cannot be obtained directly from the virtual-time Hamiltonian of the Eq. (2.12) but the notion of quantity conserved in time remain true. Hoover introduced a parameter (friction force ζ) fully compatible with the Nosé dynamics:

$$\zeta = \frac{\dot{s}}{s} = \frac{p_s}{\eta} \tag{2.15}$$

With this new parameter, the Nosé-Hoover conserved quantity can be finally written as:

$$\mathcal{H}_{\text{Nosé-Hoover}} = \sum_{i=1}^{N} \frac{\mathbf{p}_i^2}{2m_i} + \sum_{i=1}^{N} U_i(\mathbf{r}_i) + N_{\text{ind}} k_b T^{\text{TG}} \int dt\ \zeta + \frac{\eta}{2}\zeta^2 \tag{2.16}$$

The above conserved quantity is compatible with the following equations of motion (again, it must be kept in mind that these equations cannot be derived directly from Eq. 2.16):

$$\dot{\mathbf{r}}_i = \frac{\mathbf{p}_i}{m}; \qquad \dot{\mathbf{p}}_i = \mathbf{F}_i - \zeta \mathbf{p}_i; \qquad \dot{\zeta} = \eta^{-1} \left(\sum_{i=1}^{N} \frac{\mathbf{p}_i^2}{m} - N_{\text{ind}} k_b T^{\text{TG}} \right) \tag{2.17}$$

The selection of the thermostat's fictitious mass parameter η in the implementation of the Nosé-Hoover algorithm plays a crucial role in ensuring stable and efficient dynamics during simulation. Choosing too low value leads to high temperature fluctuations, causing the ζ variable to oscillate with high frequency, decoupling it from the atomic motion in the system. Conversely, a very high value results in slower response times to changes in system temperature, deferring to exceedingly long times the thermodynamic equilibrium of the system to the desired target temperature. This drawback is, in practice, equivalent to the absence of thermostat itself (this statement being strictly true for an infinite mass). In a recent paper to which I contributed [116] it was shown that Hoover's refinement of the Nosé-Hoover thermostat can be directly traced back in the original theoretical framework implemented by Nosé. Therefore, it appears that the idea by Nosé incorporates the necessary frictional force through a skillful rearrangement of Nosé's initial proposals without any need to go through the Hoover extension.

2.3 First-principles molecular dynamics

Recent advances in materials science, in particular the emergence of new classes of materials, have posed significant challenges for MD simulations. The main obstacle lies in the lack of appropriate analytic potential energy function capable of accurately describing the properties of these complex systems specially when chemical bonds are formed, broken or modified. To achieve a precise understanding of these materials, it is necessary to develop accurate force fields, a task exacerbated by the lack of effective methodologies. One approach consists in performing ab initio (i.e. first-principles) calculations on the system of interest in order to derive the potential energy function from which the forces can be derived. Therefore, there are two reasons underlying the choice of investing substantial resources in performing calculations accounting for the electronic structure of a system. The first is the access to properties depending on the nature of chemical bonding, leading to a realistic description of structure and dynamics. The second has to do with the need of extending as much as possible the time and space scale of atomic scale modelling. Instead of facing the unaffordable task of producing results based on the exclusive use of first-principles techniques, one can set the goal of exploiting them to end up with a reasonably manageable interatomic potential. This idea is the essence of machine-learning approaches that will be detailed later in this work. In what follows, we would like to provide a essential guide of comprehension and use of first-principle molecular dynamics (FPMD) that, in short, can be defined as a molecular dynamics implementation in which the force are derived on the basis of quantum mechanics via density functional theory (DFT).
Density functional theory allows electrons in orbitals to be represented as quantum entities. In this revised perspective, the potential energy function in Eq. (2.2) is replaced by the total energy derived from electronic structure calculations. However, this approach can appear as tedious and extremely demanding, due to its considerable computational cost, as it requires ground-state electronic structure calculations for every atomic position at every time step (see Sec. 2.3.4). We shall see later on in this chapter how the ideas exposed in Sec. 2.3.5 can be taken as an alternative, at certain conditions, to bypass these requirements.

2.3.1 Density functional theory in a nutshell

DFT is a computational quantum mechanical modeling method based on the Hohenberg-Kohn theorem [117]. The ground-state electron density $\mathrm{n}(\mathbf{r})$ uniquely determines the wave function and ground-state energy of a many-body system. The many-body density function $n(\mathbf{r})$ is expressed as linear combination of the square modulus of the wavefunction $\psi_i(\mathbf{r})$ of a giving particle i (Eq. (2.18))

$$n(\mathbf{r}) = \sum_{i=1}^{N_{occ}} = f_i|\psi_i(\mathbf{r})|^2 \tag{2.18}$$

N_{occ} is the total number of occupied orbitals and f_i is the occupation number equal to 2 or 1 in spin-restricted or spin-unrestricted consideration respectively. In quantum mechanics, the wavefunctions have to satisfy the orthogonality constraint of Eq. (2.19)

$$\int d^3r\psi_i^*(\mathbf{r})\psi_j(\mathbf{r}) = \delta_{ij} \tag{2.19}$$

The Kohn-Sham total energy (E_{KS}) of many-body quantum system is defined as a functional of density containing all the electron-electron, electrons-nucleus and nucleus-nucleus interactions:

$$\mathrm{E_{KS}}[\{\psi_i\}] \;=\; \mathrm{E_T}[\{\psi_i\}] + \mathrm{E_H}[n] + \mathrm{E_{XC}}[n] + \mathrm{E}_{eI}[n] + \mathrm{E}_{IJ} \tag{2.20}$$

In this Eq. (2.20), E_T represent the kinetic energy of electrons explicitly defined in Eq. (2.21) and only depends on the electronic wavefunctions.

$$E_T[\{\psi_i\}] = \sum_{i=1}^{N_{occ}} f_i \int d^3r \; \psi_i^*(\mathbf{r}) \left(-\frac{1}{2}\nabla^2\right) \psi_i(\mathbf{r}) \tag{2.21}$$

The second term E_H is the Hartree energy and it represents the classical electrostatic interaction energy arising from the Coulombic repulsion between electrons.

$$E_H[n] = \int\int d^3r \; d^3r' \; \frac{n(\mathbf{r}) \; n(\mathbf{r'})}{|\mathbf{r} - \mathbf{r'}|} \tag{2.22}$$

The third term of Eq. (2.20) ($E_{XC}[n]$) is the exchange and correlation energy (XC), whose explicit form is unknown and which incorporates all quantum (many-body) effects. This contribution aims at calculating the precise density and energy of the ground state of a many-body system. However, due to the unknown form of the XC energy, approximations are required. Considerable effort has been produced over the years to propose efficient approximations for the XC energy. Section 2.3.2 discusses some of these approximations. The fourth term $E_{eI}[n]$ accounts for the electrostatic interaction between nuclei and electrons. This interaction is explicitly defined in Eq. (2.23), where Z_I represents the charge of the nucleus I and R_I its coordinates. The computational cost of this interaction comes from the spatial dispersion of the electrons surrounding the nucleus. More specifically, core electrons, located close to the nucleus, exhibit highly fluctuating wave functions, while valence electrons, located further away, contribute to the chemical bond with more predictable wave function variations [118]. To mitigate the computational demands arising from the erratic wave functions of core electrons, these are treated as inert entities, which do not actively participate in chemical bonding processes. This approach is achieved through the use of pseudopotentials [119–122], that will be treated in more detail later in this chapter.

$$E_{eI}[n] = -\int d^3r \sum_{I=1}^{M} \frac{Z_I \; n(\mathbf{r})}{|\mathbf{r} - \mathbf{R}_J|} \tag{2.23}$$

The last term E_{IJ} in Eq. (2.20) is the classical Coulomb interaction between nuclei I and J with charges Z_I and Z_J respectively as showing in Eq. (2.24) below.

$$E_{IJ} = \sum_{I<J}^{M} \frac{Z_I \; Z_J}{|\mathbf{R}_I - \mathbf{R}_J|} \tag{2.24}$$

2.3.2 Exchange and correlation approximations

As previously stated in Eq. (2.20), the exchange and correlation approximation plays a crucial role in providing an expression for the total energy within DFT, given the stakes inherent to the access of the unknown exact total energy. The exchange-correlation (XC) energy functional can be decomposed into an exchange component, which accounts for the Pauli's exclusion principle and a correlation component, which deals with many-body effects due to electron-electron interactions.

The XC energy is commonly estimated using a variety of functional forms. Fig. 2.2 shows the Jacob's ladder proposed by J. P. Perdew [123], illustrating the different generations of approximation of XC energy functionals. These approximations can be empirical, resulting from the fitting of existing results, semi-empirical or non-empirical, based on physical laws. They aim at capturing both exchange and correlation effects accurately while maintaining computational feasibility. Among the most valuable XC functionals are several

notable examples, including the Local Density Approximation (LDA), Generalized Gradient Approximation (GGA), and Hybrid Functionals, which are further discussed below. In this thesis, GGA and the hybrid functionals were used.

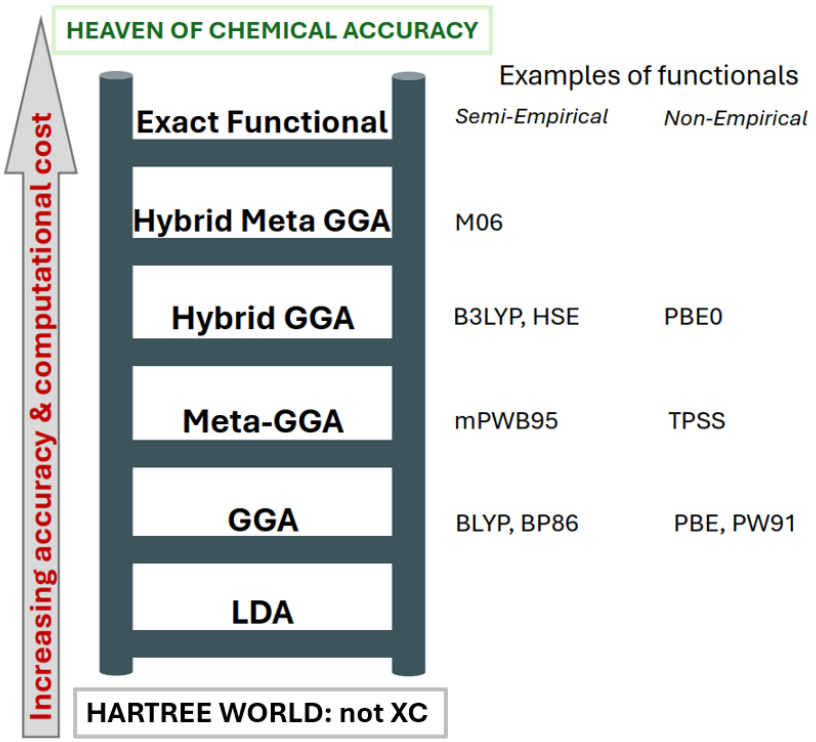

Figure 2.2. Jacob's Ladder DFT approximation for XC energy [124] with the different functional approximations, from the Hartree world at the bottom to the chemical accuracy at the top.

Local Density Approximation (LDA)

LDA is the oldest and most fundamental electron density functional, designed to deal with exchange and correlation energy. It was originally proposed in 1965 by W. Kohn and L. J. Sham [125] and works on the assumption of a uniform electron gas, with minimal density fluctuations. In the context of a spin-unpolarized system, the XC energy expression in the LDA is formulated as follows (Eq. (2.25)):

$$\mathrm{E}_{\mathrm{XC}}^{\mathrm{LDA}}[n(\mathbf{r})] = \int d^3r \; n(\mathbf{r}) \; \varepsilon_{\mathrm{XC}}^{\mathrm{unif}}[n(\mathbf{r})] \tag{2.25}$$

where $\varepsilon_{\mathrm{XC}}^{\mathrm{unif}}[n(\mathbf{r})]$ is the XC energy per particle of an electron gas with uniform density $n(\mathbf{r})$. The exchange component $\mathrm{E_X}$ was formulated analytically [126] as follows

$$\mathrm{E}_{\mathrm{X}}^{\mathrm{LDA}} = -\frac{3}{4}\left(\frac{3}{\pi}\right)^{\frac{1}{3}} \int d^3r \;\; [n(\mathbf{r})]^{\frac{4}{3}} \tag{2.26}$$

while the correlation part $\mathrm{E_C}$ was approximated and parametrized through Quantum Monte Carlo calculations [127, 128]. LDA remains widely employed in condensed matter physics due to its notable accuracy for solids [123]. It offers a reliable approximation for predicting properties such as molecular geometries, surface diffusion barriers and vibrational properties of many systems [129, 130]. However, its effectiveness diminishes in the realm of atoms and molecules, where electron distribution is less similar to a homogeneous gas and is better described by functionals higher up the Jacob's ladder. Despite its success

in solid-state physics, LDA's relatively low atomization energies have led to its underestimation in chemistry. LDA presents systematic errors, which are hard to minimize. In particular, LDA tends to underestimate exchange energy by up to 15 % and overestimate correlation energy by up to 200 % [130].

Generalized Gradient Approximation (GGA)

GGA is an advanced method within DFT, providing a refined approach to describe the XC energy of a system extensively used in computational chemistry, condensed matter physics and materials science due an improved accuracy and versatility compared to LDA. Unlike the simpler LDA previously mentioned, GGA incorporates information about the spatial variation (gradient) of the electron density, offering a more accurate representation of the electronic structure [128, 131].

$$\mathrm{E}_{\mathrm{XC}}^{\mathrm{GGA}}\left[n(\mathbf{r}), \nabla n(\mathbf{r})\right] = \int d^3r \; n(\mathbf{r}) \; \varepsilon_{\mathrm{XC}}^{\mathrm{GGA}}\left[n(\mathbf{r}), \nabla n(\mathbf{r})\right] \tag{2.27}$$

By considering not only the electron density at a point but also its spatial variation, GGA improves upon the limitations of LDA, particularly in describing properties such as bond lengths, reaction energies, and noncovalent interactions.
There are various formulations of GGA, each with its own set of parameters and functional forms. These functionals are typically developed through a combination of theoretical insights, empirical fitting to experimental data, and computational validation. Popular GGA functionals include the Perdew-Burke-Ernzerhof (PBE) [131] and the Becke-Lee-Yang-Parr (BLYP) [132, 133] used this thesis.
Typically, the contributions to the exchange and correlation terms are formulated independently,

$$\mathrm{E}_{\mathrm{XC}}^{\mathrm{GGA}} = \mathrm{E}_{\mathrm{X}}^{\mathrm{GGA}} + \mathrm{E}_{\mathrm{C}}^{\mathrm{GGA}} \tag{2.28}$$

In the BLYP, the exchange functional was proposed by Becke [132] and the correlation part derived by Lee, Yang and Parr (LYP functional) [133].

Hybrid functional

Hybrid functional combine both local and non-local XC functionals. These functionals seek to improve upon the accuracy of GGA approaches by incorporating a fraction of exact Hartree-Fock exchange in addition to the XC functional. Hybrid functionals are computationally more demanding than pure DFT methods (LDA, GGA) due to the inclusion of non-local exchange terms.
Several hybrid functions have been developed, each with its own form and parameterization. Notable examples include B3LYP [134], PBE0 [135] and the Heyd-Scuseria-Ernzerhof (HSE) screened hybrid functional [136–140]. In the case of the PBE0 used for the spin topology of some of the systems studied in this thesis, the XC energy mixes the PBE exchange energy ($\mathrm{E}_{\mathrm{X}}^{\mathrm{PBE}}$) and Hartree-Fock exact exchange functional ($\mathrm{E}_{\mathrm{X}}^{\mathrm{HF}}$), as well as the full PBE correlation energy $\mathrm{E}_{\mathrm{C}}^{\mathrm{PBE}}$, as expressed in the following Eq. (2.29):

$$\mathrm{E}_{\mathrm{XC}}^{\mathrm{PBE0}} = \frac{1}{4}\,\mathrm{E}_{\mathrm{X}}^{\mathrm{HF}} + \frac{3}{4}\,\mathrm{E}_{\mathrm{X}}^{\mathrm{PBE}} + \mathrm{E}_{\mathrm{C}}^{\mathrm{PBE}} \tag{2.29}$$

2.3.3 Basis sets and pseudopotentials

Basis sets are sets of analytical functions with well-know properties used to represent the electronic wavefunctions of a system. The idea is to represent an unknown function via a combination of known analytical forms by controlling the convergence via the calculation of accessible physical properties. In DFT, the most common types of basis sets are Gaussian-type orbitals (GTO) and plane waves (PW).

- **Gaussian basis set:** The orbital ψ_i is represented as linear combination of a basis functions f_α (Eq. (2.30))

$$\psi_i(\mathbf{r}) = \sum_\alpha C_{\alpha,i}\ f_\alpha(\mathbf{r}, \{\mathbf{R}_I\}) \tag{2.30}$$

with f_α expressed as follow:

$$f_{\mathbf{m}}(\mathbf{r}) = N_{\mathbf{m}} r_x^{m_x} r_y^{m_y} r_z^{m_z} \exp\left[-\nu_{\mathbf{m}} \mathbf{r}^2\right] \tag{2.31}$$

where $N_{\mathbf{m}}$ and $\nu_{\mathbf{m}}$ are constants fixed while calculating the electronic structure, so that only the orbital expansion coefficients $C_{\alpha,i}$ in Eq. (2.30) need to be optimized. The Gaussian basis function, centered on the position of the nucleus, is implemented using a linear combination of atomic orbitals (LCAO).
GTO are popularly deployed in computational materials science due to their computational efficiency and compact support (finite extension), but they also present several limitations such as non-orthogonality, basis set suppression error and linear dependencies for larger basis sets. Also, it is not trivial to implement force calculations and make sure that they are not affected by lack of completeness of the basis set itself.

- **Plane wave basis sets:** PW basis sets are well-suited for periodic systems because they are independent on atomic position and satisfy periodic boundary conditions. Using the Bloch Theorem [141, 142] and considering the periodicity of the system, the orbital can be written as Fourier series

$$\psi_{i,\mathbf{k}}(\mathbf{r}) = \sum_{\mathbf{G}=0}^{\mathbf{G}_{\max}} C_{i,\mathbf{k}}(\mathbf{G}) \exp\left[i(\mathbf{G}+\mathbf{k}).\mathbf{r}\right], \tag{2.32}$$

where $\mathbf{G}$ and $\mathbf{k}$ are both vectors of reciprocal space, $C_{i,\mathbf{k}}$ are the Fourier coefficient. Since this is an infinite sum, the number of reciprocal space vectors G must be truncated to allow implementation. The choice of the PW energy cutoff E_{cut} is then crucial to achieve convergence of the various properties with an acceptable precision. The number of PW (N_{PW}) is directly linked to the energy threshold by the following equation.

$$N_{PW} = \frac{1}{2\pi^2} V_{cell} E_{cut}^{\frac{3}{2}} \tag{2.33}$$

with V_{cell} the volume of the cell and E_{cut} the cutoff energy defined as follows:

$$E_{cut} = \frac{1}{2}\left[\mathbf{k} + \mathbf{G}_{\max}\right]^2 \tag{2.34}$$

The PW basis set is widely used in the materials science community due to several advantages. They are orthogonal, independent of atomic positions and can be easily distributed in parallel processing. In addition, accuracy can be consistently improved by increasing their number at will by paying attention not to increase the computational cost unnecessarily [118].

To approximate the contribution of electron-nucleus interactions (Eq. (2.23)) to the DFT-KS total energy, researchers adopt a simplified model known as pseudopotential (PP) first introduced in 1934 by H. Hellmann [143]. However, it wasn't until 1959 that J.C. Phillips and L. Kleinman [144] established a solid basis for the theory of pseudopotentials applicable to systems with a single valence electron. They achieved this by replacing the orthogonalization terms between nucleus and valence with an effective repulsive potential,

a simple procedure that was extended in 1968 by J.D. Weeks and R.A. Rice to encompass systems with several valence electrons [145]. Practically, the PP model replaces complex all electrons-nuclei interactions (full potential) with an effective potential. This potential encompasses the fundamental physics involved, while reducing computational costs. The construction of PPs has to respect a number of criteria [142]. Firstly, the PP is bound to facilitate the expansion of valence wave pseudo wavefunctions with a minimum of plane waves. Secondly, it has to prioritize transferability to enhance the accuracy of results in different applications. In addition, the charge density derived from the pseudo wavefunctions have to be an excellent representation of the real valence charge density. As represented in Fig. 2.3, core electrons are located close to the nucleus and are not involved in chemical bonding. They have minimal influence on material properties exhibit highly fluctuating wave functions, while valence electrons, located further away, contribute to the chemical bond with more predictable wave function variations.

Depending on the construction approaches of PP, we distinguish projector-augmented

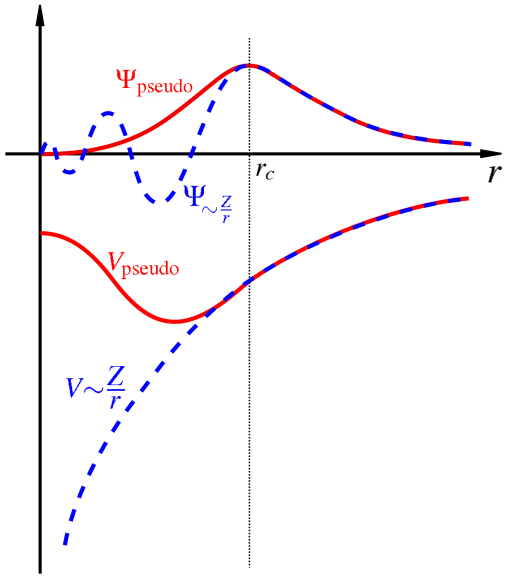

Figure 2.3. Comparison plots of the pseudopotential (solid lines) and full-potential (dashed blue lines) models, and their respective wave functions [130]. Beyond the cut-off radius r_c, the two models overlap perfectly.

wave (PAW) [146, 147], ultrasoft pseudopotentials [148, 149] and norm-conserving pseudopotentials [119, 120, 150]. In what follow the focus will be on the norm-conserving PPs used in this thesis.

The norm-conserving pseudopotential (NC-PP) was introduced by D.R. Hamann et al. [119] on the basis of the orthogonalized plane-wave approximation [151, 152]. This approach guarantees that the pseudo-wave functions and potential are the same as the true valence wavefunctions and potential beyond a cutoff radius r_c (see Fig 2.3). Within this radius, they differ, but the norm remains preserved as expressed in Eq. (2.35).

$$\int_0^{r_c} dr\ r^2 |\psi_{\text{full}}(\mathbf{r})|^2 = \int_0^{r_c} dr\ r^2 |\psi_{\text{pseudo}}(\mathbf{r})|^2 \tag{2.35}$$

The wavefunction $\psi(\mathbf{r}, \theta, \varphi)$ can be expressed in term of radial $R(\mathbf{r})$ part and spherical harmonics $Y(\theta, \varphi)$

$$\psi_{n,l,m}(\mathbf{r}, \theta, \varphi) = R_{n,l}(\mathbf{r}) Y_{l,m}(\theta, \varphi) \tag{2.36}$$

where (n, l, m) are quantum numbers and ($\mathbf{r}$, θ, φ) spherical coordinates.

Among the various types of NC-PPs present in the literature, those chosen for this thesis

are those developed by Troullier and Martins (TM) [121] and those by Goedecker, Teter and Hutter (GTH) [153]. The general form of a PP can be written as a sum of the local and non-local parts.

$$V_{\mathrm{PP}}(\mathbf{r},\mathbf{r'}) = V_{\mathrm{PP}}^{\mathrm{loc}}(\mathbf{r}) + \sum_{l}\sum_{m} Y_{l,m}^{*}(\theta,\varphi)\ \Delta V_l(\mathbf{r})\ \delta(\mathbf{r}-\mathbf{r'})\ Y_{l,m}(\theta,\varphi) \tag{2.37}$$

In Eq. (2.37), the local part $V_{\mathrm{PP}}^{\mathrm{loc}}(\mathbf{r})$ account for core and short-range contribution.

2.3.4 Born-Oppenheimer molecular dynamics (BOMD)

BOMD is a first principle computational method based on the Born-Oppenheimer approximation [154], which assumes that the motion of atomic nuclei and electrons can be decoupled due to their large difference in mass. In BOMD simulations, nuclear degrees of freedom are treated classically, while electron degrees of freedom are treated quantum mechanically. This means that the positions of the atomic nuclei evolve according to classical mechanics, while the electronic wavefunction is determined self-consistently at each step of the dynamics at fixed nuclear positions in order to minimize the total energy of the system. The forces acting on the nuclei are calculated directly from the gradient of the total energy with respect to the ionic position $\{\mathbf{R}_I\}$. Practically speaking, the electronic structure of the ground state is first obtained by solving the time-independent stationary Schrödinger equation, then propagating the nuclei classically in the effective potential [118, 155], as summarized in the following equations, which govern the dynamics at each step.

$$\begin{cases} M_I\ddot{\mathbf{R}}_I & = -\nabla_I \min\limits_{\{\psi_i\}} \mathrm{E_{KS}}\left[\{\psi_i\},\{\mathbf{R}_I\}\right] \\ \mathcal{H}_e\psi_i & = \mathrm{E_{KS}}\psi_i \end{cases} \tag{2.38}$$

Here, M_I is the mass of nucleus I, ψ_i the ground state single particle orbital (wavefunction) and $\mathcal{H}_e$ the effective KS one particle Hamiltonian. The iterative procedure of Eqs. (2.38) requires electronic structure optimization and complete diagonalisation of the Hamiltonian at each step along the trajectory. The Born-Oppenheimer approach to perform first-principles molecular dynamics was available, in principle, ever since computer were made available to run calculations on condensed matter or molecular systems. However, it should kept in mind that their tremendous computational cost discouraged any application of this recipe and, as such, the approach became rapidly only a potentially available tool not suitable for practical applications. Curiously enough, it was only after the advent of the Car-Parrinello scheme (see next section, Sec. 2.3.5 that some pratictioners realized that the BO approach could be pursued, provided efficient minimization techniques were put to good use.

2.3.5 Car-Parrinello molecular dynamics (CPMD)

Introduced by Roberto Car and Michele Parrinello (CP) in 1985 [156], CPMD[1] is a methodology that incorporates the electronic wavefunctions as active degrees of freedom, with the aim of updating them as ions undergo dynamic displacement. This avoids the calculation of the electronic structure at each step of the dynamics [157] as request by BOMD approach. In the CPMD scheme, the Lagrangian expressed in classical form as a function of the atomic positions $\mathbf{R}_I$ and mass M_I is extended by including the fictitious

[1]It should be made clear that, in what follows, CPMD stands for both the methodology invented by R. Car and M. Parrinello in 1985 and the for the code employed in this thesis, historically conceived as the practical realization of the ideas proposed in the Car-Parrinello methodology. Over the year this code has been extended to account also for alternative approaches to first-principles molecular dynamics. For instance, it is possible to run a Born-Oppenheimer trajectory by using the CPMD code.

dynamics of the ground state electronic wavefunctions $\psi_i(\mathbf{r})$ (electronic degrees of freedom). In the general case when an additional dynamical variable α_l (such as thermostat or barostat), the CP Lagrangian is then given by the following Eq. (2.39)

$$\begin{aligned}\mathcal{L}_{\mathrm{CP}} = \; & \mu \sum_i \int d^3r \; |\dot{\psi}_i(\mathbf{r})|^2 + \frac{1}{2}\sum_I M_I \dot{\mathbf{R}}_I^2 + \frac{1}{2}\sum_l \eta_l \dot{\alpha}_l^2 \\ & - \mathrm{E_{KS}}\left[\{\psi_i\}, \{\mathbf{R}\}, \alpha_l\right] - \sum_{ij} \lambda_{ij} \left(\int d^3r \; \psi_i^*(\mathbf{r})\psi_j(\mathbf{r}) - \delta_{ij} \right)\end{aligned} \tag{2.39}$$

The initial three terms denote the kinetic energy of the fictitious electronic degrees of freedom, nuclei, and supplementary dynamic variables respectively, followed by the total energy functional. The final term serves as the orthogonality constraint for the wavefunctions/orbitals. μ is the fictitious mass associated to the wavefunctions and λ_{ij} is the Lagrangian multipliers.
The equation of motion ensuring the time conservation of Eq. (2.39) are

$$\mu \ddot{\psi}_i(\mathbf{r}) = -\frac{\delta \mathrm{E_{KS}}\left[\{\psi_i\}, \{\mathbf{R}\}, \alpha_l\right]}{\delta \psi_i^*(\mathbf{r})} + \sum_j \lambda_{ij}\psi_j(\mathbf{r}) \tag{2.40}$$

$$M_I \ddot{\mathbf{R}}_I = -\nabla_{\mathbf{R}_I} \mathrm{E_{KS}}\left[\{\psi_i\}, \{\mathbf{R}\}, \alpha_l\right] \tag{2.41}$$

$$\eta_l \ddot{\alpha}_l = -\frac{\partial \mathrm{E_{KS}}\left[\{\psi_i\}, \{\mathbf{R}\}, \alpha_l\right]}{\partial \alpha_l} \tag{2.42}$$

The dynamical nature of the orbital $\psi_i(\mathbf{r})$ of a given state i, allow a departure from the Born-Oppenheimer (BO) surface. Selection of the appropriate fictitious electron mass μ, ensures effective control of deviations from the BO surface (see Fig 2.4) [115]. Evidence has shown that the CPMD trajectory $\{\mathbf{R}_{\mathrm{CP}}\}$, remains in proximity to the BOMD trajectory $\{\mathbf{R}_{\mathrm{BO}}\}$ (Fig 2.4), with the upper limit being proportional to the square root of the fictitious electron mass [157].

$$\| \; \mathbf{R}_{\mathrm{CP}} - \mathbf{R}_{\mathrm{BO}} \; \| < C\sqrt{\mu} \tag{2.43}$$

with C is a positive constant.

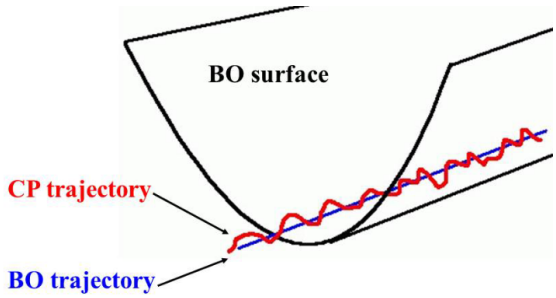

Figure 2.4. An illustration of CPMD (red) and BOMD (blue) trajectories on a DFT-derived potential energy surface. Adapted from [157].

Adiabaticity control in CPMD is a crucial to ensure the separation of electronic and nuclear degrees of freedom. The appropriate μ value needs to be selected as a balance between minor deviations from the BO surface and time steps of adequate length, which are feasible for affordable time trajectory lengths.
The intrinsic dynamics of orbitals can be depicted as a combination of oscillatory motions between unoccupied and occupied levels [158], characterized by a frequency of:

$$\omega_{ij} = \sqrt{\frac{f_j(\varepsilon_i - \varepsilon_j)}{\mu}} \tag{2.44}$$

with ε_i and ε_j indicate the eigenvalue of i^{th} unoccupied and the j^{th} occupied level respectively of the KS Hamiltonian and f_j the occupation number as introduce in Eq. (2.18). The minimum (ω^e_{min}) and maximum (ω^e_{max}) attainable electronic frequencies can subsequently be estimated as:

$$\omega^e_{\text{min}} \sim \sqrt{\frac{E_{\text{gap}}}{\mu}} \tag{2.45}$$

where E_{gap} is the electronic energy gap between the LUMO and HOMO orbital and

$$\omega^e_{\text{max}} \sim \sqrt{\frac{E_{\text{cut}}}{\mu}} \tag{2.46}$$

with E_{cut} the plane wave kinetic energy cutoff as defined in Eq. (2.34)
In practice, the value of μ must be determined depending on the system. Adiabatic separation of the two subsystems is guaranteed when the minimum orbital frequency significantly exceeds the maximum ionic frequency. This means that the electronic and ionic subsystems must not exchange energy, as illustrated in Fig. 2.5 for $GeSe_2$ at 1100 K. Consequently, the CP method should be effective for systems with a well-defined energy bandgap. For gap-closing systems, a physical condition that can be encountered also in semiconductors at thigh temperature, it is recommended to use the free-energy molecular dynamics method [159]. For optimum selection of μ, the maximum integration time step for the equation of motion is obtained by Eq. (2.47):

$$\Delta t_{\text{max}} \sim \sqrt{\frac{\mu}{E_{\text{cut}}}} \tag{2.47}$$

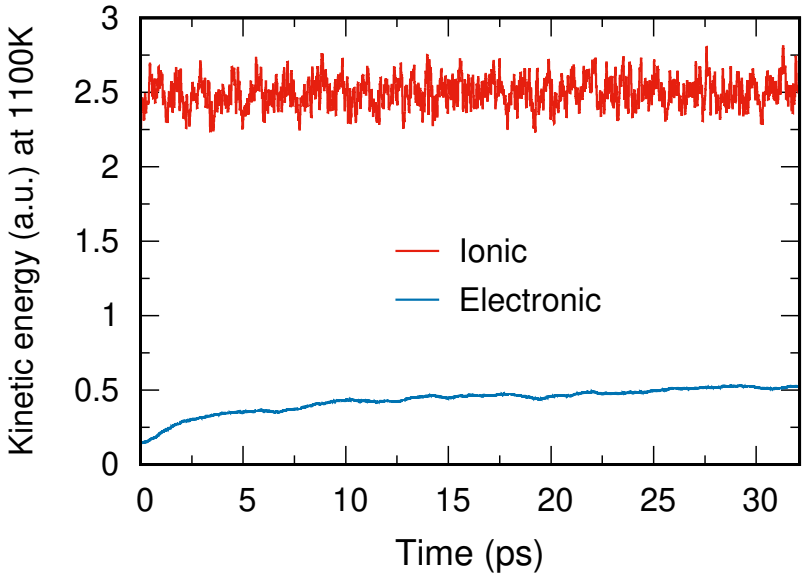

Figure 2.5. Kinetic energies of the ionic subsystem (red curve) and the fictitious electronic subsystem (blue curve) for the $GeSe_2$ liquid at 1100 K and comprising 480 atoms, showing a clear energetic separation of the two subsystems.

2.3.6 Maximally Localized Wannier Function (MLWF)

Analysis of the electronic structure and bonding properties in MD trajectory can be performed in terms of electronic density of states or the MLWF [160, 161]. In this study, the utilization of MLWF centers enables us to achieve a visualization of the valence electronic

configuration by allowing the analysis of chemical bonds. In the standard procedure, the n^{th} MLWF $w_n(\mathbf{r})$ and the corresponding center $\mathbf{r}_n^{\mathrm{WFC}} = (x_n, y_n, z_n)$ are obtained as unitary transformation (iterative) of the Kohn-Sham orbitals $\psi_i(\mathbf{r})$

$$w_n(\mathbf{r}) = \sum_{i=1}^{N_{occ}} \left\{ \prod_p e^{-A_{i,n}^p} \psi_i(\mathbf{r}) \right\} \tag{2.48}$$

where N_{occ} is the total number of occupied states (i.e. electrons, in a spin-unrestricted approach), $A_{i,n}^p$ is a matrix generalization of the Berry phase connector, and p is the order of the iteration [162]. Among all the possible (equivalent) unitary transformations, in the case of MLWF we chose the one that minimized the spread of the orbitals. This is obtained by minimizing the spread functional Ω. This quantity represents the spatial extension of the Wannier orbital:

$$\Omega = \sum_{i=1}^{N_{occ}} \left\{ \langle i|r^2|i\rangle - \langle i|\mathbf{r}|i\rangle^2 \right\} \tag{2.49}$$

The Wannier function centers (WFC) of each Wannier orbital n are given by:

$$x_n = -\frac{L_x}{2\pi} Im \ln \langle w_n | e^{-\frac{i2\pi\ x}{L_x}} | w_n \rangle \tag{2.50}$$

where L_x corresponds to the length of the simulation cell along x. Similar equations are used for the coordinates along y and z.

2.4 Machine-learning interatomic potentials

2.4.1 Introduction to machine learning interatomic potentials

Machine learning (ML) methods is a sub-field of artificial intelligence that has emerged as powerful computational tools across diverse fields. In recent years, ML methods have been widely applied and are still gaining significant impact in various domains, including computer vision [163, 164], natural language processing [165], finance [166], healthcare [167], physics, chemistry and materials science [168–179]. Unlike conventional algorithms, ML algorithms acquire knowledge from a portion of the data (training set), by learning underlying patterns and rules. They then build a model, evaluated using another part of the data (testing set), to predict the desired properties. In what follows, and in the context of this thesis, our focus will be on machine learning interatomic potentials (MLIP), which is one of the many applications of ML in materials science, helping to understand the structures, reactivity and properties of materials at the atomistic level. MLIP can be defined as a mathematical representation of the high dimensional potential energy surface (PES) of a given set of atomic positions [170]. In atomistic modeling, the efficiency of MD simulations depends fundamentally on the accuracy of the underlying PES. The PES represents the energy landscape that governs the behavior of the system providing crucial insights into its stability, reactivity, and dynamics. An accurate representation of the potential energy surface can be obtained by first-principles electronic structure calculations such as DFT, albeit at considerable computational cost. This motivates the use of empirical potentials, offering a faster way to access energy and forces. However, these empirical potentials quickly show their limits specially for complex systems and often lead to erroneous results. On the other hand, MLIP enables the mapping of a smooth, continuous, simple expression, accurate and low-cost high-dimensional PES based on DFT calculations. MLIP provides predictive force fields that are computationally cheap and allow simulations at large time and length scales with high computational efficiency at the

level of quantum mechanical accuracy [170, 180–182].

The first attempt to model the surface properties of potential energy using MLIP was made in 1995, by T. B. Blank et al.[183]. In this pioneering effort, using neural networks (NN) with limited degrees of freedom, the authors demonstrated the effectiveness and promising future of this innovative approach. A few years later, additional explorations still based on the NN and incorporating a greater fixed degree of freedom were carried out [184, 185]. In 2007, J. Behler and M. Parrinello introduced a generalized NN approach for constructing the PES, which addresses the limitations previously hindering the use of NN in higher-dimensional PES [186]. The authors demonstrated the high accuracy of the method for bulk silicon with respect to the empirical potentials and DFT. Their contribution marks a decisive turning point in this field and continues to be one of the most impacting. Using an approach based on high dimensional neural network potential (HDNNP) [181, 187–189], the potential energy of the system is decomposed into atomic contributions, allowing good flexibility in terms of the number of atoms involved. Three years later, A. P. Bartok and coworkers introduced the Gaussian Approximation Potential (GAP) framework [190], which is a Gaussian Process Regression (GPR) based on the smooth overlap of atomic positions (SOAP) kernel [191, 192]. Since then, MLIP development has made considerable progress in modeling systems characterized by short-range interactions. The past decade has witnessed a rapid proliferation of MLIP methodologies across diverse systems, primarily employing artificial neural networks (NNs) and Gaussian approximation potentials (GAPs). Notable advancements include DeepMD [193], equivariant neural networks [194], and graph-based neural networks [195]. These approaches have significantly expanded the capabilities and applicability of MLIPs in materials science and molecular dynamics simulations (Fig. 2.6, (a)).

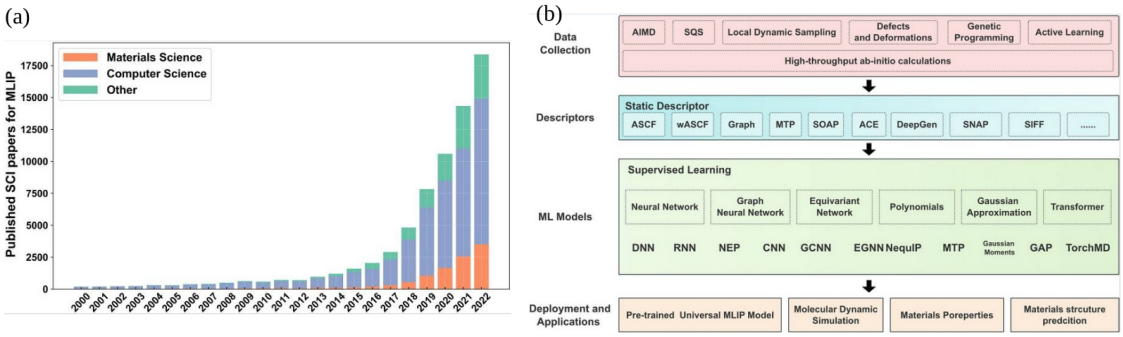

Figure 2.6. (a) Growth in MLIP-related publications across different fields in the last two decades across different fields. (b) Schematic overview of the MLIP development pipeline, including data collection, descriptor generation, machine learning models, and applications. Adapted from [196].

These studies have covered a variety of systems in both solid and liquid state, including the examination of defects in silicon [197], the graphite-diamond phase transition [198] and the exploration of ionic diffusion in amorphous solids such as Li_3PO_4 [199] and TaO_5 [200], bulk TiO_2 [201] as well as alloying systems such as Li-Si [202], thermal properties in phase-change materials [203–205] and surfaces phenomena [206–208].
Figs. 2.6 (b) and 2.7 illustrate the main steps in the MILP development process. The three request ingredients for generate a MLIP are: a database of reference structures with corresponding quantum-mechanical data; a mathematical representation of the atomic structure suitable for input into the ML algorithm with the so called descriptors, and finally the learning task.
Reference database building : Establishing a reference database of atomic configurations is a crucial initial step for MLIP, as it is for any machine learning model. The

choice of atomic structures and the accuracy of the labeled data are of great importance. Exploiting the system's scientific knowledge can contribute to this selection process. Iterative and active learning methodologies [173, 209, 210] can also help to supervise database construction in order to identify and exclude highly correlated configurations. Once selected, atomic configurations need to be transformed into a machine-readable format to encode the local atomic environment.

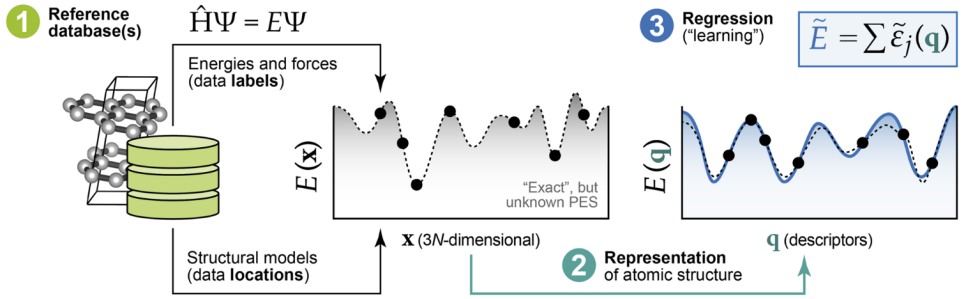

Figure 2.7. Schematic overview of the general methodology for developing MLIP, highlighting the three key stages: (1) Compilation of a labeled database featuring representative structural models, with energy, force and virial stress calculated via reference quantum mechanical method such as DFT; (2) Representation of atomic environment through comprehensive mathematical descriptors; (3) The learning process (regression task) of the potential energy surface to create the model. Adapted from [211].

Representation of atomic environments : The atomic structures information in the database are directly related to their coordinates, providing an unambiguous description of the systems. However, comparing structures based solely on cartesian positions poses challenges, as the arbitrary arrangement of coordinates makes establishing meaningful comparisons difficult. Additionally, structures that seem different may be equivalent under rotation, reflection, or translation transformations. Hence, converting these positions into a different mathematical invariant representation proves useful. This transformation is done using suitable tools called descriptors (features in ML jargon) with a set of requested properties: invariant with respect to translations, rotations, and permutations of atoms, computational efficient, and complete as possible [170, 211, 212]. The choice of descriptors is related to the system and the properties of interest starting from two body (pair-wise interaction) to many body descriptors such as Many-body Tensor Representation (MBTR), smooth overlap of atomic positions (SOAP), Atom-Centered Symmetry Function (ACSF) descriptors among others. A suitable selection of descriptors and corresponding hyperparameters strongly affects not only the construction of the PES but also structure and properties relationship for property prediction (symmetries and permutation invariance to the resulting potential) [213].

Over the years, many different approaches have been proposed by which translations, rotations, inversion, and atom permutation symmetries can be enforced. This is reflected in the variety of alternative frameworks to achieve an effective representation to be used as the input of an atomistic machine-learning scheme [214]. In fact, symmetry is such a central principle underpinning these efforts that it can be used to construct a "phylogenetic tree" of representations, organized according to the strategy that is used to incorporate symmetry in their construction, as shown in Fig. 2.8 [214].

Learning process : Several other strategies have been employed for quality data representation, selection, and enhancement. Active learning has witnessed notable success,

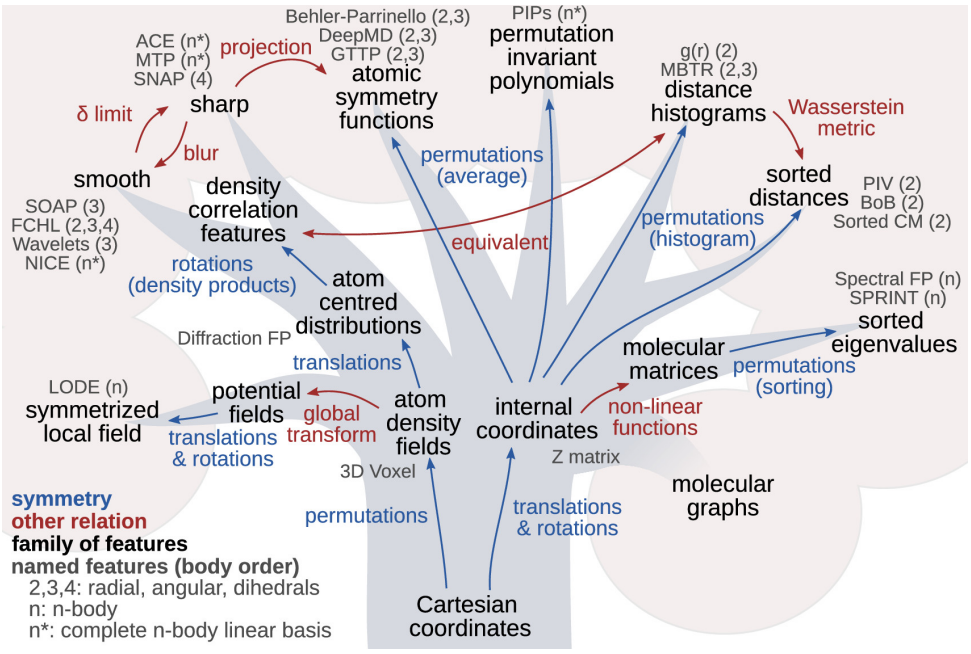

Figure 2.8. Phylogenetic tree mapping structural representations of materials and molecules. Arrows indicate relationships between feature groups, while names in gray indicate the most common implementations in each class. Fully symmetrical classes are represented by "leaves" on the tree. From [214].

contributing significantly to predicting interatomic potentials by optimizing the selection of structures and hyperparameters during the training setup. This third stage is devoted to the fitting of the PES into a highly parameterized flexible function.
Different methodologies and software for MLIP have been developed, depending on the approach used to approximate the PES based on both artificial NN [186, 195, 215] or kernel [190]. In this thesis, the focus will be on the most robust ones for modeling condensed matter systems: the Gaussian Approximation Potential (GAP) [190].

2.4.2 Gaussian Approximation Potential (GAP)

In the GAP framework, the PES is fitted by calculating and storing all the descriptors (and their partial derivative with respect to descriptor components) base on the key assumption that the total energy can be decomposed in atomic contribution ε_α accounting for all the descriptors.

$$E_{\text{tot}} = \sum_{\alpha}^{N} \sum_{j}^{N_d} \varepsilon_\alpha(\mathbf{q}_j), \tag{2.51}$$

where N_d is the total number of descriptors ($\mathbf{q}$) and N is the total number of atoms.
The GAP total energy as represented in Eq. (2.51), can alternatively be decomposed into the sum of a two-body contribution and a many-body contribution (refer to Eq. (2.52)). For the two-body descriptor, GAP employs a polynomial transformation that derives descriptors from pair distances. The parameterization of intricate many-body energy terms is facilitated through nonlinear regression, enabled by machine learning methods. This entails utilizing descriptors for many-body terms based on SOAP kernel $K(\mathbf{q}_i, \mathbf{q}_j)$ (similarity function between two atomic environments).

$$E_{\text{tot}} = \frac{1}{2} \sum_{i \neq j}^{N} U_{ij}^{2b}(r_{ij}) + \sum_{i} \sum_{j} c_j K_j(\mathbf{q}_i, \mathbf{q}_j), \tag{2.52}$$

where $U_{i,j}^{2b}$ denotes the pair potential arising from the interaction between atoms i and j, r_{ij} the distance between atoms i and j.
The SOAP descriptor for the atomic neighborhood of α is formulated by initially constructing a function based on the neighbor densities (refer to Eq. (2.53)). This function can be expanded in a basis set of orthonormal radial functions $R_n(\mathbf{r})$ and spherical harmonics $Y_{l,m}(\theta,\phi)$ to facilitate the numerical computation [173, 216].

$$\rho^{\alpha}(\mathbf{r}) = \sum_{i}^{N_n} \delta_{\alpha z_i} \exp\left[\frac{-|\mathbf{r}-\mathbf{r}_i|^2}{2\sigma^2}\right] f_{\text{cut}}(|\mathbf{r}_i|) = \sum_{n,l,m} C_{n,l,m}^{\alpha} R_n(\mathbf{r}) Y_{l,m}(\theta,\phi), \tag{2.53}$$

where n, l, and m are radial and angular index, $C_{n,l,m}^{\alpha}$ are the expansion coefficients corresponding to atom α, N_n the total number of neighbour within the cutoff distance, σ the length scale hyper-parameter that determines the regularity of the representation, $\mathbf{r}_i$ is the position of atom i with atomic number z_i, and f_{cut} the cutoff function defined by the following Eq. (2.54).

$$f_{\text{cut}} = \begin{cases} 0 & \text{if } r \geq r_{\text{cut}} \\ 1 & \text{if } r < r_{\text{cut}} - d \\ \frac{1}{2}\left[\cos\left(\frac{r - r_{\text{cut}} + d}{d}\pi\right) + 1\right] & \text{otherwise} \end{cases}, \tag{2.54}$$

with r_{cut} the cutoff distance and d the transition width evaluated for each pairwise distance.
The rotationally and permutationally invariant dot product SOAP kernel of two atomic environments is obtained by computing the overlap densities and the power spectrum elements.

$$K(\rho,\rho') = \int d\theta d\phi \left| \sum_{\alpha} \int d\mathbf{r} \rho^{\alpha}(\mathbf{r}) \rho'^{\alpha}(\mathbf{r}\theta\phi) \right|^2 \tag{2.55}$$

$$P_{n,n',l}^{\alpha\beta} = \sum_{m} (C_{n,l,m}^{\alpha})^* \; C_{n',l,m}^{\beta} \tag{2.56}$$

$$K(\rho,\rho') = \sum_{\alpha\beta} \sum_{n,n',l} P_{n,n',l}^{\alpha\beta} \; P_{n,n',l}^{'\alpha\beta} = \mathbf{P}.\mathbf{P}' \tag{2.57}$$

The normalize SOAP kernel is then obtained as

$$\bar{K}(\rho,\rho') = \delta^2 \left| \frac{\mathbf{P}.\mathbf{P}'}{|\mathbf{P}| \; |\mathbf{P}'|} \right|^{\zeta}, \tag{2.58}$$

where δ is the energy scale of the many-body term hyperparameter and ζ is the power kernel.
Typically, fine-tuning the hyperparameters is crucial to achieving a stable and accurate interatomic potential. For instance, increasing parameters such as $n_{\max}$ and $l_{\max}$ improves the resolution of the basis set expansion, thus serving as convergence indicators for the SOAP kernel. Optimal values depend on factors such as the average number of neighbors, which in turn depends on the cutoff distance and the Gaussian expansion parameter σ [216]. Nevertheless, these adjustments have a significant impact on computational efficiency and can impose substantial memory requirements.

2.5 Global comparison of the computational techniques employed

Table 2.1 provides a comprehensive summary of the various computational methods employed in this research, categorized based on the complexity of the studied systems. It

includes information about the sizes of the systems investigated in this study, along with the corresponding limits reported in the existing literature.

Table 2.1. Overview of the computational methodologies employed in this thesis, highlighting their respective advantages and limitations.

	Classical MD	CPMD	BOMD	MLIP-MD
System size (in atoms)	218–5k[a]; 1M	480[a]; 1k	400[a]; 1k	218–1.2M[a]
Integration time step (fs)	1-2	0.1-0.2	0.5-2	1-2
Computational cost	cheap	expensive	expensive	cheap
Structural properties	yes	yes	yes	yes
Dynamical properties	yes	yes	yes	yes
Electronic properties	no	yes	yes	no
Accuracy	FF dependent[b]	DFT level	DFT level	∼DFT level

[a] Models sizes simulated in this thesis.

[b] Degree of accuracy force-field dependent. For the chalcogenide- and oxide-based systems targeted in this work this degree can be defined from qualitatively to semi-quantitative in certain cases, but not truly quantitative.

Chapter 3

From FPMD to MLIP, a case study: liquid $GeSe_2$

Summary
In this chapter, the MLIP methodology is tested on a disordered binary chalcogenide system as case study, liquid $GeSe_2$; for which previous CPMD trajectories were available in our team as a result of extensive investigations well documented in the literature. The key motivation was the attempt to solve a longstanding disagreement between FPMD calculations and experiments (particularly on the partial structure factors) by invoking the occurrence of size effects on the structural properties of liquid $GeSe_2$. Liquid $GeSe_2$ can be considered as a prototype of chalcogen-based binary disordered materials. Originally, it was selected to understand the atomic-scale origins of intermediate range order. While achieving an overall agreement with experiments for a large set of structural features, some of them remained quite different from the experimental counterpart, by calling for further investigations oriented in two directions. First, the sensitivity of the results to the choice of the exchange-correlation functionals. This issue has been treated extensively by obtaining some improvements but it will not be the object of further calculations in this thesis (a short summary of previous achievements obtained in this direction will be provided to set the scene and ensure full clarity on the whole topic). Second, the impact of size effects, not to be excluded a priori when considering structural properties depending on distances well above the nearest neighbor interactions. It occurs that a thorough study of size effects is not achievable within FPMD since models and time trajectories have intrinsic well known limitations (100-500 ps of trajectory at the most for systems made of 500-1000 atoms is already a quite demanding and expensive estimate). For these reasons, the use of machine learning potentials becomes a viable solution, combining the precision of DFT calculations (over which they are fitted) and the reduced computational cost (due to the non explicit account of the electronic structure). Given the above context, we present here MLIP results enabling an evaluation of size effects on the structural and dynamical properties of the liquid $GeSe_2$ with DFT-level accuracy. In addition, this study serves as an introduction to the MLIP methodology that will be also exploited in the following Chapters for our target NVPs systems. First, we employ the CPMD scheme supported by available experimental data, to generate additional accurate structural models of liquid $GeSe_2$ to enlarge the database. Subsequently, we employ a Gaussian Approximation Potential (GAP) scheme framed within Gaussian Process Regression (GPR) kernel-based methodology to develop GAP-type MLIP. We were able to model systems up to one million atoms using the developed GAP-MLIP, providing comprehensive insights into the behavior of liquid $GeSe_2$ at large scale.

3.1 Forewords on the motivations behind the study of liquid $GeSe_2$

Liquid $GeSe_2$ (l-$GeSe_2$ from now on) is a disordered network forming-system characterized by intermediate range order, as exemplified by the presence of a first sharp diffraction peak (FSDP) in the total neutron structure factor [115]. Chemical bonding in disordered $GeSe_2$ systems is thought to result from a delicate balance between covalent and ionic characters, due to the close values of electronegativities of Ge and Se atoms. Previous research [217, 218] has illustrated the great sensitivity of intermediate order to electronic bonding properties. More specifically, by comparing the structural properties derived from LDA and GGA functionals, it was found that change in the description of the electronic structure impact on intermediate order. In the GGA framework employing the functionals proposed by Perdew and Wang (PW), the total neutron scattering structure factor agrees very well with experimental measurements for the entire range of **k**-values. The position and intensity of the FSDP were well reproduced with high accuracy, a feature totally absent from LDA calculations (see Fig. 3.1). This first tentative with PW-GGA also highlights the significant reduction in the number of homopolar connections within the network obtained using the GGA scheme compared with the LDA scheme.

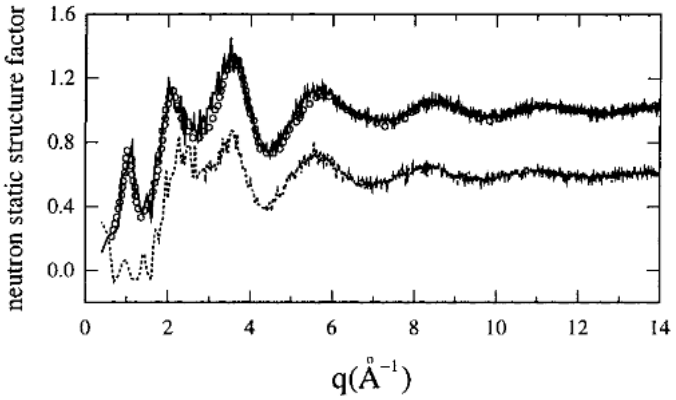

Figure 3.1. Neutron structure factor $S^N(k)$ as a function of reciprocal spatial wave vector k (noted here q) for l-$GeSe_2$, obtained by GGA (solid line) and LDA (dots), compared with experiment (circles). For clarity, the LDA curve is shifted down by 0.4 and shows the absence of FSDP. From [218].

Structural features of l-$GeSe_2$ were significantly improved under PW-GGA compared with LDA, particularly with regard to the appearance of the FSDP in the total neutron structure factors. This was ascribed to the better account of the ionic character of bonding [115].

Nevertheless, PW-GGA was not completely satisfactory in terms of the partial correlations both in real and reciprocal space. When examining the calculated partial pair correlation functions, the Ge–Ge was less structured and the first-neighbor distances exceeded the experimental values by about 15% (see Fig. 3.2 left). Also, the concentration-concentration structure factor [219] did not exhibit a FSPD of the same height as in experiment, being distinctly lower. Given the PW-GGA's inability to describe in a fully reliable manner the structural properties of l-$GeSe_2$ in the short and medium range (the Ge–Ge pair correlation, the FSDP in the concentration-concentration structure factor) alternative GGA functionals such as BLYP-GGA were selected. In particular BLYP optimizes the distribution of valence charge-density along bonds especially for pairs of components with low electronegativity difference such as Ge and Se.
In the following part of this section, we shall trace back the main results obtained when using BLYP-GGA, a framework that is intended to mitigate electron delocalization effects, which are not appropriate in binding scenarios characterized by competing ionic and covalent contributions [130]. We shall describe first what changes when using BLYP by focusing on the improvements. However, it should be kept in mind that BLYP is not able to cure some of the shortcomings observed when using PW, thereby legitimating the quest of other reasons for the observed differences.

In the context of l-$GeSe_2$, it has been demonstrated that BLYP-GGA performs better than PW-GGA and LDA methods in real and reciprocal space properties and for dynamical properties. For instance, the proportion of homopolar bonds and the average coordination number, more closely aligned with experimental data [219]. Regarding the intermediate range properties, the effects of the BLYP scheme was particularly striking. Minor improvements were observed in the intensity and position of peaks located at low k-values in the partial structure factor.
Therefore, the use of BLYP-GGA has considerably reduced the disparity between FPMD calculations and experimental observations in l-$GeSe_2$. As shown in Fig. 3.2 (left), the real-space partial pair correlations obtained with GGA-BLYP showed a clear improvement in terms of peak positions and intensities compared to those obtained with PW-GGA, bringing the calculated results into better agreement with experiments. The BLYP scheme has also enhanced the tetrahedral order, with the Se–Ge–Se bond angle becoming symmetric around 109°, whereas the PW scheme exhibits a broader and more symmetric spread around 100° [219]. The BLYP-GGA XC functionals additionally positively impact the dynamic property of l-$GeSe_2$. Specifically, the diffusion coefficient at 1050 K using BLYP-GGA (0.2×10^{-5} cm^2/s) better aligns with the experimental value (0.045×10^{-5} cm^2/s, value extracted from viscosity measurements), in contrast to the result obtained with PW (2.2×10^{-5} cm^2/s) [115, 219]. Concerning reciprocal space properties, PW and BLYP XC lead to quite similar results for the Bhatia-Thornton partial structure factors [220] (which results from the linear combination of Faber-Ziman partial structure factors, as shown later), number-number $S_{NN}(k)$ and number-concentration $S_{NC}(k)$. Nevertheless, the underestimation of FSDP in the Ge–Ge Faber-Ziman [221] partial structure factor, also appearing in the Bhatia-Thornton concentration-concentration $S_{CC}(k)$ structure factor, persists with BLYP.
Further efforts have been undertaken to improve the intermediate range order and the complex description of the Germanium environment in l-$GeSe_2$ by focusing on the impact of van der Waals dispersion forces on the structural properties [222]. As illustrated in Fig. 3.2 (right), by including the van der Waals dispersion forces in the expression of the total energy, the results structural properties (partial structure factors and pair correlation functions) are not significantly affected.

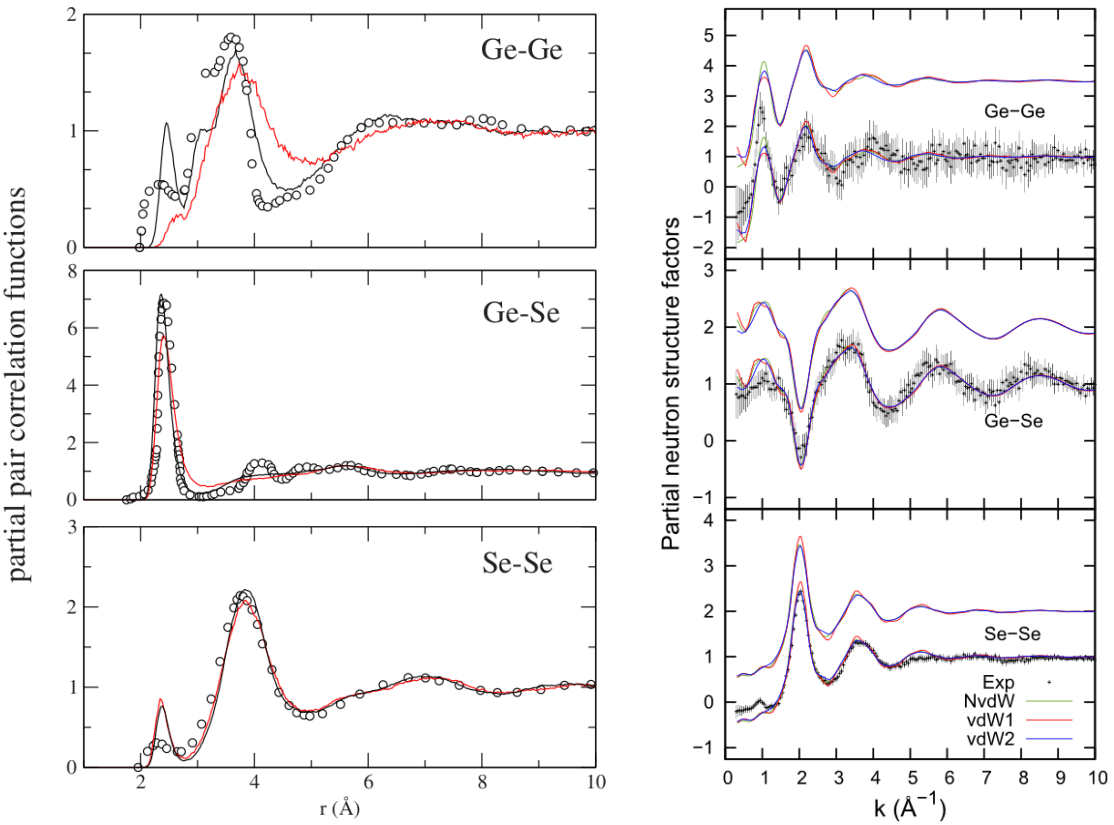

Figure 3.2. Left: Influence of the exchange and correlation functionals on the partial pair correlation functions (Ge–Ge, Ge–Se and Se–Se panels from top to bottom). The BLYP (solid black line) and PW (solide red line) results are compared with the experimental data (open circles) [223]. From [219]. Right: Faber-Ziman partial structure factors obtained with the BLYP XC functionals, displaying Ge–Ge, Ge–Se and Se–Se panels from top to bottom. The influence of dispersion forces (vdW1 and vdW2 curves) is negligible. Particularly, no improvement is found on the intensity of the FSDP in the Ge–Ge partial structure factors. Simulation results are including (lower curve) and excluding (upper curve) experimental data [223]. From [222].

Based on the above review of what has been done to improve as much as possible the atomic-scale description of this system, there are still open questions on the characterization of medium-range order in l-$GeSe_2$, preventing the exact reproduction of experimental partial structure factors in the entire range of k-values. This is the main motivation for seeking better performances in the direction of size effects that, in principle, could also affect the description of intermediate range order and, to a minor extent, some of the short range properties. For this purpose, MLIP employed in the frame of classical MD simulations as presented in Sec. 2.4 opens the way to tackle large systems with DFT level accuracy, highlighting the role played by size effects on the structure of l-$GeSe_2$.
From a broader perspective in atomistic modeling, it should be understood that the extensive use of FPMD schemes for simulating disordered chalcogenides stems from the limitations of methodologies that do not explicitly consider electronic structure in their bonding descriptions. This limitation is especially evident in cases where the models rely heavily on analytical expressions primarily grounded in empirical parameters (often) derived from a necessarily limited set of experimental data. In this respect, one can consider the pioneering interatomic potentials introduced by P. Vashista et al. [224–226] or the one by B.K. Sharma and M. Wilson [227, 228]). While these models have played a crucial role in providing qualitative insights into disordered Ge-Se systems in general, they fell short in quantitatively reproducing experimentally observed deviations from perfectly ordered structures. These deviations manifest themselves in the form of Ge-Ge and Se-Se ho-

mopolar bonds, which clearly stand out in experiments through the appearance of peaks at distances very close to those of Ge-Se bonds in both Ge-Ge and Se-Se pair correlation functions. These features have been obtained experimentally through the analysis of partial structure factors using neutron diffraction with isotopic substitution [223]. The interatomic potentials quoted above do not lead to any of these peaks, unless one heats up the structure at unphyiscally high temperature. For these reasons, as mentioned above, these description can be taken, at the very best, as qualitative while the quantitative character is totally missing. Recently, an attempt was made to employ neural network (NN) first-principles molecular dynamics (termed "quantum", NNQMD), based on machine learning, to investigate the melting behavior at 1100 K and the glass formation at 10 K [229]. The authors managed to analyze systems of substantial size, reaching up $\sim$ 37000 atoms, by obtaining valuable results in real and reciprocal space. However, when examining peak intensities, their model overestimate all peaks in both the total neutron and partial structure factors in comparison to experimental data. More specifically, their Ge–Ge and Se–Se pair correlation functions missed the first peak centered around 2.5 Å, accounting for homopolar bonds, a feature commonly observed in many published FPMD studies of l-$GeSe_2$ [219, 222, 230, 231] and validated by experimental data [223]. Additionally, the authors did not compare their results with available experimental partial correlations.

In view of these interesting and yet incomplete results, there is a need to implement alternative machine learning techniques. Specifically, the MLIP-GAP method, as introduced earlier in Sec. 2.4 of Chapter 2, emerges as a promising tool for the development of MLIP potentials. These potentials rely on a database derived from accurate DFT-FPMD calculations and are increasingly gaining popularity in various applications. Our starting point was the production of two additional FPMD models of $GeSe_2$ trajectories in order to build a consolidated database for the development of MLIP-GAP. The following section describes the computational details and the different models simulated in this context.

3.2 Computational procedures and FPMD models

FPMD simulations were carried out by using the CPMD scheme implemented in the cpmd code [232] on two l-$GeSe_2$ systems, referred to as model 1 and model 2, each comprising 480 atoms in periodic cubic cells. The use of the CPMD method for these systems is validated by a clear decoupling of the kinetic energies of the electronic and ionic subsystems, as illustrated in Fig. 2.5 of chapter 2. The well-established melt-quenching procedure, previously used in similar works [217–219, 230, 231], was employed for both systems. Periodic boundary conditions were applied on the systems with initial configuration adapted from previously published work [230]. The preliminary step in each CPMD simulation involves wavefunctions optimization, aimed at finding the electronic ground state the electronic system for the initial ionic configuration. The systems are then annealed to near T = 0 K and heated to T = 1100 K via increments of 300 K. For model 1, the box size was adjusted to match the experimental density of $GeSe_2$ glass [233, 234], while for model 2, the box size was modified in a stepwise fashion at different temperatures. These procedures are illustrated in Fig. 3.3 in terms of temperature versus simulation time. The electronic structure was described within DFT and evolved self-consistently in time by CPMD approach as implemented in the cpmd code [232]. The BLYP-GGA was used, based on the exchange energy obtained by Becke [132], and the correlation energy according to Lee, Yang, and Parr [133] as previously described in Sec. 2.3.2. Valence electrons have been treated explicitly, in conjunction with norm conserving pseudopotentials of the Trouiller-Martins [121] type to account for core-valence interactions. The wave functions have been

expanded at the Γ point of the supercell on a plane wave basis set with an energy cutoff $E_{cut} = 30$ Ry. In our FPMD approach, a fictitious electron mass $\mu = 1000$ a.u., and a time step of $\Delta t = 0.12$ fs have been used (based on previous work) to integrate the equations of motion. The control of the temperature has been implemented for both the ionic and electronic degrees of freedom by using Nosè-Hoover thermostats [112, 113, 235]. In the following section, we present the details of our analysis based on structural and dynamical properties.

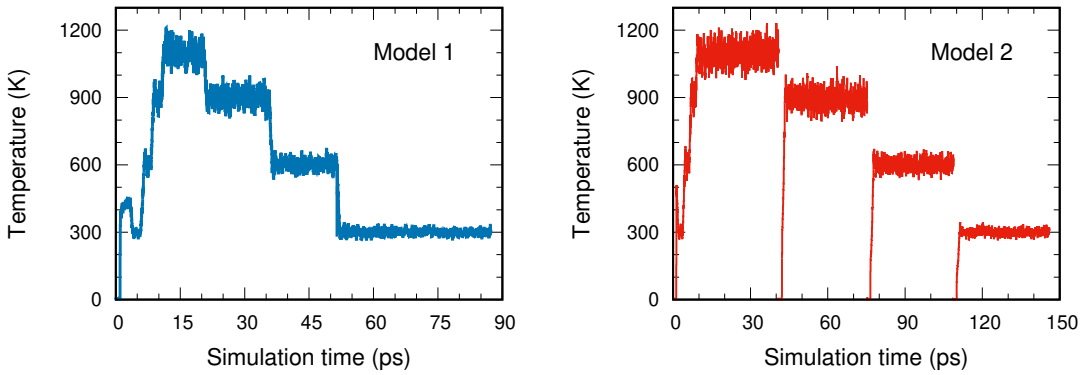

Figure 3.3. Full thermal cycle for the two $GeSe_2$ models: heating up to 1100 K and then cooled down from 1100 K to 300 K.

3.3 Calculation strategy and properties obtained

In general terms, having an equilibrium MD trajectory, the structure factors (total structure factor, $S(k)$, or partial structure factors, $S_{\alpha\beta}(k)$) can be directly calculated in reciprocal space [236] or as Fourier transform of the real space corresponding pair correlation functions g(r) and $g_{\alpha\beta}$(r). In both cases, one needs to keep track of the atomic coordinates, not necessarily at each time step (typically with a storage periodicity in between 10^{-14}-10^{-15} s to describe accurately all vibration frequencies inherent in the system). The total and partial pair correlation function can be computed directly from atomic coordinates using the standard equation:

$$\begin{aligned} g(r) &= \frac{1}{4\pi r^2 N\rho}\left\langle \sum_{\alpha}^{N}\sum_{\beta\neq\alpha}^{N}\delta(r-r_{\alpha\beta})\right\rangle \\ &= \frac{1}{N^2}\sum_{\alpha\beta}N_\alpha N_\beta g_{\alpha\beta}(r), \end{aligned} \tag{3.1}$$

where N refer to the total number of atoms, $r_{\alpha\beta}$ the relative distance between chemical species α and β, ρ the atomic number density, r a distance in real space and $g_{\alpha\beta}$(r) are the partial pair-correlation functions.
Having the partial pair correlation function $g_{\alpha\beta}(r)$, one can derive the mean partial coordination number $\bar{n}_{\alpha\beta}$ of atoms of type β, contained in a volume defined by two concentric spheres of radii r_1 and r_2 centered on an atom of type α by integrating $g_{\alpha\beta}(r)$ over the first shell of neighboring atoms:

$$\bar{n}_{\alpha\beta} = 4\pi\rho c_\beta \int_{r_1}^{r_2} dr\ r^2 g_{\alpha\beta}(r), \tag{3.2}$$

with c_β the atomic concentration of species β.
From the real space properties, the so-called Faber-Ziman partial structure factors [221]

can be easily derived by Fourier transform as function of modulus of the wave vector k following this relationship:

$$S_{\alpha\beta}(k) = 1 + 4\pi\rho \int_0^\infty r^2 \left[g_{\alpha\beta}(r) - 1\right] \frac{\sin(kr)}{kr} dr. \tag{3.3}$$

With the Faber-Ziman partial structure factors $S_{\alpha\beta}(k)$ in hand, a linear combination can be performed to derive the Bhatia-Thornton partial structure factors [220] number-number $\mathrm{S_{NN}}(k)$, number-concentration $\mathrm{S_{NC}}(k)$ and concentration-concentration $\mathrm{S_{CC}}(k)$ as follows:

$$S_{\mathrm{NN}}(k) = c_\alpha c_\alpha S_{\alpha\alpha}(k) + c_\beta c_\beta S_{\beta\beta}(k) + 2c_\alpha c_\beta S_{\alpha\beta}(k), \tag{3.4}$$
$$S_{\mathrm{NC}}(k) = c_\alpha c_\beta \left[c_\alpha \left(S_{\alpha\alpha}(k) - S_{\alpha\beta}(k)\right) - c_\beta \left(S_{\beta\beta}(k) - S_{\alpha\beta}(k)\right)\right], \tag{3.5}$$
$$S_{\mathrm{CC}}(k) = c_\alpha c_\beta \left\{1 + c_\alpha c_\beta \left[\left(S_{\alpha\alpha}(k) - S_{\alpha\beta}(k)\right) + c_\beta \left(S_{\beta\beta}(k) - S_{\alpha\beta}(k)\right)\right]\right\}, \tag{3.6}$$

where, c_α and c_β are respectively the atomic concentration of species α and β.
Having established that one can have access to the partial structure factors from an equilibrium trajectory (and in the absence of experimental information on these quantities), the total structure factors (neutron or X-ray) are readily obtainable. The total neutron structure factor $S^N(k)$ is defined by:

$$S^N(k) = 1 + \frac{1}{\langle b\rangle^2} \sum_{\alpha\beta} c_\alpha c_\beta b_\alpha b_\beta \left[S_{\alpha\beta}(k) - 1\right] \tag{3.7}$$

where b_α and b_β are respectively the coherent scattering length of species α and β and $\rho = \mathrm{N/V}$ is the atomic number density (N is the total number of atoms and V the volume of the system), $\langle b\rangle = \sum_\alpha c_\alpha b_\alpha$ is the mean coherent scattering length.
This total neutron structure factor (Eq. (3.7)) can be expressed in terms of the Bhatia-Thornton partial structure factors as follow:

$$S^N(k) = S_{\mathrm{NN}}(k) + c_\alpha c_\beta \frac{(b_\alpha - b_\beta)^2}{\langle b\rangle^2} \left[\frac{S_{\mathrm{CC}}(k)}{c_\alpha c_\beta} - 1\right] + \frac{2(b_\alpha - b_\beta)}{\langle b\rangle} S_{\mathrm{NC}}(k) \tag{3.8}$$

In this specific scenario involving the $GeSe_2$ system, where the coherent scattering lengths of the Ge and Se chemical species are very similar, with values of $\mathrm{b_{Ge}} = 8.185$ fm and $\mathrm{b_{Se}} = 7.970$ fm [237], and considering the limited range of variation of $S_{\mathrm{NC}}(k)$ and $S_{\mathrm{CC}}(k)$, it can be demonstrated that $S_{\mathrm{NN}}(k)$ serves as a highly accurate approximation for the total structure factor. Consequently, the analyses presented here regarding $S_{\mathrm{NN}}(k)$ are equally applicable to the total neutron structure factor $S^N(k)$. In this thesis, the reciprocal space properties (structure factors) are obtained by Fourier transform of the pair correlation function, since direct calculation in reciprocal space yields a highly noisy structure factor that can be somewhat hard to interpret.
By considering an entire MD trajectory at the melting temperature, the mean square displacement (MSD) of a given chemical specie α can computed as follow:

$$\mathrm{MSD}_\alpha(t) = \frac{1}{N_\alpha} \left\langle \sum_i^{N_\alpha} \left|\mathbf{r}_\alpha^{(i)}(t) - \mathbf{r}_\alpha^{(i)}(t_0)\right|^2 \right\rangle, \tag{3.9}$$

where N_α is the total number of chemical specie α, $\mathbf{r}_\alpha^{(i)}(t)$ is the coordinate of the i^{th} atom of chemical specie α at time t. In the diffusive regime, one can extract the diffusion coefficient Diff_α of specie α from its MSD as:

$$\mathrm{Diff}_\alpha = \frac{\mathrm{MSD}_\alpha(t)}{2\ n\ t}, \tag{3.10}$$

with n the dimension of the simulation cell (in our case with cubic cell, $n = 3$).
The level of agreement between theory (FPMD and MLIP-GAP) and experiments is assessed by determining the R_χ parameter, as defined by the following equation proposed by Wright [238].

$$R_\chi = 100 \times \left(\frac{\sum_i \left[\mathrm{Exp}^{(i)} - \mathrm{Sim}^{(i)} \right]^2}{\sum_i \left[\mathrm{exp}^{(i)} \right]^2} \right)^{1/2}, \tag{3.11}$$

where $\mathrm{Exp}^{(i)}$ and $\mathrm{Sim}^{(i)}$ represent the i^{th} experimental and calculated value respectively, of a given property. The lower the R_χ parameter, the more accurate the calculated model is with respect to experience.
As highlighted in the previous section, two 480-atom models were melted at 1100 K in order to explore a wide phase space so as to extract an accurate and stable MLIP. In addition, model 1 has undergone full thermal cycle at the glass $GeSe_2$ density at room temperature. It is worth noting that in this study, FPMD trajectories for 480 atoms were not expected to produce significant size-related effects or structural improvements (see Fig. 3.4 for a revealing illustration), in agreement with what has been already established in the literature [219, 222, 230]. In fact, previous studies of FPMD size effects, such as the comparison of l-$GeSe_2$ models with 120 and 480 atoms [230], have reported negligible size-related impacts. Given the computational requirements of FPMD simulations and current cluster capabilities, studying models with a few thousand atoms using FPMD was not feasible. The generation of these two new trajectories is mainly motivated by the need to construct a comprehensive database of accurate DFT-FPMD results. This initiative aims at facilitating the development of MLIP accurately representing the different phases of the $GeSe_2$ system, involving both amorphous and liquid states, thereby enabling the simulation of these phases. Knowing that there are no relevant differences between the 480 models obtained in the context of this thesis and previously published results, the rest of this chapter will exploit the FPMD reference result obtained from a 240-atom model of ref. [222] to infer the reliability and robustness of our different MLIP-GAP structural models.

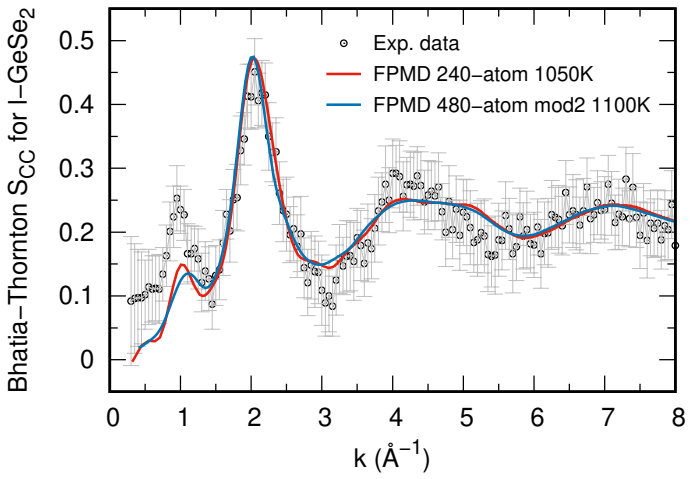

Figure 3.4. Comparison of the Bhatia-Thornton partial structure factor $S_{\mathrm{CC}}(k)$ for our 480-atom model with the reference structure of a 240-atom model [222] and experimental data.

3.4 MLIP modeling of liquid $GeSe_2$

3.4.1 Development of a MLIP: training, testing and fitting performance

The MLIP developed for l-$GeSe_2$ followed the general procedure presented in Sec. 2.4 in the framework of Gaussian Approximation Potential. The database was build based on the two news trajectories of 480 atoms produced along this work, in addition to models made of 120 [234] and 240 [222] atoms already available from previous works. This database comprises reference configurations sampled from specific regions of phase space, along with associated observable such as energies, forces, and virial stresses. These configurations were extracted from FPMD trajectories at various temperatures (1100, 1050, 900, 600, and 300 K) for a total of 215 representative instances. To ensure high accuracy, we recalculated DFT energies, forces, and virials for all configurations using an energy cutoff of 100 Ry. Subsequently, the constructed database was partitioned into training (80%) and testing (20%) sets.

The effectiveness of our MLIP model's predictions can be assessed through the calculation of the mean absolute error (MAE). This metric reflects the average disparity between the predicted values and the actual FPMD values within the dataset comprising N observations (see Eq. (3.12)).

$$\mathrm{MAE} = \frac{1}{N}\sum_{i}^{N}\left|\mathrm{FPMD}^{(i)} - \mathrm{MLIP}^{(i)}\right| \tag{3.12}$$

We evaluate the accuracy of our GAP model by comparing it with DFT-FPMD reference data. The training and testing datasets consist of 174 and 43 configurations respectively, encompassing energy, force, and virial components. As depicted in Fig. 3.5, our model's predictions for formation energy per atom and atomic forces quantities are in good correlation with those obtained from DFT-FPMD. The same level of accuracy was obtained with the virial stress components. Notably, our GAP model achieves excellent agreement with the reference data, exhibiting a low mean absolute error (MAE) of 1.34 meV/atom for the testing datasets. This performance is significantly better than the commonly quoted threshold of 5 meV/atom, indicative of a high-performing MLIP [197, 239]. Furthermore, the forces in the datasets are predicted with a MAE of 0.13 eV/Å.

These results underscore the high accuracy of our developed GAP-MLIP, highlighting its robust fit to the first-principles potential energy surface for l-$GeSe_2$. The second level of validation for our MLIP potential lies in modeling l-$GeSe_2$ using classical MD and comparing the resulting properties with those obtained from FPMD.

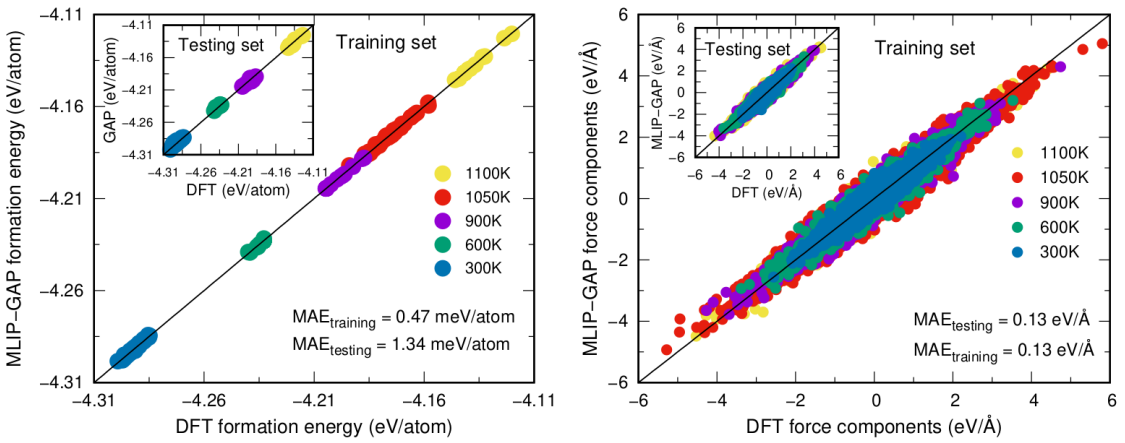

Figure 3.5. Scatter plots illustrating the correlations between the computed DFT and MLIP-GAP predicted energies (left) and force components (right) for both training and testing sets, with insets highlighting the testing data. Mean Absolute Error (MAE) values for both datasets are displayed.

3.4.2 CPMD *vs* MLIP models: same sizes

The newly developed MLIP-GAP has been employed in classical MD simulations to generate new models of l-$GeSe_2$ from random initial configurations within the NVT ensemble. Four replicas of varying system sizes (240, 1920, 15360, 51840, and one million atoms) were randomly placed in a cubic box, with the box size chosen to match the experimental density [240] of l-$GeSe_2$ at 1050 K. These simulations were performed using the QUIP package [241] integrated into the LAMMPS code [242]. A timestep of 1 fs was selected for integrating the equation of motion, and temperature control was achieved using the Nosé-Hoover thermostat as implemented in LAMMPS. Following energy minimization and an equilibration period at 300 K for 5 ps, the systems were gradually heated from 300 K to 1100 K. After 20 ps at 1100 K to loose any memory of the initial configuration, the systems were brought to 1050 K followed by 100–200 ps at the same temperature to reach stable diffusive regime. The final run for equilibrated trajectories of 10 ps (for the one million atoms models) and 100 ps (for smaller models) at 1050 K stored every 10 fs were employed for analysis. In what follows the structural analysis based on the equilibrated trajectories will be presented. The 240-atom models were used to validate the MLIP with respect to reference FPMD results of same sizes, exhibiting quantitative agreement. The MLIP-GAP potential was then applied to models of larger sizes (up to about one million atoms).

Faber-Ziman and Bhatia-Thornton partial structure factors

The Faber-Ziman partial structure factors $S_{GeSe}(k)$, $S_{SeSe}(k)$, and $S_{GeGe}(k)$ for l-$GeSe_2$ at 1050 K are calculated through Eq. (3.3) and shown in Fig. 3.6 (left) in three panels, highlighting comparisons concerning systems of the same size (240-atom). MLIP-GAP results reproduce with high accuracy the FPMD reference data, both showing quantitative agreement with the experimental results for $k \geq 1.5$ Å^{-1}. However, slight intensity discrepancies are observed at the FSDP level around $k = 1$ Å^{-1}, particularly in $S_{GeSe}(k)$ and $S_{SeSe}(k)$, while the FSDP of $S_{GeGe}(k)$ shows a non-negligible underestimate of intensity in both MLIP-GAP and FPMD data with respect to experiments.
In Fig. 3.6 (center), the Bhatia-Thornton partial structure factors $S_{NN}(k)$, $S_{NC}(k)$ and $S_{CC}(k)$ (from the top to the bottom) calculated according to Eqs. (3.4), (3.5), and (3.6) are presented, showing an excellent agreement among MLIP-GAP, FPMD, and experimental data across the entire range of k-values for $S_{NN}(k)$ (which can be treated as the total neutron structure factor, as described in the previous section) and $S_{NC}(k)$. The only noticeable deviation between the calculated (FPMD and MLIP-GAP) and experimental data lies in the intensity of the FSDP of $S_{CC}(k)$, reflecting the situation observed in $S_{GeGe}(k)$. Understanding and circumventing the differences recorded between theory and experiments in the intensities of FSDP in both $S_{GeGe}(k)$ and $S_{CC}(k)$ is the main motivation for the present study, which aims at assessing whether or not size effects can be at the origin of this behavior. In this context, the availability of a MLIP potential allows considering systems of unprecedented size. However, in the next section, we shall continue to describe the comparison between FPMD and MLIP for the system made of 240 atoms, before extending our rationale to larger systems.
To quantify the agreement between our MLIP-GAP and FPMD models with experimental results, the goodness of fit, as defined in Eqt. (3.11), which measures the percentage deviation between two sets of results, was calculated for the Faber-Ziman and Bhatia-Thornton partial structure factors and summarized in Tab. 3.1. The values obtained for FPMD and MLIP-GAP (average over the four replicas with standard error) are found very close (with less than 5% difference), confirming a very good quantitative agreement between these two sets of results. It is important to note that some values are quite large,

especially for S_{GeGe} (38.0% for MLIP-GAP and 33.7% for FPMD) and S_{NC} (22.5% and 18.3% for MLIP-GAP and FPMD respectively), despite very good visual agreement with the plots. This is primarily due to a slight shift of approximately 0.1 $Å^{-1}$ between the calculated results and the experimental data observed around the first peaks.

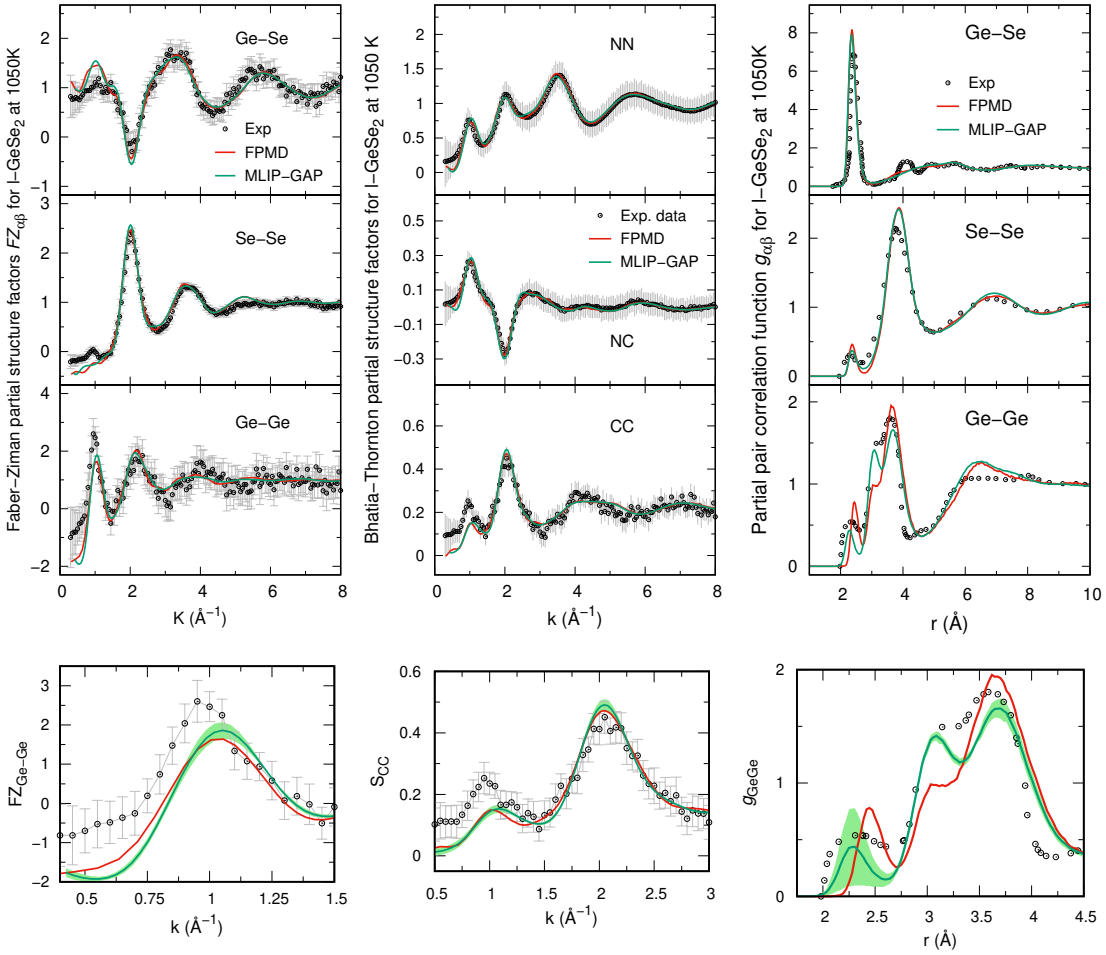

Figure 3.6. Partial structure factors as a function of wave vector in the Faber-Ziman (left panels) and Bhatia-Thornton (middle panels). Partial pair correlation function as a function of distance (right panels). The structure obtained with MLIP-GAP is compared with a reference FPMD data of same sizes (240 atoms) from ref. [222] together with the experimental data from [223]. A zoom on the first peaks is included for clarity.

Table 3.1. Goodness-of-fit R_χ parameters obtained from FPMD and MLIP-GAP data (240-atom models), indicating the level of agreement with experimental data. From left to right, the results include Faber-Ziman partial structure factors (S_{GeGe}, S_{GeSe}, and S_{SeSe}) and Bhathia-Thornton partial structure factors (S_{NN}, S_{NC}, and S_{CC}). All MLIP-GAP calculated values presented here are averaged over four parallel runs with standard error.

R_χ	S_{GeGe}	S_{GeSe}	S_{SeSe}	S_{NN}	S_{NC}	S_{CC}
FPMD	33.7	14.9	11.4	3.9	18.3	15.9
GAP	38.0±1.9	15.7±1.5	11.5±1.0	5.2±0.2	22.5±1.1	16.5±1.5

Partial pair-correlation functions

Fig. 3.6 (right) features a comparative analysis (again, for the 240 atoms system) of the pair correlation functions $g_{GeSe}(r)$, $g_{SeSe}(r)$, and $g_{GeGe}(r)$ derived from MLIP-GAP, FPMD

(from ref. [222]) and experimental data. The validation of the MLIP-GAP result in real space is quantified by calculating the Wright parameter ((3.11)) between the calculated partial pair correlation functions and the experimental ones, as done previously for the structure factors. The results are summarized in Tab. 3.2, where we observe very good agreement between FPMD and MLIP-GAP, with a difference of less than 4%, which falls within the statistical error bar quantified by averaging MLIP-GAP data over the four replicas. However, it is important to note that the slight shift of 0.06 Å between the calculated results (both FPMD and MLIP) and the experimental data for the first peaks of g_{GeSe} and g_{GeSe} is responsible for the relatively high Wright numbers (for example, 33.5% vs 36.7% for the Ge—Se correlation in FPMD and MLIP, respectively).

Table 3.2. Goodness-of-fit R_χ parameters obtained from FPMD and MLIP-GAP data (240-atom models) indicating the level of agreement with experimental data of partial pair correlation (g_{GeGe}, g_{GeSe}, and g_{SeSe}). All MLIP-GAP calculated values presented here are averaged over four parallel runs with standard error.

R_χ	g_{GeGe}	g_{GeSe}	g_{SeSe}
FPMD	18.5	33.5	12.1
GAP	16.0±2.3	36.7±0.8	11.0 ±0.7

The only noticeable discrepancy here concerns the Ge—Ge pair correlation function, where a significant variation in the intensity of the first peak is observed, as indicated by the statistical error that we present as a band to highlight the variation among the available data used to obtain an average (see Fig. 3.6 bottom right). Interestingly, the first peak position from the MLIP-GAP model (located at 2.29±0.03 Å) aligns better with the experimental one (at 2.33±0.03 Å) compared to the FPMD model (2.42 Å) as indicated in Tab. 3.3. Additionally, the second peak of Ge–Ge pair correlation function centred at 3.10±0.01 Å is well-defined and shows better agreement with the experiment in terms of intensity compared to FPMD. This is further confirmed by the lower goodness-of-fit parameter of 16.0% compared to 18.5% for FPMD.

Coordination numbers and network topology

The total coordination numbers n_α and partial coordination numbers $\bar{n}_{\alpha\beta}$, calculated by integrating the pair correlation function over the first shell of neighboring atoms, are presented in Tab. 3.3. Additionally, the nearest-neighbor interatomic distances $r_{\alpha\beta}$ in Å are summarized. They are identified by the position of the first maximum of the pair correlation functions $g_{\alpha\beta}(r)$. The total coordination numbers for Ge and Se are obtained by summing the partial coordination as follows $n_{Ge} = \bar{n}_{GeSe} + \bar{n}_{GeGe}$ and $n_{Se} = \frac{1}{2}\bar{n}_{GeSe} + \bar{n}_{SeSe}$. Concerning the bond length, a slight discrepancy is found for the Ge–Ge bond, 2.42 Å for the FPMD against 2.29 ± 0.03 Å (MLIP) closer to the experimental value (2.33 ± 0.03 Å). Overall, these results in real space confirm that our MLIP-GAP potential provide a quantitatively description of l-$GeSe_2$ with an accuracy comparable to the one of DFT-FPMD accuracy.
As shown in Tab. 3.4, we have also calculated the distribution of structural coordination units $n_\alpha(l)$ characterizing the environment of the Ge and Se atoms. It is important to recall the difference between $n_\alpha(l)$ and n_α while n_α provides an average behavior derived from all neighbors without detailing the chemical nature of the bond, the structural coordination units $n_\alpha(l)$ focus on how each atomic specie organizes itself when connecting to atoms of the same or a different type. Therefore, for a given number of neighbors l and a given atomic species, the chemical nature of the neighbors can be extracted from each configuration.

Tab. 3.4 shows a general agreement between the total percentages for each l-fold coor-

Table 3.3. Upper part: partial $\bar{n}_{\alpha\beta}$ coordination numbers obtained by integrating the first peak of partial pair correlation function $g_{\alpha\beta}$ and average total coordination numbers n_α obtained as sum of the partial coordination number (with $\bar{n}_{GeSe} = 2\bar{n}_{SeGe}$ according to the chemical composition of l-$GeSe_2$). Lower part: bond lengths $r_{\alpha\beta}$ (in Å) (taken as the position of the first maximum of the pair correlation functions $g_{\alpha\beta}(r)$).

	Exp. ref. [223, 243]	FPMD ref. [222]	MLIP-GAP
$\bar{n}_{GeSe}$	3.50 ± 0.20	3.68	3.75 ± 0.11
$\bar{n}_{SeSe}$	0.23 ± 0.05	0.20	0.20 ± 0.05
$\bar{n}_{GeGe}$	0.25 ± 0.10	0.18	0.14 ± 0.06
n_{Ge}	3.75 ± 0.30	3.86	3.89 ± 0.17
n_{Se}	1.98 ± 0.15	2.04	2.07 ± 0.11
r_{GeSe}	2.42 ± 0.02	2.36	2.36 ± 0.01
r_{SeSe}	2.30 ± 0.02	2.36	2.37 ± 0.01
r_{GeGe}	2.33 ± 0.03	2.42	2.29 ± 0.03

dination in the FPMD and MLIP models, particularly when accounting for the computed statistical error. However, a non-negligible difference between the FPMD and MLIP models emerges upon closer analysis of the data. The FPMD model displays a slightly narrower distribution of structural units, predominantly featuring four-fold coordinated Ge and two-fold coordinated Se. On one side, this suggests a higher degree of local ordering in the FPMD model, with a clear preference for these coordination environments. However, the MLIP model, while showing a broader distribution of structural environments, deviating from the predominant four-fold Ge and two-fold Se coordination (with slightly lower total percentage of four-fold coordinated Ge and two-fold coordinated Se), shows a considerably higher content of well-ordered fingerprints typical of crystalline $GeSe_2$, with Ge coordinated to four Se. It also shows a lower content of Ge-Ge homopolar bonding (16.8% in FPMD compared to 11.4% in MLIP), while maintaining a similar content of Se-Se homopolar bonding. Despite these differences, both models demonstrate an excellent level of agreement overall in terms of total l-fold coordination, validating the use of MLIP as a reliable and simplified representation of the first-principles potential energy surface. However, the varying degrees of chemical order indicate different levels of atomic arrangement and structural diversity.

Considerations on the comparative cost of FPMD and MLIP approaches

The developed MLIP-GAP achieved a computational speed up of approximately 337 times compared to FPMD for running a 1 ps MD simulation of l-$GeSe_2$ with 240 atoms. While FPMD requires about 27 hours, MLIP-GAP only takes 0.08 hours (see the table in the appendix A.1.1 for a comparison of the computational costs of typical FPMD and MLIP). This results in a speed up of about 62 times in generating a statistically reliable trajectory of l-$GeSe_2$ using MLIP-GAP compared to FPMD. This assessment is based on the analysis of structural and dynamical properties over 55 ps and 300 ps, respectively. It's important to note that the initial FPMD work and associated computational costs are essential for constructing the MLIP. However, once the MLIP is developed, it can reduce computational costs by approximately 337 times for individual simulations and 62 times for generating complete trajectories, compared to FPMD. This computational speed up should be considered as reference point, especially for the production of new structural models and trajectories.
Having confirmed that our newly developed MLIP-GAP shows FPMD accuracy (we can take the above results as a second step of validation), we can now investigate the occurrence of size effects by modeling significantly larger systems.

Table 3.4. Distribution of individual $n_\alpha(l)$ structural units, where an atom of species α (Ge or Se) is l-fold coordinated, computed for 240-atom models using both FPMD and MLIP-GAP. Total percentages for each l-fold coordination are highlighted in bold. These quantities were calculated including neighbors separated by a cutoff corresponding to the first minimum in $g_{\alpha\beta}(r)$. For Ge–Ge, Ge–Se, and Se–Se interactions, pair cutoff values of 2.73 Å, 3.00 Å, and 2.73 Å were used for FPMD, and 2.60 Å, 3.06 Å, and 2.74 Å were used for MLIP-GAP, respectively. A total cutoff of 2.85 Å was defined from the total pair correlation function. Only fractions greater than 0.1% are reported.

	FPMD	MLIP		FPMD	MLIP		FPMD	MLIP
Ge			$l=1$	**0.3±0.1**	**0.5±0.3**	$l=2$	**5.0±1.4**	**6.1±3.4**
			Ge	-	0.3±0.2	Ge_2	-	3.0±2.6
			Se	0.3±0.1	0.2±0.1	GeSe	-	0.2±0.1
						Se_2	5.0±1.4	2.9±0.7
$l=3$	**8.9±0.9**	**12.2±2.7**	$l=4$	**84.6±2.9**	**80.4±2.1**	$l=5$	**1.2±0.3**	**0.9±0.2**
Ge_3	-	0.3±0.2	$GeSe_3$	16.8±1.8	0.8±0.2	Se_5	0.3±0.1	0.7±0.1
Ge_2Se	-	1.2±0.9	Se_4	67.8±1.1	79.5±1.9	$GeSe_4$	0.7±0.1	0.2±0.1
$GeSe_2$	0.7±0.3	0.2±0.1	Ge_2Se_2	-	0.1±0.0	Ge_2Se_3	0.2±0.1	-
Se_3	8.2±0.6	10.5±1.5	Ge_4	-	-	Ge_3Se_2	-	-
Se			$l=1$	**2.9±0.6**	**4.7±0.7**	$l=2$	**93.0±1.6**	**88.8±6.8**
			Ge	2.6±0.5	4.0±0.4	Ge_2	76.0±1.0	75.2±3.6
			Se	0.3±0.1	0.7±0.3	GeSe	15.8±0.4	12.1±2.2
						Se_2	1.2±0.2	1.5±1.0
$l=3$	**4.0±0.7**	**6.5±1.2**	$l=4$	-	-	$l=5$	-	-
Ge_3	2.9±0.3	3.6±0.6	$GeSe_3$	-	-	Se_5	-	-
Ge_2Se	0.9±0.3	2.0±0.2	Se_4	-	-	$GeSe_4$	-	-
$GeSe_2$	0.2±0.1	0.8±0.3	Ge_2Se_2	-	-	Ge_2Se_3	-	-
Se_3	-	0.1±0.1	Ge_4	-	-	Ge_3Se_2	-	-

3.4.3 Size effects assessed by MLIP

The size effect of l-$GeSe_2$ was investigated using developed MLIP-GAP. Fig. 3.7 shows the snapshots of models with the details of simulated systems for FPMD and MLIP-GAP.

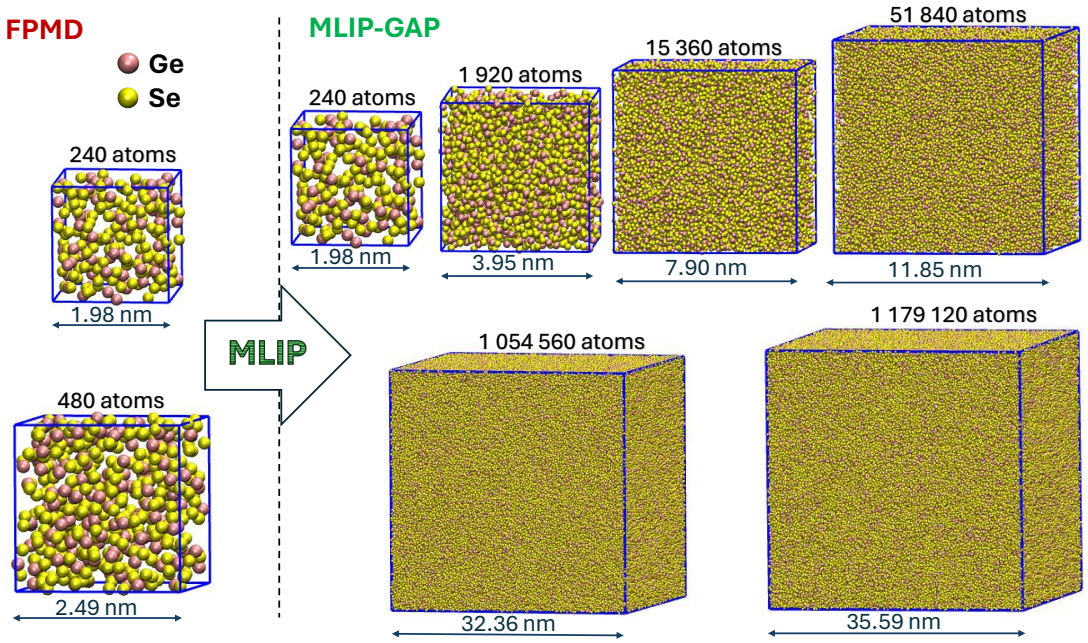

Figure 3.7. Comparison between l-$GeSe_2$ cubic supercells simulated by FPMD and those simulated by MLIP-GAP, the latter being able to access sizes of up to a million atoms. Cell parameters are given in nanometers, as well as the total number of atoms in each model.

A similar analysis to that conducted for the FPMD and MLIP-GAP models with 240 atoms in the previous section is carried out here for the different sizes investigated. The structural results (structure factors and partial pair correlation functions) are shown in Fig. 3.8. A general overview highlights that for all simulated sizes, the Ge—Se and Se—Se correlations are in perfect agreement with the FPMD results and the experimental data, both in reciprocal and real space. The same observation is made for the S_{NN} and S_{NC} partial structure factors. However, when focusing on the three most challenging cases involving the Ge—Ge correlation, an improvement in the intensity of the first peak of the S_{GeGe} structure factor for the all larger systems is observed, although it is less visible in the FSDP of the S_{CC}. Fig. 3.9 provides a zoomed-in view of these three partial correlations, comparing the results of the first peaks of the systems of one million atoms with FPMD and the experimental data. In real space, a better alignment with respect to the experiment of the position of the first peak of the Ge–Ge correlation representing the homopolar bond population is observed with the MLIP-GAP. Nevertheless, significant fluctuation in the intensity of this peak is noteworthy, as indicated by the statistical error band around the averaged plot (over four replicas). Importantly, the MLIP-GAP results more clearly highlight the second peak (position and intensity) of g_{GeGe} pair correlation function located at 3.10 $\pm$0.01 Å, representing the fraction of Ge atoms involved in edge-sharing connection.

3.4.4 Dynamical properties of liquid $GeSe_2$ by MLIP-GAP

In this section, we compute and present the mean square displacement (MSD) and diffusion coefficients of l-$GeSe_2$ systems using MLIP-GAP according to Eqs. (3.9) and (3.10). Accurately describing dynamical properties with MLIP often requires refining the training database beyond the inherent complexity of diffusional variable statistics computed at the FPMD level, as forces alone may be insufficient for this purpose. This refinement can be achieved by incorporating configurations obtained through enhanced sampling methods, such as metadynamics or the Bluemoon scheme, which enable a more precise assessment of energy barriers in diffusion processes [244–246].
The diffusion coefficients of Ge and Se chemical species for different simulated MLIP systems together with the FPMD results and the experimental one are given in Tab. 3.5. The experimental value presented here is extracted from viscosity measurements, and to date, we do not have any other experimental results for this system to confirm the reliability of the experimental diffusion presented here. The large discrepancy with the FPMD result (over 4 times larger) thus seems to question the process of obtaining this experimental value. In the present study, the diffusion coefficient derived from MLIP simulations using the Nosé-Hoover thermostat further overestimated that obtained from FPMD. This overestimation suggests the need for refining the MLIP training database to more accurately capture the diffusion mechanism [244–246]. Our findings align with recent studies on supercooled liquid $Ge_2Sb_2Te_5$ using GAP-type MLIPs, which reported similar overestimations. To address this discrepancy, Zhou et al. [247] suggested the use of the Langevin thermostat with a carefully tuned damping coefficient, which allows for precise control of the system's fictitious friction. The Langevin thermostat [248] is an alternative to the Nosé-Hoover thermostat for controlling the temperature of a system. It operates under the assumption that the system consists of large particles moving through a continuum of smaller particles. The Langevin thermostat simulates the effect of a heat bath by incorporating a stochastic term into the Langevin equations of motion (Eq. (3.13)) [249].

$$m\frac{d^2\mathbf{r}}{dt^2} = -\frac{\partial V(r)}{\partial r} - \gamma\frac{dr}{dt} + (2mk_BT)^{1/2}\xi(t), \tag{3.13}$$

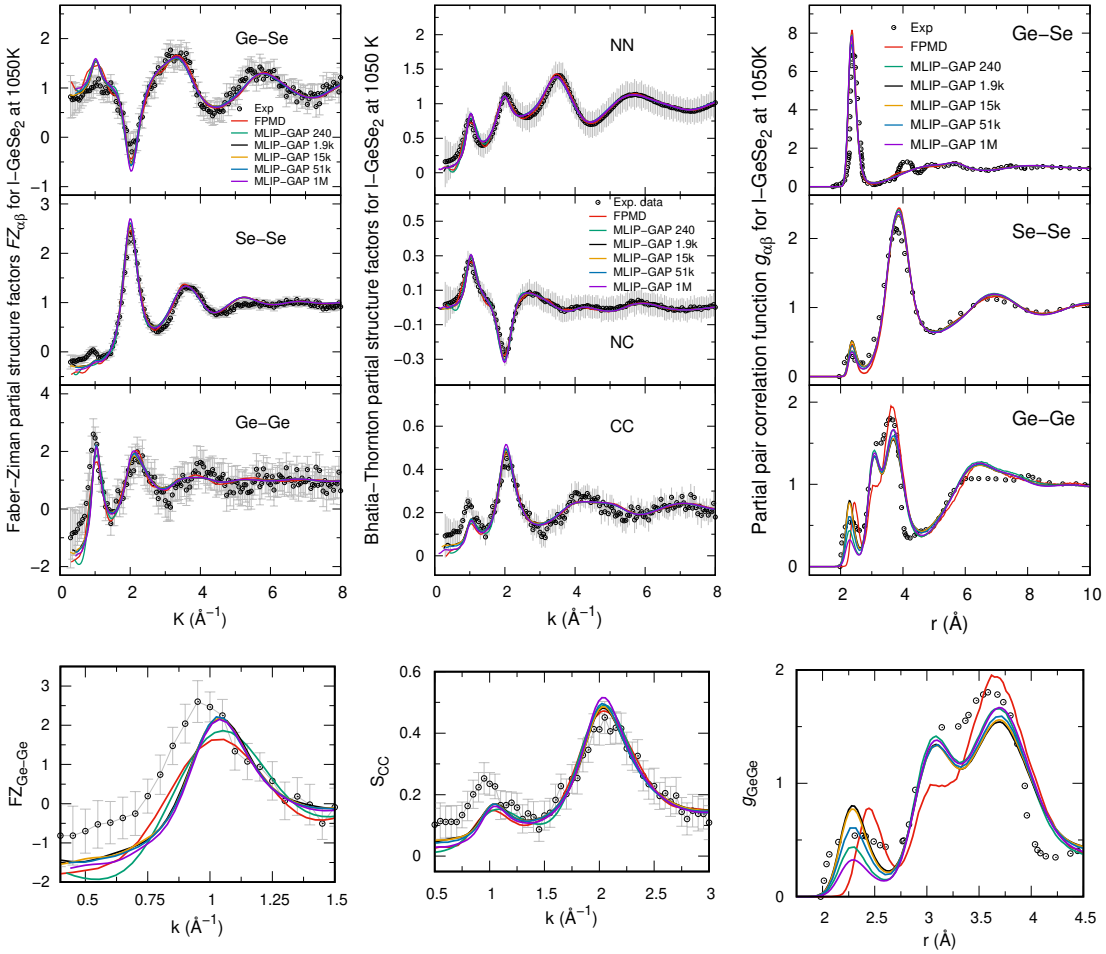

Figure 3.8. Partial structure factors as function of wave vector in the Faber-Ziman (left panels) and Bhatia-Thornton (middle panels). Partial pair correlation function as function of distance (right panels). The structure obtained with a reference FPMD data (240 atoms) from ref. [222] is compared to different sizes of MLIP-GAP models (240, 1920, 15360, 51840, and 1 million-atom) together with the experimental data from [223]. The impact of the systems sizes on the three correlations showing the effects of the complexity of the Ge environment are displayed below the three main panels, with a zoom on the first peaks where the differences between the calculated results and the experimental data are more manifested.

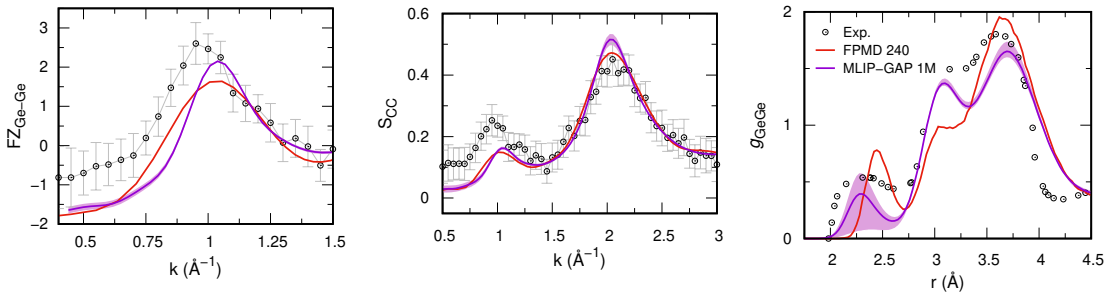

Figure 3.9. First peak of the Faber-Ziman Ge–Ge (left panel) and S_{CC} (center panel) partial structure factors as function of wave vector with the right panel showing the Ge–Ge partial pair correlation function up to 4.5 Å. The reference FPMD data (240-atom) from [222] is juxtaposed with the MLIP-GAP model average across four replicas of one million atoms, with the filled curve indicating the standard deviation. Experimental data from [223] is included for comparison.

where $V(r)$ represents the potential energy, r the position of the particle of mass m, $(2mk_BT)^{1/2}\xi(t)$ represents the random force term, which mimics the random collisions the particle would undergo with the surrounding smaller particles in the heat bath at

temperature T with $\xi(t)$ the Gaussian white noise, and $-\gamma dr/dt$ term represents the damping force created by smaller particles as they are pushed back by larger ones. This stochastic term, represented as a random force, induces fluctuations in the system's velocities, enabling it to reach and maintain a desired temperature.
Fig. 3.10 and Fig. 3.11 show a comparison of NVT simulations of liquid $GeSe_2$ at 1050 K using the Nosé-Hoover and Langevin thermostats, depicting MSD and force distributions respectively. A significant impact on diffusion coefficients over time is observed. By adjusting the friction coefficient $\gamma = 1/\tau$, notable effects on force distribution and diffusion coefficients are evident (Fig. 3.11). Specifically, for Ge and Se, the diffusion coefficients are found with MLIP-GAP (Tab. 3.5) to be 0.53×10^{-5} cm^2/s and 0.66×10^{-5} cm^2/s with the Nosé-Hoover thermostat, and 0.55×10^{-5} cm^2/s and 0.63×10^{-5} cm^2/s with the Langevin thermostat using $\gamma = 0.1$ ps^{-1}. With $\gamma = 11.11$ ps^{-1} (corresponding to a damping time of $\tau = 0.09$ ps), we observe 0.18×10^{-5} cm^2/s and 0.22×10^{-5} cm^2/s for Ge and Se, respectively. These latter values closely align with those obtained by FPMD at 1050 K (0.2×10^{-5} cm^2/s for both Ge and Se). As shown in Fig. 3.11, damping times $\tau \leq 0.1$ ps exhibit minimal effect on the force distribution compared to that computed with the Nosé-Hoover thermostat using MLIP-GAP and CPMD. It is important to note that changing the thermostat should not fundamentally alter the overall output. Our investigation of this approach aimed to assess its impact on force distributions in comparison to GAP-NH and CPMD forces. Notably, GAP-NH forces closely match CPMD forces, consistent with our previous analyses during the MLIP fitting section. Additionally, GAP-Langevin forces with damping time parameters $\tau = 0.09$ ps and 0.01 ps align well, while higher values significantly affect the force distribution.

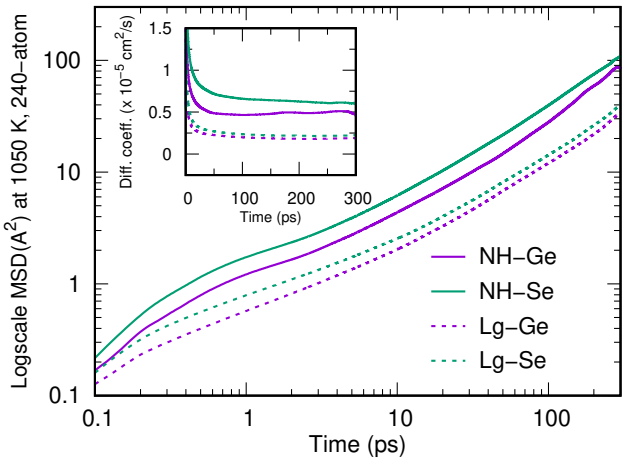

Figure 3.10. Mean square displacement (MSD) for Ge and Se atoms in liquid $GeSe_2$ at 1050 K, derived from the MLIP-GAP trajectory of 240 atoms obtained with the Nosé-Hoover (solid lines) and the Langevin (dashed lines) thermostat. The main plot shows the MSD on a logarithmic scale, while the inserts show the diffusion coefficient.

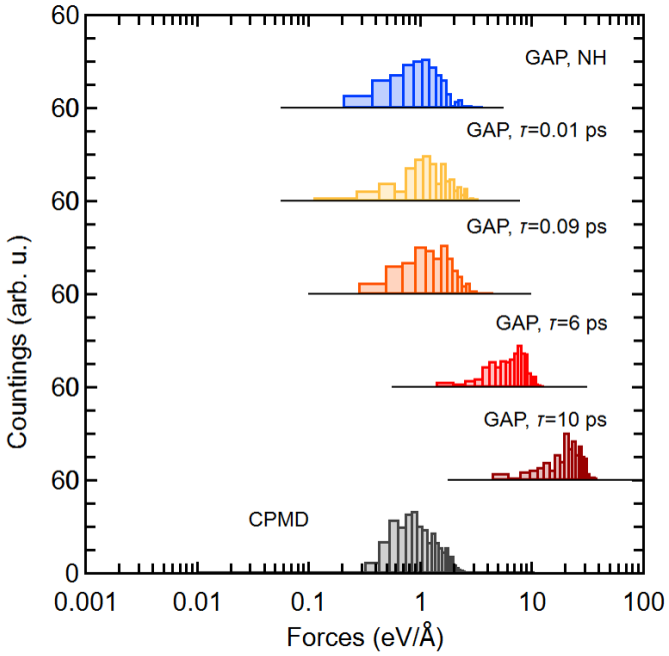

Figure 3.11. Forces distributions computed on atoms employing different thermostat Nosé-Hoover and Langevin thermostats with different friction parameters. For comparison we also report the CPMD forces.

Table 3.5. Comparative diffusion coefficients for l-$GeSe_2$ at 1050 K: FPMD, MLIP-GAP and experiment.

Systems with size (number of atoms)	Diffusion Coefficients ($\times 10^{-5}$cm^2/s)	
	Ge	Se
Experiment*	0.045	0.045
FPMD (120) [219]	0.20	0.20
FPMD (240) [222]	0.17	0.22
FPMD (480) [230]	0.20	0.19
Average FPMD	**0.19 ± 0.02**	**0.20 ± 0.02**
MLIP (240)	0.53	0.66
MLIP (1920)	0.56	0.84
MLIP (15360)	0.56	0.82
MLIP (51840)	0.52	0.71
MLIP (1054560)	0.62	0.73
MLIP (1179120)	0.51	0.72
Average MLIP	**0.55 ± 0.04**	**0.73 ± 0.07**
MLIP (240)**, γ=0.1 ps^{-1}	**0.55 ± 0.03**	**0.63 ± 0.02**
MLIP (240)**, γ=11.11 ps^{-1}	**0.18 ± 0.03**	**0.22 ± 0.02**

*Exp. value extracted from viscosity measurements [250]. **MLIP with Langevin thermostat.

3.5 Conclusive remarks

Our detailed study of l-$GeSe_2$ using FPMD simulations and especially MLIP-GAP, has clearly demonstrated the MLIP's capability to model disordered systems with covalent and ionic bonds, achieving FPMD level accuracy and thus improving our understanding of their atomic structure. Our results have confirmed the complexity of Ge's atomic environment description as revealed by FPMD. Consequently, we were able to investigate the potential size effect on the structure of l-$GeSe_2$, revealing an improvement of S_{GeGe} first peak intensity and insignificant effects on S_{CC} partial structure factor. Specifically, by modeling up to four replicas of systems with over a million atoms, we observed an enhancement in the FSDP intensity of the Ge—Ge structure factor. However, this enhancement did not seem to affect the intensity of the FSDP of the S_{CC} structure factor in the Bhatia-Thornton formalism. Our investigation suggests that there is a negligible size

effect on the structural properties of l-$GeSe_2$ across different model sizes.
The MLIP-GAP model, in particular, exhibits remarkable fidelity in capturing the structural characteristics of this material, as confirmed by FPMD simulations and experimental measurements. Nevertheless, we observed significant variability in the intensity of the first peak of the partial pair correlation Ge—Ge, which persists even in systems with over a million atoms. However, the proportion of Ge—Ge homopolar bonds decreased as the system size increased from 240 atoms to a million.
This study significantly advances our understanding of the structural characteristics of l-$GeSe_2$ and contributes to elucidating the potential size effect on the description of the local environment of Ge atoms in this material. These findings provide a foundation for future studies on the properties of liquid and amorphous materials, particularly in their potential technological applications, such as energy storage batteries.

Chapter 4

Structure, bonding and electronic properties of binary $50V_xO_y$-$50P_2O_5$ (VP50) glass

Summary

This chapter investigate in detail the structure, bonding and electronic properties of V_xO_y–P_2O_5 (VP50) glass by both CMD and FPMD. All results presented here have been summarized and published in ref. [251]. The BOMD data for VP50 (at PBE0 level) are available at the European Center of Excellence Novel Materials Discovery (CoE-NOMAD) [252].

4.1 Context and motivation

As detailed in Sec. 1.2.3, vanadophosphate (VP) glasses have emerged as promising cathode materials for ion batteries, owing to their multivalent redox behavior and exceptional cycling stability [16, 70, 83, 253–256]. Their diverse applications have motivated extensive experimental investigations employing advanced techniques such as X-ray and neutron diffraction [53–55], Raman Spectroscopy [56], Nuclear Magnetic Resonance (NMR) [57, 58], X-ray Photoelectron Spectroscopy (XPS) [59], Infrared Spectroscopy (IR) [60], Extended X-ray Absorption Fine Structure (EXAFS) [61, 62], and X-ray Absorption Near-Edge Structure (XANES) [59, 62, 63]. The coexistence of various vanadium oxidation states (V^{5+}, V^{4+} and V^{3+}) with varying coordination numbers leads to a complex glass network structure composed of a wide array of structural units [53, 60].
This structural complexity has posed challenges for precise atomic-scale characterization, leading to the use of quantitative modeling tools to gain a deeper understanding of the topology of these amorphous systems.

4.2 computational details

4.2.1 Classical molecular dynamics

Following the CMD methodology presented in Sec. 2.2 of Chapter 2, three CMD interatomic force field (FF) schemes are used for our study. The first one, known as PMMCS, was developed by Pedone *et al.* [87] and is based on a Morse-type potential. We employed its recent upgraded version, BMP-shrm, as introduced by Bertani *et al.* [108]. The initial pairwise interatomic potential PMMCS was chosen because of its reliability and the availability of parameters for many cation-oxygen pairs [257]. Also, its ability to predict the mechanical properties has been well assessed for oxide glasses and oxide nanoparticles [258, 259]. The revised BMP-shrm version allows reproducing better the Si–O–Si and P–O–P bond angle distributions (BADs) and the oxygen-oxygen distances of the network former. In this work for BMP-shrm FF, we employed the two-body potential parameters developed for V^{5+} and V^{4+} by Ori *et al.* [80] together with the P–O–P three-body parameters proposed by Bertani *et al.* [108], this FF scheme refers hereafter as CMD1. The second FF we tested includes the potential parameters of CMD1 in conjunction with the V–O–V and V–O–P three-body parameters recently reported by Malavasi *et al.* [88]. This second FF is denoted as CMD2. The third FF tested is developed by Lu *et al.* [59], and it is based on a two-body Buckingham-type potential. This FF scheme refers hereafter as CMD3. A full detailed account of the FF parameters employed in this work is reported in appendix, in Tab. A.3, A.4, and A.5.

To ensure statistical significance, for each CMD scheme (CMD1, CMD2 and CMD3) four VP50 replicas were generated, each consisting of 218 and 5450 atoms (with a V^{4+}/V^{tot} ratio of 0.375), placed in a cubic box with dimensions adjusted to match the experimental density value of 2.8 g/cm^3 [53]. The large models (5450 atoms) were selected to assess potential size effects throughout the study and to determine whether the 218-atom model can be considered representative of the structure for such glass system. Subsequently, the 218-atom models were employed for the BOMD study. In our CMD simulations, the short-range interactions were truncated at a distance of 6.0 Å and 10.0 Å for the 218 and 5450 atoms model respectively, whereas the long-range interactions were calculated using the Ewald summation method with a precision of 10^{-5} eV, up to a cutoff distance of 7.03 Å and 13.03 Å for the 218- and 5450-atom models respectively. For CMD1 and CMD2 simulations were performed using the DL-POLY code version 4.10.0 [260] whereas for CMD3 we employed LAMMPS code [242]. The Velocity Verlet algorithm was em-

ployed with a time step of 1 fs to integrate the equation of motion. The VP50 glass models were obtained by melt-quenching thermal cycles following a well established computational strategy [80, 81, 87, 108]. The temperature control was implemented via the Nosé-Hoover thermostat [112–114, 116]. First, the initial structures were randomly generated and relaxed at 300 K in the canonical (NVT) ensemble. Each system was heated to 5000 K and kept for 100 ps at this temperature. Then, cooling took place from 5000 K to 300 K with a cooling rate of 2.5 K/ps, close to typical rates used within CMD for this type of glasses [59, 80–82, 87, 108]. Averages of relevant properties are taken on a structure obtained from the last 150 ps of a trajectory lasting for 300 ps at T= 300 K.

4.2.2 First-principles molecular dynamics

The first attempt to study this system was based on the CPMD approach as detailed in Chapter 2. This preliminary investigation serves to highlight the reasoning behind our choice of BOMD over the CPMD method. Our exploratory CPMD simulation provides valuable insights into the challenges and limitations of this approach when applied to complex systems like VP glass. By critically analyzing the results of this test, we aimed to illustrate the key factors that influenced our decision to adopt BOMD as the primary method for our subsequent, more comprehensive investigations.
This approach allows us to justify our methodological decisions transparently, ensuring that the subsequent detailed analyses of VP50 using BOMD are grounded in a well-reasoned selection process.
The FPMD study of the VP50 system was initially tested using the CPMD scheme, which, involves a single optimization of the electronic structure at the beginning of the simulation, followed by maintaining the trajectory in the vicinity of the minimum of the potential energy surface during dynamics. This results in a decoupling between the kinetic energies of the ionic and electronic subsystems, as illustrated in Fig. 2.5. Our first attempt to simulate the VP50 system using CPMD failed to meet this requirement for the applicability of the CPMD approach. Fig. 4.1 shows the ionic and electronic kinetic energies. The decoupling, which is quite weak at 300 K, gradually narrows, and at 600 K, there is an energy exchange between the two subsystems, which must evolve at complementary decoupled frequencies. This failure of the CPMD approach for VP50 systems led us to the use of BOMD approach. In the remainder of this work, our FPMD calculation will be based on BOMD, as the following chapter is devoted to NVP glasses. The first-principles molecu-

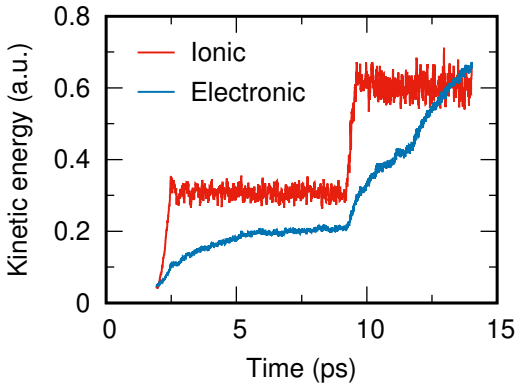

Figure 4.1. Time evolution of the fictitious Car-Parrinello electron kinetic energy (in blue) and ionic kinetic energy (in red) for VP50 glass as the system temperature increases from 300 K to 600 K. The plot demonstrates the failure of energy decoupling between the electronic and ionic subsystems, evidenced by energy transfer at 600 K.

lar dynamics simulations were carried out employing the Born-Oppenheimer approach as

implemented in the CP2K package [261]. In such scheme, atom-centered Gaussian-type basis functions are used to describe the orbitals and an auxiliary plane-wave basis set is employed to re-expand the electron density. We employed double-ζ polarized MOLOPT basis sets [262] for V, P, and O, and used a cutoff energy of 800 Ry for the plane waves at the Γ point only. Goedecker–Teter–Hutter pseudopotentials were used to describe core-valence interactions [263] together with the semilocal Perdew-Burke-Ernzerhof (PBE) exchange–correlation functional within a spin unrestricted density functional theory (DFT) formalism. The ionic temperature was controlled by a Nosé-Hoover thermostat [112–114, 116]. Initially, four BOMD simulations equilibrated at T = 300 K during 5 ps were performed starting from an equal number of initially uncorrelated configurations sampled from the trajectories produced employing the three different CMD schemes. The resulting BOMD models are denoted as BO1, BO2, and BO3 hereafter, representing the averages of the four individual configurations for each model. Then, we performed a final optimization at 300 K (∼0.5 ps) of the electronic structure employing the hybrid functional PBE0 [135], in which 25 % of PBE exchange is replaced by nonlocal Hartree-Fock exchange, with a cutoff energy of 600 Ry [264, 265]. This final step allows a more accurate description of the electronic structure and spin topology [266]. The final 3 ps of the trajectory of each replica computed at the PBE level combined with 0.5 ps at the PBE0 level at T = 300 K were used to describe the structural properties of the VP50 model. The final BOMD run at the PBE0 level proved essential to achieve convergence in the spin localization of V sites, as detailed in Sec. 4.3. Its impact on the structural properties was found to be negligible. Analysis of the electronic structure and bonding properties was performed in terms of electronic density of states and the maximally localized Wannier functions (MLWF) [160, 161].

4.3 Sites speciation in VP50 glass: the case of Vanadium

Vanadium, as a transition element, exhibits varying speciation (oxidation and coordination) in glasses [62, 267, 268], with oxidation states of V sites impacted by factors such as synthesis conditions, bulk chemistry, and total V amount. This results in the stabilization of V^{5+}, V^{4+}, and V^{3+} oxidation states, each with a unique local bonding environment [62, 63, 66, 267]. V^{5+} and V^{4+} states are the most commonly observed, as the highly reducing environment required for stabilizing V^{3+} is often difficult to achieve. From atomic-scale calculations standpoint, classical MD use predefined indexing to represent V sites in glasses, with V atoms in different oxidation states being labelled according to corresponding force field parameters. In contrast, BOMD simulations like all DFT approaches do not require a priori indexing of V sites, as the final V speciation is determined solely by the number of total oxygen atoms, corresponding to a defined $50V_xO_y[sV_2O_5$-zV_2O_4-$wV_2O_3]$-$50P_2O_5$ composition.

Various electronic charge determination methods, including Mulliken [269], Bader [270], and Qeq [271], have been tested to obtain information on vanadium speciation as post-processing of the configurations sampled from the BOMD trajectories. However, none of them was able to distinguish between different vanadium sites. To address this limitation and ensure accurate identification of V speciation, we employed local spin density projections of V sites while calculating energy bandgaps, as depicted in Fig. 4.2. All the detailed values found for the three models are reported in Tab. 4.1. Both the PBE and hybrid PBE0 functionals were utilized for this analysis. Notably, when employing the PBE functional, only values of bandgaps $\leq$ 0.1 eV were obtained, while at the PBE0 level, as anticipated, greater accuracy was achieved, yielding well-defined energy bandgaps falling within the range of 2.3 to 2.8 eV. Particularly noteworthy is the observation that three models exhibited slight variations, with BO1 at 2.4 eV, BO2 at 2.6 eV, and BO3 at 2.8 eV. The difference in energy between spin-up and spin-down states (i.e. spin splitting)

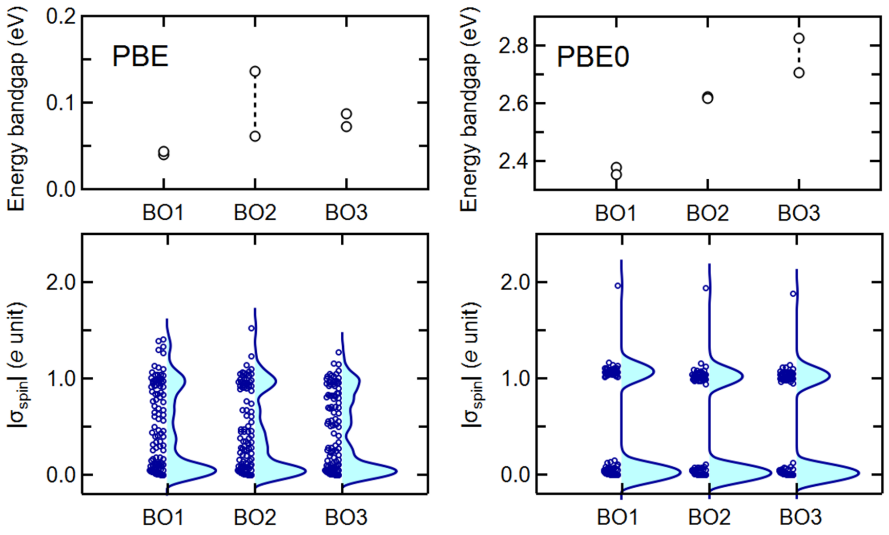

Figure 4.2. Averaged values of energy bandgap (top, in eV) and spin densities σ_{spin} (bottom, in e units) computed for each V site at the PBE (left) and PBE0 (right) levels for the three BOMD models. Note that the bandgap values for both spin-up and spin-down states are reported as average of the four configurations simulated for each BOMD model. Spin densities are reported as violin plots showing the distribution of individual data points of the four individual configurations for each BOMD model simulated.

accounts for the non-negligible magnetic character of the VP50 glass, which can be associated to the possible presence of V^{4+} and V^{3+} sites. Although the three BO models display distinct degrees of spin splitting (0.02 eV (BO1), 0.005 eV (BO2), and 0.12 eV (BO3)), implying differing levels of magnetic character, it is noteworthy that these values remain within the range of the computed statistical error. At the PBE level, the spin analysis

Table 4.1. Energy bandgaps (eV) for spin-up and spin-down states, along with average spin values calculated within specified spin ranges in e unit, computed at the PBE and PBE0 levels. The percentage content is also indicated. The data is reported for the three BO models and averaged over four individual run per model

	PBE			PBE0		
	BO1	BO2	BO3	BO1	BO2	BO3
Bandgap (eV)						
spin-up	0.04±0.02	0.14±0.09	0.09±0.07	2.4±0.2	2.6±0.1	2.8±0.2
spin-down	0.04±0.02	0.06±0.04	0.07±0.05	2.3±0.2	2.6±0.1	2.7±0.2
$\lvert\sigma_{spin}\rvert$						
0 - 0.2	0.05±0.01 (50.0%)	0.05±0.01 (49.2%)	0.04±0.01 (50.0%)	0.02±0.01 (64.6%)	0.02±0.01 (63.3%)	0.02±0.01 (63.3%)
0.2 - 0.8	0.50±0.06 (21.9%)	0.43±0.06 (25.0%)	0.49±0.07 (25.0%)	–	–	–
0.8 - 1.2	0.97±0.03 (24.2%)	0.98±0.02 (24.2%)	0.95±0.03 (24.2%)	1.07±0.01 (34.6%)	1.02±0.01 (35.9%)	1.03±0.01 (35.9%)
1.2 - 1.8	1.34±0.05 (3.9%)	1.1±0.3 (1.6%)	1.3±0.3 (0.8%)	–	–	–
1.8 - 2.2	–	–	–	1.95±0.04 (0.8%)	1.94±0.04 (0.8%)	1.88±0.04 (0.8%)

of the three BO models indicates two predominant spin values, with approximately 50% of V sites exhibiting $\sigma_{spin} = 0.05$, and around 24% displaying $\sigma_{spin} = 0.97$. Notably, up

to 23–29% of V sites exhibit more widely dispersed spin values in the 0.2–0.8 and 1.2–1.8 ranges. In contrast, when employing the PBE0 level, our spin analysis unveils three well-defined σ_{spin} sets for V sites, with values hovering around 1.95, 1.07, and 0.02 for BO1, 1.94, 1.02, and 0.02 for BO2, and 1.88, 1.03, and 0.02 for BO3 whereas all P and O atoms demonstrate values below 0.05. The values for V sites are indicative of the oxidation states of V^{3+}, V^{4+}, and V^{5+}, respectively, which correspond to the valence electronic configurations [Ar]$3d^2$, [Ar]$3d^1$ and [Ar]$3d^0$. This finding is consistent with the magnetic character of V^{3+}, V^{4+}, and non-magnetic character of V^{5+} sites. V sites can be assigned in percentage to V^{3+} (0.8 %), V^{4+} (35.9 %), and V^{5+} (63.3 %) sites for the three BO models, in excellent agreement with the experimental determination by Hoppe *et al.* [53] (35.2 % for V^{4+} and 64.8 % for V^{5+} with a negligible content of V^{3+}). Based on these values, our calculations point toward a chemical composition corresponding to $50V_xO_y$[31.6V_2O_5-18.0V_2O_4-0.4V_2O_3]-50P_2O_5 (clearly denoting a negligible content of V_2O_3). This is in contrast with the commonly referred composition 50V_2O_5-50P_2O_5, typically reported in the literature [53, 272].

4.4 Structural properties: structure factors and pair correlation functions

4.4.1 Total X-rays and neutron structure factors

Fig. 4.3 shows the total structure factors, $S^X(k)$ and $S^N(k)$, obtained by CMD and BOMD simulations of the VP50 system for the 218 atoms models. We also show the data obtained for 5450 atoms models with CMD. Our data are compared to the experimental results by Hoppe *et al.* [53]. We used the neutron scattering lengths and X-ray form factors reported in Tab. 4.2.

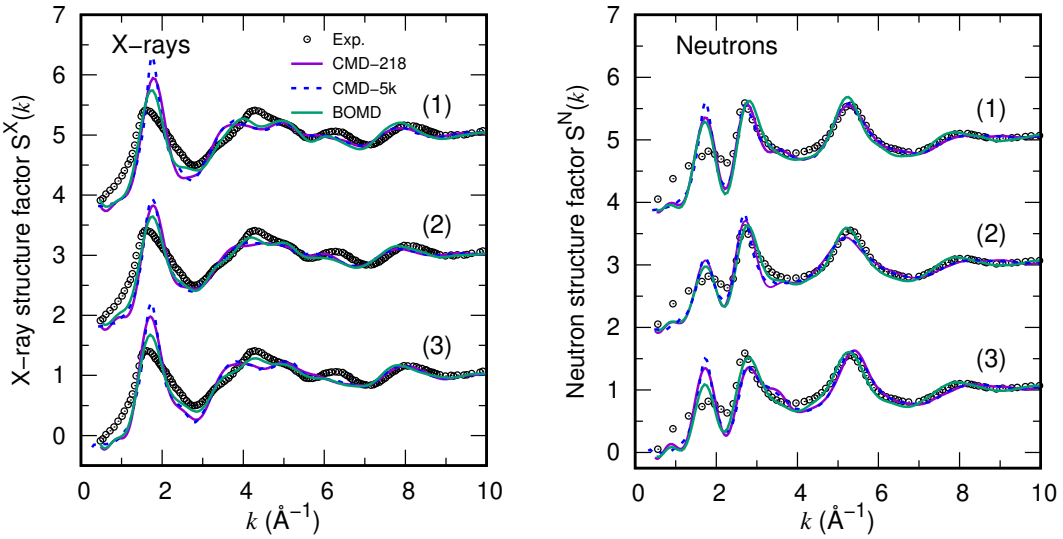

Figure 4.3. Total X-ray (left) and neutron (right) structure factors for VP50 glass simulated by CMD and BOMD obtained through Fourier transform (FT) of the pair correlation functions, for the three models indicated as (1), (2), and (3). We report the analysis for the 218 atoms model (CMD (purple) and BOMD (green)), the 5450 atoms model (CMD, dashed blue line), and also report the experimental data (black circles) [53].

Concerning $S^N(k)$, we obtain a good agreement with the experimental results when considering peak positions and intensities for k values ≥ 3 Å^{-1}. However, both calculated neutron and X-ray structure factors overestimate the intensity of the first peak, located

Table 4.2. Neutron scattering lengths b and X-ray atomic form factors f of V, P and O calculated at k=0 and for incident photon energy of 121.9 keV [273, 274].

Element	b (fm)	f (e/atom)
V	-0.382	23.022
P	5.131	15.005
O	5.803	8.000

at ∼2 Å^{-1}. Furthermore, $S^X(k)$ is less performing at high k. This can be attributed to the fact that X-ray are more sensitive to the vanadium atomic environment due to the comparatively smaller vanadium neutron scattering length (-0.382 fm). The variety of local V coordination featuring multiple oxidation states leads to less structured $S^X(k)$ peaks compared to $S^N(k)$.

The agreement between theory and experiments is quantified by calculating the R_χ factor [238] defined by the Eq. (3.11) Negligible variations are noted in the comparison between the 5450 and 218-atom models simulated by CMD, with only a slightly more pronounced first peak observed for the larger models. This implies that the 218-atom size is indicative of VP50 glass, without significant size effects being found. Considering the 0.5-10 Å^{-1} range of k, the R_χ values obtained for the three BOMD models fall within the range of 8.4-9.8 for X-ray and 8.4-12.0 for neutron. In comparison, the corresponding values for CMD span 11.3-12.8 for X-ray, as presented in Tab. 4.3 (see Tab. 4.4 for CMD 5450 atom models). This indicates a substantial enhancement of BOMD over CMD when evaluating the total X-ray structure factor. Nevertheless, the overall performance of the two methodologies lead to more comparable results in the case of neutrons. Furthermore, it is worth emphasizing that CMD2 shows the lowest X-ray and neutron R_χ values in comparison to CMD1 and CMD3. This indicates the closest alignment with BOMD and experimental results, particularly evident in terms of the intensity of the first peak in the $S^N(k)$ at about ∼1.8 Å^{-1}. The significant R_χ reduction obtained when adopting BOMD instead of CMD in the X-rays case is indicative of a drastic improvement in describing the local environment of V sites in VP50. Similarly, the reduced disparity between CMD and BOMD neutron R_χ values underscores the overall effectiveness of the three force field schemes in accurately describing both O and P environments, despite undergoing further improvements.

Table 4.3. Goodness-of-fit R_χ parameters obtained from CMD and BOMD data (218 atoms models) indicating the level of agreement with the experimental data for neutron and X-ray structure factors ($R_\chi^{S^X(k)}$ and $R_\chi^N(S(k))$, respectively) and total pair correlation functions ($R^X_{T(r)}$ and $R^N_{T(r)}$, respectively). All calculated values presented here are averaged over four parallel runs.

	CMD1	CMD2	CMD3	BO1	BO2	BO3
Neutrons						
$R^N_{S(k)}$	11.5 ± 0.1	9.8 ± 0.1	10.9 ± 0.1	12.0 ± 0.1	8.4 ± 0.2	8.9 ± 0.1
$R^N_{T(r)}$	37.9 ± 0.4	26.7 ± 0.1	45.8±0.3	31.0 ± 0.4	28.6 ± 0.5	27.7± 0.4
X-Rays						
$R^X_{S(k)}$	12.8 ± 0.1	11.3 ± 0.1	11.8 ± 0.1	9.8 ± 0.1	8.4 ± 0.2	8.4 ± 0.1
$R^X_{T(r)}$	45.0 ± 0.2	36.6 ± 0.3	52.0± 0.1	32.0 ± 0.2	28.7 ± 0.3	28.4 ± 0.4

4.4.2 Total pair correlation functions

Here we introduce the notion of total pair correlation function T(r) and its relationship with the total pair correlation function g_{tot}(r) commonly employed to identify short-range

Table 4.4. Goodness-of-fit R_χ parameters obtained from CMD (5040 atom models) data indicating the level of agreement with the experimental data for X-ray and neutron structure factors (($R^X_{S(k)}$ and $R^N_{S(k)}$, respectively) and total correlation functions ($R^X_{T(r)}$ and $R^N_{T(r)}$, respectively). All calculated values presented here are averaged over the four individual run per model.

	CMD1-5k	CMD2-5k	CMD3-5k
X-Ray			
$R^X_{S(k)}$	13.62 ± 0.02	10.79 ± 0.05	12.27 ± 0.01
$R^X_{T(r)}$	43.86± 0.01	35.64 ± 0.01	50.56± 0.07
Neutron			
$R^N_{S(k)}$	11.64 ± 0.01	9.12 ± 0.02	10.46 ± 0.01
$R^N_{T(r)}$	35.43±0.06	23.53 ± 0.03	43.80 ±0.03

structural features in a disordered solid as it was not mentioned in Chapter 2. By referring to the case of neutron diffraction measurements, these two quantities are related by the following equation :

$$\begin{aligned} T(r) &= 4\pi\rho r + \frac{4\pi\rho r}{|\langle b\rangle|^2}\sum_{\alpha\beta} c_\alpha c_\beta b_\alpha b_\beta \left[g_{\alpha\beta}(r) - 1\right] \\ &= 4\pi\rho r g_{tot}(r), \end{aligned} \tag{4.1}$$

A similar expression holds for the X-ray case provided the form factors take the place of the coherent scattering lengths. T(r) can be also obtained by Fourier transform of the total structure factor through the following equation, in which $S(k)$ is a generic total structure factor obtained, as in the case of the experiments considered in this work, by X-ray or neutron measurements [53, 236].

$$T(r) = 4\pi\rho r \; + \; \frac{2}{\pi}\int_0^{k_{max}} dk \; k \; (S(k) - 1) \; M(k) \sin(kr), \tag{4.2}$$

where $M(k)$ is a modification function used to truncate $S(k)$ with $M(k) = 1$ for k $\leq$ k$_{max}$ and $M(k) = 0$ for k $>$ k$_{max}$.

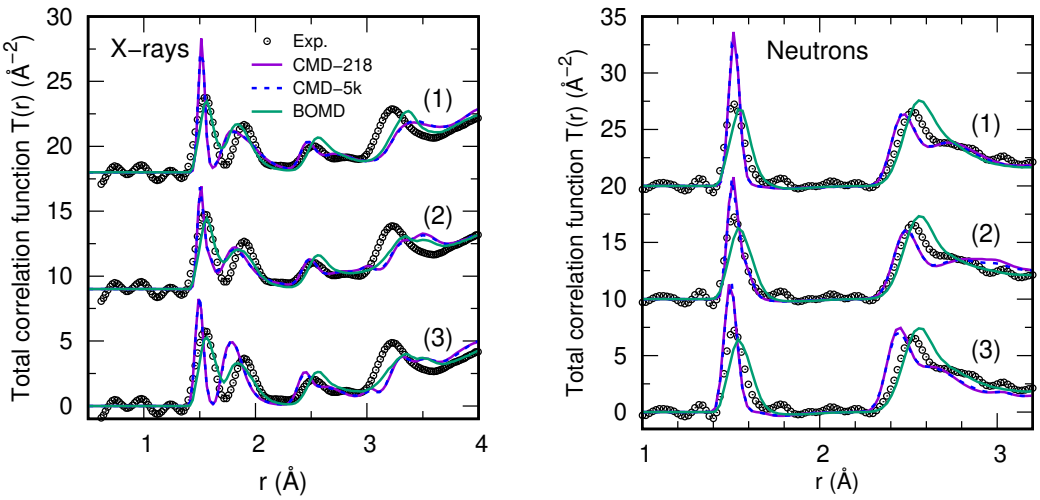

Figure 4.4. Calculated X-ray (top) and neutron (bottom) total pair correlation functions for VP50 glass obtained by CMD and BOMD simulations at 300 K for the three models indicated as (1), (2), and (3). We report the analysis for the 218 atoms model (CMD (purple) and BOMD (green)), the 5450 atoms model (CMD, dashed blue line), and also report the experimental data (black circles) [53].

The total pair correlation functions obtained for CMD and BOMD models (Eq. (4.1)) are shown in Fig. 4.4, together with the experimental data [53] (Eq. (4.2)). Collectively, we discern very marginal distinctions between CMD 218 and 5450-atom models, fully aligning with previous observations derived from the total structural factors. This reinforces the representative description of VP50 glass with the 218 atoms models, and dismissing any potential size effects. Each of the three CMD models shows a noticeable overestimation of the first peak in both X-ray and neutron total pair correlation functions when compared to BOMD data. CMD3, in particular, shows the least agreement with BOMD and experimental data, notably in relation to the second and third peaks in X-rays (attributed to O–O and V–P correlations, [53]) and the second peak in neutrons total correlation functions (attributed to O–O correlations [53]). In contrast, CMD2 shows the most favorable overall performance when compared to CMD1 and CMD3. It notably improves in reproducing the intensity of the first peak in both X-ray and neutron total pair correlation functions. Nevertheless, all three BOMD models unequivocally exhibit improvements over the three CMD models in the intensity of the first peak for both X-ray and neutron total pair correlation functions. Remarkably, the results remain very similar across all BOMD models, irrespective of the initial CMD scheme employed. This improvement is substantiated by the R_χ parameter values in Tab. 4.3 within the 1-3.2 Å range, unequivocally highlighting the superior quantitative description of the BOMD approach compared to CMD.

4.4.3 Partial pair correlation functions

CMD and BOMD partial pair correlation functions $g_{\alpha\beta}(\mathrm{r})$ are shown in Fig. 4.5 and Fig. 4.6 (left). In what follows, $g_{\alpha\beta}(\mathrm{r})$ calculated via the CMD or the BOMD approach will be also referred to as $g_{\alpha\beta}(\mathrm{r})$ (CMD) and $g_{\alpha\beta}(\mathrm{r})$ (BOMD), respectively. Bond distances are taken to correspond to the position of the first maximum of $g_{\alpha\beta}(\mathrm{r})$, allowing a comparison with experimental values, as reported in Tab. 4.5.
Fig. 4.7 illustrates the deconvolution fitting analysis conducted on BO1 $g_{\alpha\beta}(\mathrm{r})$ data, as an example of the procedure used; the same approach was applied to BO2 and BO3 $g_{\alpha\beta}(\mathrm{r})$ data. Tab. 4.7 reports the bonds distances calculated for the 5450 atom models simulated by CMD.

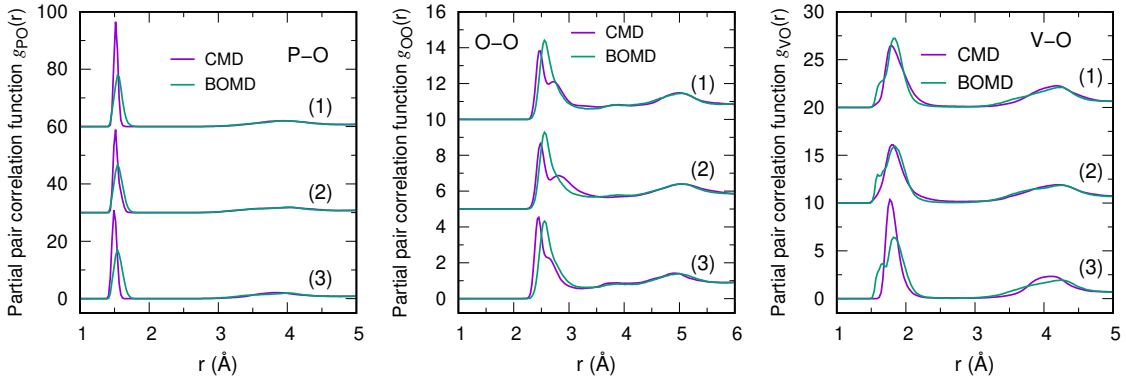

Figure 4.5. Partial pair correlation functions for the simulated VP50 glass at T = 300 K for the three models (1), (2), and (3). Shown from left to the right are $g_{\mathrm{PO}}(\mathrm{r})$ (left), $g_{\mathrm{OO}}(\mathrm{r})$ (middle), and $g_{\mathrm{OO}}(\mathrm{r})$ (right). BOMD results are represented by green lines, while CMD results are illustrated by purple lines.

P–O pair

The first peak of $g_{\mathrm{PO}}(\mathrm{r})$ is due to the four P–O bond distances of PO_4 tetrahedral units. These units are composed of longer P–O bonds that connect P with three bridging oxygen

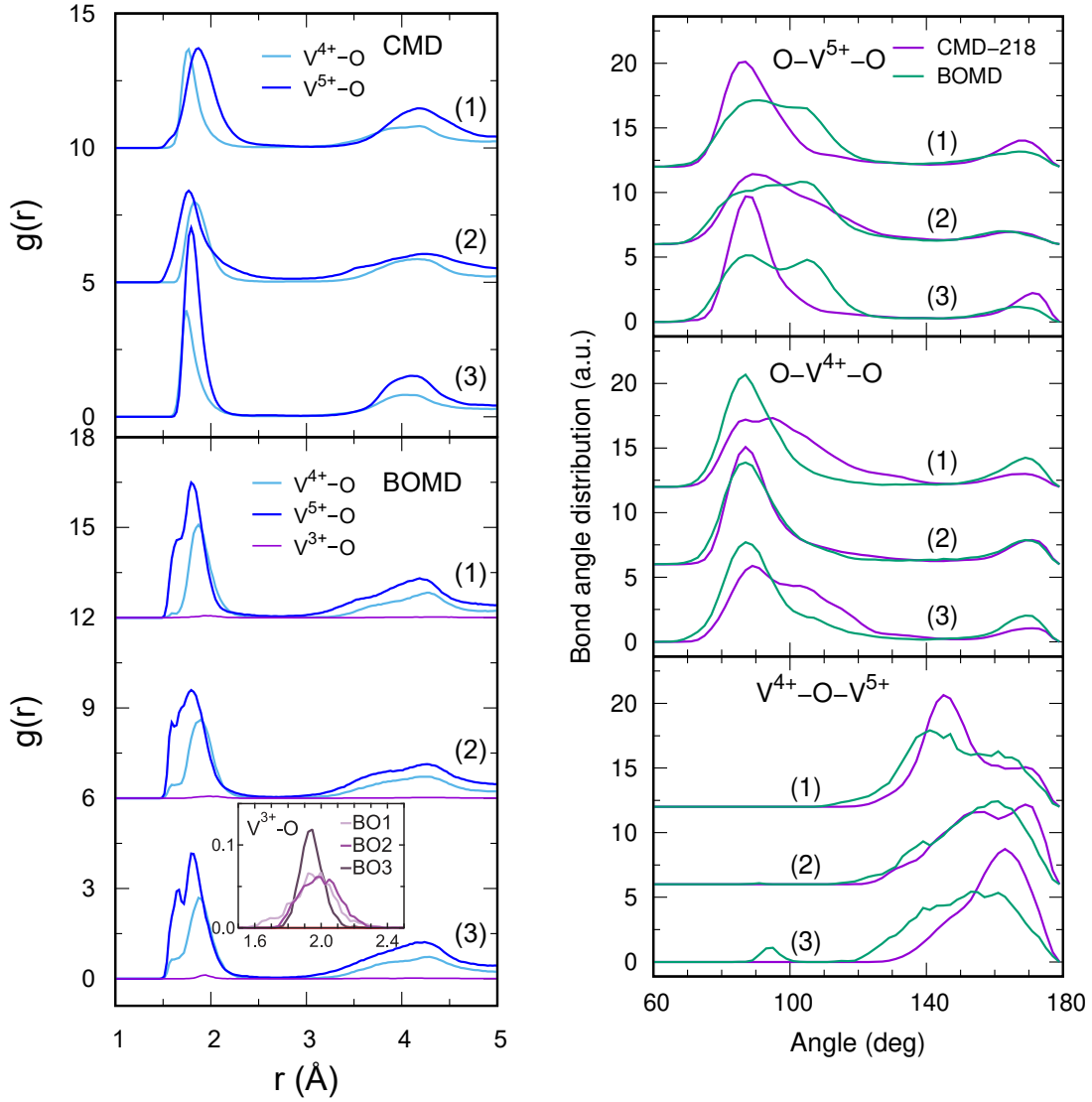

Figure 4.6. **(Left)** : Comparison of V–O partial pair correlation functions for various oxidation states of V sites. The upper part shows CMD data, while the lower part depicts BOMD data. The inset provides a close-up view of the V^{3+}–O partial pair correlation functions obtained for the three BOMD models. All these plots represent the decomposition of the V–O partial pair correlation function for the total V, wherein the sum of these individual g(r) functions yields the $g_{V^{tot}O}$(r) reported in Fig. 4.5 (right). **(Right)** : O–V^{5+}–O (top), O–V^{4+}–O (center), and V^{4+}–O–V^{5+} (bottom) bond angle distributions obtained via CMD and BOMD at T = 300 K.

(BO, two-folded O) atoms and one shorter P–O bond. This bond connects P to one nonbridging oxygen (NBO, one-folded O) atom. NBO bonds are associated with double P=O bonds, characterized by shorter bond lengths. Looking at Fig. 4.5 (left part), it appears that CMD and BOMD results have in common a sharp first peak centered at 1.50 Å and 1.55 Å, respectively. However, the first peak in g_{PO}(r) for the three CMD models is sharper and much more intense, accounting for a significant overstructuring of bond distances between P and O atoms. On the contrary, g_{PO}(r) for the three BOMD models provides a more broadened description of the bond distances of PO_4 units. P−NBO and P−BO bond distances obtained by CMD are found very close, being both about 1.50 Å. This can be interpreted as a shortcoming of the three classical force fields since measurements have revealed a well-defined difference in bond lengths between the short double P=O bond and the longer single P–O bond, with values of 1.52 Å and 1.60 Å respectively [53]. It is worth noting that this was not the case for glasses containing alkali

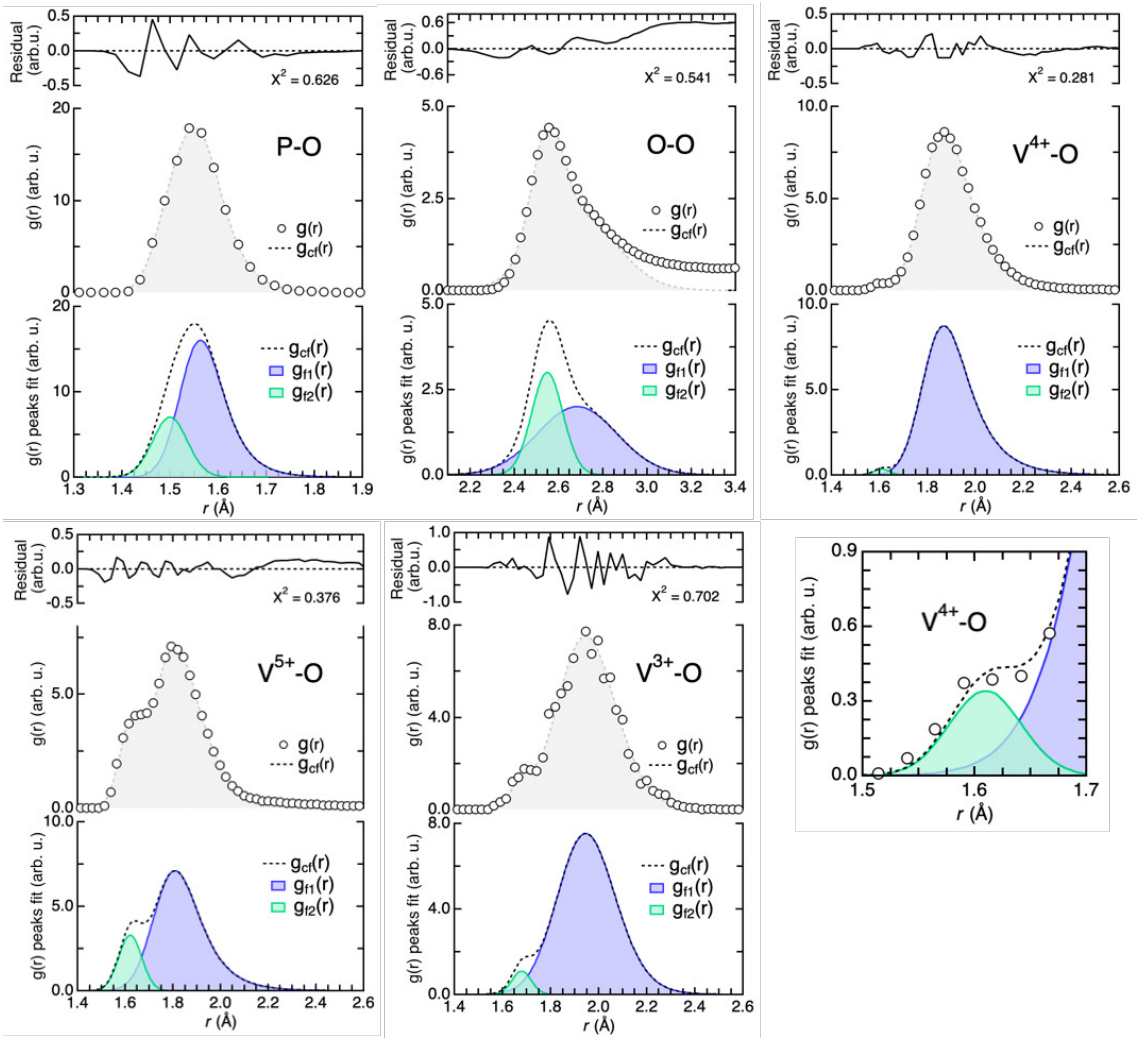

Figure 4.7. Deconvolution fitting of the P-O, O-O, V^{5+}-O, V^{4+}-O, and V^{3+}-O partial pair correlation functions computed for BO1 model. We report the calculated data ($g_{\alpha\beta}(r)$, black circle), the cumulative fit ($g_{\rm cf}(r)$, dashed gray line), the deconvolution fits of the peaks corresponding to the single and double bonds ($g_{\rm f_{1,2}}$(r), blue and green data) and the residual data. We give also the final χ^2 as an indicator of the quality of the fit. For the V^{4+}-O partial pair correlation function, a zoom-in in the 1.5-1.7 Å interval is made available. The same analysis was performed for BO2 and BO3 sets, results are reported in Table 4 of main text of the manuscript.

or earth ions, such as Na and Ca since the PMMCS/BMP force fields (CMD1 and CMD2) were able to accurately capture the difference in bond lengths between P–NBO and P–BO bonds, with values equal to 1.47 Å and 1.58 Å, respectively, closer in agreement with experimental data [108]. In the present case, our deconvolution fitting of $g_{\rm PO}$(r) (BOMD) leads to bond lengths equal to 1.51 Å and 1.56 Å for the P=O and P–O bonds, respectively for the three BOMD models (see Fig. 4.7), in much better agreement with experiments. Of particular note is that the three BOMD models exhibit very similar $g_{\rm PO}$(r) profiles, both in terms of peak intensities and positions. Therefore, to attain a more quantitative description of alkali ions-free vanadophosphate glasses, particularly regarding the bonding within PO_4 units, opting for BOMD over classical MD and force fields is advisable due to its superior quantitative approach.

Table 4.5. Bond lengths r_{ij} (in Å) (taken as the position of the first maximum of the pair correlation functions $g_{\alpha\beta}(r)$) and average coordination numbers n_i, computed for the 218 atoms models. For BOMD data, we report the distances obtained from the first maximum of $g_{\alpha\beta}(r)$. We also report the experimental values for VP50 glass [53, 276] and those found in crystalline vanadophosphate phases [67, 68, 275]. The average statistical error, computed across the replicas, for the simulated data (CMD and BOMD), is 0.02 Å.

	Exp. [53, 67, 68, 275, 276]	CMD1	CMD2	CMD3	BO1	BO2	BO3
r_{PO}	1.52	1.50	1.51	1.49	1.50	1.51	1.51
	1.60	-	-	-	1.56	1.56	1.56
r_{VO}	1.58	-	-	-	1.62	1.59	1.65
	1.90	1.79	1.81	1.78	1.84	1.83	1.83
$r_{V^{5+}O}$	1.59–1.78[a]	-	-	-	1.62	1.59	1.65
	1.80–2.35[a]	1.88	1.76	1.79	1.81	1.79	1.82
$r_{V^{4+}O}$	1.59–1.74[a]	-	-	-	1.61	1.60	1.59
	1.80–2.12[a]	1.76	1.83	1.74	1.87	1.90	1.87
$r_{V^{3+}O}$	-	-	-	-	1.68	-	-
	1.88–2.18[a]	-	-	-	1.95	1.99	1.95
r_{OO}	2.52	2.47	2.48	2.46	2.54	2.56	2.56
	2.74	2.70	2.81	2.63	2.72	2.71	2.70
r_{VV}	3.50	3.54	3.51	3.50	3.50	3.52	3.52
r_{PV}	3.24	3.35	3.30	3.28	3.35	3.32	3.30
n_P	3.9	4.00	4.00	4.00	4.00	4.00	4.00
$n_{V^{tot}}$	5.1-5.4	5.09	4.73	5.01	5.06	4.97	5.02
$n_{V^{5+}}$	4.0-6.0[a]	5.38	4.48	5.28	4.81	4.73	4.78
$n_{V^{4+}}$	5.0-6.0[a]	4.61	5.15	4.55	5.53	5.36	5.44
$n_{V^{3+}}$	6.0[a]	-	-	-	5.99	5.99	6.00
n_O	2.0–4.0[b]	1.89	1.83	1.91	1.88	1.86	1.88

[a] Characteristic bond lengths intervals analysed from about 520 vanadophosphate crystalline phases [67, 68, 275].
[b] Mean coordination number interval of O atoms vanadium oxides and VP crystalline compounds reported by [53].

O–O pair

The first peak of $g_{OO}(r)$ of the three CMD models is located at about ∼2.47 Å and it is found very sharp, followed by a less intense feature centered at different position depending on the force field, at 2.70 Å (CMD1), 2.81 Å (CMD2), and 2.63 Å (CMD3). Previous studies have indicated that the ratio of these two peaks depends on the glass composition [81]. In contrast, $g_{OO}(r)$ of the three BOMD models show similar behaviour with a positively-skewed peak with a maximum at about 2.54-2.56 Å. Further analysis through deconvolution peak fitting (see Fig. 4.7) reveals that the BOMD data can be fitted, minimizing the goodness-of-fit R_χ parameter, with two peaks centered at 2.54-2.56 Å and 2.70-2.72 Å. The first peak is commonly associated with oxygen atoms in PO_4 tetrahedra units, which is a characteristic feature of other phosphate glasses [276]. The second peak at longer distances is attributed to oxygen atoms in corner-sharing VO_n structural units [53, 276, 277]. The distances obtained by both CMD and BOMD agree fairly well with experimental data reported by Hoppe *et al.* [53] for VP50 glass (2.52 Å and 2.74 Å).

V–O pair

The first peak of $g_{VO}(r)$ is due to the bond distances between O and V atoms in distinct VO_n structural units, which result from the different oxidation states of V. The picture of V−O bonding arising from $g_{VO}(r)$ differs when comparing CMD and BOMD models. Specifically, $g_{VO}(r)$ in CMD1 displays an asymmetrical peak centered at 1.79 Å, while $g_{VO}(r)$ in CMD2 and CMD3 exhibit symmetrical peaks centered at 1.81 Å and 1.78 Å, respectively. Notably, CMD3 shows a much more intense and sharp peak compared to CMD1 and CMD2. On the contrary, $g_{VO}(r)$ of the three BOMD models feature a similar behaviour with a peak with a maximum at about 1.83-1.84 Å that is preceded by a clear shoulder. To better understand the scenario of bond distances in VO_n polyhedra, we show the breakdown of $g_{VO}(r)$ for the V sites with different oxidation states for both CMD and BOMD data in Fig. 4.6, Left. The asymmetrical profile of $g_{VO}(r)$ in CMD1 primarily arises from the distinct peak positions and intensities of V–O bonds promoted by V^{5+} and V^{4+}, centered at 1.88 Å and 1.76 Å, respectively. In contrast, $g_{VO}(r)$ in CMD2 exhibits V–O bonds promoted by V^{5+} and V^{4+} centered at 1.76 Å and 1.83 Å, respectively. Meanwhile, $g_{VO}(r)$ in CMD3 shows V–O bonds promoted by V^{5+} and V^{4+} with distinct sharpness and peak maxima positions, at 1.79 Å and 1.74 Å, respectively. These results clearly indicate a significant divergence in the description of V–O bond interactions among the different force fields.

A different situation is observed in $g_{VO}(r)$ BOMD models, the three showing very similar behaviour, with $g_{V^{5+}O}(r)$ exhibiting a peak with maximal intensity at 1.79-1.82 Å that is preceded by a shoulder centered at 1.59-1.61 Å. In contrast, $g_{V^{4+}O}(r)$ has a small peak at 1.59-1.61 Å, followed by a more intense one centered at 1.87-1.90 Å. We also included $g_{V^{3+}O}(r)$ for completeness, although BOMD calculations revealed only a minor content of V^{3+}. BOMD results are highly consistent with experimental data, since they capture the short vanadyl (double) bond V=O and longer single V–O bonds. These bonds lie in the range 1.55–1.78 Å and 1.80–2.35 Å, respectively. A notable feature reported in the literature for vanadophosphate crystalline phases is the increase of the length of V–O single bonds with decreasing V oxidation state [67–69]. Also, V^{5+} and V^{4+} exhibit at least one vanadyl bond, while V^{3+} does not show any. For the VP50 glass, Hoppe *et al.* [53] reported multiple bonding distances for V^{tot}–O, including 1.58 Å, 1.90 Å, 2.10 Å, and 2.48 Å. Overall, BOMD calculations accurately describe the untrivial bonding pattern of VO_n polyhedra in good agreement with the reported experimental trends. In fact, one obtains short vanadyl and long single bonds of VO_n as well as an ordering of distances of single bonds with respect to the V oxidation state that goes as follows: V^{5+}–O < V^{4+}–O < V^{3+}–O (the respective values being 1.79-1.82 Å, 1.87-1.90 Å, and 1.95-1.99 Å). CMD results obtained with the three force fields tested in the present work fall short when compared to the BOMD outcomes in faithfully reproducing the intricate bonding patterns of VO_n polyhedra. However, a few critical remarks can be delineated. The selection of force field parameters in CMD1 introduces a notable disparity in describing V^{5+}–O and V^{4+}–O bonds, contrary to experimental findings that highlight longer V^{4+}–O distances compared to V^{5+}–O bonds. CMD3 force field exhibits very negligible differences in V^{5+}–O and V^{4+}–O bond distances, again reflecting V^{4+}–O bonds as shorter than V^{5+}–O bonds, both portrayed by extremely structured $g_{V^{5+/4+}O}(r)$ first peaks. The CMD2 force field choice emerges as the most effective among CMD1 and CMD3, manifesting a notable difference in V^{4+}–O and V^{5+}–O bonds and aligning with the trend observed in experiments.The sole noteworthy limitation of CMD2, shared across all three force fields, is its inability to precisely characterize both short V=O and long V–O bonds inherent in VO_n polyhedra, aspects that can only be accurately described at the BOMD level. The first peaks in $g_{V^{5+/4+}O}(r)$ (CMD) are centered at distances between the vanadyl and individual V–O

bonds. However, it is important to highlight that for a relatively low V oxide content, the CMD1 force field has demonstrated the ability to accurately capture both short and long V–O bonds [80].

4.5 Structural properties: atomic scale tools to describe the network

4.5.1 Coordination numbers and structural units identification

To gain further insights into the VP50 glass network, we can examine the averaged coordination numbers (n_i with i=P, O, V) by integrating the first peak of $g_{\alpha\beta}$(r) up to a cutoff distance corresponding to the position of the first minimum. This allows us to extract the coordination numbers n_i. Fig. 4.8 displays the running integrals of the individual partial correlation functions $g_{\alpha\beta}$(r) for CMD1/BO1, CMD2/BO2 and CMD3/BO3. The calculated coordination numbers n_i are listed in Tab. 4.5, along with available experimental data. For V, we also report the contribution of individual oxidation states (V^{4+} and V^{5+} for CMD and V^{3+}, V^{4+}, and V^{5+} for BOMD).
As depicted in Fig. 4.8 and summarized in Tab. 4.5, both CMD and BOMD yield comparable values for the average coordination of P and O atoms, aligning reasonably well with reported experimental data, obtaining values of ∼4 and ∼1.9, respectively. Regarding the total V coordination, CMD1 and CMD2 exhibit close values (5.0 - 5.1), while CMD2 displays a slightly lower value (4.73). All three BOMD models demonstrate very similar coordination values for total V, at about 5.0 - 5.1.

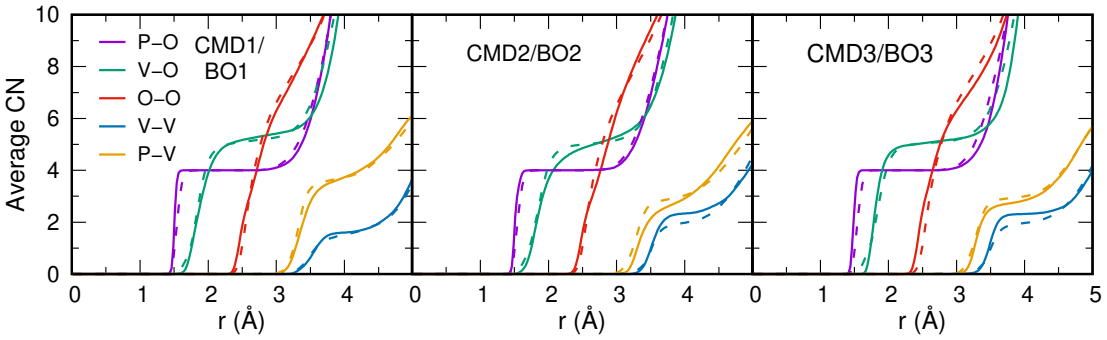

Figure 4.8. Running averaged coordination number of the three models obtained by CMD (solid line) and BOMD (dashed line).

However, when analysing the breakdown of V coordination into distinct oxidation states, more pronounced and contrasting trends become evident between the three CMD force fields and between CMD and BOMD data. The average n_V decreases with the increase of the V oxidation state for CMD1 and CMD3 (from 5.4 – 5.3 to 4.6 for V^{5+} and V^{4+}, respectively). Conversely, CMD2 exhibits an opposite trend, aligning with experimental findings (from 4.5 to 5.2 for V^{5+} and V^{4+}, respectively). Notably, all three BOMD models follow a consistent trend, aligning with CMD2 data and fully concurring with experimental observations (4.7 – 4.8, 5.4 – 5.5, and 6.0 for for V^{5+}, V^{4+}, V^{3+} respectively).

We also computed the distribution of the structural coordination units $n_\alpha(l)$ characterizing the environment of each atom. In this way, for a given number of neighbors l and a given atomic species, one can extract from each configuration the chemical nature of the neighbors. It is important to underline the difference between n_i and $n_\alpha(l)$. The quantities n_i give an average behavior stemming from all neighbors with no insight into

the detailed chemical nature of bonding, while the coordination structural units $n_\alpha(l)$ focuses on how each atomic species organizes itself when connecting to atoms of the same or of a different kind. The distributions of $n_\alpha(l)$ structural units for P, O, and V (V^{tot} and V^{3-5+}) are reported in Tab. 4.6, together with the breakdown of the chemical composition of each structural unit for a given l. The findings reveal that the initial coordination shell of P comprises exclusively fourfold connections, resembling PO_4 units, fully consistent with experimental data [53]. Concerning the first coordination shell of O atoms, CMD and BOMD results exhibit similar results, considering the computed error uncertainty. Remarkably, the large models (5k atoms) simulated by CMD consistently align with the values obtained for the smaller model (see Tab. 4.7).

Table 4.6. Distribution of the individual $n_\alpha(l)$ structural units where an atom of species α (P, V or O) is l-fold coordinated, computed for the 218 atoms models. In bold are reported the total percentages determined for each l-fold coordination. These quantities have been calculated including neighbours separated by a cutoff corresponding to the first minimum in the $g_{\alpha\beta}$(r). For the present work, the cutoffs of 2.0 and 2.4 Å was used for the P-O and V-O bonds respectively. The values with a star (*) correspond to the appearance of certain vanadium environment configurations in low concentrations. Only fraction greater than 0.5 % are reported.

		CMD1	CMD2	CMD3	BOMD1	BOMD2	BOMD3
V^{tot}							
$l=4$	O_4	22.2 ± 1.4	41.8 ± 0.4	25.3 ± 0.6	26.9 ± 0.5	26.4± 0.6	30.2± 0.8
$l=5$	O_5	46.3 ± 1.2	40.6 ± 0.5	48.8 ± 0.9	40.4 ± 0.6	51.4 ± 1.1	38.2± 1.8
$l=6$	O_6	31.5 ± 0.7	16.6 ± 0.2	25.9±0.6	32.0 ± 0.3	21.4 ± 0.7	30.5± 1.2
V^{5+}							
$l=4$	O_4	4.8 ± 0.6	36.5 ± 0.5	4.5 ±0.5	25.7 ± 0.5	24.1 ± 0.6	26.0 ± 1.2
$l=5$	O_5	28.9 ± 0.7	19.2 ± 0.7	36.1 ± 1.1	24.7 ± 0.4	32.0± 0.6	24.2±0.8
$l=6$	O_6	28.8 ± 0.7	5.9 ± 0.4	21.9 ± 0.7	12.3 ± 0.5	5.8± 0.5	12.3± 0.9
V^{4+}							
$l=4$	O_4	17.4 ± 1.1	5.3 ± 0.2	20.8 ± 0.6	1.2 ± 0.2	2.1 ± 0.5	3.9 ± 0.7
$l=5$	O_5	17.4 ± 0.9	21.5 ± 0.5	12.7±0.7	14.7 ± 0.6	19.7 ± 0.8	14.1± 1.1
$l=6$	O_6	2.8 ± 0.3	10.8 ± 0.3	4.0 ±0.3	20.1 ± 0.5	15.3 ± 0.5	18.0± 1.6
V^{3+}							
$l=6$	O_6	-	-	-	0.8* ± 0.0	0.8* ± 0.0	0.8* ± 0.0
P							
$l=4$	O_4	100.0 ± 0.0	100.0± 0.0	100.0± 0.0	99.3 ± 0.1	98.8 ± 0.3	99.2 ± 0.2
O							
$l=1$		**11.0 ± 0.5**	**18.2±0.3**	**12.7±0.3**	**12.1 ± 0.2**	**14.0 ±0.3**	**12.8 ± 0.5**
	P	10.0 ± 0.4	16.5 ± 0.1	11.8 ± 0.2	9.1 ± 0.1	8.1 ± 0.1	7.8± 0.3
	V	1.0 ± 0.1	1.7 ± 0.2	0.9 ± 0.1	2.9 ± 0.1	5.9 ± 0.2	5.0 ±0.2
$l=2$		**87.8 ± 0.5**	**80.7 ±0.6**	**85.4±1.3**	**87.6 ± 0.2**	**85.4± 0.6**	**86.9± 1.4**
	VP	71.6 ± 0.5	49.6 ± 0.3	55.3± 0.8	73.6 ± 0.1	58.7 ± 0.3	60.2 ± 0.8
	V_2	16.2 ± 0.1	23.2 ± 0.1	23.2±0.2	13.9 ± 0.1	18.8 ± 0.1	19.3 ± 0.3
	P_2	0.4 ± 0.0	7.9 ±0.2	6.9 ± 0.3	0	7.9± 0.2	7.4± 0.3

Our findings reveal that the three CMD models show that 79% to 88% of oxygen atoms exhibit two-fold coordination, with 11% to 18% characterized by one-fold coordination. Similarly, in the three BOMD models, a comparable trend is observed. However, there is a narrower variability among the three BOMD models, with 86% to 88% of oxygen atoms exhibiting two-fold coordination, and 12% to 24% characterized by one-fold coordination. The decomposition in terms of chemical species reveals that two-folded O atoms are mainly coordinated with one P and one V (VP), however the three different CMD models show different values with ∼72% (CMD1), ∼50% (CMD2), and ∼55% (CMD3). Similar trend is found with BOMD, with ∼74% (BO1), and ∼60% (BO2 and BO3). Additionally, O coordinated by two V atoms (V_2) accounts for 16 – 23% (CMD) and 14 – 19% (BOMD)

Table 4.7. Distribution of the individual $n_\alpha(l)$ structural units where an atom of species α (P, V or O) is l-fold coordinated, computed for the CMD 5040 atoms models. In bold are reported the total percentages determined for each l-fold coordination. These quantities have been calculated including neighbours separated by a cutoff corresponding to the first minimum in the $g_{\alpha\beta}(r)$. For the present work, the cutoffs of 2.0 and 2.4 Å were used for the P-O and V-O bonds respectively. Only fraction greater than 0.5 % are reported.

		CMD1-5k	CMD2-5k	CMD3-5k
V^{tot}				
$l = 4$	O_4	22.2 ± 1.1	42.5 ± 1.3	28.9±1.6
$l = 5$	O_5	44.7 ± 2.4	40.8 ± 1.4	43.4±2.0
$l = 6$	O_6	33.1 ±1.5	16.1 ± 0.2	27.7±0.8
V^{5+}				
$l = 4$	O_4	8.0 ±0.8	36.5 ± 0.8	7.1±0.4
$l = 5$	O_5	25.6 ±1.5	20.6 ± 0.4	30.0±0.8
$l = 6$	O_6	28.9 ±1.2	4.8 ± 0.5	25.4±0.8
V^{4+}				
$l = 4$	O_4	14.2 ±0.7	6.02 ± 0.54	21.8±1.9
$l = 5$	O_5	19.1±1.0	20.2 ± 1.0	13.4±1.4
$l = 6$	O_6	4.3 ±0.3	11.3± 0.5	2.3±0.6
V^{3+}				
$l = 6$	O_6	-	-	-
P				
$l = 4$	O_4	100.0± 0.0	99.95 ± 0.1	99.8±0.2
O				
$l = 1$		**10.7 ± 0.4**	**18.5 ± 0.3**	**13.0 ±0.4**
	P	9.9 ±0.3	17.0 ± 0.1	12.1±0.3
	V	0.8 ± 0.1	1.5 ± 0.2	0.9±0.1
$l = 2$		**88.8 ± 0.4**	**80.8 ± 0.9**	**84.7±1.0**
	VP	72.0± 0.3	48.1 ± 0.5	54.1±0.6
	V_2	16.4±0.1	24.09± 0.10	23.6±0.3
	P_2	0.4 ± 0.0	8.6 ± 0.2	7.0±0.1

of the coordination units.

Regarding the total V, the three CMD models exhibit both similarities and differences. Notably, CMD1 and CMD3 reveal a predominant five-fold coordination in the majority of V atoms, accounting for 46% to 49%, respectively. CMD1 shows 32% and 22% of six- and four-folded V, respectively, while CMD3 exhibits 26% and 25% of six- and four-folded V. In contrast, CMD2 demonstrates an almost equipartition of total V between four- and five-coordination (42% and 41%) and a minority of six-folded V (17%). All these values closely align with the trend obtained with the larger CMD models (Table S7). Conversely, all three BOMD models display a highly similar trend. The majority of total V is five-folded (38% to 47%), with a nearly equal distribution of the remaining V between four- and six-folded (27% to 30% and 23% to 32%, respectively).

An analysis of the breakdown of V units in different oxidation states reveals significant differences among the three CMD models, whereas the three BOMD models align with a similar trend. CMD1 exhibits an almost equal distribution of V^{5+} between five-folded (VO_5) and six-folded (VO_6) coordination, each constituting ∼29%. In contrast, CMD3 displays a slightly higher proportion of five-folded units (36%) compared to six-folded units (22%). Both CMD1 and CMD3 show a minority (5%) of four-folded units (VO_4). Conversely, CMD2 presents a different profile with a majority (37%) of V^{5+} as four-folded units, followed by 19% five-folded and a minority of six-folded (6%) units. Shifting to

V^{4+}, the three CMD models yield distinct outcomes. CMD1 exhibits a similar content of four- and five-folded units (17%) and a minority of six-folded VO_6 units. CMD2 shows a preference for five-folded VO_5 units (22%) with minor contents of six-folded and four-folded units. Meanwhile, CMD3 shows a preference for four-folded VO_4 units (21%) with minor contents of five-folded and six-folded units. These results underscore the divergent behavior of the three force-field schemes when the V coordination units analysis is broken down according to different oxidation states of V. All the results are substantiated by the findings obtained for the larger CMD models (Table S8).
On the other hands, the three BOMD allign on very similar trends for the three different oxidation states of V. For V^{5+}, VO_4 and VO_5 are present in very close percentages (24% – 28%), while for VO_6 one has ∼12% for BO1 and BO3 and ∼6% for BO2. Notably, for V^{4+}, BOMD leads to the majority of V^{4+} found in VO_6 and VO_5 coordination units, accounting for ∼17–20% and ∼14–19%, respectively and a negligible content of VO_4 units (≤5%). The content of V^{3+} is negligible in the BOMD case, this motifs being found in VO_6 units, in accordance with experimental evidence. Overall, the BOMD results exhibit robust alignment with experimental data [53, 67, 68, 275]. Moreover, the CMD2 scheme aligns with BOMD data for V^{5+} and V^{4+}, in contrast, CMD1 and CMD3 exhibit complete deviation.

4.5.2 Bond angle distributions, local order parameter and network connectivity

The bond angle distributions (BAD) of triads O-V-O, centered around V^{5+} and V^{4+} atoms are shown in Fig. 4.6 (right). For O–V^{5+}–O triads, the three CMD models exhibit both similarities and discrepancies.

Notably, CMD1 and CMD3 display a distinct right-skewed peak around 90°, accompanied by a secondary peak at 170°. These angles are interpreted as representing (defective) octahedral and pyramidal units for the first peak and defective square and trigonal pyramids for the second. In contrast, CMD2 reveals a peak around 90° at a significantly lower intensity, accompanied by a more pronounced shoulder centered at approximately 109°. Additionally, CMD2 shows a less intense peak at 170° compared to CMD1 and CMD3. The greater contribution around 109° in CMD2 is attributed to the increased presence of VO_4 of V^{5+} and is linked to the implementaion of a three-body V–O–V potential in the CMD2 scheme.
The O–V^{4+}–O CMD1 and CMD3 results display a wide distribution spanning from 85° to 120°, accompanied by a minor peak at 170°. In contrast, CMD2 reveals a prominent peak centered at 90° with a minimal contribution observed at 109°. This latter feature is attributed to the vey minor presence of VO_4 in V^{4+}, as obtained with CMD2. Regarding the V^{4+}–O–V^{5+} triad, which pertains to the connection of VOn polyhedra, all three CMD models exhibit contributions centered around ∼148° and ∼165°, albeit with notable variations in their respective magnitudes.
In contrast, BOMD O–V^{5+}–O data are characterized by a double peak with maxima at around 90° and 106°, which corresponds to octahedral and pyramidal units (the former) and to the tetrahedral structure of $V^{5+}O_4$ units (the latter). There is also a less intense third peak centered at approximately 170° due to contributions from defective square and trigonal pyramids. For O–V^{4+}–O, BOMD features a prominent peak at 90°, which is typical of octahedral, pyramidal, and square pyramidal structures, and no contribution at around 109°, in agreement with the negligible quantity of $V^{4+}O_4$ connections found experimentally. Finally, a second minor peak is found at 170° due contributions from defective square and trigonal pyramids. Concerning the V^{4+}–O–V^{5+} triad, BOMD results reveal a wide distribution spanning from approximately 130° to 180°, displaying less structure compared to CMD datasets. However, CMD2 shows the closest alignment among the CMD

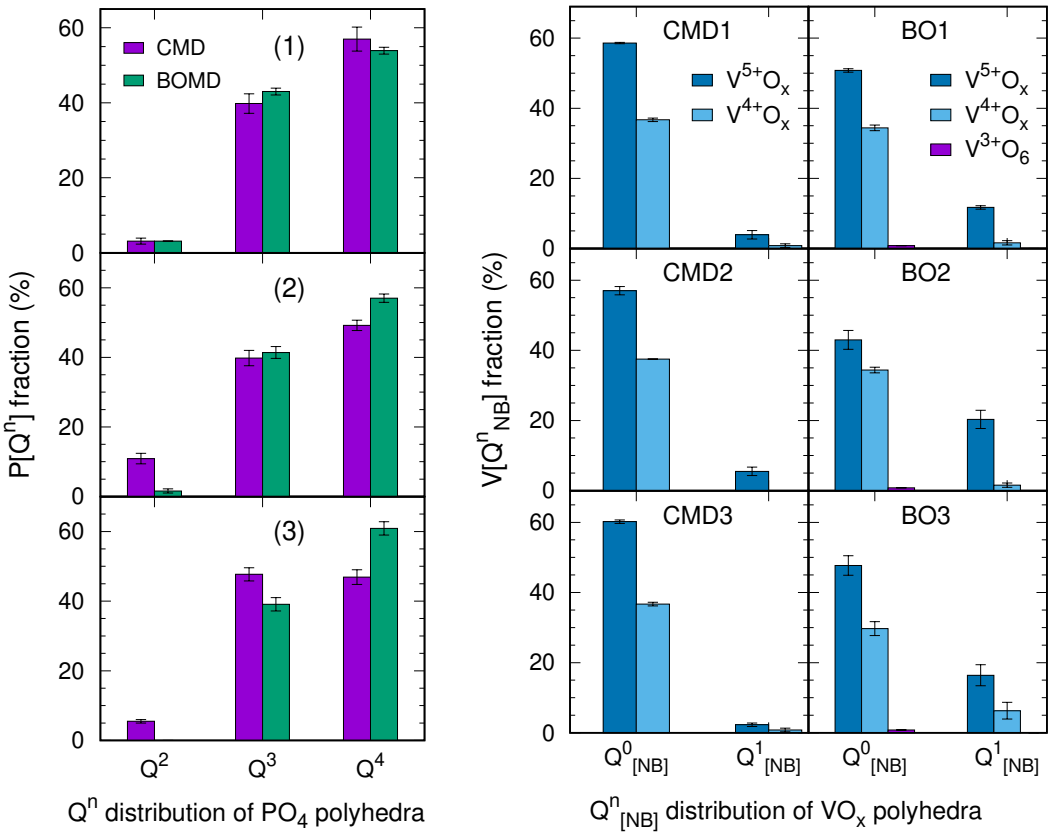

Figure 4.9. **Left**: Q^n distribution (with n the number of bridging oxygen per polyhedra unit) of PO_4 units in VP50 glass for CMD and BOMD calculations. **Right**: Distribution of $Q^n_{[NB]}$ (where n represents the number of non-bridging oxygen per polyhedra unit) of VO_x units, illustrating network connectivity in glassy VP50. The figure showcases V^{5+}, V^{4+}, and V^{3+} oxidation states obtained from CMD and BOMD.

models. Overall, the CMD1 and CMD3 datasets for O-V-O triads, focusing on V^{5+} and V^{4+}, exhibit notable disparities when compared to BOMD data. In contrast, the CMD2 scheme demonstrates the highest level of agreement, closely aligning with both BOMD results and, consequently, providing the closest match to experimental observations.
To further gain insights into the structural properties of VP50, we calculated the q parameter indicative of structural order,

$$q = 1 - \frac{3}{8} \sum_{j} \sum_{k \neq j} \left(\cos \theta_{jik} + \frac{1}{3} \right)^2 , \tag{4.3}$$

where θ_{jik} is the bond angle constructed from the central atom i and its neighbours j and k $(j, k \leq 6)$. q varies is equal to 0 for perfect six-fold octahedral and to 1 for four-fold tetrahedral structure [278]. This parameter is a useful tool for identifying the individual contributions of different structural units to the overall structural order as proven for a variety of amorphous systems, including glassy chalcogenides [279], chalcohalides [280], and phase-change materials [281, 282]. The calculation of q for P sites in VP50 glass yielded a value near 1 for both CMD and BOMD simulations, which is indicative of the presence of P uniquely in tetrahedral PO_4 units, in a way consistent with experimental observations.

As shown by the analysis of the V sites, VO_5 is the dominant vanadium structural units, comprising 38–47% of the vanadium content, with and VO_4 and VO_6 showing lower contents (27–30%, and 23–33%, respectively) in the BOMD models. Their corresponding q-parameter ranges in between 0.65 to 0.85, indicating the prevalence of defective square

pyramids (VO_5) and distorted octahedra (VO_6), with a few trigonal bi-pyramidal units observed in VO_5. Notably, V^{5+} units form mostly tetrahedral connections similar to PO_4 with a q-value close to 1, in addition to a similar content of defective square pyramids. Apart from tetrahedral polyhedra, the parameter q has limitations in quantitatively assessing the various VO_n polyhedra in the VP50 glass structure. This is due to the distorted nature of these polyhedra, resulting in varying q values even for polyhedra with the same geometric shape. These values deviate significantly from the reference ones [115].

Additional calculations were performed to obtain the Q^n species distribution, providing information on the degree of polymerization of the polyhedra into the three-dimensional network [48, 283]. Q^n is defined as a unit in which n bridging-oxygen (BO) atoms are directly linked to a network former ion, such as Si and P in silicate and phosphate glasses. Fig. 4.9 shows the breakout of the Q^n distribution for P sites in PO_4 tetrahedral units, with the three BOMD models featuring a majority of Q^4 (55–60%) and a non-negligible content of Q^3 (37–42%). The amount of Q^2 is negligible ($\leq$3%). These findings are in excellent agreement with the experimental data of Hoppe *et al.* [53] pointing to a coexistence of Q^4 and Q^3 units. CMD1 and CMD2 results show overall similar results to BOMD calculations, albeit with CMD2 showing a lower content of Q^4 ($\sim$50%) and a non-negligible content Q^2 ($\sim$10%). Whereas CMD3 shows a equal content of Q^3 and Q^4 ($\sim$47%) and minority of Q^2 ($\sim$5%).

We further explored the Q distribution for the V sites in VP50 glass, and the analysis was organized into contributions from V^{5+}, V^{4+}, and V^{3+}, as illustrated for both CMD and BOMD in Fig. 4.9. In alignment with the methodology employed by Hoppe *et al.* [53], our analysis involves the Q^n_{NB} notation for V sites, where n denotes the number of non-bridging oxygen atoms. This approach, differing from the Q^n notation used for P sites, proves to be more informative for characterizing V sites in the VP50 glass. The three CMD models indicate that the predominant local connectivity for V^{5+} and V^{4+} consists of Q^0 species, constituting 57-60% and 35-37%, respectively. Notably, there is minimal content of Q^1 ($\leq$5%) observed for V^{5+}. In contrast, the BOMD models exhibit a similar dominance of Q^0 for V^{4+} (30-34%), while for V^{5+}, the majority of Q^0 is somewhat reduced (44-50%) with a non-negligible content of Q^1 (10-20%). The few V^{3+} sites found with BOMD have been identified as Q^0. Overall, this analysis demonstrates that the VP50 glass is a highly polymerized disordered network.

4.6 Electronic and bonding properties

As a first piece of information, the electronic properties of glassy VP50 are investigated via the electronic density of states (EDOS) shown in Fig. 4.2. To mitigate the inherent underestimation of the band gap in DFT, we employed the PBE0 hybrid functional, designed to yield more realistic values by incorporating a Hartree-Fock contribution to the exchange part of the functional. The resulting band gap values for the three BOMD models ranged approximately from $\sim$2.4 to 2.8 eV. Notably, small yet finite differences between spin-up and spin-down states band gaps are obtained, indicating a discernible magnetic character. This means that VP50 glass is a wide-bandgap semiconductor with a small and yet sizeable magnetic character as several crystalline phases of $VOPO_4$ vanadyl phosphates, for which reported bandgap values are in between 2.5–2.9 eV [284].

To gain a deeper understanding of chemical bonding we resorted to the maximally localized Wannier function centers (WFC) by focusing mostly on the WFC proximal to O atoms, as O is the most electronegative element in VP50 and neither P or V contribute

with any lone pair electrons. We considered the pair correlation function $g_{O-WFC}(r)$ obtained at the PBE0 level, shown in Fig. 4.10(a). The partial pair correlation function $g_{O-W}(r)$ exhibits a distinct band ranging from 0.2–0.5 Å, characterized by three maxima and a very minor contribution at about 0.23 Å. About the three maxima, the more intense one is located at 0.29 Å, while the other two are centered at 0.40 Å and 0.47 Å. The three BOMD models show very similar $g_{O-W}(r)$ profiles, with negligible differences, mostly in terms of peak intensity. In what follows, we focus on the contributions of PO_4 and VO_n polyhedra to the peaks of $g_{O-W}(r)$.

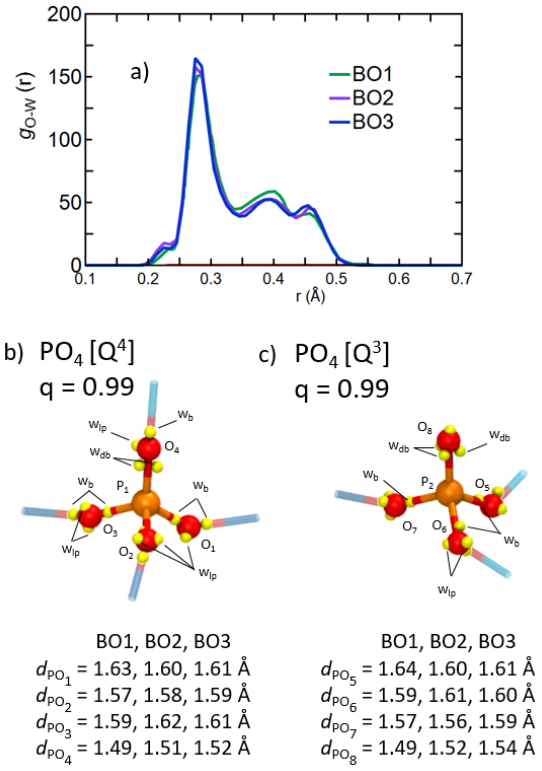

Figure 4.10. a) Partial pair correlation function $g_{O-WFC}(r)$. b,c) Atomistic view of two tetrahedral PO_4 units found in VP50 glass by BOMD at 300 K. We show P and O atoms in orange and red respectively. P-O bonds are colored as orange-red. Their bond distances as well as the PO_4 order parameter values q are reported. The transparent red/blue bonds correspond to neighbouring V-O bonds. P_1 atom is surrounded by four V-O-P bridging oxygen atoms (Q^4) whereas P_2 atom is surrounded by three V-O-P bridging oxygen atoms and one non-bridging oxygen (Q^3). We also show the Wannier centers (yellow) involved in the local environment of each PO_4 unit, as in single bonds (w_b; P_1–$O_{1,2,3}$ and P_2–$O_{5,6,7}$), lone pairs (w_{lp}) and as centers involved in double P=O bonds (w_{db}; such as P_1–O_4 and P_2–O_8).

4.6.1 P–O chemical bonding

Fig. 4.10 (b) and (c) provides an atomistic view of two tetrahedral PO_4 units (with ∼109° $\hat{OPO}$ angles), observed via BOMD calculations at 300 K. The first is a tetrahedral Q^4 PO_4 unit (q= 0.99), composed of one P (P_1) bonded to four bridging oxygen atoms via P–O–V linkages. The second unit also comprises a tetrahedral Q^3 PO_4 unit (q= 0.99), consisting of one P (P_2) bonded to three bridging O atoms through P-O-V linkages and one non bridging O atom. The arrangement of WFC centers in the local atomic environment surrounding these units is representative of three different WFC types, to be correlated to distances identified by the three maxima of $g_{O-WFC}(r)$. Specifically, we are referring to:

i) WFC due to lone pair electrons (w_{lp}) having very short O-WFC distances (0.29 Å).

ii) individual WFC (w_b) involved in single σ_{P-O} bonds (∼1.60 Å; e.g. P_1–O_{1-3} and P_2–O_{5-7} in Fig. 4.10 b)-c) and displaying a long O-WFC distance (0.48 Å).

iii) double or triple WFC (w_{db}; P_1–O_4 and P_2–O_8 in Fig. 4.10 (b), (c) respectively) involved in short bonds (∼1.49–1.54 Å) and featuring an intermediate O-WFC distance (0.40 Å).

All bonding WFC are found closer to O atoms than to P atoms, denoting highly polarized iono-covalent P–O bonds with localized distribution of valence electron density closer to O sites [285]. The presence of two WFCs in the short bonds is consistent with the simple Lewis picture of double P=O bonding, while the presence of three WFC identifies mixed σ–π orbitals that give rise to so-called "banana bond" τ orbitals [286, 287]. We have observed that P=O and O-WFC distances remain the same regardless of the nature of the Wannier centers and the bridging or non-bridging character of oxygen atoms allowing us to identify these bonds as double P=O bonds. The WFC approach promoted a more precise scrutiny of P–O interatomic distances, thus substantiating the values previously determined through the analysis of $g_{P-O}(r)$. Overall, all values obtained (P–O:∼1.60 Å and P=O: ∼1.50 Å, respectively) are found in excellent agreement with the experimental data [53].

4.6.2 V–O chemical bonding

The kind of $V^{5+}O_n$ units found in the VP50 glass are shown in Fig. 4.11. These units are: a four-folded V^{5+} tetrahedral Q^1_{NB}, a five-folded V^{5+} in square pyramidal or trigonal bi-pyramidal Q^0_{NB} configuration, and a six-folded V^{5+} in a distorted octahedral Q^1_{NB} unit [67, 68]. The arrangement of WFC centers in the local atomic environment of these units correspond to three different WFC types. These are characterized by different O-WFC distances identified by the three maxima of $g_{O-WFC}(r)$. One has:

i) WFC representing lone pair electrons (w_{lp}) at short O-WFC distances (0.29 Å);

ii) individual WFC (w_b) involved in single $\sigma_{V^{5+}-O}$ bonds with O-WFC distance of 0.40 Å;

iii) double or triple WFC (such as V_1–$O_{3,4}$, V_2–O_9, V_3–$O_{13,14}$, and V_4–O_{20}) involved in short bonds (∼1.60–1.72 Å) with longer O-WFC distance (0.48 Å).

The analysis of chemical bonds and related distances based on the WFC approach enables us to classify any V–O interaction longer than ∼2.4 Å as a non-chemical bond. This is because the next closest O atom is associated to a WFC with w_{lp} characteristics.
All the bonding WFC found in the local atomic environment of V are in closer proximity of O atoms than V, prompting a description in terms of highly polarized iono-covalent bonds [285]. Furthermore, in the case of VO_n polyhedra, the finding of double or triple WFC in short bonds is consistent with the picture of double or τ bonds and are denoted as vanadyl bonds [67, 68, 275]. These WFC are referred to as w_v in Fig. 4.11, allowing us to describe the coordination of VO_n within the formalism used in [53, 67, 68]. This consists in replacing the subscript n with two indexes, the first one being the number of vanadyl bonds and the second one the number of single bonds, the sum of the two being the total coordination of the V atom (i.e. $V^{5+}O_{[1+4]}$ identifies a $V^{5+}O_5$ unit with one vanadyl bond and four single bonds). The single and vanadyl bond distances obtained from the WFC analysis are found better agreement with the range of values reported in the experiments than those previously extracted from $g_{V-O}(r)$. For instance, averaged V^{5+}–O single and vanadyl bonds are ∼1.93 Å and ∼1.65 Å, respectively. These distances increase when the V^{5+} coordination increases such as ∼1.86 Å (VO_4) < ∼1.92 Å (VO_5) < ∼2.00 Å (VO_6), in

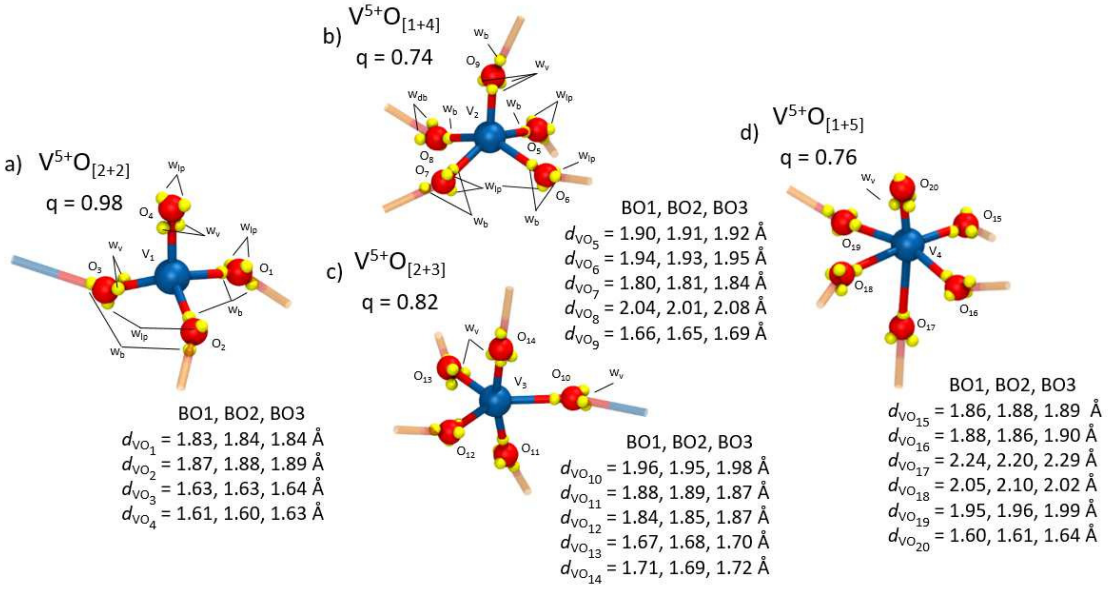

Figure 4.11. Snapshot of various $V^{5+}O_n$ polyhedra units within the VP50 glass network. The local atomic environment of V^{5+} sites is described by V^{5+}-O bond lengths and associated Wannier centers (highlighted in yellow). The polyhedra include: a) a tetrahedral unit standing for a VO_4 polyhedron with order parameter $q = 0.98$, b) a square pyramidal unit ($q = 0.74$), c) a defective trigonal bi-pyramidal unit ($q = 0.82$), and d) a distorted octahedral unit ($q = 0.76$).

line with the trend reported in experimental findings [53, 67, 68, 275]. Note that the very small contribution in the $g_{O-W}(r)$ at about 0.23 Å, correspond to the lone pair electrons of non-bridging oxygen atoms involved in vanadyl bonds.

Fig. 4.12 exemplifies the typical $V^{4+}O_n$ units present in the VP50 glass, consisting of V^{4+} in a five-fold coordination, either in a square pyramidal arrangement ($V^{4+}O_{[1+4]}$) or a by-pyramidal arrangement ($V^{4+}O_{[2+3]}$), and in a six-fold coordination as a distorted octahedral unit ($V^{4+}O_{[1+5]}$) as well. $V^{4+}O_n$ polyhedra display the three types of distorted WFC centers, with average vanadyl and single bond distances of ∼1.74 Å and ∼1.98 Å, respectively. Once again, these results are in better agreement with the experimental data than the values obtained from $g_{V^{4+}O}(r)$. The contribution to $g_{V^{4+}O}(r)$ due to vanadyl bonds, which was quantified previously by deconvolution fitting of $g_{V^{4+}O}(r)$, was underestimated because of the presence of the whole $g_{V^{4+}O}(r)$ peak corresponding to single V–O bond distances. Furthermore, the average value of single bonds increases slightly from $V^{4+}O_5$ to $V^{4+}O_6$ (∼1.96 Å and ∼1.99 Å). Although the content of V^{3+} in the VP50 glass is found minimal, some details related to this unit are worth mentioning.

Fig. 4.13 illustrates the typical coordinating unit found in this case, namely a six-coordinated Q^0 $V^{3+}O_{[1+5]}$ unit in a distorted octahedral polyhedra. There is a relatively long single V–O bond distance of ∼1.99 Å, which is consistent with the range of values reported in literature. One double WFC localization along one of the V–O bonds becomes visible along a particularly elongated V–O bond (∼1.85 Å). This distance lies at the boundary between vanadyl and single bond values. However, vanadyl bonds have not been reported for V^{3+}-containing polyhedra in vanado-phosphate crystalline phases. Therefore, we can legitimately label this bond as a weak vanadyl bond or a relatively short single V–O bond.

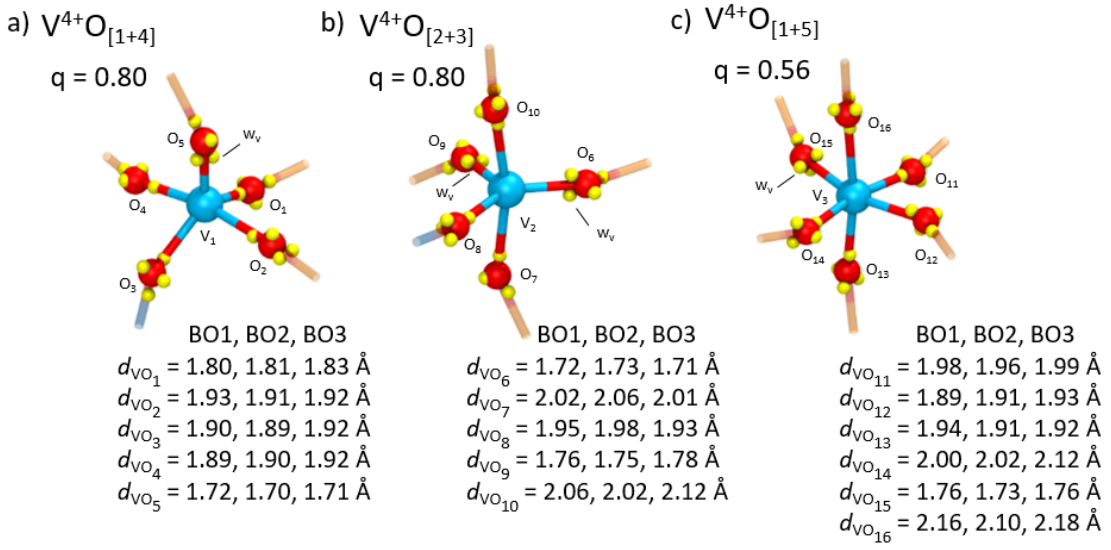

Figure 4.12. Snapshot of $V^{4+}O_n$ polyhedra units within the VP50 glass network. The local atomic environment of V^{4+} sites is described by the V^{4+}-O bond lengths and associated Wannier centers (highlighted in yellow). The polyhedra include: a) a defective square pyramidal unit with the local order parameter q = 0.80, b) a defective trigonal bi-pyramidal unit (q = 0.80), and c) a distorted octahedral unit (q = 0.56).

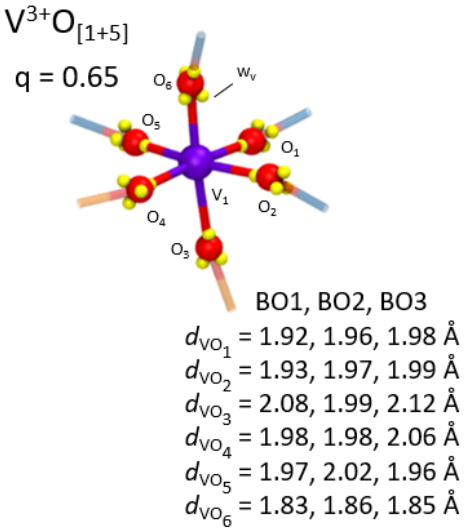

Figure 4.13. $V^{3+}O_n$ polyhedra unit the VP50 glass network. The local atomic environment of V^{3+} sites is described by the V^{3+}-O bond lengths and associated Wannier centers (highlighted in yellow). The polyhedra shows a distorted octahedral unit with local order parameter value of q = 0.65.

4.7 General remark on the atomic structure

Classical molecular dynamics has been increasingly used for modeling VP glasses, by complementing the experimental findings and offering qualitative insights into their structural properties. However, a quantitative assessment of the structural properties as well as a precise understanding of electronic structure and bonding is still missing. In this section, we delineate the limitations of CMD in modeling VP glasses while underscoring the different performance of the three distinct CMD force field schemes tested. Additionally, we emphasize the significance of integrating electronic structure considerations through FPMD, specifically within the BOMD framework, as demonstrated in the present work. One of the most significant advantages of using BOMD is its ability to determine the chemical speciation of V sites in VP50 glass. BOMD allows defining the final composition of V oxidation states, which is found in excellent agreement with experimental data (BOMD: 0.8 % V^{3+}, 35.9 % V^{4+} and 63.3 % V^{5+} *versus* exp.: 35.2 % V^{4+} and 64.8 % V^{5+} [53]) without any a priori information but the total O content. This stands in stark contrast to classical force fields used in CMD, which require the indexing of the number of different V sites with distinct oxidation states and the development of parameters for each pair at the start. The accurate determination of V speciation by BOMD is shown to be critically reliant on the correct description of the electronic properties of the glass, requiring the use of hybrid exchange-correlation functional such as PBE0 to correct energy bandgap underestimation effects. The calculated bandgap (2.4–2.8 eV) allows us to define VP50 glass as a wide-bandgap semiconductor with a small but sizeable magnetic character.

4.7.1 Short-range and intermediate-range order

The short-range order of glassy VP50 was analyzed using X-rays and neutron total structure factors in reciprocal space as well as the total pair correlation functions in real space through the use of CMD and BOMD approaches, which were compared to experimental data. BOMD captured the majority of the structural details observed in experiments, with a notable improvement over the performance of CMD. Notably, contributions from both the local atomic environment of the phosphate and vanadate polyhedra in the pair correlation functions were identified within the 1.5–2.4 Å interval of distances. The improvements observed in the BOMD description stem from the correct description of double bonds P(V)=O and single bonds P(V)–O. CMD fails to describe the short-range order of VP50 glass as shown by the very close values recorded for double P=O and single bond P–O bond distances, leading to over-structuring in the total pair correlation function at short distances. In terms of V–O bond distances, the failure of CMD is more pronounced, the splitting between the vanadyl double and single bonds being absent. Also, two out of the three CMD schemes tested (CMD1 and CMD3) cannot recover the correct single bond distance dependence on the V oxidation state. In this context, the analysis of bonding properties based on the Wannier functions centers has proved to be crucial to assess the variety and diversity of double and single V–O bonds.
As shown by experiments [53, 66–68], V^{5+} features three types of coordination in VP glasses and crystalline phases, including VO_4 (tetrahedral (T_h)), VO_5 (trigonal bi-pyramid (T_b) and square pyramid (S_p)), and VO_6 (distorted octahedra (O_d)). For V^{4+} one has VO_5 (S_p and T_b) and VO_6 (O_d) coordination, while V^{3+} can be found coordinated in regular octahedra (O_h) VO_6. Our BOMD calculations substantiated these experimental findings. For our VP50 system, the following summary of structural units can be compiled:

- V^{5+} is preferentially coordinated as four- and five-folded (∼26–28 % and ∼24–8 %, respectively), as T_h and S_p/T_b (with S_p as mostly present), and with a non-negligible content of six-folded V^{5+} (∼6–12 % as O_d);

- V^{4+} is preferentially coordinated as six- and five-folded (∼17–20 % and ∼14–19 %, respectively), as O_d and S_p/T_b (with S_p as mostly present), and with negligible content of four-folded V^{4+} (≤5 %);

- V^{3+} is preferentially coordinated as six-folded (O_d), although it has been found in negligible amount in VP50 glass (<1 %).

The absence of any peak at wave vectors smaller than the main peak in the structure factors reveal that the intermediate range order (intended as a structural organization manifesting itself via a discernible feature at short wavelength in reciprocal space) is very limited or even absent in VP50 glass. In terms of hypothetical topological features extending on intermediate range distances, we observe that the analysis of the distribution of structural units in the VP50 glass is indicative of minimal segregation of the phosphate (PO_4) units, which are well distributed throughout the glass matrix. This is shown by the very minimal signature indicating connections between the PO_4 units, with a minor percentage of two-fold coordinated O atoms bound to two P atoms (≤7 %). There is also a limited segregation within the vanadate (VO_n) network, with approximately ∼14–19 % of two-fold coordinated O atoms bound to two V atoms.

4.7.2 Performance of CMD force fields versus BOMD

Several summarizing comments can be made regarding the performance of the three CMD force field schemes tested in this work. While all three CMD schemes fall short of providing a quantitative description of the local environment around V sites in VP50 glass, they exhibit varying degrees of agreement with BOMD and experimental findings. CMD1 (PMMCS/BMP-shrm Morse-type two-body potential with P–O–P three-body potential parameters) and CMD3 (Buckingham-type two-body potential) schemes, although displaying a coordination of total V in reasonable agreement with BOMD, struggle to accurately reproduce the individual coordination of V with different oxidation states. Notably, CMD3 exhibits the poorest description, evident in discrepancies in total neutron and X-rays total pair correlation functions, overly structured V-O partial pair correlation functions, and negligible differences between V^{4+}–O and V^{5+}–O bond distances. Both CMD1 and CMD3 schemes fail to capture the local environment of V^{4+} and V^{5+} sites, notably overestimating the content of four-folded V^{4+} (VO_4).
On the other hand, the CMD2 scheme, incorporating a PMMCS/BMP-shrm Morse-type two-body potential with an explicit inclusion of V^{5+}–O–V^{5+} and P–O–V^{5+} three-body potential parameters, significantly enhances agreement with BOMD and experimental data. This improvement is particularly noteworthy in total structure factors (first peak intensity at low k), total pair correlation functions, V coordination environment, and extends to a more precise depiction of V site coordinations concerning V oxidation states. Additionally, it captures the variations in averaged V–O bond distances based on the V oxidation state with greater accuracy. Nevertheless, the shortcomings of all three CMD schemes become evident in their inability to sufficiently capture the local bonding characteristics of both single and double/vanadyl bonds between V atoms and O atoms. It is evident that an accurate description of these bonding features necessitates consideration of electronic structure and the localization of electronic charge and spin. This limitation is inherently linked to the relatively simplicity of the two-body potential form used in these force fields. In this context, the application of reactive force fields (i.e. ReaxFF [288]) and machine learning interatomic potentials [289, 290] for CMD simulations could provide an alternative way to address these limitations, although currently unavailable for systems like VP50 glass.

4.8 Conclusive remarks

This chapter underscores the limited ability of the empirical FF schemes tested in this work in precisely delineating the distinct oxidation states of vanadium in VP50 glass. Instead, it showcases the superior accuracy of BOMD in providing a quantitative depiction of the chemical speciation, bonding and structure of this system. It is noteworthy, however, that the agreement between CMD and BOMD significantly improves upon the incorporation of appropriate V–O–V and V–O–P three-body potential parameters.

By performing a detailed comparison with experimental data, we found that BOMD accurately determines the final composition of V oxidation states without relying on any a priori information, except for the total O content. BOMD also provides an accurate description of the local electronic and bonding environment around both P and V sites, allowing for a clearer signature of single V–O and double V=O bonds, and an overall improved description of the distribution of VO_n coordinating polyhedra. Furthermore, our investigation includes a thorough analysis of bond angle distributions, order and connectivity parameters, and local bonding features based on Wannier functions formalism.

Overall, our findings provide a deeper understanding of VP50 glass paving the way to the development of future (reactive or machine learning) interatomic potentials stemming from first-principles data and expect to bring quantitative comprehension and design of VP-based amorphous materials.

Chapter 5

Structure, bonding and electronic properties of ternary Na_2O-V_xO_y-P_2O_5 (NVP) glasses

Summary

This chapter focuses on ternary NVP systems. We briefly present the motivation for the chosen compositions, detail the experimental and computational methodologies, and describe the properties of the resulting glasses. In the first part, we present two NVP systems where the thermal cycle is driven by a classical force field, followed by a short VP50-type dynamics using BOMD on the glass produced by CMD. In the second part, we produce two other NVP glass compositions using a complete thermal cycle with BOMD. Structural and electronic results are presented and discussed, with comparisons to experimental measurements of the total X-ray structure factor S(k) and pair distribution function G(r). Some of the results presented in this chapter have been summarized and published in ref. [291].

5.1 Motivations behind the study of NVP glasses

Vanadium phosphate glasses (VP, also referred as vanadophosphate in literature and hereafter), as explored in the previous chapter, have been study in the past as promising materials for solid-state batteries and electrochemical storage devices. Their appeal stems from a unique combination of physical and chemical properties, including high glass-forming ability, wide vitrification range, low glass transition and melting temperatures, and high thermal expansion coefficients [275, 292]. These glasses have also demonstrated enhanced energy density performance due to their capacity to promote multi-electron reactions [50, 275, 292].

The incorporation of alkali ions into the matrix of vanadium phosphate (VP) glasses significantly enhances their functional properties, broadening their potential applications across various fields. Sodium ions introduce mobile charge carriers within the glass matrix, boosting ionic conductivity, a critical feature for efficient energy storage in solid-state batteries. The initial focus on lithium oxide addition in VP glasses was driven by the rapid development and widespread adoption of lithium-ion batteries (LIB). However, the research interest has gradually partially shifted also towards sodium-based systems (SIB), including sodium vanadium phosphate (NVP) glasses, for several compelling reasons as detailed in Chapter 1, these include:

i. **Abundance and cost**: Sodium is far more abundant in the Earth's crust than lithium, making it a better cost-effective choice for certain large-scale energy storage applications.

ii. **Sustainability**: The increasing demand for lithium has raised concerns about its long-term availability and the environmental impact of its extraction with respect to sodium-based systems.

iii. **Similar chemical properties**: Sharing, in part, similar chemical properties, allows to apply much of the knowledge gained from lithium-based systems to sodium-based ones.

iv. **Larger ion size**: While the larger size of sodium ions initially posed challenges for intercalation materials, it has proven advantageous in some glass systems. The larger ion size can lead to more open structures in glasses [293, 294].

v. **Unique redox behavior**: In NVP glasses, the interaction between sodium ions and vanadium's variable oxidation states can lead to interesting and potentially beneficial redox behaviors that differ from those observed in lithium-based systems.

vi. **Complementary technology**: Rather than fully replacing lithium-based systems, sodium-based materials like NVP glasses are seen as complementary technologies. They may be particularly suited for stationary energy storage applications where the higher energy density of lithium-based systems is less critical [295].

Overall, the partial shift in focus reflects the scientific community's ongoing efforts to develop more sustainable, cost-effective, and diverse energy storage solutions. The research on NVP glasses contributes to this broader goal while also expanding our fundamental understanding of glass structure and ion dynamics in these complex systems.
As presented in Chapter 1, over the past 15 years, various atomistic studies have been dedicated to the investigation of NVP glasses. Most of these studies have employed CMD simulations driven by empirical potentials. Building upon the methodology established and the findings presented in the previous chapter, this chapter focus into the investigation

of NVP glasses, employing a procedure analogous to that employed for VP50. Additionally, this investigation will be furthered through a purely ab-initio approach.
In the first part, we compare the performance of the most effective empirical force field identified earlier with a final BOMD equilibration at 300 K. This BOMD equilibration is performed using both PBE and PBE0 functionals, as done previously for VP50 glass.
The second part extends this approach by employing full BOMD to conduct a complete thermal cycle for a third NVP glass composition. This comprehensive study aims to evaluate the improvements offered by the BOMD approach compared to classical potentials. Additionally, it assesses the benefits of conducting a full BOMD thermal cycle versus merely performing a final equilibration at the BOMD level.

Throughout this two-part study, all computational results will be thoroughly compared with available experimental data provided by collaborating experimental groups at the IRCER Lab within the framework of this project and the ANR project AMSES [296]. This rigorous comparison between computational predictions and experimental measurements will validate our modeling approaches and provide deeper insights into the structure-property relationships of NVP glasses.
By combining advanced computational methods and experimental validation, this comprehensive approach seeks to enhance our understanding of modeling techniques for NVP glasses and their impact on predicting glass structure and properties.

5.2 X-ray diffraction experiments

For completeness, we have summarized the main details of NVP glasses sample synthesis (conducted by R. Piotrowski and G. Dealizir at IRCER) and X-ray scattering characterization (conducted by O. Masson at IRCER). For more detailed information, please refer to R. Piotrowski's Ph.D. project [297]. The experimental total X-ray structure factor S(k) and total pair distribution functions G(r) of our NVPs systems were determined through X-ray total scattering (XRD) by our collaborators at the European Ceramics Centre (IRCER) in Limoges, following procedures similar to those employed in [298]. X-ray scattering measurements were conducted at room temperature using a specialized laboratory setup based on a Bruker D8 Advance diffractometer. This instrument was equipped with a silver sealed tube ($\lambda = 0.559422$ Å) and a rapid LynxEye XE-T detector. Modifications were made to this setup to maximize the collected intensities, minimize spurious signals from the empty environment, and achieve good counting statistics up to a large scattering vector length of 21.8 $Å^{-1}$ Approximately twenty milligrams of each sample's powder were placed in a thin-walled (0.01 mm) borosilicate glass capillary with a diameter of about 0.7 mm to limit absorption effects. The μR values (where R is the capillary radius and μ is the sample's linear attenuation coefficient) were estimated based on precise measurements of the mass and dimensions of the samples, yielding values of 0.17, 0.21, 0.18, and 0.22 for NVP25, NVP33, NVP40, and NVP43 glasses, respectively.

After sealing, the capillary was mounted on a goniometric head and aligned so that its axis coincided with the diffractometer's goniometer axis. Data acquisition involved multiple scans over the 0–152°, 50–152°, and 100–152° 2θ ranges with a step size of 0.01°. These scans were then merged, resulting in a total equivalent acquisition time of approximately 50 hours per sample. The raw data were corrected, normalized, and Fourier transformed using custom software [299] to obtain the reduced atomic pair distribution functions G(r). Corrections accounted for capillary contributions, empty environment, Compton and multiple scatterings, absorption, and polarization effects. The necessary X-ray mass attenuation coefficients, atomic scattering factors, and Compton scattering functions for data

correction and normalization were calculated from tabulated data provided by the DABAX database [300]. Absorption corrections were evaluated using a numerical midpoint integration method, where the sample cross-section was divided into small subdomains, following a method similar to that proposed by A. K. Soper and P. A. Egelstaf [301]. The normalization constant was determined using the high-angle method, ensuring that the coherently scattered intensity oscillated weakly around the sample's average atomic scattering factor at high scattering vector lengths (from $k_{max}/2$ to k_{max}).

5.3 Structure, bonding and electronic properties of NVP25 and NVP43 glasses

The selection of the first two NVP case study glass compositions, referred to as NVP25 and NVP43, indicates their total vanadium oxide content (see Tab. 5.1), was primarily motivated by their promising potential in various applications and their relevance to ongoing research collaborations. The lithium-based equivalent of NVP25 has demonstrated significant value as a starting point for synthesizing lithium oxide-based precursor glasses [50]. This precursor glass has been successfully used to obtain glass-ceramics composed of $Li_3V_2(PO_4)_3$, which have shown interesting electrochemical performance with valuable cathode capacity [51]. Furthermore, our experimental collaborators have proposed NVP25 as a potential glass precursor for obtaining $Na_2VOP_2O_7$ glass-ceramics, which are expected to exhibit high performance in various applications [297].
NVP43, on the other hand, is a glass composition proposed by our experimental collaborators and has been tested as a precursor glass for producing high-performance glass-ceramics composed of other NVP crystalline phases, particularly $Na_2V_3P_2O_{13}$, another promising NVP phase as cathode component for energy storage applications [302, 303].
The two glass compositions, NVP25 and NVP43, provide a valuable opportunity to extend the computational procedures previously validated on VP50 to more complex NVP systems. This extension is particularly significant given the greater potential of these NVP glasses for practical applications.

5.4 Methodology details

5.4.1 Computational details

The computational procedure employed in Chapter 4 was adopted, consisting of a full CMD thermal cycle followed by a final equilibration by means of BOMD at 300 K for 5 ps [251]. We employed BMP-shrm (denoted CMD2) introduce in the previous chapter and developed by Bertani *et al.* [108] as it was found to be the best force field among the three tested previously. Three replicas of NVP25 and NVP43 were generated randomly and placed in a cubic cell with dimensions adjusted to match the reference densities values (see Tab. 5.1). The nominal composition and details of each model are summarised in Tab. 5.1 and Tab. 5.2 respectively. In our CMD simulations, the short-range interactions

Table 5.1. Nominal composition and experimental densities of the two NVP systems simulated using CMD and BOMD.

Systems	Na_2O(%)	V_xO_y [V_2O_4 + V_2O_5] (%)	P_2O_5(%)	density (g/cm^3)
NVP25	37.50	25.00 [2.75 + 22.25]	37.50	2.8074
NVP43	28.50	43.00 [6.45 + 36.55]	28.50	2.9390

were truncated at a distance of 7.00 Å and the long-range interactions were calculated

Table 5.2. Details of the two NVP systems simulated by by full CMD and short BOMD equilibration with the nominal V^{4+} ratio of each composition.

Systems	V^{4+} ratio (%)	number of atoms	box size (Å)
NVP25	11.0	394 [54Na + 36V + 54P + 250O]	17.2960898
NVP43	15.0	405 [40Na + 60V + 40P + 265O]	17.4811087

using the Ewald summation method with a precision of 10^{-5} eV, up to a cutoff distance of 8.50 Å. The DL-POLY code version 4.10.0 [260] was employed. The Velocity Verlet algorithm was employed with a time step of 1 fs to integrate the equation of motion. The NVP glasses models were obtained by the same melt-quenching thermal cycles as the VP50 glass. The Nosé-Hoover thermostat was used to control the temperature. First, the initial structures were relaxed at 300 K in the NVT ensemble. Each system was heated to 4000 K and kept for 150 ps at this temperature followed by the cooling from 4000 K to 300 K with a constant rate of 2.5 K/ps. The relevant properties are averaged over the structures obtained from the final 150 ps of a 300 ps trajectory at 300 K across different replicas. FPMD calculations for these two glasses were performed at 300 K after the CMD dynamics. Using the CMD-derived structures as a starting point, we performed a BOMD simulation at 300 K for approximately 5 ps using PBE functional followed by a final optimization of the electronic structure with PBE0 hybrid functional (similar to the BOMD procedure performed in Chapter 4 for VP50 system). The BOMD simulations were conducted using the CP2K package, as with VP50 system. For the BOMD analysis, the last 3 ps of the trajectories were used and the results averaged over the three replicas.

5.4.2 Structural properties

This section presents and discusses the structural analysis of the NVP25 and NVP43 models obtained at 300 K from equilibrated trajectories averaged over three replicas for both CMD and CMD+BOMD simulations in both reciprocal and real space properties (following the same Faber-Ziman strategy/equations presented in Sec. 3.3, Chapter 3). In subsequent discussions, the CMD+BOMD results will be referred to as BOMD for simplification as for the Chapter 4.

5.4.2.1 Reciprocal space properties

Fig. 5.1 presents an analysis of the reciprocal space X-ray and neutron structure factors for NVP25 and NVP43 glasses. For X-ray structure factors, calculated data (CMD and BOMD) are compared with experimental measurements. Neutron structure factors, on the other hand, are derived solely from simulations. The discrepancies observed between the CMD and BOMD results show significant limitations inherent in the CMD methodology. These findings underscore the critical importance of incorporating electronic structure considerations to achieve a more accurate description of these complex glass systems, consistent with $R_{\chi}^{S(k)}$ parameter (as defined in Eq. (3.11)) presented in Tab. 5.3 first row. $R_{\chi}^{S(k)}$ quantifies the level of agreement with the experimental data, reminding that a lower $R_{\chi}^{S(k)}$ values indicate better agreement between the model and experimental data. For the X-ray structure factors, the most notable difference is observed in the first peak, centered around 2 $Å^{-1}$. In both NVP25 and NVP43, CMD overestimates the intensity of this peak compared to BOMD and experiment. In both systems, the BOMD results demonstrate good agreement with experimental data in terms of peak position and intensities. This is reflected in the $R_{\chi}^{S(k)}$ values of (10.1±0.9)% and (9.8±1.2)% for the NVP25 and NVP43 systems, respectively, compared to the significantly higher values of (14.4±0.2)%

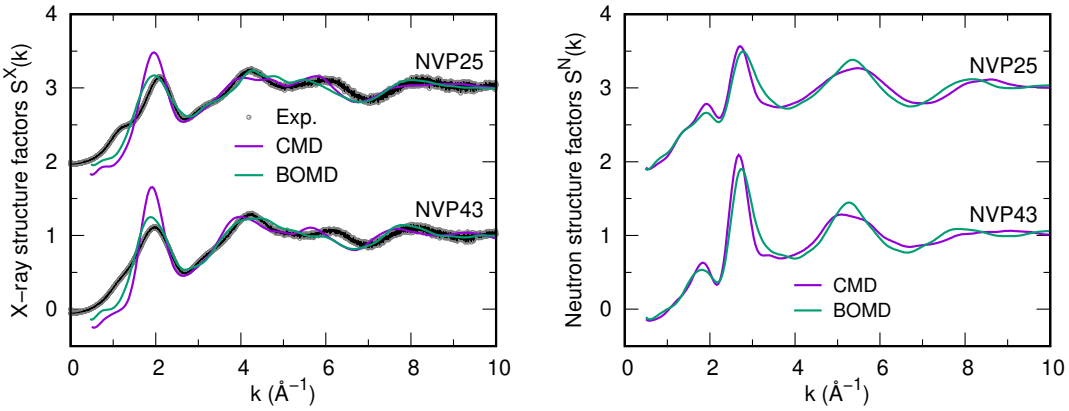

Figure 5.1. X-ray (left) and neutron (right) total structure factors for NVP25 and NVP43 glasses, comparing CMD and BOMD data.

and (17.1±1.0)% obtained using the CMD method.

These differences in the first peak of the X-ray structure factors are particularly significant because they reflect discrepancies mainly around the short-range order (e.g. corresponding to the environment spanning over the first- and second-coordination shells) and the important role of accounting of the electronic structure. The neutron structure factors show better agreement between CMD and BOMD for both glass compositions, with differences in peak intensities generally less than 5%. However, minor discrepancies remain evident, especially in the precise peak positions and shapes. For instance, in NVP25, the first peak in the neutron structure factor (around 1.9 Å^{-1}) shows a slight shift to lower k values in the BOMD results compared to CMD, indicating small but non-negligible differences in the average interatomic distances predicted by the two methods.

The more pronounced differences observed in the X-ray structure factors, compared to the neutron structure factors, provide crucial insight into the limitations of CMD in modeling NVP glasses. X-ray scattering is particularly sensitive to the local environment of V sites due to its relatively low neutron scattering length. The inability of CMD to accurately capture the local V environments underscores the necessity of more accurate modeling approaches that explicitly account for electronic structure effects. In contrast, the higher agreement in neutron structure factors between CMD and BOMD results suggests that both methods describe the P and O local environments more consistently, yet still showing minor discrepancies. This differential performance of CMD more accurate for P and O but less so for V - emphasizes the complexity of modeling these multi-component systems and reinforces the value of computational scheme grounded on an electronic structure description. These insights highlight the importance of employing BOMD simulations in accurately capturing the local structure around V sites, which is particularly relevant for predicting and understanding the functional properties of NVP glasses that are heavily influenced by the V environment.

The substantial improvement in structure factors with respect to experiment, particularly for X-ray scattering, achieved through even a brief final BOMD equilibration aligns with previous findings for the VP50 glass. This consistency across diverse compositions (VP50, NVP25, and NVP43) underscores the critical importance of incorporating electronic structure effects in the modeling of complex oxide glasses. The differences between CMD and BOMD results become less pronounced at higher k values (beyond about 4 Å^{-1}) for both X-ray and neutron structure factors. Moving forward, this comparison suggests

that while CMD remains a valuable tool for initial structural modeling and long timescale simulations, integrating BOMD approaches is crucial for obtaining more accurate and reliable structural descriptions of complex oxide glasses like NVP25 and NVP43.

5.4.2.2 Real space properties

Total pair distribution function

Fig. 5.2 presents a comparative analysis of reduced total X-ray pair distribution function G(r) for NVP25 and NVP43 glasses, comparing experimental data with CMD and BOMD simulation results. The experimental G(r) obtained via Fourier transform of the total structure factors is linked to the total pair correlation function through Eq. (5.1). This data allows for direct comparison with our calculated results for the NVP25 and NVP43 glasses.

$$G(r) = 4\pi r\rho\left[g_{\mathrm{tot}}(r) - 1\right], \tag{5.1}$$

where ρ is the number density and $g_{\mathrm{tot}}(r)$ the X-ray total pair correlation function.
The analysis reveals significant discrepancies between CMD predictions and experimental measurements, while BOMD results demonstrate markedly improved agreement across the examined r range. In the short-range order region (1–3 Å), BOMD simulations capture the experimental features with notable accuracy for both glass compositions. The first peak, centered at approximately 1.5-1.6 Å and primarily attributed to P–O and V=O bonds, is well-reproduced by BOMD in terms of position, intensity, and shape. In contrast, CMD simulations consistently overestimate the intensity of this peak by about 20-30%, indicating an overstructuring degree of short-range correlations. This overestimation is more pronounced for NVP43, suggesting that CMD's limitations become more severe with increasing V content. The peak found experimentally at about 1.96 Å is shifted at lower value for both CMD and BOMD (at about 1.8 Å). The intermediate-range order (3–5 Å)

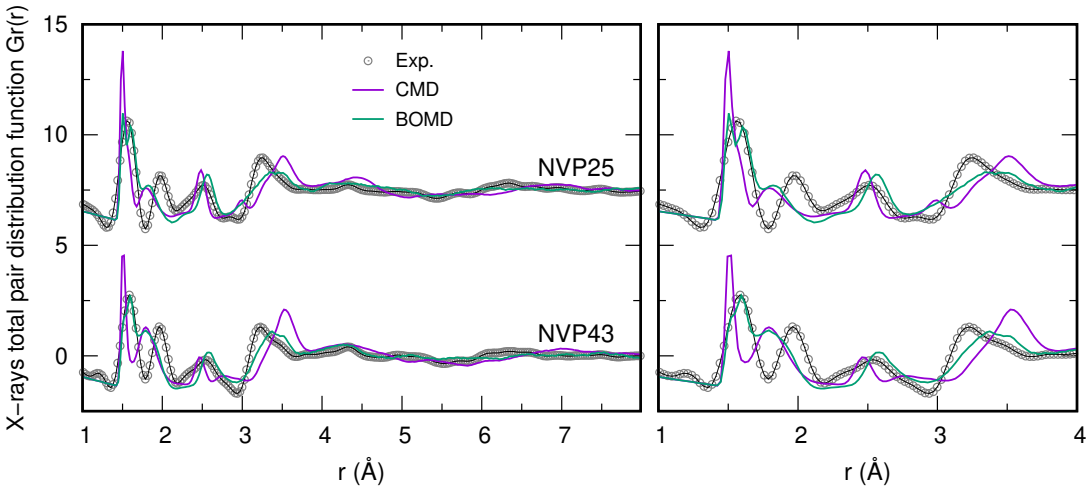

Figure 5.2. (Left) total pair distribution function for NVP25 and NVP43 glasses, illustrating the comparison between the calculated data (CMD and BOMD) and the experimental data obtained by our collaborators in Limoges. (Right) zoom in on the 1–4 Årange.

reveals further limitations of the CMD approach. A consistent shift of approximately 0.5 Å towards larger r values is observed in CMD results compared to experimental data for both NVP25 and NVP43. This shift indicates systematic errors in predicting second-neighbor distances and overall network connectivity. BOMD results, however, align closely with experimental peak positions in this range, with deviations typically less than 0.1 Å. Peak shapes and relative intensities in the 2–4 Å range are more accurately reproduced by BOMD. CMD tends to predict sharper, more intense peaks, while BOMD captures the

Table 5.3. Comparison of the agreement between CMD, and BOMD simulations and experimental data using goodness-of-fit R_χ parameters for X-ray total structure factor S(k) and pair distribution function G(r) of NVP25 and NVP43 glasses at 300 K.

	NVP25		NVP43	
X-rays	CMD	BOMD	CMD	BOMD
$R_\chi^{S(k)}$	14.4 ± 0.2	10.1 ± 0.9	17.1 ± 1.0	9.8 ± 1.2
$R_\chi^{G(r)}$	87.3 ± 2.3	62.9 ± 2.0	96.2 ± 3.1	65.0 ± 4.8

broader, more realistic features observed experimentally. This difference is particularly evident in the region around 2.25–3.50 Å, where CMD overestimates the intensity of secondary peaks by up to 30% for NVP43. Beyond r values of 4 Å, the limitations of CMD potentials in describing these complex glass structures extend to medium and possibly long-range order.

The superior performance of BOMD in reproducing the experimental G(r) underscores the critical role of explicitly accounting for electronic structure effects in modeling sodium vanadium phosphate glasses. The significant improvements offered by BOMD, particularly in capturing the subtleties of short and medium-range order, highlight the limitations of the CMD2 potential for accurate structural predictions in these multicomponent oxide glass systems. The positions of the peak maxima in the 1–4 Å interval are summarized in Tab. 5.4, where the values obtained from CMD and BOMD simulations are compared with experimental data. The inadequacy of the CMD method in describing these complex systems is further highlighted by the Goodness of Fit ($R_\chi^{G(r)}$) parameter values calculated within the 1–4 Å range (Tab. 5.3, second row). The CMD consistently yields substantially higher $R_\chi^{G(r)}$ values compared to the BOMD method, indicating poorer agreement with experimental data. For instance, the NVP43 system exhibits a $R_\chi^{G(r)}$ of (96.2±3.1)% for CMD versus (65±4.8)% for BOMD. This discrepancy is partially attributed to the observed shift between experimental and calculated second and fourth peaks' positions. This comparative analysis demonstrates that BOMD simulations provide a substantially more accurate structural description of NVP25 and NVP43 glasses compared to CMD, especially in the critical short and medium-range order regions that significantly influence the glasses' physical and chemical properties. Once again, these results underline the need to use advanced computational methods that incorporate the effects of electronic structure to achieve reliable modeling of the complex atomic arrangements in sodium vanadium phosphate glasses.

Table 5.4. Positions of the first four peaks of the total pair distribution function: A comparison of the calculated values (CMD and BOMD) with experimental measurements for NVP25 and NVP43 systems.

	NVP25			NVP43		
Peak positions	Exp.	CMD	BO	Exp.	CMD	BO
1^{st} peak	1.56	1.50	1.50	1.59	1.51	1.59
2^{nd} peak	1.96	1.80	1.84	1.96	1.79	1.78
3^{rd} peak	2.51	2.48	2.56	2.57	2.46	2.58
4^{th} peak	3.26	3.52	3.39	3.23	3.53	3.37

Partial pair correlation function

The $g_{\mathrm{VO}}(r)$ partial pair correlation functions (see Fig. 5.3) for NVP25 and NVP43 glasses reveal significant discrepancies between CMD and BOMD predictions, particularly in the short-range order region. For both compositions, as seen in the previous chapter for the case of VP50, BOMD shows a splitting of the first peak of the $g_{\mathrm{VO}}(r)$ in two peaks with well-defined maxima at about 1.6 Å and 1.8–1.9 Å, respectively, while CMD shows an averaged peak at about 1.7–1.8 Å with only showing a small shoulder at 1.6 Å for NVP25. BOMD's sharper, more well-defined peaks indicate a better description of V–O chemical

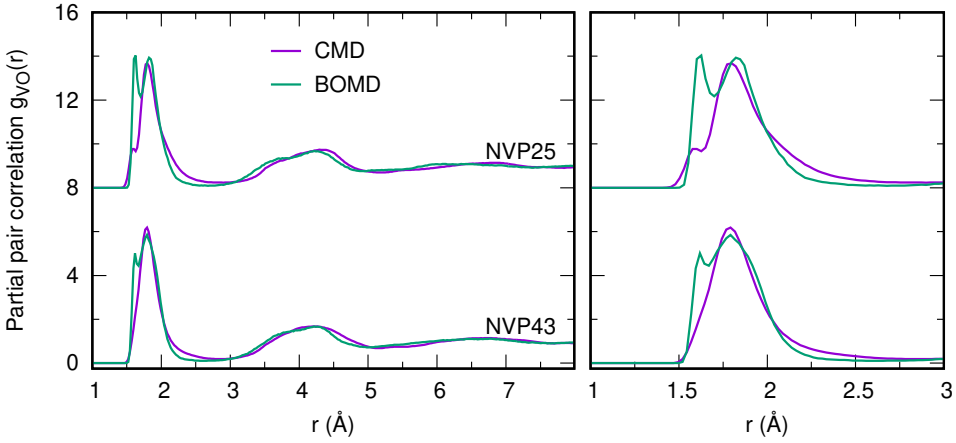

Figure 5.3. (Left) Partial pair correlation function $g_{\mathrm{VO}}(r)$ showing results from CMD and BOMD. (Right) Zoom in on the first peak between 1 and 3 Å.

interactions, due to more accurate representation of single V–O and double V=O bonding and electronic valence charge localization around V sites. Beyond 3 Å, both methods show similar trends, but CMD consistently predicts features at slightly larger r values. The more pronounced differences in NVP43 suggest that CMD's accuracy diminish with increasing vanadium content, likely due to challenges in modeling complex Na-V-P-O interactions using the empirical potential (CMD2). These results highlight the crucial role of electronic structure effects in determining vanadium's local environment in NVP glasses. Overall, these results further support the limitations of classical force fields in capturing V's coordination chemistry in these complex oxide glasses.

Fig. 5.4 presents a comparison of the partial pair correlation functions $g_{\mathrm{OO}}(r)$, $g_{\mathrm{NaO}}(r)$, and $g_{\mathrm{PO}}(r)$ for NVP25 and NVP43 glasses, as predicted by CMD and BOMD simulations. While Na–O and P–O pairs' correlations show broadly similar behavior between

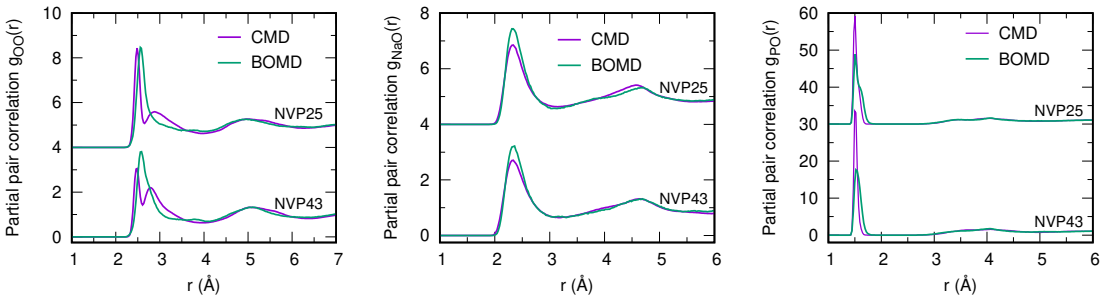

Figure 5.4. Partial pair correlation functions for NVP25 and NVP43 glasses, displaying CMD and BOMD results for $g_{\mathrm{OO}}(r)$, $g_{\mathrm{NaO}}(r)$, and $g_{\mathrm{PO}}(r)$, respectively, from left to right.

the two methods, with CMD exhibiting slightly less intense peaks for O–O and overstruc-

turing for P–O, the O–O correlations reveal more significant discrepancies. For the O–O pair, BOMD demonstrates a marked improvement in structural description, consistent with findings for the VP50 glass. BOMD predicts a single, broad peak centered at approximately 2.56–2.58 Å for both NVP25 and NVP43. In contrast, CMD produces an overly structured profile characterized by a main peak at 2.48–2.49 Å, followed by a less intense secondary peak at 2.78–2.88 Å. This split-peak feature in CMD results suggests an artificial bimodal distribution of O–O distances, which is not supported by the BOMD calculations.

Coordination number and structural units

Tab. 5.5 presents the average coordination for species Na, V, P, and O, as well as the chemical bond lengths calculated obtained as the position of the maximum of the first peak of the partial pair correlation function $g_{\alpha\beta}(r)$, in comparison with experimental values. Overall, phosphorus is well defined with an average coordination of 4.00 for both systems, both with CMD and BOMD, in full agreement with the experiment. For vanadium, the coordination predicted by CMD (4.37 and 4.44 Å respectively) is slightly lower than the BOMD values (4.76 and 4.75 Å), but these CMD and BOMD values remain consistent with the experimental range of 4.20–5.40 Å. The calculated average coordination of Na is slightly higher than the experimental reference for the two systems.

Next, we analyzed the average distribution of VO_n and Na^+O_n structural units, with

Table 5.5. Average coordination numbers n_i bond lengths r_{ij} (in Å) (taken as the position of the first maximum of the pair correlation functions $g_{\alpha\beta}(r)$), computed for the NVP25 and NVP43 models and averaged over the three replicas. For BOMD data, we report the distances obtained from the first maximum of $g_{\alpha\beta}(r)$. The average statistical error, computed across the replicas is 0.02 Å.

		NVP25		NVP43	
	Exp.[a]	CMD	BOMD	CMD	BOMD
n_{Na}	5.90	6.15	6.58	6.41	6.81
n_P	4.00	4.00	4.00	4.00	4.00
n_V	4.20-5.40	4.37	4.76	4.44	4.75
n_O	2.00-4.00	1.66	1.71	1.73	1.79
r_{NaO}	2.3-2.6	2.33	2.33	2.33	2.34
r_{PO}	1.52-1.60	1.50	1.50	1.50	1.53
r_{VO}	1.58	1.59	1.62	-	1.62
	1.90	1.80	1.84	1.79	1.78
r_{OO}	2.52-2.79	2.48/2.88	2.56/2.78	2.49	2.58
r_{VV}	3.50	3.53	3.50	3.53	3.47
r_{PV}	3.24	3.32	3.20	3.33	3.29

[a]Estimated from X-ray and neutron diffraction measurements on V_xO-P_2O_5[39] and Na_2O-V_xO_y[55] glasses

sodium in the latter case having an ionic interaction with neighboring non-bridging oxygen. Tab. 5.6 presents the values obtained at the CMD and BOMD levels for both systems. As previously noted with the average coordination, it is observed that vanadium in the glasses produced by CMD prefers low coordination with a dominance of VO_4 units (60.7 and 56.4% respectively for the NVP25 and 43 systems) followed by VO_5 units (25.2 and 31.0%) and a small proportion of VO_3 and VO_6 polyhedra. In contrast, BOMD in both systems shows an opposite evolution. The VO_n units are mainly VO_5, about 50%, followed by VO_4 units (around 35% for both systems), then a non-negligible proportion (12.9 and 10.6% respectively) of VO_6 units. Unlike the CMD result, BOMD does not present VO_3 units. These results are consistent with those obtained for the VP50 system

in the previous chapter. This analysis reveals a less ordered CMD structure (presence of VO_3 polyhedra) compared to the BOMD structure, thus reinforcing the importance of electronic contribution in the description of these complex systems. Regarding Na^+O_n polyhedra, coordination numbers for Na fluctuate between 4 and 9 for both systems, with a predominance of Na^+O_6 for CMD and Na^+O_7 for BOMD.

Table 5.6. Distribution of the individual $n_\alpha(l)$ structural units where an atom α (V or Na) is l-fold coordinated to oxygen atom, computed for the both NVP25 and NVP43 using CMD and BOMD. These values have been calculated including neighbours separated by a cutoff corresponding to the first minimum in the $g_{\alpha\beta}(r)$ and average over the three replicas with standard error indicated. The cutoffs of 2.4 and 3.2 Å were used for the Na–O and V–O bonds respectively. Only fraction greater than 0.1 % are reported.

		NVP25		NVP43	
		CMD	BOMD	CMD	BOMD
V					
$l=3$	O_3	5.5 ± 0.4	-	4.22 ± 0.45	-
$l=4$	O_4	60.7 ± 3.4	36.5 ± 7.5	56.4 ± 0.3	35.3 ± 1.9
$l=5$	O_5	25.2 ± 3.9	50.6 ± 8.4	31.0 ± 1.5	54.1 ± 5.6
$l=6$	O_6	8.7± 0.9	12.9 ± 0.9	8.4 ± 0.92	10.6 ± 3.7
Na^+					
$l=4$	O_4	3.2 ± 0.4	0.8 ± 0.5	2.2 ± 1.0	0.7 ± 0.4
$l=5$	O_5	21.7 ± 3.0	12.7 ± 3.7	18.7 ± 5.6	8.5 ± 0.2
$l=6$	O_6	40.1 ± 2.2	33.2 ± 1.9	32.5 ± 3.7	31.7 ± 2.7
$l=7$	O_7	27.0 ± 2.5	36.6 ± 5.3	30.6 ± 2.5	34.8 ± 2.2
$l=8$	O_8	7.1 ± 1.7	14.7 ± 0.1	13.7 ± 5.1	17.2 ± 4.8
$l=9$	O_9	0.7 ± 0.3	1.9 ± 0.2	1.8 ± 0.3	5.6 ± 1.7

5.4.3 Electronic and bonding properties

The comparative analysis of PBE and PBE0 results for NVP25 and NVP43 glass models reveals significant differences in their predictions of electronic and magnetic properties, as shown in Fig. 5.5. While the PBE functional severely underestimates the bandgap, yielding an averaged (0.02±0.02) eV for both models, the PBE0 hybrid functional provides more accurate values ranging from (1.53±0.39) to (1.94±0.33) eV. This substantial improvement in bandgap prediction by PBE0 is inline with what found previously for VP50, albeit with slightly smaller gaps compared to VP50 glass (2.4–2.8 eV). Both functionals predict a discernible magnetic character in the glasses, evidenced by small but finite differences between spin-up and spin-down state bandgaps. However, PBE0 results demonstrate more pronounced spin polarization, suggesting a superior capture of magnetic effects compared to PBE.

The analysis of V speciation, based on V sites' local spin, further highlights the disparities between the two functionals. PBE results show a varied distribution of local spin on V sites, with a majority having spins σ_{spin} close to zero (associated with non-magnetic V^{5+}), but also a significant number of sites with ill-defined spins between 0.2 and 1.2. In contrast, PBE0 provides a much more defined spin distribution, offering a more distinct separation between V^{5+} (σ_{spin} ∼0) and V^{4+} (σ_{spin} ∼1) sites as clearly illustrated by the distribution plot in Fig. 5.5, bottom. This clearer delineation allows for a more featured comparison between NVP25 and NVP43, revealing that NVP25 has a slightly higher content of V^{5+} sites, while NVP43 exhibits a marginally higher content of V^{4+} sites. Based

on these σ_{spin} values, our calculations point toward a chemical composition corresponding to 37.5Na_2O-25.0V_xO_y[22.2V_2O_5-2.8V_2O_4]-37.5P_2O_5 and 28.5Na_2O-43.0V_xO_y[35.8V_2O_5-7.2V_2O_4]-28.5P_2O_5 for NVP25 and NVP43, fairly inline with the experimental compositions (Tab. 5.1).

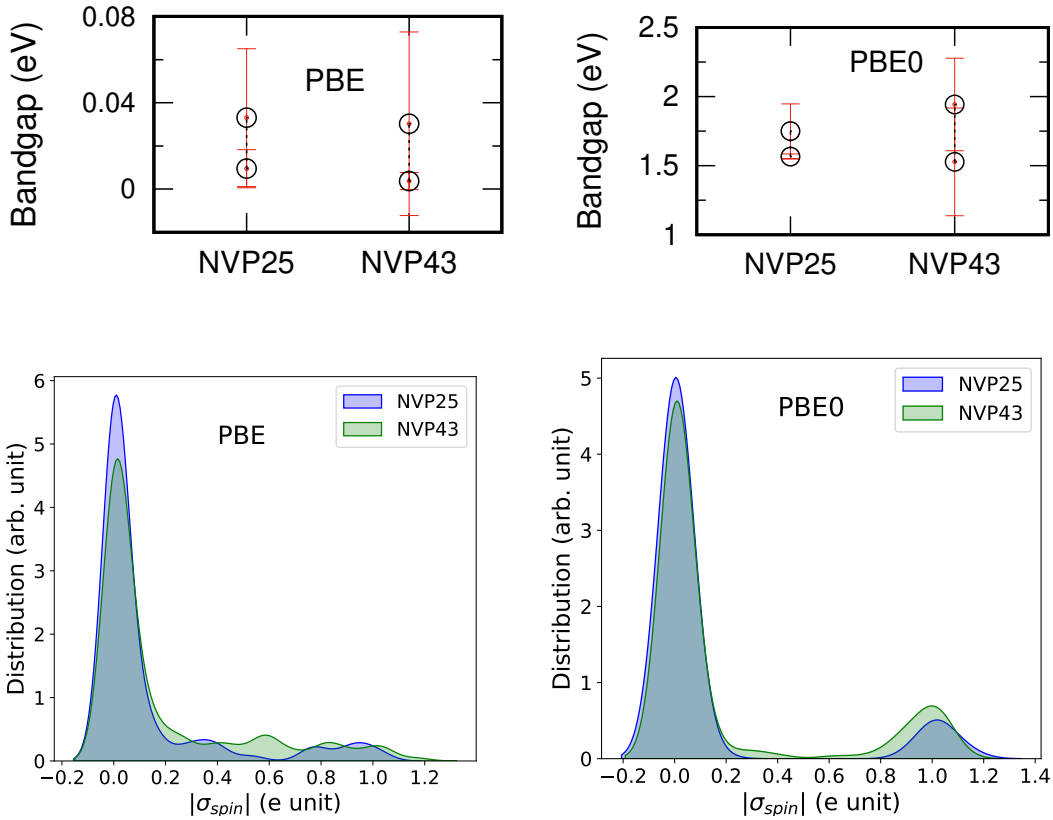

Figure 5.5. Averaged values of the energy bandgap (in eV) are shown at the top, and spin densities (in e units) are shown at the bottom. The results are computed for all Vanadium sites at the PBE (left) and PBE0 (right) levels for both NVP25 and NVP43 glasses using BOMD. Bandgap values for both spin-up and spin-down states are averaged over three configurations simulated for each system. Spin densities display the distribution of individual data points across the three configurations for each glass.

5.5 NVP glasses produced employing a full BOMD thermal cycle

The NVP40 glass model, with its nominal composition of 10Na_2O–40V_xO_y–50P_2O_5, served as a focal point in our study of sodium vanadium phosphate (NVP) glasses. This study aimed to unravel the structural features of these complex materials by employing different computational strategies, each offering unique insights into the glass's properties. Building upon our previous investigations of VP50, NVP25, and NVP43 glasses, we now extend our analysis to NVP40, a composition that promises to bridge the gap between theoretical predictions and experimental observations. Our approach encompasses three distinct computational schemes:

- A full thermal cycle using CMD with an empirical potential (CMD2/FF2 as defined in Sec. 4.2.1 of Chapter 4), tested on VP50, NVP25, and NVP43 glasses. This will be referred to as **CMD** in the following sections.

- A hybrid approach combining CMD with BOMD, tested on VP50, NVP25, and

NVP43 glasses. This will be referred to as **BOMD**, as it has been used in Chapter 4 and in the previous section dedicated to NVP25 and NVP43.

- A full thermal cycle employing BOMD. This will be indicated as *f***BOMD** to avoid confusion with the hybrid approach.

This multi-pronged strategy allows us to consistently evaluate the impact of electronic structure accounting on the accuracy of the NVP40 glass model, offering a detailed understanding of the trade-offs between computational efficiency and precision in modeling complex glass systems. The selection of NVP40 is not merely an academic exercise but is driven by its potential practical applications. Our collaborators at the IRCER laboratory have initially identified this composition, among others, as a promising candidate for glassy cathodes in sodium-ion batteries. By assessing its structural properties, we aimed to pave the way for significant advancements in modeling NVP disordered systems for energy storage technology. Furthermore, NVP40's role as a precursor for glass-ceramics with enhanced electrochemical properties underscores the broader implications of this research for material design and optimization. In the context of the AMSES-ANR project [296], our study of NVP40 will serve as additional significance as with the comparison with a telluride-substituted analog, the $10Na_2O$-$40V_xO_y$-$50TeO_2$ (NVT) system [304]. This parallel investigation seeks as follow-up of this PhD project to show how the substitution of phosphate with telluride influences the structural and electronic properties of these glasses, potentially uncovering materials with superior characteristics for targeted applications [305].
By thoroughly comparing our computational predictions with experimental data, we aim to refine our modeling techniques and contribute valuable insights to the ongoing quest for next-generation energy storage materials. This research not only advances our knowledge of glass structure and properties but also exemplifies the synergy between computational modeling and experimental research in driving materials science forward.

5.5.1 Computational details

The inability of the CPMD scheme to effectively decouple the electronic and ionic subsystems in the preliminary VP50 glass tests (Sec. 4.2.2, Chapter 4) led us to adopt the BOMD approach for our FPMD simulations of the NVP40 glass models. This approach was implemented using the CP2K software package [261]. In CP2K, atom-centered Gaussian-type basis functions are used to describe the orbitals and an auxiliary plane-wave basis set is employed to re-expand the electron density. We employed double-ζ polarized MOLOPT basis sets [262] for Na, V, P, and O, and used a cutoff energy of 500 Ry for the plane waves at the Γ point only. GTH pseudopotentials were used to describe core-valence interactions [263] together with the semilocal PBE XC functional within a spin unrestricted DFT formalism. The ionic temperature was controlled by a Nosé-Hoover thermostat [112–114, 116]. Initially, two NVP40 systems, referred to as NVP40A and NVP40B (see Tab. 5.8 and Tab. 5.7 for details), were prepared and equilibrated using CMD. These systems differ in total oxygen content, with NVP40A corresponding nominally to 100% V^{5+} and NVP40B to a 67.7%/33.3% mixture of V^{5+}/V^{4+}, respectively. These two NVP40 models, differing in oxygen and V^{4+} content, were chosen to evaluate potential structural effects dependent on vanadium speciation. Initially, on the experimental side, both glass density and vanadium speciation were unknown. The initial densities of the NVP40 glasses models to be modelled were estimated using Priven's empirical method [306], as implemented in SciGlass [307] and following the same procedure used in [80]. These estimated densities were then used to equilibrate the systems at zero pressure in the NPT ensemble at 300 K using a classical force field (CMD2/FF2).
Comparing the simulated models in terms of density, NVP40A exhibits a much closer

(∼2% difference) density to the later obtained experimental value (see Tab. 5.7), suggesting it is likely closer to the actual synthesized glass composition, predominantly rich in V^{5+} with minimal V^{4+} content.The BOMD simulation started with annealing at 0.5 K. The systems were then gradually heated in the NVT ensemble from 300 K up to 3500 K. Melting occurred at 3500 K over 7.9 ps to reach the diffusive regime, as indicated by the MSD profile reported in Fig. 5.6. Subsequently, the systems were gradually cooled to

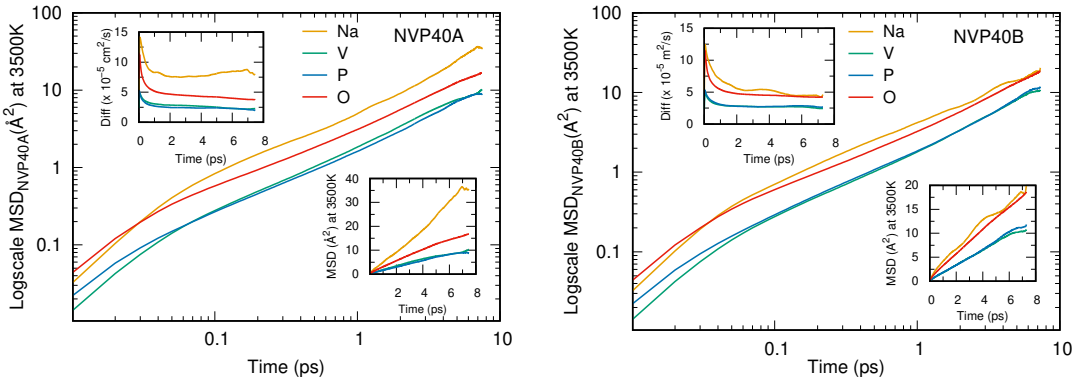

Figure 5.6. MSD in logarithmic scale at 3500 K for the two NVP40 models: Model A (left) and Model B (right). The insets show the diffusion coefficient in cm^2s^{-1} and the MSD in normal scale in Å.

300 K with temperature plateaus at 2000 K for 9.3 ps, 1200 K for 7.3 ps, 900 K for 7.0 ps, 600 K for 6.0 ps, and finally 300 K for 7.1 ps. This corresponds to an exceptionally high cooling rate of 10^{14} K/s.

Table 5.7. Nominal composition and densities of the two NVP40 systems simulated by full BOMD.

Systems	Na_2O(%)	V_2O_4(%)	V_2O_5 (%)	P_2O_5(%)	density (g/cm^3)
NVP40A	10.00	0.00	40.00	50.00	2.7190[a] / 2.7771[b]
NVP40B	10.00	13.20	26.80	50.00	2.5461[a] / –

[a]Estimated value; [b]Experimental measurement

Table 5.8. Details of the two NVP40 systems simulated by full CMD and short BOMD equilibration with the nominal V^{4+} ratio of each composition.

Systems	V^{4+} ratio (%)	number of atoms	box size (Å)
NVP40A	0.0	396 [12Na + 48V + 60P + 276O]	17.6448450
NVP40B	33.3	388 [12Na + 48V + 60P + 268O]	17.9496717

The necessity for such a high cooling rate arises from the substantial computational cost of BOMD for these NVP systems. Specifically, the NVP40A system requires, on average, $(1.31\pm0.88)\times10^4$ CPU hours per ps, while the NVP40B system demands $(1.94\pm1.00)\times10^4$ CPU hours per ps. The relatively higher computational cost for NVP40B is attributed to the increased effort required to converge the electronic structure of this model. Figs. 5.7 and 5.8 illustrate the thermal cycle (left) and the temporal evolution of the total system energy (right) of the NVP40A and NVP40B systems respectively. A slight drift of up to 0.02 % (equivalent to 12.34 meV/ps/atom) at high temperature (3500 K) for the both system is observed, which is attributed to the systematic error inherent in BOMD approach. This occurs because the convergence criterion cannot be set infinitely to perfectly satisfy the condition of the potential energy surface minimum. The last 5 ps of the final equi-

libration at 300 K were used to describe the structural properties of the NVP40 models. The final DFT calculation at the PBE0 level allow the description of the spin localization of V sites as well the electronic density of states.

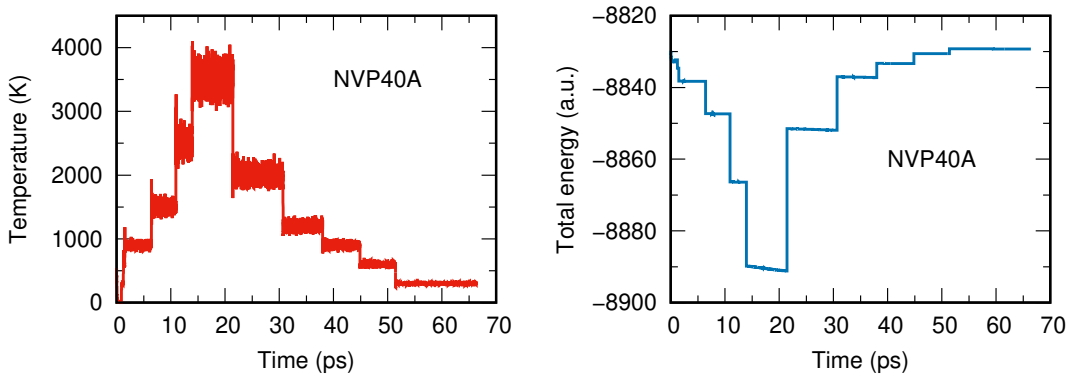

Figure 5.7. Left: Full BOMD thermal cycle performed for the NVP40A glass systems. Right: Time evolution of the total energy (in atomic units) during the simulation showing a slight drift of 0.02 % is observed at high temperature (3500 K), which decreases to nearly 0 % as the temperature decreases.

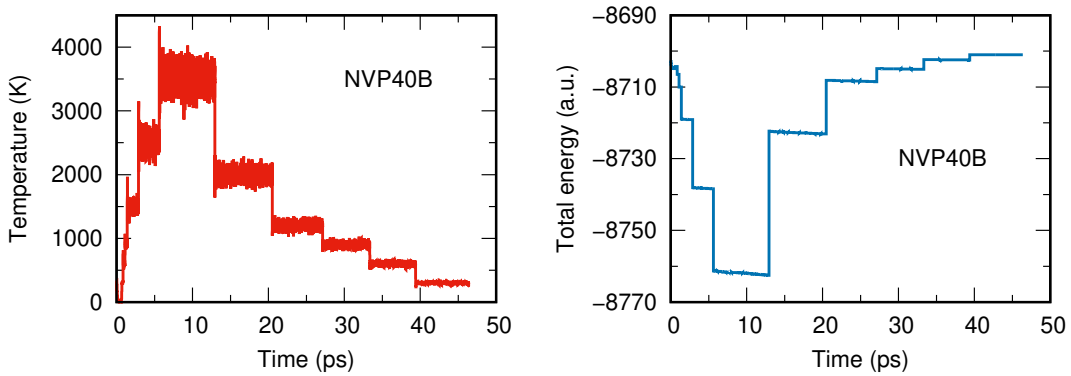

Figure 5.8. Left: Full BOMD thermal cycle performed for the NVP40B glass systems. Right: Time evolution of the total energy (in atomic units) during the simulation showing a slight drift of 0.02 % is observed at high temperature (3500 K), which decreases to nearly 0 % as the temperature decreases.

5.5.2 Structural properties

The structural analysis of the NVP40 glasses obtained through complete CMD and BOMD and thermal cycling is detailed in this section. Unlike the NVP25 and NVP43 glasses, where BOMD studies were conducted only at 300 K, a full BOMD dynamic reveals more pronounced structural differences in both reciprocal and real space.

5.5.2.1 Reciprocal space analysis

The structural factors from X-ray and neutron analysis, shown in Fig. 5.9 (left and right respectively), compare the results of full thermal cycle by CMD, full thermal cycle by CMD and final relatively short equilibration at 300 K by BOMD, and full thermal cycle by BOMD (denoted as **CMD**, **BOMD**, and *f***BOMD** hereafter, respectively), revealing significant structural discrepancies, particularly in the first peaks. Our collaborators successfully conducted X-ray diffraction measurements for the NVP40 system.

For the NVP40A system at low k-values (less than 2.50 Å^{-1}), the *f*BOMD results exhibit two distinct peaks at 1.49 Å^{-1} and 2.00 Å^{-1}, whereas CMD presents a single broader

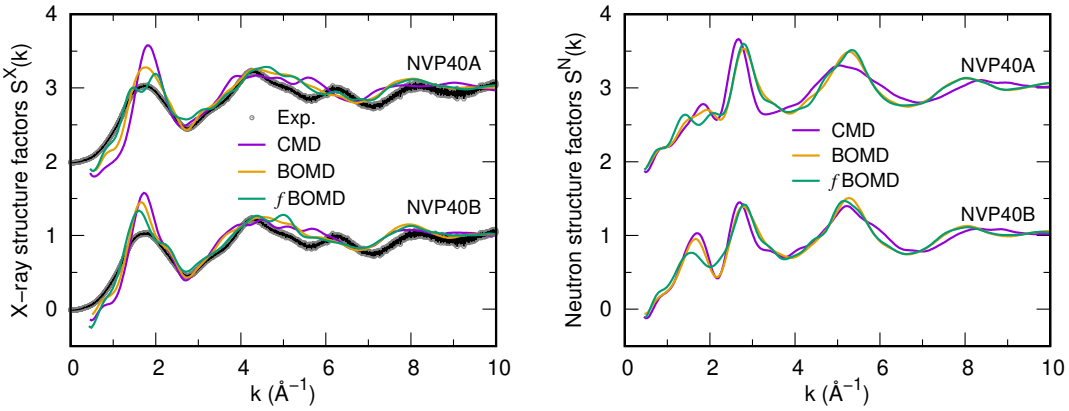

Figure 5.9. X-ray (left) and neutron (right) total structure factors for NVP40A and NVP40B glasses, comparing CMD, BOMD and fBOMD data.

peak centered at 1.82 Å^{-1}. This indicates that fBOMD captures more detailed structural features that CMD tends to average out, highlighting the finer features in the atomic arrangement. In the NVP40B system, the primary peak occurs at 1.61 Å^{-1} for fBOMD and at 1.72 Å^{-1} for CMD, with the latter also displaying a higher intensity. This difference suggests variations in the local structure and density between the two computational schemes, where CMD might predict a more compact structure than fBOMD. The analysis of the BOMD approach provides an intermediate perspective, showing features that are more refined than those in CMD but not as distinct as those in fBOMD as confirmed by the $\$R_chi$ parameter presented in Tab. 5.9, first row. This suggests that even a short BOMD equilibration after CMD can significantly enhance the structural details captured in the model. Additionally, the neutron structure factors reveal slight differences in peak intensity and position for both systems. These variations are crucial as they reflect the sensitivity of neutron scattering to different atomic species and their spatial distribution within the glass network.
Overall, the reciprocal space analysis via X-ray and neutron structure factors underscores the detailed and structural distinctions captured by a full thermal cycle by fBOMD compared to a full thermal cycle by CMD and the intermediate nature of the BOMD approach.

Table 5.9. Assessment of the accuracy of CMD, BOMD, and fBOMD simulations using goodness-of-fit (R_χ) parameters for X-ray total structure factor and pair distribution function G(r) of NVP40 glasses at 300 K. The results for CMD and BOMD are presented as averages over three replicas, with standard error indicated. The fBOMD results are averaged over two separate trajectory segments to assess the standard error.

	NVP40A			NVP40B		
X-rays	CMD	BOMD	fBOMD	CMD	BOMD	fBOMD
$R_\chi^{S(k)}$	20.9 ± 0.3	14.2 ± 0.1	11.4 ± 0.1	17.2 ± 0.1	14.4 ± 1.2	12.8 ± 0.1
$R_\chi^{G(r)}$	90.6 ± 1.5	74.1 ± 0.4	58.9 ± 0.5	86.1 ± 2.0	70.7 ± 2.1	62.0 ± 0.2

5.5.2.2 Real space analysis

Total and partial pair correlation functions

In this section, we present the total pair distribution function for the two NVP40 systems, calculated using three distinct methods: full CMD, CMD completed with BOMD equi-

libration, and full BOMD thermal procedures. The calculated structures are compared with experimental measurements. Furthermore, we present the partial pair correlation functions for V–O, O–O, P–O, and Na–O pairs, derived from each of the aforementioned computational methods and finally the
The total pair distribution functions, shown in Fig. 5.10, reveal distinct differences between the CMD, BOMD, and *f*BOMD results when compared to the experimental data. Tab. 5.10 summarizes the positions of the first four peaks within the 1–4 Å range for both NVP40 systems, comparing calculated and experimental data. For the NVP40A system, *f*BOMD results exhibit a closer alignment with the experimental measurements, particularly in accurately capturing the heights and positions of the peaks. For the NVP40A

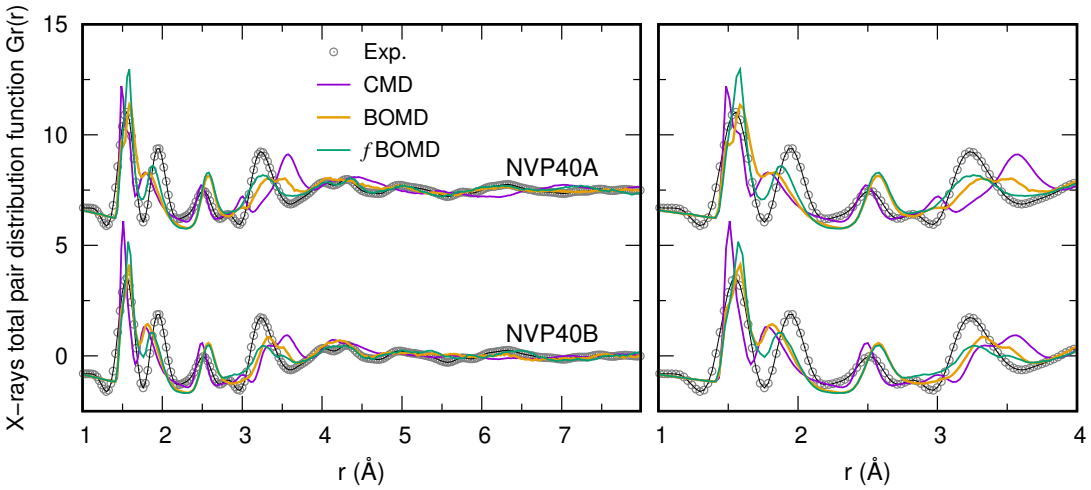

Figure 5.10. (Left) Total pair distribution function for NVP40A (top plot) and NVP40B (bottom plot) glasses, illustrating the comparison between the calculated data (CMD, BOMD and *f*BOMD) and the experimental data (Right).

Table 5.10. Positions of the First Four Peaks of the Total Pair Distribution Function: A Comparison of Calculated Values (CMD, BOMD and *f*BOMD) with Experimental Measurements for NVP40A and NVP40B Systems.

	NVP40A			NVP40B	
Peak positions	Exp.	CMD	*f*BOMD	CMD	*f*BOMD
1^{st} peak	1.56	1.48	1.58	1.51	1.57
2^{nd} peak	1.96	1.77	1.88	1.78	1.86
3^{rd} peak	2.51	2.48	2.58	2.50	2.59
4^{th} peak	3.23	3.57	3.26	3.55	3.25

system, the first peak around 1.6 Å, previously found to be corresponding to both P–O bonding and the short V=O double bonds, is more accurately captured by *f*BOMD, closely matching the experimental data. The CMD method shows a broader and slightly shifted peak, while the BOMD method presents intermediate characteristics. This indicates that *f*BOMD provides a more precise depiction of the atomic arrangement, whereas BOMD improves upon CMD by incorporating elements of *f*BOMD's accuracy. The second peak, around 1.9 Å, which primarily corresponds to single V–O bonds, is particularly better resolved in *f*BOMD compared to CMD and BOMD. This highlights how the full thermal cycle in *f*BOMD allows for the optimal arrangement of V–O interactions, achieving a more accurate representation of the local structure. In contrast, the BOMD approach, while an improvement over CMD alone, does not fully capture the detailed organization of these bonds.

For the NVP40B system, similar trends are observed. fBOMD captures sharper and more accurately positioned peaks compared to CMD, which tends to produce broader features. The BOMD approach shows a balanced representation, demonstrating improvements over CMD but not reaching the full accuracy of fBOMD. This again highlights the superior capability of BOMD in modeling the structural features of these glassy systems.
The improvement in the total pair correlation function predictions from CMD to BOMD and fBOMD is further supported by the goodness-of-fit parameter R_χ, as shown in Tab. 5.9, second row. This parameter assesses the degree of agreement with experimental data, where a lower value indicates better agreement. For both NVP40A and NVP40B systems, fBOMD shows the lowest parameters, underscores the enhanced accuracy of fBOMD over CMD in modeling the NVP40 glass systems. The short BOMD approach is found to be perform as partial improvement, offering improvements over CMD while being less computationally intensive than full fBOMD. This comprehensive comparison helps validate the computational models and provides deeper insight into the atomic arrangements within these materials. This analysis, also further suggest that NVP40A is found matching closer the experimental data, showing the lowest R_χ, indicating that the experimentally obtained NVP40 glass much show a high majority of V^{5+}.

In the following, we analyze the partial pair correlation functions for V–O pairs in the NVP40A and NVP40B systems, calculated using CMD, BOMD, and fBOMD methods. The results are presented in Fig. 5.11, highlighting the performance of each computational scheme. For the NVP40A system, the first peak around 1.6 Å, corresponding to the V=O

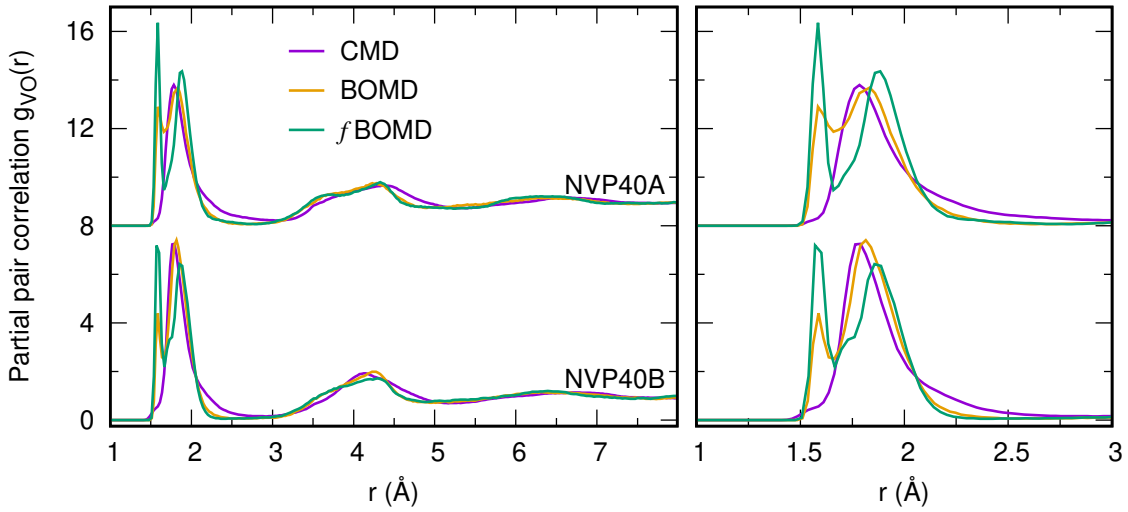

Figure 5.11. (Left) Partial pair correlation function $g_{VO}(r)$ showing results from CMD, BOMD and fBOMD. (Right) Zoom in on the first peak between 1 and 3 Å.

double bond, is more accurately captured by fBOMD, closely matching the expected bond length. The second peak, centered around 1.8–2.0 Å, which corresponds to the V–O single bond, is also better resolved in fBOMD. CMD, however, shows a single broader peak that averages these two distinct V-O interactions, reflecting the limitations of a simple two- and three-body empirical potential in describing the complex variety of V–O bonding in these systems. The short BOMD approach exhibits an intermediate behavior, with a sharper peak than CMD but not as well-defined as fBOMD. This suggests that while BOMD improves upon CMD by incorporating quantum mechanical effects, it does not yet achieve the level of detailed precision provided by a fBOMD cycle.
In the NVP40B system, similar trends are observed. The first peak, indicative of V=O double bond lengths, and the second peak, corresponding to V–O single bond lengths, are

most accurately represented by *f*BOMD. CMD results display a broader and less defined peak, while BOMD shows improved accuracy over CMD but does not achieve the precision of *f*BOMD. This underscores the enhanced capability of a full thermal cycle by *f*BOMD in capturing the fine details of atomic interactions, even in more complex systems with mixed valence states.

The comparative analysis reveals that *f*BOMD consistently shows sharper and more accurately positioned peaks, indicating a better representation of V–O bond distances. CMD displays broader peaks, suggesting less precise modeling of V–O interactions due to its inability to distinguish between the different types of V–O bonds. BOMD provides a middle ground with improved peak sharpness and positioning over CMD, but not as precise as *f*BOMD. The full thermal cycle in *f*BOMD allows for the optimal arrangement of V–O interactions, achieving a more accurate representation of the local V sites environment.
Fig. 5.12 presents the partial pair correlation functions for O–O, Na–O, and P–O pairs in the NVP40A and NVP40B systems. These functions were calculated using CMD, BOMD, and *f*BOMD methods, showcasing the performance of each computational approach.
For the O–O pairs, the partial pair correlation function reveals significant discrepancies between the methods. CMD results show an overly structured correlation function, indicating an unrealistic representation of O–O interactions. This excessive structuring suggests that the empirical potentials used in CMD may not adequately capture the true behavior of oxygen correlation in the glass network. In contrast, *f*BOMD produces a smoother and more realistic correlation function, closely aligning with the expected behavior. BOMD shows very similar results, partially mitigating the over-structuring seen in CMD. This highlights the limitations of empirical potentials in CMD and the improvements gained by incorporating quantum mechanical effects for the O–O correlations. In addition, for NVP40A, a very low-intensity peak at about 1.2 Å is observed, which might be associated with the formation of a small amount of molecular O_2 during the *f*BOMD thermal process. If this is the case, the oxygen forming these molecules should be considered as removed from the overall glass network composition. This reduction in available oxygen could affect the total oxygen content for the glass components, potentially altering the final speciation of vanadium sites.

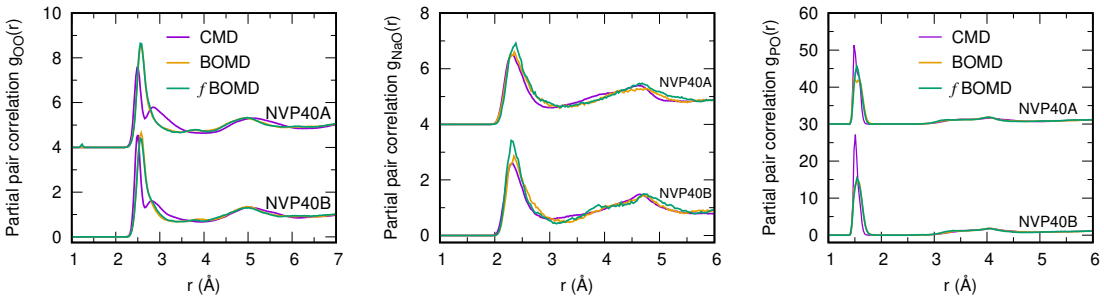

Figure 5.12. Partial pair correlation functions for NVP40A and NVP40B glasses, displaying CMD, BOMD and *f*BOMD results for $g_{OO}(r)$, $g_{NaO}(r)$, and $g_{PO}(r)$, respectively, from left to right.

The Na–O pair correlation functions indicate a different trend. The first peak, corresponding to Na–O interactions, is relatively well-resolved across all methods, reflecting the fairly good empirical potential parameters for these pairs. However, *f*BOMD shows a slight less broadening of the first peak compared to CMD, suggesting a slightly more structured representation of the Na–O bond environment. BOMD results are similar to those of CMD, indicating that the Na–O interactions are less sensitive to the incorporation of quantum mechanical effects than other pairs. This reflects the adequacy of the empirical potentials

for modeling Na–O interactions in these systems.
For P–O pairs, the first peak is also well-resolved across all methods, with *f*BOMD showing only a relatively small broadening compared to CMD. This suggests that the empirical potentials for P–O interactions are reasonably accurate, providing a good representation of the local bonding environment. BOMD results are again intermediate, with the first peak slightly broader than CMD but not as broad as *f*BOMD. This indicates that while the empirical potentials for P–O pairs are adequate, incorporating quantum mechanical effects through *f*BOMD provides a more refined and accurate depiction of the bond environment.

Overall, the comparative analysis of partial pair correlation functions for O–O, Na–O, and P–O pairs reveals significant differences in the performance of CMD, BOMD, and *f*BOMD methods. For O–O pairs, *f*BOMD provides a much smoother and realistic correlation function, whereas CMD shows overly structured results. Na–O and P–O interactions are reasonably well-represented by empirical potentials, with *f*BOMD showing minor differences of the first peak compared to O–O interaction. Further insights into the NVP40 glasses networks structures are gained by analyzing coordination numbers and structural units.

Coordination number and structural units

The average coordination number for each atom is calculated by summing the partial coordination numbers (as described in Sec. 3.4.2 of Chapter 3). This is achieved by integrating the first peak of the corresponding partial pair correlation function up to the cutoff distance defined by the first minimum. Tab. 5.11 presents the calculated total coordination numbers for Na, V, P, and O atoms, compared with experimental data as well as the nearest-neighbour interatomic distances $r_{\alpha\beta}$ in Å identified by the position of the first peak maximum. of the pair correlation functions $g_{\alpha\beta}(r)$.

Table 5.11. Bond lengths r_{ij} (in Å) (taken as the position of the first maximum of the pair correlation functions $g_{\alpha\beta}(r)$) and average coordination numbers n_i, computed for the two NVP40 models with CMD, BOMD and *f*BOMD thermal cycle in comparison with experiment. The average statistical error, computed across the replicas is 0.02 Å.

		NVP40A			NVP40B		
	Exp.[a]	CMD	BOMD	*f*BOMD	CMD	BOMD	*f*BOMD
n_{Na}	5.90	5.62	6.16	6.44	5.09	5.58	5.57
n_P	4.00	4.00	4.00	4.00	4.00	4.00	4.00
n_V	4.20-5.40	4.18	4.79	4.85	4.33	4.73	4.60
n_O	2.00-4.00	1.63	1.73	1.74	1.70	1.76	1.74
r_{NaO}	2.3-2.6	2.32	2.33	2.38	2.32	2.35	2.30
r_{PO}	1.52-1.60	1.50	1.56	1.54	1.51	1.56	1.54
r_{VO}	1.58	-	1.61	1.59	-	1.59	1.57
	1.90	1.77	1.83	1.88	1.78	1.82	1.86
r_{OO}	2.52-2.79	2.50/2.86	2.58	2.56/2.81	2.50	2.58	2.55
r_{VV}	3.50	3.57	3.52	3.38	3.57	3.52	3.54
r_{PV}	3.24	3.36	3.24	3.20	3.31	3.31	3.25

[a]Estimated from X-ray and neutron diffraction measurements on V_xO-P_2O_5[39] and Na_2O-V_xO_y[55] glasses

We analyzed the individual cation-anion structural units for V and Na to gain further insight into the NVP40 glasses networks structures. Tab. 5.12 presents the $n_\alpha(l)$ distribution, which specifies the fraction of cations of type α (V or Na) coordinated to l oxygen

atoms. These values are computed for NVP40 glasses using the three different computational approaches and include neighboring atoms within a cutoff distance corresponding to the first minimum in the $g_{\alpha O}$(r)) pair correlation functions (2.4 Å and 3.2 Å for V and Na, respectively).

For both NVP40A and B glasses, the CMD proposes a structure with vanadium favoring low coordination dominated by VO_4 polyhedra (approximately 62.8% and 60.6% respectively) with 11.1% and 4.2% of 3-fold coordination (VO_3) respectively and a small percentage of VO_6 (2.7% and 4.2% respectively). In contrast, BOMD and *f*BOMD favor larger coordinations dominated by VO_5-type units with approximatly 50% for both systems with BOMD versus 76.0% and 50.3% with *f*BOMD for NVP40A and B systems respectively. On the other hand, BOMD shows a higher rate of VO_6 units for both systems compared to *f*BOMD and CMD. Overall, while the network of NVP40A and B glasses produced by CMD is dominated by VO_4 and PO_4 polyhedra, BOMD and *f*BOMD show a majority VO_5 and PO_4 units.

Table 5.12. Distribution of individual $n_\alpha(l)$ structural units of atoms α (V or Na) l-fold coordinated, computed for the both NVP40A and NVP40B using CMD, BOMD and *f*BOMD. These values have been calculated including neighbours separated by a cutoff corresponding to the first minimum in the $g_{\alpha\beta}(r)$. The cutoffs of 2.4 and 3.2 Å were used for the Na–O and V–O bonds respectively. Only fraction greater than 0.5 % are reported.

		NVP40A			NVP40B		
		CMD	BOMD	*f*BOMD	CMD	BOMD	*f*BOMD
V							
$l=3$	O_3	11.1 ± 4.4	-	-	5.1± 1.5	-	-
$l=4$	O_4	62.8 ± 2.6	35.6 ± 0.5	19.6 ± 0.6	60.6 ± 2.1	38.4 ± 1.9	44.7 ± 0.1
$l=5$	O_5	23.5 ± 2.3	49.4 ±3.8	76.0 ± 0.4	30.1 ± 2.3	50.2 ± 2.9	50.3 ± 0.2
$l=6$	O_6	2.7 ± 0.5	15.0 ± 4.3	4.4 ± 0.2	4.2 ± 1.3	11.4 ± 4.7	5.0 ± 0.1
Na^+							
$l=4$	O_4	12.3 ± 9.8	1.5 ± 1.0	2.8 ± 1.3	25.3 ± 8.8	15.7 ± 6.9	6.0 ± 3.3
$l=5$	O_5	32.8 ± 3.3	17.4± 2.2	10.6 ± 1.7	30.7 ± 3.1	29.7 ± 4.3	41.7 ± 3.7
$l=6$	O_6	36.1 ± 10.0	50.8 ± 1.3	36.5 ± 3.6	25.3 ± 9.0	34.9 ± 10.7	42.7 ± 0.6
$l=7$	O_7	15.5 ± 2.6	24.9 ± 1.9	41.1 ± 0.7	9.3 ± 0.5	13.4 ± 4.2	9.0 ± 0.5
$l=8$	O_8	2.7 ± 0.9	5.1 ± 0.1	8.0 ± 0.8	1.9 ± 1.3	4.0 ± 1.6	0.7 ± 0.2

5.5.3 Electronic and bonding properties

The comparison between PBE and PBE0 functionals for NVP40A and NVP40B (Fig. 5.13) reveals striking differences in their predictions of electronic and magnetic properties, following trends similar to those observed for NVP25, NVP43, and VP50. PBE dramatically underestimates the bandgap, showing values near zero for both NVP40A and NVP40B, consistent with its performance for the previously studied glass models. In contrast, PBE0 predicts much wider bandgaps, ranging from about (1.1±0.4) to (1.6±0.3) eV. This significant improvement in bandgap prediction by PBE0 aligns with the findings for NVP25, NVP43, and VP50, though the gaps for NVP40A and NVP40B appear slightly smaller than those reported for VP50 (2.4–2.8 eV). Both functionals hint at the magnetic nature of these glasses, evident from the slight differences in spin-up and spin-down bandgaps. However, PBE0 appears to capture these magnetic effects more prominently, a trend consistent across all the glass models studied. The distribution of local spins on V sites further highlights the disparities between the two methods, mirroring the observations made for NVP25 and NVP43. PBE results show a somewhat ambiguous picture, with a significant

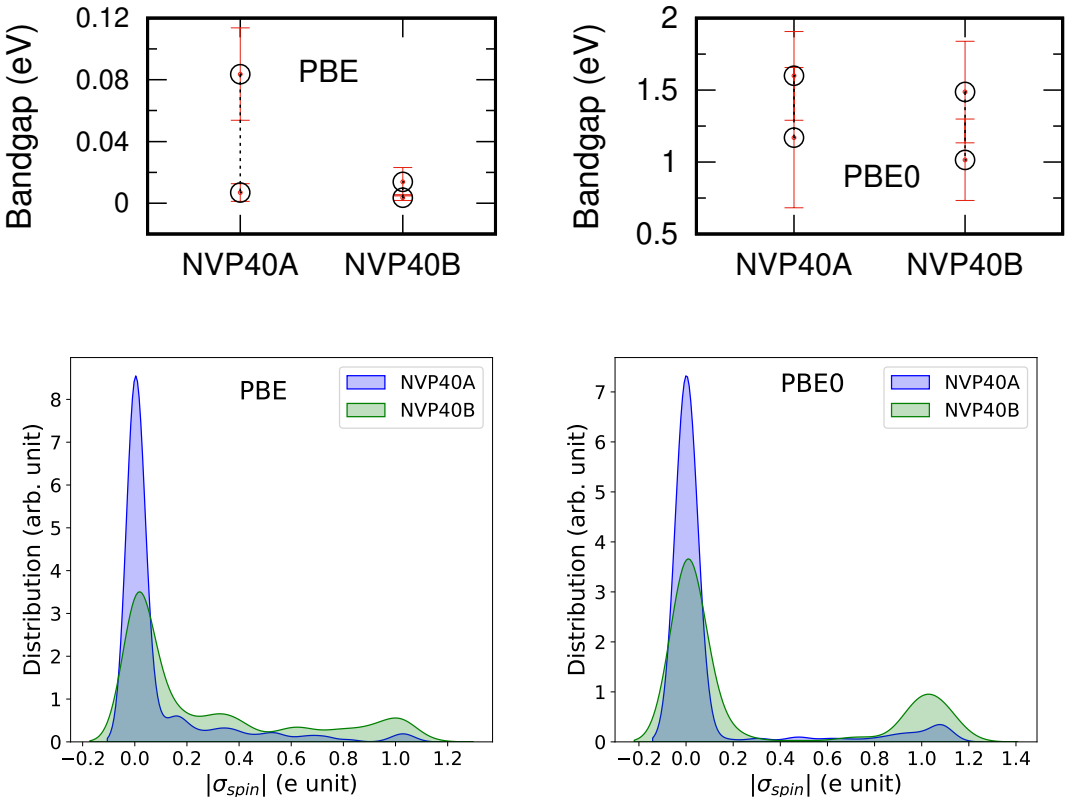

Figure 5.13. Averaged values of the energy bandgap (in eV) are shown at the top, and spin densities (in e units) are shown at the bottom. The results are computed for all Vanadium sites at the PBE (left) and PBE0 (right) levels for the two NVP40 (NVP40A and NVP40B) glasses using BOMD. Bandgap values for both spin-up and spin-down states are averaged over three configurations simulated for each system. Spin densities display the distribution of individual data points across the three configurations for each glass.

spread of V sites with intermediate spin values. This makes it challenging to clearly differentiate between V^{4+} and V^{5+} states, a limitation also noted in the previous glass models. PBE0, on the other hand, shows a clearer picture, as it did for NVP25 and NVP43. It shows a more distinct separation between V^{5+} sites (with spins near zero) and V^{4+} sites (with spins around 1 e unit). This sharper delineation allows for a more meaningful comparison between NVP40A and NVP40B, much like it did for the previous models. The PBE0 results suggest that NVP40A has a slightly higher proportion of V^{5+} sites, while NVP40B shows a marginally higher content of V^{4+} sites. These subtle differences in V speciation between the two glass models hint at slight variations in their chemical compositions. Both likely have structures based on a Na_2O–V_xO_y–P_2O_5 system, but with NVP40A leaning towards a higher V_2O_5 content and NVP40B towards a bit more V_2O_4. This detailed view of composition aligns well with the insights gained from the analysis of NVP25 and NVP43. Based on the this analysis, the exact composition of these two glasses are: $10Na_2O$–$40V_xO_y[35.8V_2O_5$–$4.2V_2O_4]$–$50P_2O_5$ and $10Na_2O$–$40V_xO_y[30V_2O_5$-$10V_2O_4]$–$50P_2O_5$ for NVP40A and NVP40B respectively. Overall, this analysis underscores the necessity of the accuracy of the PBE0 functional in capturing the electronic and magnetic subtleties of these complex glass systems, providing insights that are more aligned with experimental expectations and offering a clearer picture of the V oxidation states within these materials. The consistency of these trends across NVP40A, NVP40B, and the previously studied NVP25, NVP43, and VP50 glass models reinforces the reliability of the PBE0 approach for analyzing these complex vanadate-phosphate glass systems.

The analysis of electronic structure through WFC has offered us a deeper analysis into

the chemical intricacies of NVP40 glasses, building upon our previous insights from VP50. This approach has cleared the complex bonding landscape within VO_n polyhedra, revealing a featured picture of vanadium-oxygen interactions. We have observed a spectrum of V–O bonds, ranging from single bonds stretching between 1.8 and 2.0 Å to shorter, stronger double or vanadyl bonds at about 1.6 Å. The distinction between these bond types is captured by the WFC-single bonds show shared WFC along the V–O interaction (overlapping pairs of WFC in LSD calculation), while the stronger double bonds is characterized by multiple shared WFCs, showing a complex picture of electron density distribution. The WFC analysis also further revealed and supported the formation of molecular oxygen (O_2) entity within the NVP40A model. This feature, depicted in Fig. 5.14 (a), shows an O–O bond measuring 1.2 Å a fingerprint sign of molecular oxygen. The bond is further characterized by two shared WFCs, confirming its double bond nature.

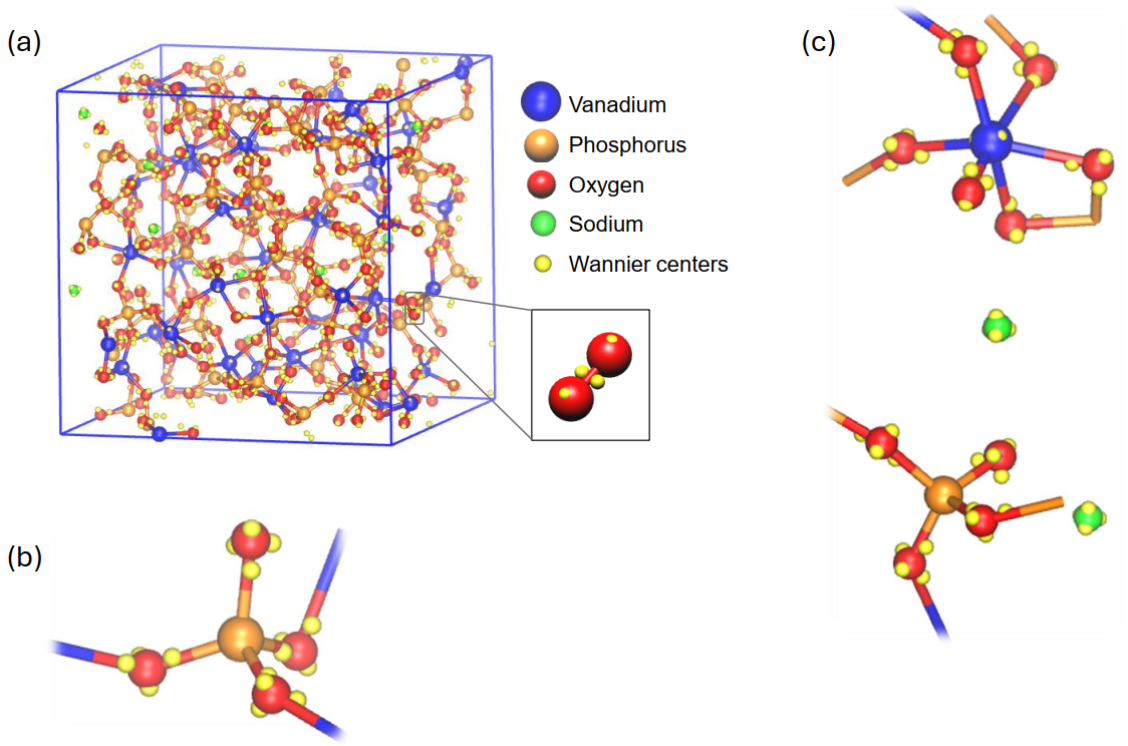

Figure 5.14. Snapshot of the NVP40A simulation cell at 300 K showing a formation of an O_2 molecule (a). A PO_4 polyhedron (b). A Na^+ ion intercalated between VO_6 and PO_4 polyhedra (c). Wannier centers characterizing a chemical bonds are shown in yellow.

The WFC analysis has also provided a further comprehensive chemical bonding picture of the NVP40A and B glasses. Fully inline with our previous results on VP50 glass, at the core of NVP40 glasses lies a rigid network made of VO_n and PO_n polyhedra. These structural units are bound together through a mix of single and double bonds with oxygen atoms, creating a three-dimensional lattice that forms the skeleton of the material. The WFC analysis allowed to further analyse their bonding features, showcasing the varying electron density distributions that characterize these different bond types within the polyhedra (see Fig. 5.14 (b) and (c)). Interestingly, the role of Na in this glass network has been further elucidated by our WFC analysis. Rather than being merely interspersed throughout the structure, Na atoms play a crucial role as network modifiers. They interact with the glass framework through ionic bonds, primarily engaging with non-bridging oxygen (NBO) atoms (see Fig. 5.14, (c)). These interactions are characterized by lone

pair WFCs on the oxygen atoms, which are directionally oriented towards neighboring Na atoms at distances of 2.2–2.4 Å. This precise spatial relationship, captured by the WFC analysis, provides strong evidence for the nature of the Na–O interactions and their role in modifying the glass network.

The presence of these directional lone pairs not only confirms the ionic nature of the Na–O interactions but also suggests how Na influences the overall glass structure. By interacting with NBO oxygens, Na atoms likely contribute to the network's flexibility and may play a role in ion transport properties of the glass. This detailed structural insight, combining the rigid polyhedra network with the modifying influence of sodium, paints a more complete picture of the NVP40A and B glasses. It showcases how different elements come together to create a material with complex bonding arrangements, from the strong covalent bonds within the polyhedra to the ionic interactions with sodium. These findings not only deepen our understanding of NVP40A and B but also provide a solid foundation for future investigations into structure-property relationships in vanadate-phosphate glasses. They invite us to explore how subtle variations in composition and processing might influence this intricate structural arrangement and, consequently, the macroscopic properties of these complex disordered materials.

5.6 Conclusive remarks

In this chapter, we explored the structural, bonding, and electronic properties of ternary Na_2O-V_xO_y-P_2O_5 (NVP) glasses using different computational schemes. The study aimed to evaluate the limitations of empirical force fields and highlight the improvements brought by *f*BOMD, along the same lines of previous Chapter on VP50 glass. Our findings reveal that classical FF are limited in accurately modeling the local environment of vanadium in NVP glasses, often approximating their short-range order. *f*BOMD, on the other hand, significantly enhances the accuracy of these models, particularly in delineating the V–O interactions and oxidation states. A major advancement in this study is the demonstration that a *f*BOMD thermal cycle offers superior structural details compared to CMD and even CMD followed by short BOMD equilibration. The BOMD method provides intermediate results, better than CMD alone but not as accurate as a complete *f*BOMD cycle. *f*BOMD simulations capture the fine details of the local bonding environment, accurately representing single V–O and double V=O bonds. This leads to a well-defined short-range V–O polyhedra environment, crucial for understanding the functional properties of NVP glasses. The comparison with experimental data confirms that *f*BOMD accurately determines the V oxidation states and provides a reliable depiction of the local electronic and bonding environments and local structure around phosphorus and vanadium sites. This comprehensive analysis underscores the necessity of advanced computational methods for accurately modeling the complex structures of NVP glasses.
In summary, the study showcases the limitations of current available empirical force fields and the significant improvements offered by *f*BOMD. The detailed insights provided by *f*BOMD pave the way for future research and the development of improved interatomic potentials, contributing to the design of better NVP-based materials for technological energy storage applications.

Chapter 6

Development of a MLIP for NVP glasses

Summary

In this chapter, we present the development of a GAP-type machine learning interatomic potential for NVP glasses. The newly developed MLIP demonstrates superior performance compared to classical empirical potentials in terms of prediction of structural properties, achieving quasi-accuracy comparable to FPMD for NVP40 glass. Moreover, the chapter includes tests of the MLIP's transferability to other VP and NVP glass compositions beyond the original training dataset. The results indicate that the MLIP maintains high accuracy and reliability across these compositions. We also make a preliminary study and related considerations on the dynamical properties of NVP, focusing on ionic conductivity of sodium ions as well as V–V features as important for electronic conductivity. The MLIP's accuracy in predicting these properties highlights its potential for speeding-up these calculations and advancing our understanding and design of materials with desirable ionic transport characteristics. A summary of these findings has been published in ref. [308].

6.1 Motivations behind the need of Machine learning interatomic potential (MLIP) for NVP systems

The development of a MLIP for the NVP glass system represents a significant advancement and challenge in computational materials science. This Chapter focuses on leveraging the Gaussian Approximation Potential (GAP) scheme to produce an MLIP for NVP glasses, a complex four-elements system that includes a transition metal vanadium, which exhibits multiple oxidation states. The primary motivation is to assess the feasibility to create a potential that can model these complex disordered systems with first-principles accuracy, yet perform simulations much faster than the computationally expensive FPMD method. As previously presented in Chapters 3, 4, and 5, the FPMD simulations, while providing high accuracy, are prohibitively expensive for large systems or long simulation times due to their computational cost. This limitation has been highlighted in studies of disordered systems, such as liquid $GeSe_2$, where the high computational cost of CPMD-scheme restricted the ability to explore extensive configuration spaces (over milion-atom systems) and long timescales (see Chapter 3). For NVP glasses, these constraints are even more pronounced, making it challenging to obtain accurate structural models necessary for understanding their properties.

In this chapter, we aim to address these challenges by developing a MLIP using the GAP scheme, which is potentially tailored for complex multi-component systems like NVP glasses, following the procedure previously presented for $GeSe_2$ and already validated for amorphous solid-state electrolyte Na_3OCl [309, 310]. This approach allows for efficient simulations that maintain high fidelity to the underlying potential energy surface, thus enabling more extensive and detailed investigations of NVP glass structures. We begin by focusing on NVP40 glass, which is the NVP composition of choice due to the availability of experimental and *f*BOMD data (with a full thermal cycle, see Chapter 5). This comprehensive dataset provides an optimal starting ground for training the MLIP-GAP model, ensuring that it captures the essential interactions and behaviors within NVP glass systems.
The MLIP-GAP developed here is designed to potentially handle the additional complexity introduced by the transition metal (V), which can exist in different oxidation states (V^{5+}, V^{4+}, V^{3+}). This feature is rarely explored in the literature for four-element glass systems by MLIP, making this study particularly novel. By incorporating extensive training data from high-fidelity *f*BOMD simulations, the MLIP-GAP can accurately represent the diverse bonding environments and oxidation states of V, leading to more accurate and realistic models.
Moreover, the MLIP-GAP model not only aims to match the accuracy of BOMD simulations but also has the potential to surpass it. By enabling longer thermal cycles and more realistic cooling rates, which were previously limited by computational costs, the MLIP-GAP can provide deeper insights into the structural properties and behaviors of NVP glasses. Once validated on NVP40, the model are tested on other NVP compositions to further demonstrate its transferability and robustness.

In summary, the development of an MLIP using the GAP scheme for NVP glass systems is motivated by the need to perform accurate, large-scale simulations efficiently. By overcoming the computational limitations of nowadays-available classical empirical potentials and the computational cost of BOMD, the MLIP-GAP developed here represents a significant step forward for modeling complex multi-component NVP glass systems.

6.2 MLIP development for NVP systems

6.2.1 DFT-FPMD database building

The database, which includes a wide range of atomic configurations and corresponding energies and forces, provides the data required for the fitting procedure. By systematically comparing model predictions with database values, we can iteratively optimize potential parameters to achieve the best possible agreement with reference data. In this work, the database is constructed from two previously generated NVP40 trajectories (NVP40A and NVP40B), which were produced by full *f*BOMD thermal cycle simulations using the PBE functional, as detailed in Sec. 5.5 of Chapter 5. Single-point DFT calculations (energy, forces and virial) were performed at the PBE0 level with a 100 Ry energy cutoff on selected configurations at temperatures of 300, 600, 900, 1500, 2000, 2500, and 3500 K. The initial database version (GAP-v1) consists of 360 representative configurations, divided into a training set (287 configurations) and a testing set (73 configurations, representing 20% of the total). A second version (GAP-v2) incorporates an additional 15 uncorrelated configurations from the NVP40B glass at 300 K, which were unavailable during the construction of GAP-v1. This results in a total of 375 representative configurations, comprising 300 for training and 75 for testing. Having constructed a comprehensive dataset capturing the relevant atomic configurations, we can now proceed to the fitting process, using this information to refine the potential's parameters.

6.2.2 Model fitting and energy/forces performance assessment

The MLIP-GAP developed for NVPs systems followed the same kernel-based methodology as the scheme introduced in Chapter 2, Sec. 2.4 , and previously tested on a simpler binary system in Chapter 3. Details of the optimized hyperparameters used for constructing the descriptors in both versions of the GAP potential are summarized in Tab. A.6 of Appendix A.3.
Fig. 6.1 showcases a comparative analysis between two MLIP, GAP-v1 and GAP-v2, illustrating their efficiency in predicting formation energy and forces when benchmarked against BOMD/DFT results. In terms of formation energy, GAP-v1 shows mean absolute errors (MAEs) of 8.40 meV/atom for the training set and 8.73 meV/atom for the testing set. Although the predictions align reasonably well with the BOMD values, there's a noticeable scatter, indicating some deviations. On the other hand, GAP-v2 significantly reduces these errors, with MAEs dropping to 5.64 meV/atom for the training set and 5.83 meV/atom for the testing set, reflecting a more accurate and consistent prediction capability for formation energy compared to GAP-v1. Typically, MAE error of about $\sim$ 5 meV/atom or lower supports the argument that GAP-based atomistic models predict the local properties of the systems with good accuracy for liquid and amorphous states [311]. In terms of force predictions, the improvement from GAP-v1 to GAP-v2 is minimal but present. GAP-v1 has shows a MAE of 0.39 eV/Å for the training set and 0.42 eV/Å for the testing set, whereas GAP-v2 shows a reduction in training and testing set errors to 0.37 eV/Å and 0.41 eV/Å. This significant decrease in the training set error indicates a significant improved model, leading to highly accurate force predictions.

The cumulative error distributions for energy and forces (Fig. 6.1, (c) and (d) respectively) in GAP-v1 and GAP-v2 exhibit similar profiles. Furthermore, the overlap observed between the training and testing sets for both models suggests that neither is underfitting (not capturing the underlying patterns) nor overfitting (memorizing the training data). Essentially, GAP-v2 demonstrates a significant improvement in performance compared to GAP-v1. The reduced mean absolute errors (MAEs) observed in both formation energy

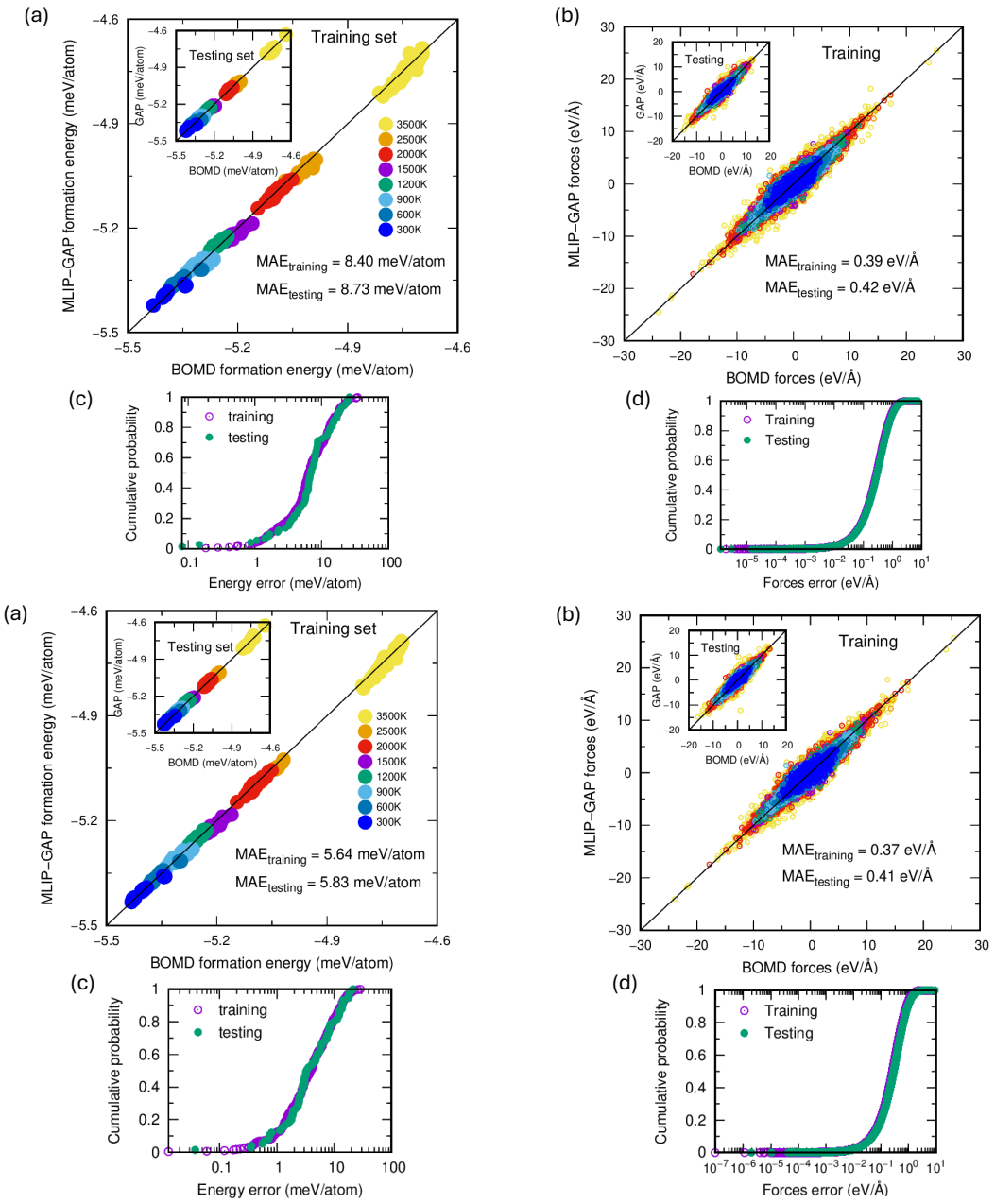

Figure 6.1. Scatter plots and cumulative error distributions demonstrating the accuracy and generalization of MLIP-GAP predictions. (a, b) Correlations between DFT-computed and MLIP-GAP-predicted energies (a) and force components (b) for both training and testing sets. Insets magnify the testing data. Mean Absolute Errors (MAE) are provided for each dataset. (c, d) Cumulative error distributions for energy (c) and forces (d) across training and testing sets, confirming the absence of over-fitting during model training. The results on the top panel is derived from version v1 of the potential and the bottom panel from version v2, for which the database has been enriched with 16 configurations at 300 K from the NVP40B glass.

and force predictions indicate that GAP-v2 generates more accurate and precise results, aligning closely with the BOMD reference data. This highlights a successful refinement of the MLIP. In the following, we will utilize our MLIP to model glasses of the same size as the BOMD reference system, before extending to larger systems.

6.3 MLIP *vs* BOMD simulations of NVP40A/B glasses

6.3.1 Structural properties

Structure factors

To further assess the performance of GAP-v2 compared to GAP-v1, we analyze the X-ray total structure factors of the NVP40A and NVP40B models (as illustrated in Fig. 6.3). We also refer to the R_χ values of both MLIP-GAP potentials, quantified against experimental and BOMD data (see Tab. 6.1). This dual comparison allows us to evaluate the agreement for NVP40A, which is intended to closely correspond to the experimentally synthesized NVP40 glass composition. For NVP40A, both GAP-v1 and GAP-v2 show similar R_χ values, close to the BOMD data (10.72 and 11.63 versus 11.37%).

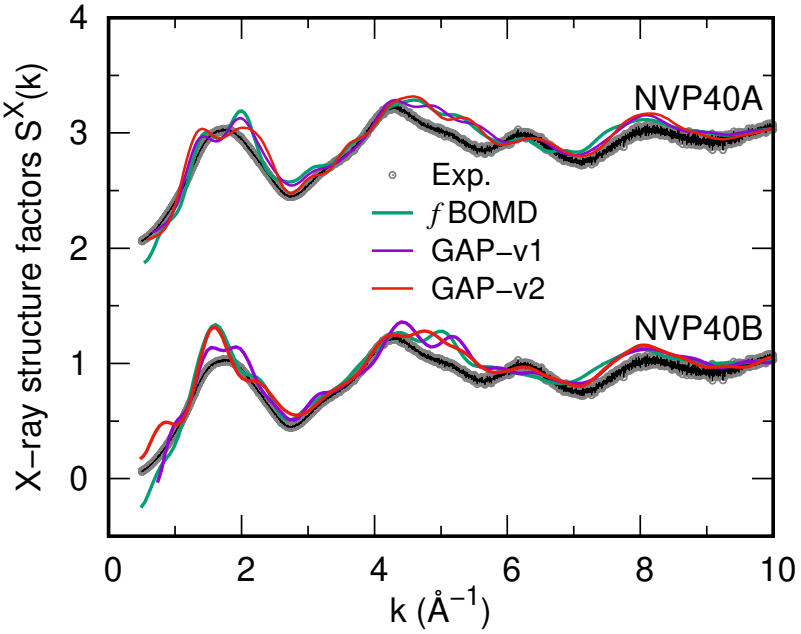

Figure 6.2. Comparison of total X-ray structure factors for NVP40A and NVP40B glasses at 300 K. Results obtained from MLIP-GAP versions GAP-v1 (red) and GAP-v2 (blue) are shown alongside reference BOMD simulation data for each glass composition and experimental measurements.

Table 6.1. Goodness-of-fit (R_χ) parameters for BOMD, GAP-v1 and GAP-v2 data, showing the level of agreement with experimental total X-ray structure factor for NVP40 systems (first row). In the second row, R_χ for the two version of GAP is quantify with respect to the BOMD reference data

	NVP40A			NVP40B		
X-ray	BOMD	GAP-v1	GAP-v2	BOMD	GAP-v1	GAP-v2
$R_\chi^{S(k)}$ vs Exp.	11.37	10.72	11.63	12.73	11.23	11.98
$R_\chi^{S(k)}$ vs BOMD	-	4.19	6.50	-	6.70	6.73

For NVP40B, comparison with BOMD data demonstrates comparable performance (11.23% and 11.98%). Notably, GAP-v2 reproduces the *f*BOMD profile of the first peak of the total structure factor at around 2 Å^{-1} more accurately than GAP-v1, despite showing a slight spurious shoulder at about 1 Å^{-1}. Given the similar performance of the two versions and the superior shape reproduction by GAP-v2, coupled with lower errors in energy and forces prediction, the subsequent section will focus exclusively on GAP-v2 data

when referencing MLIP-GAP.
We present here a comparative analysis of BOMD, *f*BOMD, and MLIP-GAP (GAP-v2) schemes, revealing significant insights into how each schemes models the structure of NVP40 glasses. By analysing the X-ray and neutron total structure factors, as well as the total pair distribution functions, we can evaluate the accuracy and reliability of these methods in capturing the atomic arrangements within these glasses.
The X-ray structure factors $S^{\mathrm{X}}(k)$ for NVP40A and NVP40B highlight clear differences among the methods. CMD data shows noticeable discrepancies compared to *f*BOMD and MLIP-GAP, particularly at low k-values. *f*BOMD and MLIP-GAP exhibit very similar degrees of accuracy, indicating that MLIP-GAP performs at a level comparable to *f*BOMD. MLIP-GAP, in particular, aligns closely with *f*BOMD, demonstrating its capability to achieve ab-initio accuracy efficiently. Similarly, the neutron structure factors

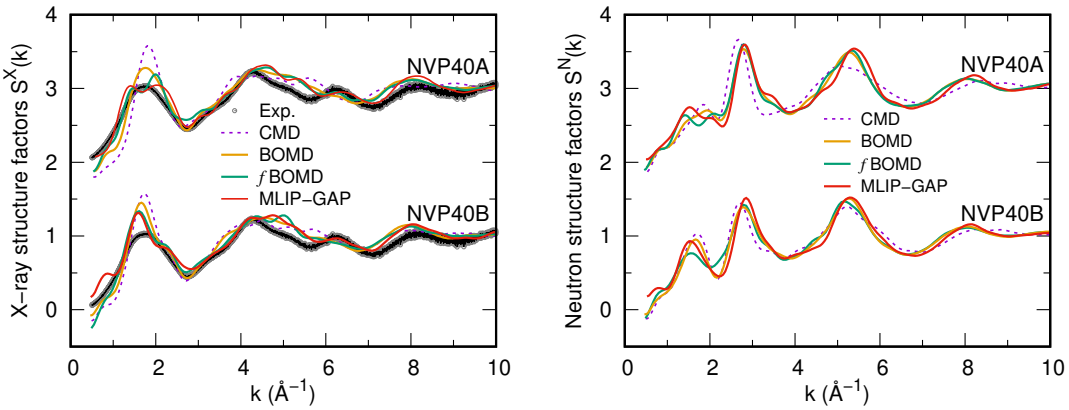

Figure 6.3. Total structure factors for NVP40 glasses obtained from X-ray diffraction (left) and neutron scattering (right). X-ray data includes experimental measurements and simulation results (CMD, BOMD, *f*BOMD, and MLIP-GAP), while neutron data shows only simulation results.

$S^{\mathrm{N}}(k)$ reveal that CMD slightly deviates in both peak positions and intensities compared to *f*BOMD and MLIP-GAP. Both *f*BOMD and MLIP-GAP shows fair agreement with each other, capturing detailed atomic interactions and effectively modeling both short- and intermediate-range orders. The close alignment between *f*BOMD and MLIP-GAP suggests that MLIP-GAP can replicate the high fidelity of *f*BOMD while being computationally more efficient. Tab. 6.2 (first row of data for each system) provides a quantitative assessment of the agreement between simulation results and experimental data using R_χ parameter.

Table 6.2. Assessment of the accuracy of MLIP-GAP versus CMD, BOMD, and *f*BOMD using goodness-of-fit (R_χ) parameters for X-ray total structure factor and pair distribution function of NVP40 glasses at 300 K.

	NVP40A			
X-rays	CMD	BOMD	*f*BOMD	MLIP-GAP
$\mathrm{R}_\chi^{S(k)}$	21.5 ± 0.3	14.2 ± 0.1	11.4 ± 0.1	11.0 ± 0.8
$\mathrm{R}_\chi^{G(r)}$	90.6 ± 1.5	74.1 ± 0.3	58.9 ± 0.5	72.5 ± 1.9
	NVP40B			
X-rays	CMD	BOMD	*f*BOMD	MLIP-GAP
$\mathrm{R}_\chi^{S(k)}$	17.5 ± 0.1	14.4 ± 1.2	12.8 ± 0.1	12.0 ± 0.1
$\mathrm{R}_\chi^{G(r)}$	86.1 ± 2.0	70.7 ± 1.5	62.0 ± 0.1	69.9 ± 0.7

Total pair distribution function

The X-ray total distribution function (G(r)) for NVP40A and NVP40B further shows the performance of each method: CMD shows significant discrepancies in peak positions and intensities, with less sharp and misaligned peaks. This indicates CMD's limitations in accurately modeling short-range order within these NVP glasses as discussed in the previous chapter. In contrast, BOMD, *f*BOMD and MLIP-GAP show a high degree of agreement, with MLIP-GAP found more similar to *f*BOMD than BOMD data.

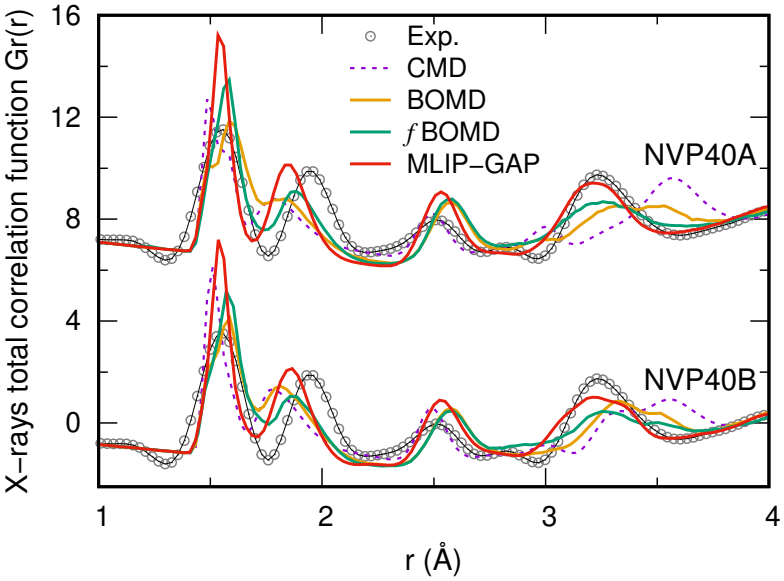

Figure 6.4. Total pair distribution function G(r) of NVP40 glasses at 300 K: Assessment of MLIP-GAP results against CMD, *f*BOMD, and experimental data.

Focusing on the region from 1 to 4 Å highlights the finer details of atomic interactions. The peak positions and intensities in *f*BOMD and MLIP-GAP results are sharper, with the second, third, and fourth peaks better aligned with experimental data than CMD, and BOMD. They only show an overstructuring degree for the first peak, reflecting the P–O overstructured peak as illustrated by the partial pair correlation function $g_{PO}(r)$ in Fig. 6.6. Overall *f*BOMD and MLIP-GAP show greater capability to effectively capture both short- and intermediate-range interactions of these NVP glasses as confirmed by the R_χ parameter in Tab. 6.2 (second row of data for each system). CMD fails to capture these details accurately, as seen in the misaligned and broadened peaks. In contrast, *f*BOMD and MLIP-GAP reproduce these features with high precision. MLIP-GAP, in particular, aligns closely with *f*BOMD, demonstrating its effectiveness in replicating the complex bonding environments within NVP glasses. Deeper insights can be gleaned from an examination of the partial correlation functions.

Partial pair correlation function

In Fig. 6.5 and Fig. 6.6, we provide a comprehensive comparison of CMD, BOMD, and MLIP-GAP schemes of the partial pair correlation functions of NVP40A and NVP40B glasses. Tab. 6.4 shows the bond distance values corresponding the first maximim of the partial pair correlation functions. By examining these functions, we can assess how well each method captures the atomic interactions and structural properties of these glasses. Across all partial pair correlation functions, CMD consistently shows deviations compared

to BOMD and MLIP-GAP. CMD's peaks are generally less sharp and sometimes shifted, indicating its limitations in accurately capturing atomic arrangements, due to relatively "simple" empirical two-body and three-body potentials forms. In contrast, BOMD and MLIP-GAP exhibit a high degree of similarity, suggesting that MLIP-GAP can replicate BOMD's accuracy efficiently.

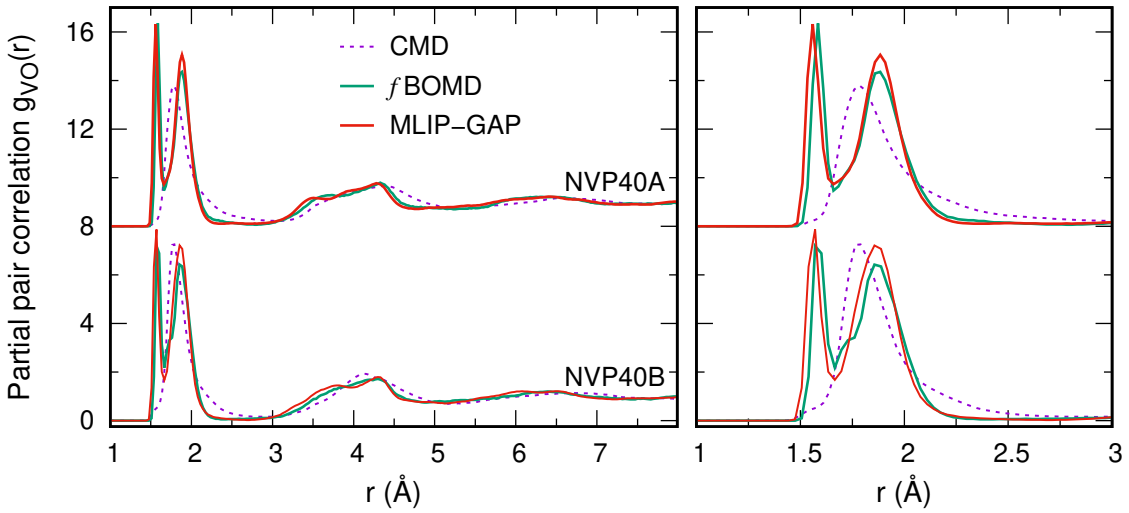

Figure 6.5. Partial pair correlation function $g_{V\text{-}O}$ for NVP40 systems, calculated using MLIP-GAP (red line), CMD (dashed line), and fBOMD (green line) simulations. The right side magnified a view of 1–3 Å region highlighting key differences.

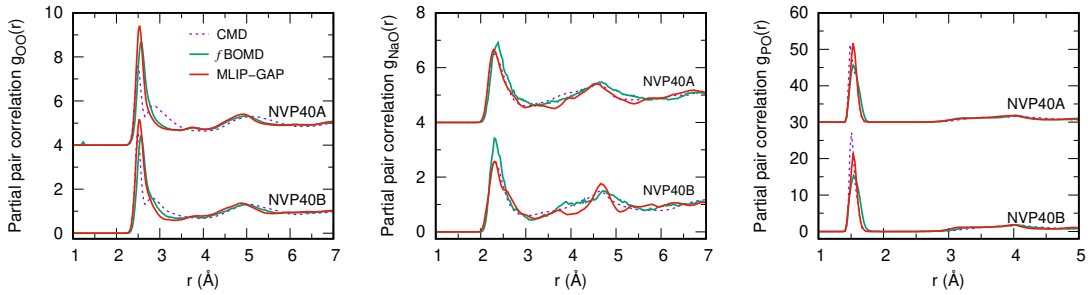

Figure 6.6. Partial pair correlation function $g_{OO}(r)$ (left), $g_{OO}(r)$ (middle), and $g_{PO}(r)$ (right) for NVP40 glasses: Comparison of CMD, fBOMD, and MLIP simulations.

For both NVP40A and NVP40B compositions, the first peak in $g_{VO}(r)$ around 1.6 Å represents the relatively short andd strong V=O double bonds. BOMD and MLIP-GAP results align closely, capturing this peak with high accuracy, both in position and intensity. CMD, however, shows a broader and less defined peak, indicating a less accurate representation of the V-O bonding environment. The second peak, around 1.8–1.9 Å, which represents the longer V–O single bond, is also more accurately captured by BOMD and MLIP-GAP compared to CMD. The alignment of BOMD and MLIP-GAP in these peaks underscores the ability of MLIP-GAP to model the complex interactions involving vanadium accurately. The other partial pair correlation functions, such as $g_{NaO}(r)$, $g_{OO}(r)$, and $g_{PO}(r)$, follow similar trends. For the $g_{NaO}(r)$, the first peak around 2.2-2.4 Å, representing the nearest neighbor Na–O bonds, shows that CMD deviates from BOMD and MLIP-GAP, with the latter two providing a slightly much sharper and well-defined peak. The $g_{OO}(r)$ and $g_{PO}(r)$ functions are crucial for understanding the oxygen and phosphorus environments in these glasses. For $g_{OO}(r)$, the first peak around 2.7 Å is accurately captured by BOMD and MLIP-GAP, while CMD shows discrepancies in peak shape and intensity,

showing overly structured functions. Similarly, the $g_{\mathrm{PO}}(r)$ functions display a significant peak around 1.5–1.6 Å, corresponding to the P–O bonds. Again, BOMD and MLIP-GAP align closely, indicating accurate modeling, whereas CMD results are less precise.
The comparative analysis of partial pair correlation functions demonstrates that MLIP-GAP significantly outperforms CMD and matches the accuracy of BOMD in capturing the local atomic structures of NVP glasses. This is particularly evident in the VO partial pair correlation functions, where the complex interactions involving V are modeled with high precision by MLIP-GAP, reflecting its robustness and efficiency in describing the complex short (i.e. double) and long (i.e. single) VO bonds. The close alignment between MLIP-GAP and BOMD across all partial pair correlation functions underscores the potential of MLIP-GAP as a powerful and computationally efficient tool for studying complex glass systems like NVP. This capability allows for more extensive simulations and deeper insights into the structural properties of these materials, advancing the field of NVP glass science.

Average coordination number and structural units

Similar as in the previous chapter, Tab. 6.4 presents the average coordination for chemical species Na, V, P, and O, as well as the chemical bond lengths calculated obtained as the position of the maximum of the first peak of the partial pair correlation function $g_{\alpha\beta}(r)$, in comparison with experimental values. Our MLIP-GAP well defined the average co-

Table 6.3. Distribution of individual $n_\alpha(l)$ structural units of atoms α (V or Na) l-fold coordinated, computed for the both NVP40A using MLIP in comparison with the previous obtained results from CMD, BOMD, and fBOMD. These values have been calculated including neighbours separated by a cutoff corresponding to the first minimum in the $g_{\alpha\beta}(r)$ and averaged over the different replicas. The cutoffs of 2.4 and 3.2 Å were used for the Na–O and V–O bonds respectively. Only fraction greater than 0.5 % are reported.

		NVP40A			
		CMD	BOMD	fBOMD	MLIP-GAP
V					
$l=3$	O_3	11.1 ± 4.4	-	-	-
$l=4$	O_4	62.8 ± 2.6	35.6± 0.5	19.6 ± 0.6	11.0 ± 0.3
$l=5$	O_5	23.5 ± 2.3	49.4 ±3.8	76.0 ± 0.4	74.2 ± 2.8
$l=6$	O_6	2.7 ± 0.5	15.0 ± 4.3	4.4 ± 0.2	14.8 ± 2.5
Na^+					
$l=4$	O_4	12.3 ± 9.8	1.5 ± 1.0	2.8 ± 1.3	22.5 ± 3.6
$l=5$	O_5	32.8 ± 3.3	17.4± 2.2	10.6 ± 1.7	23.3 ± 3.3
$l=6$	O_6	36.1 ± 10.0	50.8 ± 1.3	36.5 ± 3.6	27.2 ± 2.4
$l=7$	O_7	15.5 ± 2.6	24.9 ± 1.9	41.1 ± 0.7	14.2 ± 1.3
$l=8$	O_8	2.7 ± 0.9	5.1 ± 0.1	8.0 ± 0.8	9.0 ± 3.5

ordination of phosphorus for both systems, in full agreement with the experiment and other calculated results (CMD, BOMD and fBOMD). For vanadium, the coordination predicted by MLIP-GAP (5.06 and 4.87 Å respectively) are found slightly greater than the fBOMD values (4.85 and 4.60 Å), but showing same trend (average V coordination found lower in NVP40B than NVP40A) and remaining consistent with the experimental range of 4.20–5.40 Å.

Next, we analyzed the average distribution of VO_n and Na^+O_n structural units in NVP40A (being the one found closer to experimental composition), with sodium in the latter case having an ionic interaction with neighboring non-bridging oxygen. Tab. 6.3 presents the

Table 6.4. Average coordination numbers n_i and bond lengths r_{ij} (in Å) (taken as the position of the first maximum of the pair correlation functions $g_{\alpha\beta}(r)$) and , computed for the two NVP40 models with CMD, BOMD, *f*BOMD, and MLIP thermal cycle. The average statistical error, computed across the replicas is 0.02 Å.

		NVP40A			
	Exp.[a]	CMD	BOMD	*f*BOMD	MLIP
n_{Na}	5.90	5.62	6.16	6.44	5.34
n_P	4.00	4.00	4.00	4.00	4.00
n_V	4.20-5.40	4.18	4.79	4.85	5.06
n_O	2.00-4.00	1.63	1.73	1.74	1.79
r_{NaO}	2.3-2.6	2.32	2.33	2.38	2.28
r_{PO}	1.52-1.60	1.50	1.56	1.54	1.54
r_{VO}	1.58	-	1.61	1.59	1.56
	1.90	1.77	1.83	1.88	1.83
r_{OO}	2.52-2.91	2.50/2.86	2.58	2.56	2.53
r_{VV}	3.50	3.57	3.52	3.38	3.36
r_{PV}	3.24	3.36	3.24	3.20	3.18
		NVP40B			
	Exp.[a]	CMD	BOMD	*f*BOMD	MLIP
n_{Na}	5.90	5.09	5.58	5.57	5.40
n_P	4.00	4.00	4.00	3.97	4.00
n_V	4.20-5.40	4.33	4.73	4.60	4.87
n_O	2.00-4.00	1.70	1.76	1.74	1.80
r_{NaO}	2.3-2.6	2.32	2.35	2.30	2.30
r_{PO}	1.52-1.60	1.51	1.56	1.54	1.54
r_{VO}	1.58	-	1.59	1.57	1.56
	1.90	1.78	1.82	1.86	1.84
r_{OO}	2.52-2.91	2.50/2.81	2.58	2.55	2.55
r_{VV}	3.50	3.57	3.52	3.54	3.36
r_{PV}	3.24	3.31	3.31	3.25	3.24

[a]Estimated from X-ray and neutron diffraction measurements on V_xO-P_2O_5[39] and Na_2O-V_xO_y[55] glasses

values obtained with MLIP-GAP scheme and compared with the other levels of description. As previously noted with the average coordination, it is observed that vanadium in the glasses produced by CMD prefers low coordination with a dominance of VO_4 units (62.8%) followed by VO_5 units (23.5%) and a small proportion of VO_3 and VO_6 polyhedra.

In contrast, MLIP shows an opposite evolution, fully inline with *f*BOMD data. The VO_n units are mainly VO_5, about 74.2% (76% by *f*BOMD), followed by a slight different ratio between VO_4 and VO_6 units with respect to *f*BOMD. Unlike the CMD result, MLIP as well as BOMD and *f*BOMD does not present VO_3 units. These results are consistent with those obtained for the VP50, NVP25 and NVP43 system in the previous Chapters. In terms of Na^+O_n units, MLIP shows, a bit higher value for low coordination but within the computed statistical uncertainty, very close agreement with respect to *f*BOMD data. Overall, this analysis reveals a very close match of description of NVP40A in terms of structural units between MLIP and *f*BOMD, further corroborating its first-principles accuracy.

6.3.2 Effect of the cooling rate on the glass structure

Given that the reference *f*BOMD structure was generated under rapid thermal cycling conditions, it is interesting to assess the influence of cooling rate on the glass structure with the MLIP-GAP. Leveraging the computational efficiency of MLIP-GAP, we conducted supplementary simulations to investigate this effect.

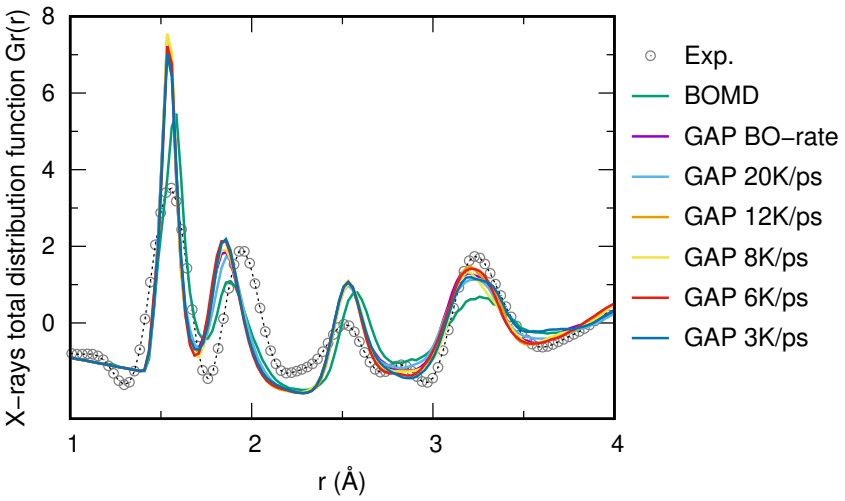

Figure 6.7. Comparison of total X-ray pair correlation functions for NVP40A glass obtained from MLIP simulations at various cooling rates (from 3 K/ps to 200 K/ps, approximating *f*BOMD), the reference *f*BOMD structure, and experimental data.

Table 6.5. Goodness-of-fit (R_χ) parameters for *f*BOMD and different MLIP-GAP cooling rate with respect to the experimental total pair distribution function for NVP40A system.

X-ray	*f*BOMD	MLIP-GAP rate					
		BO-rate	20 K/ps	12 K/ps	8 K/ps	6 K/ps	3 K/ps
$R_\chi^{G(r)}$	72.77	71.51	67.89	73.32	73.28	73.95	70.67

Fig. 6.7 illustrates the effect of varying cooling rates on the total X-ray pair distribution function G(r) of NVP40A glass, in comparison with *f*BOMD and experimental data. Specifically, cooling rates of 200 K/ps (approximating *f*BOMD rate), 20, 12, 8, 6, and 3 K/ps were examined by MLIP.
The corresponding values of the R_χ parameter, quantifying the agreement with experimental data, are presented in Tab. 6.5. These results reveal a minimal influence of cooling rate (according to the range of values tested) on the glass structure within the range tested, with all values approximating those obtained with *f*BOMD, considering the estimated error margins. Are currently in progress further tests with lower cooling rate of the order of 0.1-0.01 K/ps, still feasible with MLIP and in order to assess any possible effect.

6.3.3 Electronic and magnetic properties

The electronic properties presented here are computed as post process by single-point DFT calculations on various configurations extracted from the glass structure produced with the MLIP-GAP potential. Since **electronic properties are not directly accessible through classical simulations, even with MLIP**, this approach is necessary. The accuracy of these single-point DFT calculations, when compared to the reference FPMD data, is attributed to the indirect inclusion of electronic contributions within the MLIP-GAP training data.

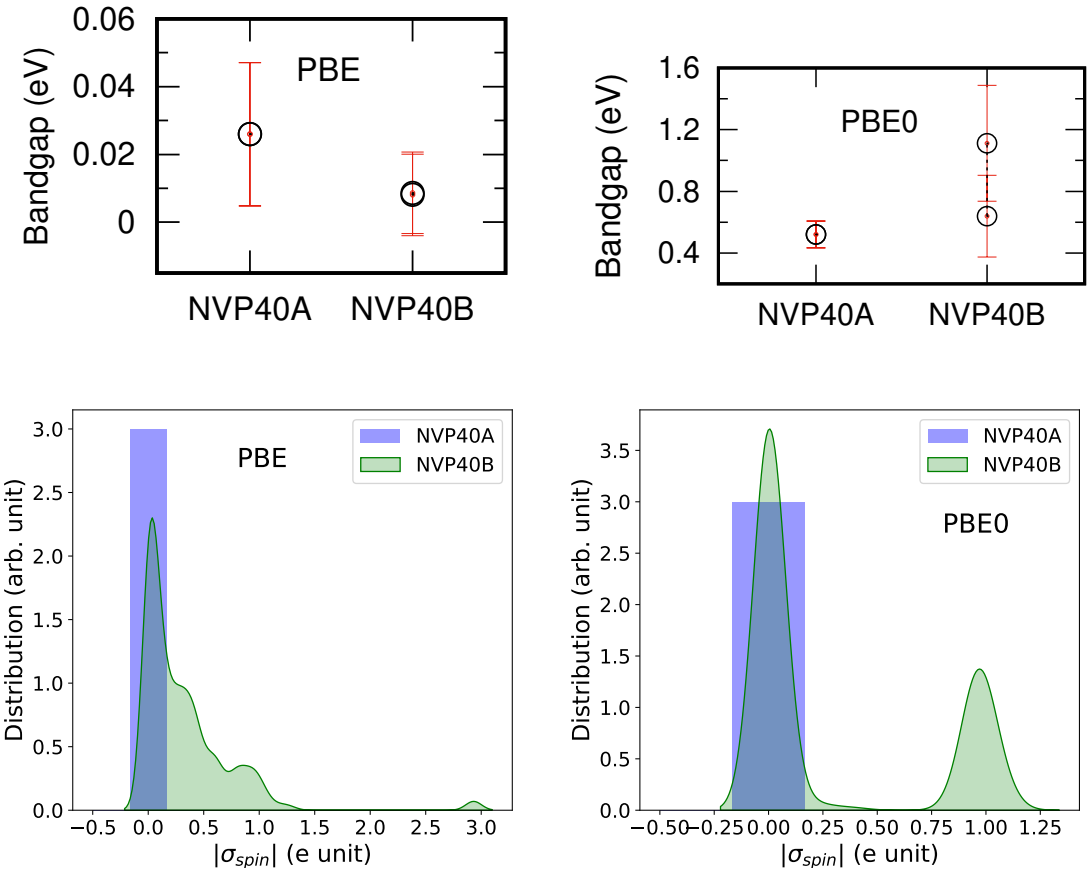

Figure 6.8. Average energy bandgap (eV, top) and spin densities (e units, bottom) for all vanadium sites in two NVP40 glasses, calculated at the PBE (left) and PBE0 (right) levels from selected configurations of glasses simulated with MLIP-GAP. Bandgap values are averaged over three replicas for both spin-up and spin-down states and the values are displayed with error bar in red. Spin density plots show the distribution of individual data points across replicas for each glass.

The comparison between PBE and PBE0 functionals for NVP40A and NVP40B (see Fig. 6.8) computed at the DFT level for glass models obtained by CMD using the newly developed MLIP-GAP reveals striking differences in their predictions of electronic and magnetic properties, following trends similar to those observed in previous Chapter. PBE dramatically underestimates the bandgap, showing values near zero (from (0.008±0.001) to (0.03±0.02) eV) for both NVP40A and NVP40B, consistent with its performance for the previously studied glass models. In contrast, PBE0 predicts much wider bandgaps, ranging from about (0.5±0.1) to (1.1±0.4) eV. The significant improvement in bandgap prediction by PBE0 is consistent with previous findings, despite the bandgap values being lower than those obtained from BOMD and . This discrepancy may be attributed to the slightly different composition of NVP40 with respect to *f*BOMD, for instance, due to

avoided formation of molecular O_2 with MLIP and the lack of equilibration at the BOMD and *f*BOMD level before computing the electronic properties.
In terms of local V sites spin, NVP40A and B models obtained by MLIP-GAP and post-optimized in terms of electronic structure at PBE0 level, whose a very well-defined V sites speciation fully inline with the the original data obtained from BOMD structure and extremely well matching the experimental glass composition. PBE results show a somewhat ambiguous picture for NVP40B, with a significant spread of V sites with intermediate spin values with values even up to 3, whereas NVP40A shows all the V sites with a close to 0 value (similar with PBE0), indicating a slight better performance with respect to data computed from *f*BOMD structure. PBE0 shows a more distinct separation between V^{5+} sites (with spins near zero) and V^{4+} sites (with spins around 1 e unit) for NVP40B (see Fig. 6.8). This clearer delimitation allows for a more meaningful comparison between NVP40A and NVP40B, much like it did for the previous models. The PBE0 results suggest that NVP40A has a totality of V sites as V^{5+} sites, while NVP40B shows a partial content of V^{4+} sites (29.17%), fully in agreement with the experimental data. Overall, this analysis underscores the ability of MLIP potential NVP models, once post-optimized at the PBE0 level to capture the electronic and magnetic subtleties of these complex glass systems, providing insights that are more aligned with experimental expectations and offering a clearer picture of the V oxidation states within these materials.

6.4 Evaluating MLIP transferability power in VP and NVP glasses beyond the training set

To further assess the robustness and transferability of our developed MLIP, we analyze its performance in reproducing the glass models of VP50, NVP25, and NVP43, which were not part of the training set used for MLIP-GAP development.
Fig. 6.9 shows the comparison of the X-ray and neutron structure factors (S(k)) for experimental data, CMD, BOMD, and MLIP-GAP for the VP50 glass. In the X-ray structure factor analysis, CMD shows significant deviations from the experimental data, particularly in the lower k-range, where it fails to accurately capture the peak positions and intensities. BOMD, on the other hand, exhibits a close match with the experimental data, accurately reflecting both peak positions and intensities, thereby validating its capability in modeling both short- and intermediate-range structures. MLIP-GAP performs similarly to BOMD, closely aligning with the experimental data and effectively reproducing the key structural features. This demonstrates MLIP-GAP's accuracy in modeling the structural characteristics of VP50 glass with high fidelity.

The neutron structure factor results further illustrate the discrepancies in CMD's performance. CMD displays significant mismatches in peak intensities and positions when compared to the experimental data, indicating its limitations in capturing the neutron structure factor accurately. BOMD once again shows strong agreement with the experimental data, capturing the key features and peaks with precision, highlighting its robustness. MLIP-GAP closely follows BOMD's performance, aligning well with the experimental data and accurately reproducing the neutron structure factor peaks. This alignment underscores MLIP-GAP's reliability and effectiveness in modeling the complex structural environments. Overall, MLIP-GAP significantly outperforms CMD in both X-ray and neutron structure factors, capturing peak positions and intensities with much higher accuracy. Its performance is comparable to BOMD, closely matching the experimental data and demonstrating its robustness. Notably, MLIP-GAP appears to reproduce the experimental peak intensities even better than BOMD. This improvement is likely because the

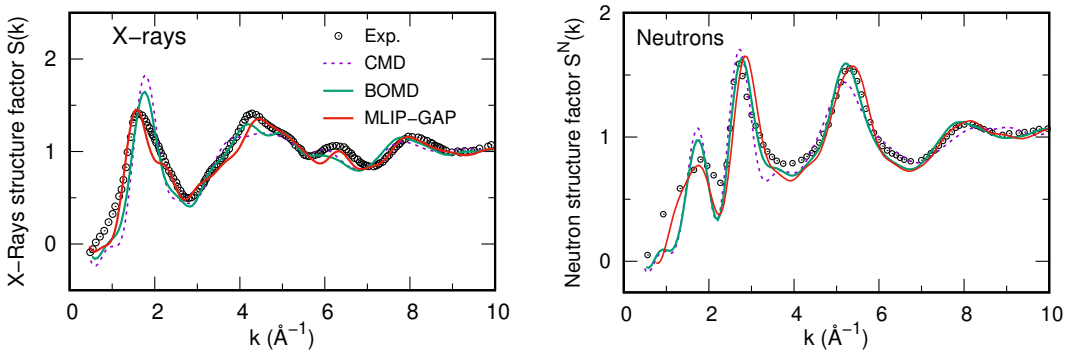

Figure 6.9. X-ray (left) and neutron (right) structure factors for VP50 glass comparing the CMD (dashed purple line), MLIP (solid red line) and BOMD (solid green line) data with the experiment (black dot).

BOMD data corresponds to the CMD+BO scheme, where only a final equilibration at 300 K was performed, rather than a full thermal cycle by *f*BOMD, which was included in the training set NVP models used for building MLIP.

For neutron structure factors, MLIP-GAP achieves the lowest R_χ value (7.1%), indicating the best agreement, followed by BOMD (8.4%) and CMD (9.8%). This superior performance highlights MLIP-GAP's robustness in capturing the subtle details of atomic interactions. For X-ray structure factors, MLIP-GAP also shows the best fit with a R_χ value of 6.3%, compared to BOMD (8.4%) and CMD (11.3%). This consistency underscores the accuracy and reliability of MLIP-GAP, even overcoming the performance of the CMD+BO scheme.

The superior performance of MLIP-GAP compared to CMD and CMD+BO can be attributed to its better description of the second and fourth peaks in the X-ray total correlation functions, which are more closely aligned with the experimental data (see Fig. 6.10).

In the total neutron pair correlation functions (T(r)), MLIP-GAP excels again with an

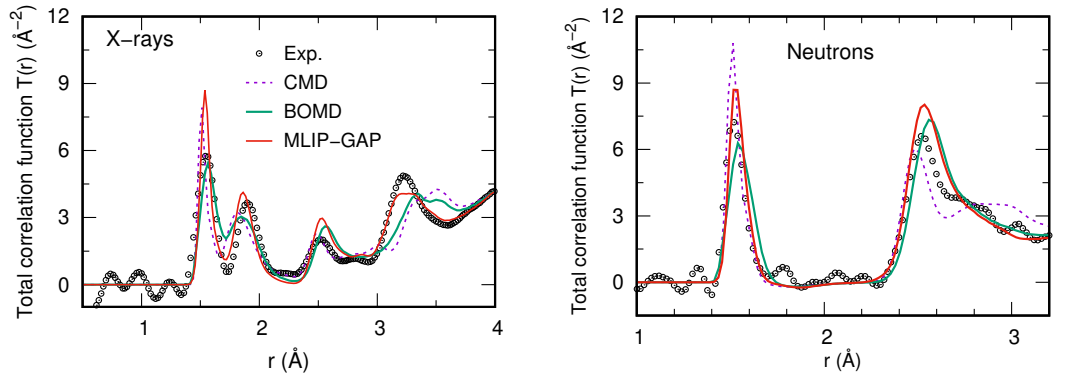

Figure 6.10. Total correlation function T(r) for VP50 glass, obtained from X-ray (left) and neutron (right) scattering. MLIP-GAP results are compared with CMD, BOMD, and experimental data.

R_χ value of 25.1%, outperforming both BOMD (28.6%) and CMD (26.7%) as indicated in Tab. 6.6. In the total X-ray pair correlation functions, MLIP-GAP achieves the lowest R_χ value of 24.4%, indicating a better match than BOMD (28.7%) and CMD (36.6%). Simultaneously, the drastic improvement in describing the local environment of VO_n polyhedra by MLIP-GAP is evident. This is demonstrated by the well-defined $g_{VO}(r)$ fingerprint peaks at approximately 1.6 Å and 1.8–1.9 Å corresponding to short double V=O and the single V–O bonds, which are completely missed by CMD and only marginally reproduced by the CMD+BO scheme (see Fig. 6.11).

Table 6.6. Goodness-of-fit R_χ parameters obtained from CMD, MLIP and BOMD results of VP50 glass indicating the level of agreement with the experimental data for neutron and X-ray structure factors ($R^X_{S(k)}$ and $R^N_{S(k)}$, respectively) and total pair correlation functions ($R^X_{T(r)}$ and $R^N_{T(r)}$, respectively).

	CMD2	BOMD	MLIP
Neutrons			
$R^N_{S(k)}$	9.8 ± 0.1	8.4 ± 0.2	7.1 ± 0.1
$R^N_{T(r)}$	26.7 ± 0.1	28.6 ± 0.5	25.1 ± 0.1
X-Rays			
$R^X_{S(k)}$	11.3 ± 0.1	8.4 ± 0.2	6.3 ± 0.1
$R^X_{T(r)}$	36.6 ± 0.3	28.7 ± 0.3	24.4 ± 0.2

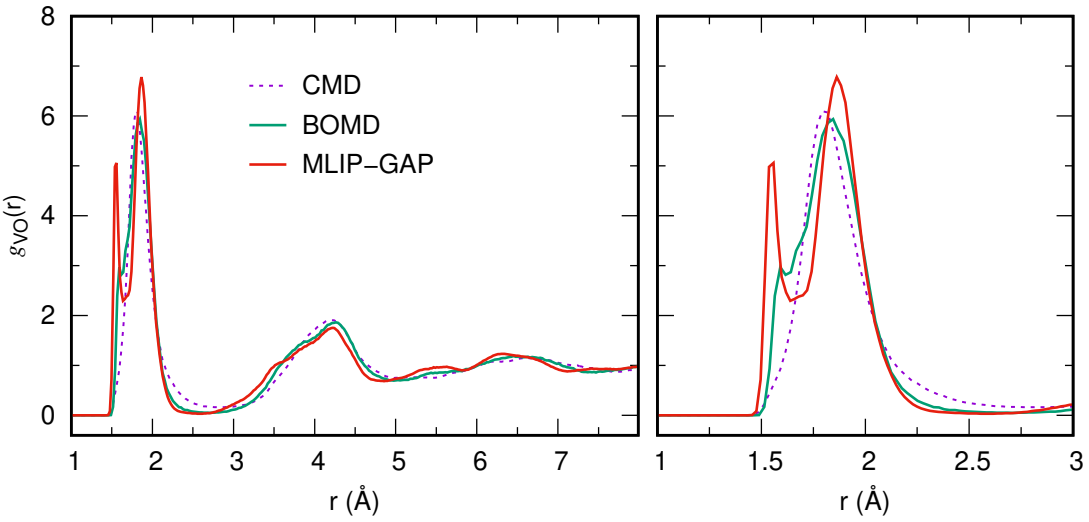

Figure 6.11. Partial pair correlation function $g_{V\text{-}O}$ for VP50 glass at 300 K. The MLIP-GAP, CMD, and BOMD results are compared. With on the right a view of 1–3 Å region highlighting key differences.

To further evaluate the transferability and robustness of our MLIP-GAP model, we applied it to generate glass models for additional NVP compositions, specifically NVP25 and NVP43.
Fig. 6.12 presents the total X-ray and neutron structure factors of NVP25 and NVP43, comparing the CMD, BOMD (as CMD+BO), and MLIP-GAP schemes with experimental data. For the neutron structure factors, we observe good agreement with the BOMD across the entire k-value range. In the X-ray structure factors, the MLIP-generated structure exhibits a slight overestimation of the first peak located at 2 Å for both systems. However, the quantitative agreement with the experiment, as shown in Tab. 6.7 (first row), demonstrates that the MLIP-GAP performance (11.9% and 10.4% for the two systems, respectively) is more consistent with the BOMD (10.1% and 9.8%) within the indicated statistical error margin and the experiment, compared to the CMD (14.4% and 17.1%).

This structural improvement of the MLIP-GAP compared to the CMD is also observed in real space. Fig. 6.13 displays the total X-ray pair distribution function in the 1–4 Åinterval for both systems. The MLIP reproduces the first peak minimum better than the BOMD, emphasizing the importance of a thermal cycle that directly or at least indirectly incorporates electronic contributions in the description of complex glasses. The level of quantitative agreement between the MLIP-GAP and the experiment is similar to the BOMD (see Tab. 6.7, second row).

An important detail to highlight is the V–O pair distribution function (gr_{VO}) presented

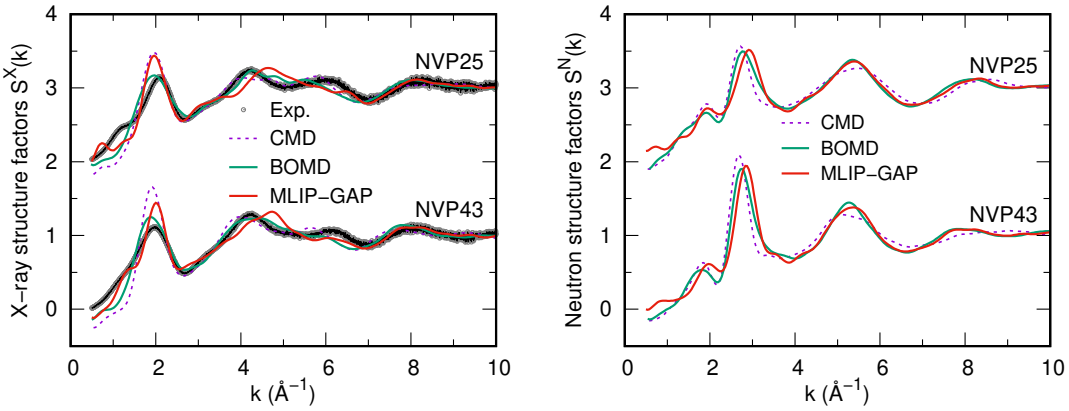

Figure 6.12. Total structure factors for NVP25 and NVP43 glasses obtained from X-ray diffraction (left) and neutron scattering (right). X-ray data includes experimental measurements and simulation results (CMD, BOMD, and MLIP-GAP), while neutron data shows only simulation results.

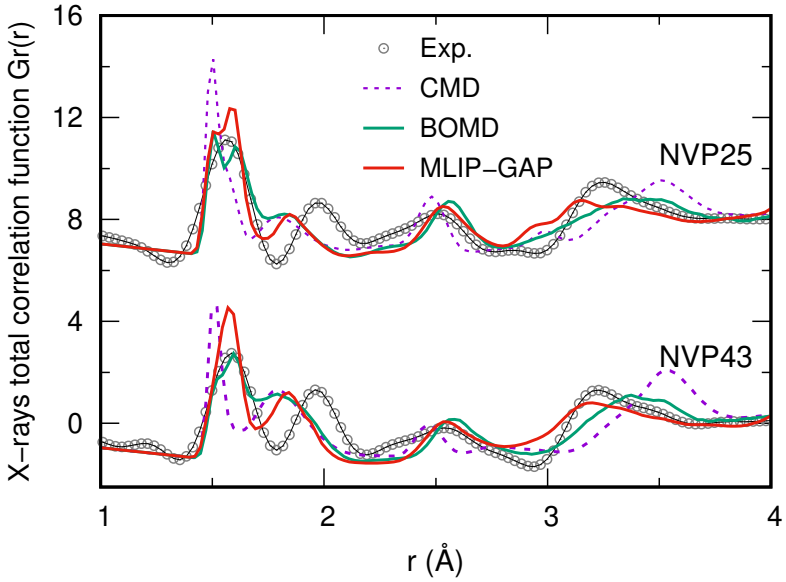

Figure 6.13. Total pair distribution function G(r) of NVP25 and NVP43 glasses at 300 K: Assessment of MLIP-GAP results against CMD, BOMD, and experimental data.

Table 6.7. Comparison of the agreement between CMD, BOMD, and MLIP-GAP simulations and experimental data using goodness-of-fit R_χ parameters for X-ray total structure factor S(k) and pair distribution function G(r) of NVP25 and NVP43 glasses at 300 K.

	NVP25			NVP43		
X-rays	CMD	BOMD	MLIP	CMD	BOMD	MLIP
$R_\chi^{S(k)}$	14.4 ± 0.2	10.1 ± 0.9	11.9 ± 0.6	17.1 ± 1.0	9.8 ± 1.2	10.4 ± 0.7
$R_\chi^{G(r)}$	87.3 ± 2.3	62.9 ± 2.0	62.08 ± 0.3	96.2 ± 3.1	65.0 ± 4.8	70.9 ± 0.9

in Fig. 6.14. The MLIP-GAP result shows a clear split of the first peak, indicating a sharp population at 1.6 Å, completely absent in the CMD and less pronounced in the BOMD, and a broader second peak at approximately 1.8 Å.

Overall, our MLIP-GAP model has demonstrated excellent performance across various VP and NVP systems, including those not involved in the model training (demonstrating

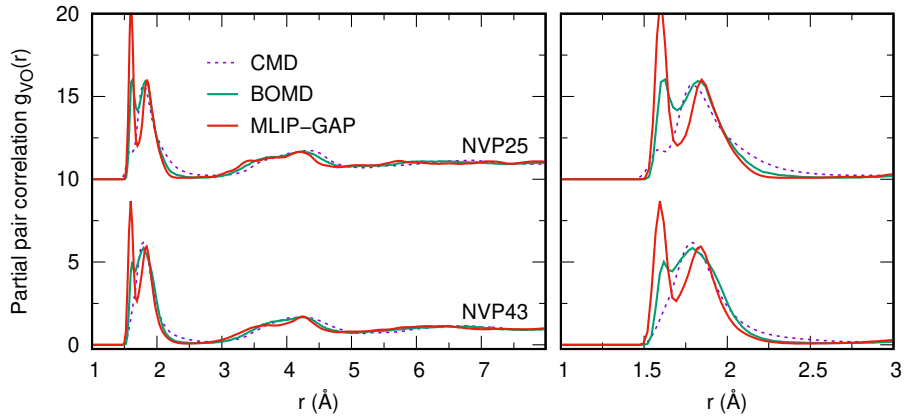

Figure 6.14. Partial pair correlation function $g_{V\text{-}O}$ for NVP25 and NVP43 systems at 300 K, obtained from MLIP-GAP (red line), CMD (dashed line), and BOMD (green line) simulations. The right side magnified a view of 1–3 Å region highlighting key differences.

transferability and reliability). Details previously accessible only through FPMD simulations have been accurately reproduced in both reciprocal and real space, with near quantum mechanical accuracy. The relatively low computational cost of the MLIP allowed us to average our results over three parallel trajectories, enabling a more realistic estimation of statistical error, whereas with full FPMD, the trajectory had to be divided into multiple segments for error estimation. Leveraging this strong performance, further exploration will involve an analysis of dynamical properties, particularly the conductivity of NVP glasses.

6.5 Preliminary results and considerations on ionic conductivity and electronic transport of NVP glasses

Glasses containing transition metal (TM) oxides such as V_xO_y and Fe_xO_y typically exhibit semiconducting behavior, owing to electron/hole hopping among the TM sites having two different oxidation states valences [34, 312–315]. However, when these glasses incorporate alkali oxides like Li_2O and Na_2O, their electrical conductivity undergoes a significant change [316, 317]. As the alkali oxide content increases, the conduction mechanism shifts from purely electronic to mixed ionic-electronic, and eventually to primarily ionic.
The overall electrical conductivity in these systems arises from two main mechanisms as we describe in the introductory Chapter 1, Sec. 1.2.3. The electronic component is due to electron/hole hopping between TM sites with different oxidation states [312, 318], while the ionic conductivity is promoted by the mobility of alkali ions [314–316, 318]. This interplay between electronic and ionic charge carriers has long been a subject of interest in glass science. However, it has experienced a renewed attention in recent years, driven by the potential application of mixed ionic-electronic conductors as cathodes in Li^+- and Na^+-ion batteries, particularly in the context of all-solid-state batteries[319–321]. The transition in charge carrier dominance from electrons/holes to ions is linked to the relative concentrations of TM and alkali ions. Moreover, it is significantly influenced by the interactions between negatively charged electrons and positively charged ions, a phenomenon known as ion-polaron interactions[322, 323]. Understanding and controlling these interactions is crucial for optimizing the electrical properties of these glasses for specific applications. This complex interplay between composition, structure, and charge transport mechanisms offers a rich field for scientific investigation and technological innovation. By tuning the glass composition and structure, it becomes possible to tailor the electrical properties to

meet the specific requirements of various energy storage and conversion devices[324]. Building upon the degree of quantitative agreement with respect to experimental data achieved with BOMD and MLIP-GAP in previous sections, we can now turn the focus to assessing other properties that are crucial for the practical implementation of NVP glasses in energy storage applications. While properties such as charge/discharge capacity and voltage stability are ultimately critical for device performance, our preliminary efforts focus on two fundamental aspects that provide valuable insights into the material's behavior: the dynamical properties of Na^+ ions as primary promoter of ionic conductivity and the electronic contribution to overall electrical conductivity.

6.5.1 Na^+ ions self-diffusion and ionic conductivity

The mobility of Na^+ ions is a key factor in determining the rate capability and power density of NVP-based electrodes[325]. By accurately modeling the dynamics of Na^+ ions within the glass structure, we can predict and potentially optimize the material's ability to facilitate rapid ion transport during charge and discharge cycles. Given the demonstrated efficacy of our BOMD and MLIP-GAP-based computational approach in predicting structural properties, we now aim to evaluate its effectiveness in determining the dynamical properties of Na^+ ions, comparing the results with available experimental data and the CMD approach. The ionic conductivity $\sigma(T)$ of NVP glasses is calculated directly from the mean square displacements and tracer diffusivity of Na^+ ions $D^*_{Na^+}(T)$ according to the Einstein and Nernst–Einstein relations for systems that reach the diffusive regime at a given temperature, by Eq. (6.1) and Eq. (6.2), respectively.

$$D^*_{Na^+}(T) = \lim_{t\to\infty} \frac{1}{N2d} \frac{\partial \langle r^2(t) \rangle}{\partial t} \simeq \frac{\sum_i \langle \Delta \mathbf{R}_i^2 \rangle}{N2dt} \tag{6.1}$$

where d is the dimensionality factor ($d = 3$ for three dimensional systems) and we have dropped the explicit dependence on time in Eq. (6.1) as a result of the infinite t limit. When the diffusive regime is reached, the Arrhenius equation [326] can be used to calculate the activation energy barrier E_a for diffusion (conductivity) by fitting the data of $\log D^*$ ($\log \sigma^*$) *vs.* $1/T$ as:

$$D^*_{Na^+}(T) = D_0 exp\left(-\frac{\Delta E_a}{kT}\right) \tag{6.2}$$

From the tracer diffusivity D^*, the idealized ionic conductivity can be calculated based on the Nernst-Einstein relation:

$$\sigma^* = D^* \frac{Nq^2}{VkT} = \frac{q^2}{2dVkT} \sum_i \left\langle \Delta \mathbf{R}_i^2 \right\rangle \tag{6.3}$$

where V is the total volume of the model system, q is the charge of mobile-ion species, T is temperature, k is the Boltzmann constant.
Fig. 6.15 presents the Arrhenius plots of the logarithmic conductivity of Na^+ as a function of inverse temperature for NVP25/43 systems. As commonly performed in CMD simulations, the diffusion and conductivity values of Na^+ ions are calculated at a temperature of practical interest (300 K – 600 K) by extrapolation from a linear fit of values explicitly computed at higher temperatures [327]. This approach makes it feasible to determine these quantities within a reasonable trajectory time for MD simulations. In our study, we simulated Na^+ diffusion across different temperatures (from 900 K to 1500 K). From these simulations, we calculated the Na^+ ions' mean square displacements and tracer diffusion coefficients, and subsequently the ionic conductivity using Eq. (6.3).
Specifically, we performed these simulations starting from the final glass configuration at 300 K and heated the systems to temperatures ranging from 900 K to 1500 K using

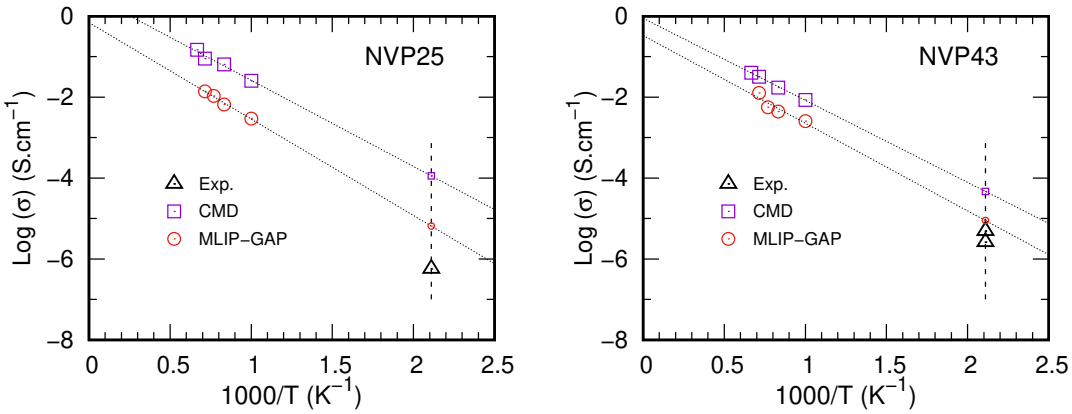

Figure 6.15. Arrhenius plot of logarithmic Na^+ ionic conductivity versus inverse temperature for NVP25 and NVP43 systems simulated by CMD (purple square) and MLIP-GAP (red circle). Extrapolated conductivity values at 473.15 K (as indicated by the black dotted vertical line) are shown for both simulations and compared to experimental data (black triangle) [316, 317] from closer compositions.

the CMD2 potential and our developed MLIP-GAP potential. The systems were maintained at these temperatures under the NVT ensemble until the diffusion regime of Na^+ was reached, for about 1 ns. The calculated ionic conductivities for NVP25 and NVP43 glasses, obtained by extrapolating the Arrhenius plots (Fig.6.15) to 473.15 K, are reported in Tab. 6.8. The data is compared with experimental electrical conductivity values

Table 6.8. Calculated ionic conductivity values of NVP25 and NVP43 glasses at 473.15 K, simulated using CMD and MLIP-GAP. These simulated values are compared with experimental conductivity values reported in the literature. [316–318]

		Ionic conductivity σ ($\times 10^{-2}$ mS/cm)	
Model (% of Na_2O)	Exp. data	CMD	MLIP-GAP
NVP25 (40%)	0.058 [317]	11.35	0.65
NVP43 (28.5%)	0.26–0.49[a] [316, 318]	4.69	0.89

[a]Experimental NVP glass composition: $30Na_2O$-$20V_xO_y$-$50P_2O_5$ [$10V_2O_5$ + $10VO_2$] [316, 318].

obtained for NVP glass compositions with overall similar components for NVP25 and NVP43, with the exact content of Na_2O oxide but different V_xO_y and P_2O_5 contents. For the both systems NVP25 and NVP43, the experimental electrical conductivity is primarily attributed to the ionic conduction from Na^+ ion mobility. Tab. 6.9 displays the activation energies for NVP25 and NVP43, derived from the slopes of the Arrhenius plots of conductivity (Fig. 6.15). The calculated values are lower than their experimental counterparts, explaining the overestimation of electrical conductivity observed in both CMD and MLIP simulations. Notably, the MLIP results exhibit closer agreement with experimental data.

As reported, CMD data significantly overestimates the ionic conductivity of NVP25 and NVP43 by several orders of magnitude. This aligns with the general understanding that CMD simulations, particularly those using two/three-body (CMD2-type) force fields, tend to overestimate Na^+ ion diffusion and conductivity in glass systems [327]. This overestimation can be attributed to several factors, mostly related to a simplified representation of many-body interactions also connected to an overall approximated description of the complex glass network structure and possibly the lack of polarization effects.
On the other hand, the MLIP-GAP potential, while still overestimating ionic conductivity compared to experimental values, provides results much closer to reality. Accordingly

Table 6.9. Calculated activation energy as the slope of Arrhenius plot of the conductivity for NVP25 and NVP43 glasses at 473.15 K, simulated using CMD and MLIP-GAP. These simulated values are compared with experimental conductivity values reported in the literature. [316–318]

		Activation energy E_a (eV)	
Model (% of Na_2O)	Exp. data	CMD	MLIP-GAP
NVP25 (40%)	0.80 [317]	0.18	0.21
NVP43 (28.5%)	0.56[a] [316, 318]	0.17	0.19

[a]Experimental NVP glass composition: $30Na_2O$-$20V_xO_y$-$50P_2O_5$ [$10V_2O_5$ + $10VO_2$] [316, 318].

with previous findings [327, 328], the Na^+ ions dynamical mechanism involves the correlated jump of neighbouring cations inside percolation channels created by non-bridging oxygen (NBO) atoms which are linked to network former ions and waggle to accompany the alkaline jump. Fig. 6.16 depict this scenario from a snapshots of the NVP25 model simulated by MLIP-GAP at 1200 K. This improved performance not only supports the MLIP-GAP's superior ability to describe the structure of NVP glasses but also extends to a more accurate representation of their dynamical properties. The enhanced accuracy of the MLIP-GAP potential can be attributed to its ability to capture more complex interatomic interactions and its data-driven approach, which allows it to implicitly account for many factors that simple CMD potentials struggle to represent. Despite this analysis being preliminary, our findings indicate that the newly developed MLIP-GAP already surpasses the performance of available CMD potentials in describing the dynamical properties of Na^+ ions in NVP glasses. Future work is needed to fully understand the dynamical properties of NVP glasses, including potential collective effects that extend beyond the analysis of conductivity based solely on the tracer diffusivity of Na^+ ions. Nevertheless, this improved description of both structural and dynamical properties underscores the potential of MLIP-GAP in advancing our understanding and prediction of complex glass systems.

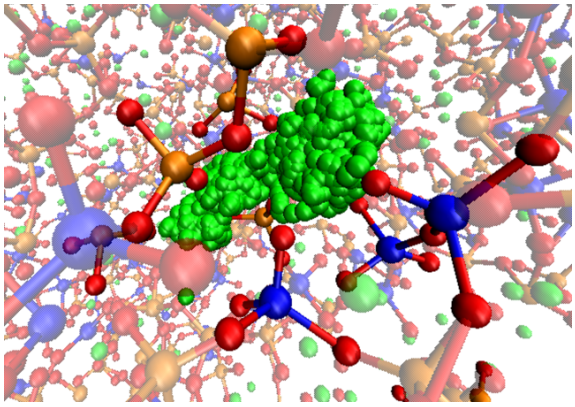

Figure 6.16. Snapshot of a percolation channel created in NVP25 glass by Na^+ ions mostly interacting with neighbouring NBOs, as simulated by MLIP-GAP at 1200 K.

6.5.2 Hopping conductivity

The study of electronic conduction phenomena in transition metal oxide systems has been a relatively active field, witnessing significant advancements in recent years [329–331]. In particular, the small-polaron hopping mechanisms in these systems are now being assessed using techniques such as constrained-DFT (CDFT) methods, where charge/hole hopping between sites is analyzed [332–334]. Among the systems studied in the literature, Ti-, Hf-,

and V-containing crystalline phases have been extensively investigated. However, there is a notable gap in research concerning amorphous systems. Experimental data interpretation often involves approximations to apply theoretical models of small-polaron hopping mechanisms, typically based on the estimated distances between V–V sites through which charge/hole hopping occurs. Often, approximated molecular dynamics or reverse Monte Carlo simulations are employed to estimate these V–V distances [89, 313, 335]. Alternatively, these distances have been otherwise assumed to be homogeneously distributed within the glass network. Typically, within the frame of theoretical interpretation of experimental DC conductivity data, the Mott's model [34, 312] of polaron-conducting glasses is employed to analyse the conductive behaviour of TMO glasses. Such model is typically employed to interpret the Arrhenius-like behaviour of the temperature dependence of DC conductivity of TMO glasses following the relation:

$$\sigma_{DC} = \frac{v_{ph} e^2 C(1-C)}{k_B T R} \exp(-2\alpha R) \exp\left(\frac{-E_{DC}}{k_B T}\right) \tag{6.4}$$

at temperatures higher than $\theta_D/2$, where θ_D is Debye temperature, where the conduction occurs by phonon-assisted hopping of small polarons between nearest localized states [34, 312]. ν_{ph} is the phonon frequency (10^{13} Hz), e the charge of an electron, C the fraction of metal ions in a lower oxidation state, k_B the Boltzmann constant, T the temperature, α the tunneling factor, and E_{DC} the activation energy for DC conduction. In such model, R is the average spacing between TM ions and it is often calculated as homogenously distribution ($R = N^{-1/3}$) or by approximated MD or reverse Monte Carlo simulations.
As shown in Fig. 6.17, the first prominent peak of the V–V partial pair correlation functions obtained in the present work for NVP40A glass occurs at different positions (R) when comparing NVP models obtained by CMD2, fBOMD, and MLIP-GAP (see Tab. 6.10). The MLIP-GAP results align more closely with fBOMD, while CMD data show a clear over-structuring of the pair correlation function. This overestimation is indicative of an over-structuring of the glass network, as thoroughly analyzed in previous sections.
This emphasizes the need for accurate modeling of the structural, bonding, and electronic properties of NVP glasses. Structural information, such as V–V correlations, is often used to theoretically interpret experimental conductivity data. Accurate structural models are essential before explicitly studying the polaron behavior of NVP glasses using advanced techniques like CDFT previously mentioned. Our preliminary results set the groundwork for future research by demonstrating that the developed MLIP-GAP can deliver structural NVP glass models that are nearly as accurate as BOMD and surpass widely used empirical potentials in CMD simulations. This provides a more realistic representation of the structural properties in amorphous transition metal oxide systems, thereby improving our understanding and interpretation of their electronic conduction phenomena.

Table 6.10. Calculated V–V (R) interatomic distance in NVP40A and VP50 glasses models by CMD, BOMD, and MLIP-GAP.

Model	R (Å)	Exp. data	CMD	BOMD	fBOMD	MLIP-GAP
NVP40	R_{peak}	–	3.56	3.51	3.37	3.37
	R_{min}/R_{max}		3.25/4.03	2.99/4.00	2.94/(3.65)4.13	2.67(2.95)/3.70
VP50	R_{peak}	3.56	3.53	3.51	–	3.43
	R_{min}/R_{max}	3.10/3.90	3.20/3.91	3.14/3.84	–/–	3.08/3.73

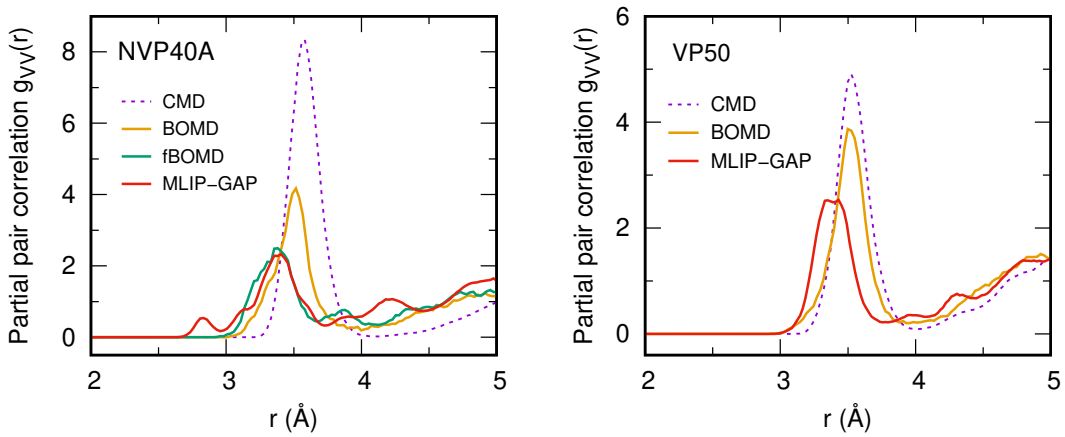

Figure 6.17. Partial pair correlation function $g_{VV}(r)$ computed at CMD, BOMD, and MLIP level for NVP40A (left) and VP50 (right) glasses.

6.6 Conclusive remarks

In this final Chapter, dedicated to the study of (N)VP glasses using a machine learning interatomic potential (MLIP), we first developed a GAP-type MLIP from the two FPMD trajectories of NVP40 glasses produced in Chapter 5. This MLIP-GAP was tested and validated on NVP40 glasses through a detailed comparative study similar to the one conducted in Chapter 5. We thus demonstrated the superiority of MLIP compared to the current empirical interatomic potentials tested.
A study of the transferability of this potential was conducted on ternary NVP glasses not included in the training database and then on the VP50 glass studied in Chapter 4. The results obtained show a good agreement in both reciprocal and real space.
We also performed an electronic analysis of the NVP structures produced by MLIP through post-procedure DFT calculations. The results obtained reveal a structure quite similar to that of BOMD with an accurate speciation of the oxidation levels of the vanadium sites. For example, our MLIP predicted an NVP40A structure with all vanadium in the V^{5+} state, in agreement with expectations.
Furthermore, we conducted a preliminary study of the dynamic properties of NVP glasses with our MLIP. The ionic conductivity of Na^+ ions was studied for NVP25 and 43 systems, and a better agreement was obtained with experimental data compared to the CMD results.
Although this MLIP-GAP potential could be further improved to make it more robust, it shows a prediction very close to quantum mechanics while allowing a significant reduction in calculation time, approximately 1045 times cheaper than BOMD for the example of the NVP40 system with 396 atoms (See Appendix A.1.2, for a comparison of computational cost BOMD *vs* MLIP.)

Chapter 7

General conclusions and perspectives

7.1 General conclusions

In this thesis, we focused on the study of glassy materials for their potential application in energy storage devices, particularly sodium-ion batteries. Glassy and glass-ceramic systems, a family of polyanionic compounds, are emerging as an innovative solution for second-generation solid-state batteries due to their simplicity of design, relatively low production cost, low environmental impact, and safety. This work focused on sodium-vanadium-phosphorus (NVP) oxides systems, for which we conducted a detailed study to shed more light on their structure, bonding, and electronic and magnetic properties. To conduct this study, we relied on atomic-scale modeling tools detailed in Chapter 2 of this thesis. Our approach consisted of first employing classical MD based on empirical force fields which does not take into account the electronic description, then a hybrid method combining long CMD complemented by short first-principles molecular dynamics to incorporate the electronic contribution in the description of these systems. We also employed a more computationally expensive approach based entirely on FPMD, and finally, an approach integrating artificial intelligence. This last approach consisted of performing classical dynamics with a machine learning interatomic potential developed on DFT observable calculated on trajectories produced by FPMD. These four approaches were thoroughly applied to the study of different NVP systems, and the results obtained and presented in Chapters 3-6 are summarized below.

In Chapter 3, we validated the MLIP methodology on a binary system as study case: l-$GeSe_2$, a disordered chalcogenide with available CPMD trajectories from the team and in literature. Our primary aim was to address a persistent discrepancy between FPMD calculations and experimental partial structure factors by examining potential size effects on the structural properties of liquid $GeSe_2$. Our comprehensive study of l-$GeSe_2$ with MLIP-GAP confirmed its capability to accurately model disordered systems with covalent and ionocovalent bonds, achieving FPMD-level accuracy and improving our understanding of their structural properties. Our results corroborated the complexity of Ge's atomic environment as revealed by FPMD. Consequently, we investigated potential size effects on l-$GeSe_2$'s structure, observing an enhancement of the S_{GeGe} first peak intensity but negligible effects on the S_{CC} partial structure factor. By modeling up to four replicas of systems exceeding a million atoms, we found an FSDP intensity enhancement in the Ge–Ge structure factor, which did not affect much the FSDP intensity of the S_{CC} structure factor. This suggests a negligible size effect on the structural properties of l-$GeSe_2$ across various model sizes. Our MLIP-GAP model significantly advanced our understanding of l-$GeSe_2$'s structural characteristics and the potential size effect on describing this system with a complex Ge environment. This initial MLIP study provides a foundation for investigating more complex systems, such as NVP materials.

In Chapter 4, we initiated our investigation of oxide systems by focusing on a vanadophosphate (VP) glass system made of 50%-50% of vanadium oxide and phosphorus oxide, respectively. We conducted a detailed exploration of its structural, bonding, and electronic properties, starting by evaluating the performance of three different empirical CMD force fields. Through in-depth comparison with BOMD simulations and experimental data, we demonstrated BOMD's effectiveness in addressing CMD's shortcomings, achieving a significantly improved quantitative description of VP50 glass structures. BOMD enabled unprecedented agreement with experimental data in both reciprocal space (neutron and X-ray structure factors) and real space (total pair correlation functions) properties. The key improvement stems from a superior description of the local electronic and bonding environment around P and, especially, V sites, unattainable with empirical force fields. BOMD revealed clear signatures of single V–O and double V=O bonds, along with a more accurate description of the VO_n coordinating polyhedra distribution that forms the glass network. We enriched our study with a comprehensive analysis of bond angle distributions around VO_n units, order parameter, network connectivity, and local bonding features based on Wannier functions formalism. Additionally, we assessed which CMD scheme aligns more closely with BOMD and experimental data, finding that including three-body potential parameters associated with the local environment of V sites significantly improves CMD performance. However, even with this enhancement, CMD still falls short of BOMD's accuracy in describing V_xO_y–P_2O_5 glass. Based on the V sites speciation, our calculation indicate a chemical composition corresponding to $50V_xO_y[31.6V_2O_5–18.0V_2O_4–0.4V_2O_3]–50P_2O_5$ in contrast with the commonly referred composition $50V_2O_5–50P_2O_5$, typically reported in the literature [53, 272]. Collectively, our results establish the computational foundation for a deep understanding of VP amorphous glasses, outlining the requirements for developing interatomic potentials that enable quantitative comprehension and design of VP-based amorphous materials.

In Chapter 5 focusing on ternary systems, we explored the structural, bonding, and electronic properties of Na_2O-V_xO_y-P_2O_5 (NVP) glasses using three different computational approaches. The limitations of empirical force fields, assessed as the most suitable in Chapter 4, were highlighted, and we showcased the improvements brought by FPMD, initially through a short post-equilibration at 300 K with BOMD of the structure simulated

by CMD, and more thoroughly through a complete thermal cycle study with full BOMD. The results obtained reveal that classical force fields are limited in accurately modeling the local environment of vanadium in NVP glasses, often approximating their short-range order. In contrast, FPMD significantly enhances the accuracy of these models, particularly in distinguishing V–O interactions and oxidation states. A significant advancement emerging from our study is the demonstration that an FPMD thermal cycle offers superior structural details compared to CMD and even CMD followed by a short BOMD equilibration. The short BOMD method provides intermediate results, better than CMD alone, but not as accurate as a complete FPMD cycle. FPMD simulations enable accurate distinction between single V–O bonds and double V=O bonds through a detailed description of the local vanadium environment. This leads to a well-defined short-range V–O polyhedral environment, crucial for understanding the functional properties of NVP glasses. Comparison with experimental data in both reciprocal and real space confirms the superiority of FPMD in accurately determining V oxidation states and provides a reliable representation of local electronic environments, as well as the local structure around phosphorus and vanadium sites. This comprehensive analysis underscores the necessity of advanced computational methods for accurately modeling the complex structures of NVP glasses.
With this superiority of the BOMD method in determining the properties of complex glasses such as NVP systems, the path is paved for future research, particularly the development of machine learning-enhanced interatomic potentials, shedding more light on the design of more realistic models of NVP-based materials for technological energy storage applications.

In Chapter 6, we developed a machine learning interatomic potential (MLIP) within the GAP framework to investigate (N)VP systems. This MLIP demonstrated accuracy comparable to FPMD in predicting structural properties of these materials. The electronic properties, obtained as post-processing to the charge density with the MLIP-GAP, align well with FPMD results and enable speciation of V oxidation states, leading to accurate chemical compositions. This advancement in MLIP development for NVP glasses provides a valuable tool for exploring complex material behaviors with greater efficiency and accuracy.

7.2 Future perspectives and directions

7.2.1 Assessing electronic transport of application-relevant NVP glasses using FPMD and CDFT

This thesis has made a significant advancement in the quantitative description of NVP glass structures and local environments, advancing beyond previous models. While a comprehensive structural analysis based on the varying oxidation states of V sites in NVP glasses remains to be fully explored (as was done for VP50 glass in this work), the groundwork has been laid for future investigations. The combination of improved structural models and access to electronic structure data through FPMD/BOMD schemes now paves the way for a deeper understanding of electronic transport in NVP glass systems. This advancement is particularly crucial given the pivotal role of electronic transport in determining the performance of these materials in energy applications. Moving forward, the integration of structural insights with electronic properties promises to unlock new avenues for optimizing NVP glasses for specific energy-related uses. While current understanding has been largely based on macroscopic conductivity data interpreted through the lens of Mott's small polaron hopping model [34, 312], this approach has shown limitations in accurately predicting and explaining observed phenomena.

A promising avenue for advancement lies in revisiting this theoretical framework with more realistic structural information. By leveraging BOMD and MLIP, we can obtain more accurate representations of polaron site distances and local environments. This refined structural data, when incorporated into the traditional Mott model, has the potential to improve theoretical predictions with experimental observations, particularly in terms of temperature-dependent conductivity behavior. However, the true leap forward in understanding these systems comes from the application of Constrained Density Functional Theory (CDFT) to explicitly characterize polaron features and transport mechanisms [333, 334, 336]. CDFT allows for a detailed examination of polaron properties, including their spatial extent, formation energies, and coupling to local lattice distortions, nowadays largely applied to crystalline system but not yet to amorphous systems. By using structural models derived from BOMD and MLIP simulations, we can map out the V_xO_y polyhedra local environment landscape and its influence on polaron formation and transport.
This approach enables the identification of preferential sites for polaron localization and provides insights into the dynamics of polaron transport [330]. The detailed analysis of polaron mobility and its dependence on local structure promises to unveil the intricate relationships between atomic-scale structure and macroscopic transport properties in NVP glasses for energy storage applications. This perspective outlines a path towards a more comprehensive and accurate theoretical treatment of electronic conductivity in NVP glass systems. By combining this knowledge with the assessment of ionic conductivity performance of NVP glasses derived from MD (BOMD and MLIP), we stand to gain unprecedented insights into the fundamental mechanisms of charge transport in these important materials. This enhanced understanding has the potential to significantly impact the development of next-generation energy storage materials.

7.2.2 Advancing MLIP development: Implementing active learning and automated strategies for minimal training set generation and optimization

The development of MLIP for amorphous systems has, in general, improved our ability to model complex amorphous materials as presented in this thesis for $GeSe_2$ and VP/NVP systems, bridging the gap between the accuracy of first-principles methods and the efficiency required for large-scale and longer-scale simulations. However, the process of generating and optimizing these potentials often relies heavily on human intuition and manual intervention, potentially introducing biases and requiring computational overly-workloads. This perspective explores the promising direction of implementing active learning (AL) and automated strategies to enhance MLIP development, with a particular focus on minimizing the training set size while maximizing potential accuracy and transferability. AL approaches offer a paradigm shift in how we construct MLIPs. By intelligently selecting the most informative configurations for training from a given DB, these methods can dramatically reduce the amount of high-quality reference data needed. This is particularly crucial for complex systems like NVP glasses, where generating ab initio data is computationally expensive. Our preliminary efforts int his direction follows a two-fold strategies. On one side, we are testing the AL algorithm based on the strategies proposed by Deringer et al. [337] and Milardovich et al. [338, 339]. This AL approach improved the training dataset by adding configurations from MD simulations, each driven by newly developed GAP. With each iteration, a new GAP potential was created. We then selected and recalculated the energies, forces, and virials at DFT level of new configurations from novel classical MD trajectory, incorporating this data into the training datasets. This approach is showing great promise in reducing possible unphysical atomic clustering at

high temperatures. On the other side, we are also testing the innovative AL scheme based integrating Bayesian Optimization (BO) to dynamically optimize the MLIP-GAP hyperparameters proposed by Sivaraman et al. [311]. This AL strategy allows minimizing the MAE of GAP-predicted energies using an initially defined testing dataset and allows to minimized the effect of DB building by human bias.
Looking forwards, prioritize developing robust metrics to evaluate the performance, robustness [170, 340], and transferability of MLIPs will be crucial. Incorporating prior physical knowledge into automated MLIP processes will also be a key point. These advancements in MLIP development to have broad implications. For NVP glasses and similar complex materials, improved MLIP potentials will facilitate more extensive simulations, yielding deeper insights into structure-property relationships. Furthermore, the methodologies presented here have the potential to be generalized, accelerating materials discovery and optimization across diverse applications.

7.2.3 From NVP glasses to engineered glass-ceramics: designing next-generation energy storage materials

The frontier of energy storage materials is continually advancing, and a promising direction lies in the development of engineered glass-ceramics derived from NVP glass systems. This perspective explores the potential of bridging the gap between glassy and crystalline materials, combining the structural flexibility and ease of synthesis characteristic of glasses with the superior conductivity and mechanical robustness of crystalline materials. Such an approach holds immense promise for designing next-generation cathode materials for energy storage applications [341, 342]. Our preliminary work has been focused first on extending our MLIP modeling to larger NVP glass systems, pushing the boundaries to systems of up to 3168 atoms. This scaling-up is crucial for tentatively assess and capture the full complexity of these materials and improving the quantitative agreement between our MLIP, BOMD, and experimental data. The refinement of MLIPs for these larger systems will provide a solid foundation for exploring more complex structures and interfaces (see Fig.7.1).

The primary direction of our future work lies in the exploration of glass-crystal interfaces, which form the core of glass-ceramic materials. Our preliminary investigations have focused on the interface between NVP33 glass and $NaVOPO_4$ crystalline materials. This choice is motivated by the observation in lithium oxide containing similar parent glasses [50, 51] serves as an ideal precursor for the crystalline glass-ceramic, exhibiting promising conductivity and charge/discharge performance for energy storage applications. Our initial studies have centered on an interface model comprising about 700 atoms, combining NVP33 glass and $NaVOPO_4$ crystal structures (Fig. 7.2)[1]. We've tested the capabilities of CMD2, MLIP, and BOMD in describing this complex interface. A key aspect of this work has been the evaluation and improvement of our CMD2 and MLIP potential to accurately represent both the crystalline and glassy phases. Additionally, we've made strides in refining our MLIP-GAP model by incorporating a small set of defected $NaVOPO_4$ crystal models into the training set. While the results are promising, further refinement is needed to fully capture the complexities of these interfaces.
Looking ahead, our research will drive deeper into the structural, bonding, and Na^+ conductivity properties of these glass-crystal interfaces. We plan to expand our investigations to other crystalline phases that have shown promise in experimental collaborations, such as $Na_2V_3P_2O_{13}$ and $Na_3V_2(PO_4)_3$ systems. This broader exploration will provide a more

[1]Interface model under study within the present PhD thesis and the M2 internship project (2024) of A. Familiari, an Erasmus+ M2 candidate from the University of Modena and Reggio Emilia (Italy), with whom I closely collaborated during the final months of this PhD thesis.

comprehensive understanding of the potential glass-ceramic compositions and their properties. The ultimate goal of this research direction is to engineer glass-ceramic materials that optimize the beneficial properties of both glassy and crystalline phases. By fine-tuning the interface between these phases, we aim to enhance ionic conductivity, improve mechanical stability, and optimize charge/discharge characteristics. This approach could lead to the development of cathode materials with superior performance for next-generation energy storage devices.

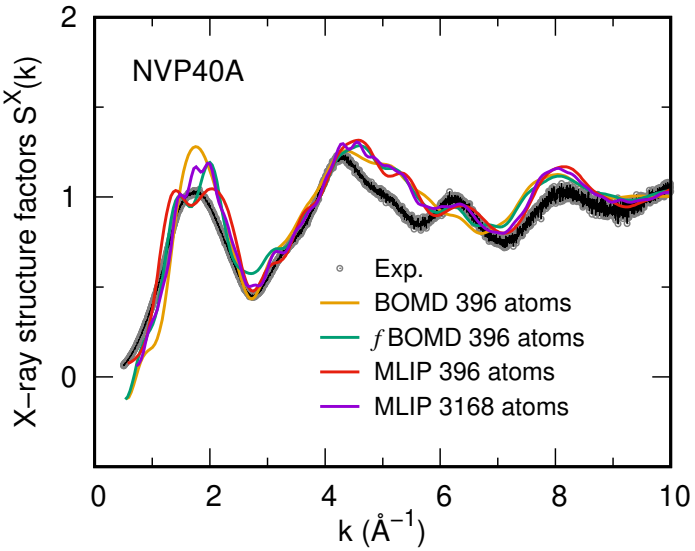

Figure 7.1. X-ray structure factor comparing two MLIP NVP40A models (396 atoms and 3168 atoms) alongside BOMD data and experimental results.

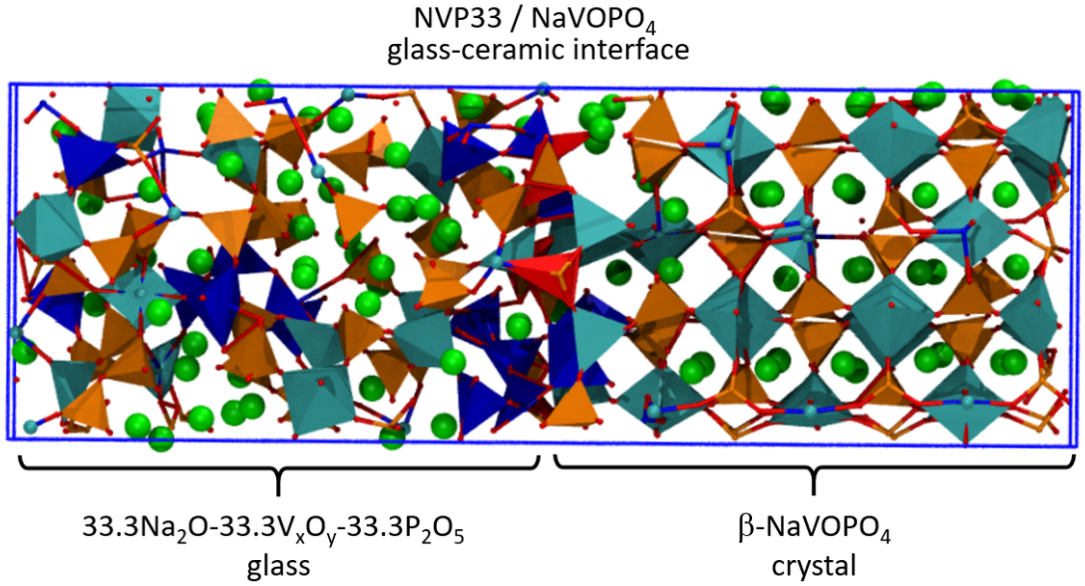

Figure 7.2. Snapshot of the NVP33/$NaVOPO_4$ glass-ceramic interface current under study by atomistic modeling as perspective work of the present PhD thesis (Colors legend: Na, green; P, orange; O, red; V^{5+}, blue; and V^{4+}, light blue).

Appendix

A.1 Computational workload and cost

A.1.1 CPMD simulation (cpmd code v4.3)

System size = 240 atoms
Simulation cell = $(19.76)^3$ Å^3.
Integration time step = 0.012 fs (5 a.u.)
Number of cores = 168 (24 MPI*7OMP) on a Linux HPC Intel
Time for one iteration = 1.28 s
Cost for one step = 1*168*1.28 = 0.0597 h/mpc (hours/mono-processor)
Time for to produce 100 ps trajectory = 497777.78 h/mpc
HPC center = Pole HPC ÉquipeMeso of the University of Strasbourg.

A.1.2 CMD simulations, MLIP-GAP with LAMMPS

Table A.1. Computational cost for CMD with MLIP-GAP potential on LAMMPS for $GeSe_2$ and NVP systems.

	$GeSe_2$		NVP40	
System size (atoms)	240	1179120	396	3168
Cubic box length (Å)	19.76	355.92	17.64	35.29
Integration time step (fs)	1	1	1	1
Number of cores (CPU)	168	504	168	336
Time for one iteration (s)	0.0682	35.5001	0.5376	1.302
Cost for 100 step (h/mpc)	0.32	497.00	2.51	12.15
Cost for 100 ps (h/mpc)	318.3	497001.0	2510.0	12520.0
Linux HPC cluster Intel Cascade Lake with Mellanox Infiniband 100 Gbp Pole HPC ÉquipeMeso of the University of Strasbourg				

A.1.3 BOMD simulations (CP2K)

Table A.2. Computational cost for BOMD simulations of NVP40 systems with CP2K package.

	NVP40A	NVP40B
System size (atoms)	396	388
Cubic box length (Å)	17.64	17.95
Integration time step (fs)	1	1
Number of cores (CPU)	320	320
Time for one iteration (s)	295.445	437.393
Cost for one step (h/mpc)	26.262	38.879
Cost for 60 ps (h/mpc)	1575706.67	2332762.67
Cluster: HPE SGI 8600 14PF Jean Zay platform		
HPC center: Jean Zay, IDRIS – GENCI, Paris		

A.2 Two and three body parameters for CMD

Table A.3. Atomic charge of different atoms used in classical MD simulations of VP50 glass.

Elements	Na^+	V^{4+}	V^{5+}	P	O
Charges	0.6	2.4	3.0	3.0	-1.2

Table A.4. Parameters used for BMP-shrm potential (FF1 and FF2), from ref. [80, 87, 88, 108].

Morse parameters				
Pairs	D_{ij}(eV)	r^0(Å)	a_{ij}(Å^{-2})	B_{ij}(eV Å^{12})
Na–O	0.023363	3.006315	1.763867	1.0
O–O	0.042395	3.618701	1.379316	100.0
P–O	0.831326	1.790790	2.585833	1.0
V^{4+}–O	0.032832	2.663618	2.109308	1.0
V^{5+}–O	0.021911	3.398507	1.495955	1.0
Buckingham parameters				
	A_{ij}(eV)		ρ_{ij}(Å^{-2})	
P–P	5.093669		0.905598	
Three-body screened harmonic parameters				
Triplets	K_{ijk}(eV rad^{-2})		θ_0(deg)	ρ (Å)
P–O–P	65.0		109.47	1.0
P–O–V	120.0		109.00	1.0
V–O–V	30.0		109.00	1.0

Table A.5. Parameters used for FF3, from ref. [32, 59].

Pairs	A_{ij}(eV)	ρ_{ij} (Å)	C_{ij}(eVÅ^6)	r^s_{ij}(Å)	B_{ij}(eVÅ^n)	D_{ij}(eV Å^{-2})	n_{ij}
O–O	2029.2204	0.3436	192.580	1.906	46.339	-0.328	3.424
P–O	26655.4720	0.1820	86.856	1.169	28.566	-3.406	4.636
V^{4+}–O	6199.7311	0.2152	25.516	1.093	39.879	-5.599	3.065
V^{5+}–O	23300.0000	0.1799	8.649	0.684	255.295	-229.2793	2.314

A.3 Hyper parameters for MLIP-GAP fitting for NVP and $GeSe_2$ systems

Table A.6. Summary of MLIP-GAP potential fitting hyperparameters: Descriptions and optimized values.

Hyper-parameters	**Descriptions**	**Values**		
Two-body descriptor		**$GeSe_2$**	**NVP-v1**	**NVP-v2**
cutoff	Cutoff distance in kernel in Å	2.5	5.0	6.0
n_sparse	Number of representative points	20	50	80
delta	Scaling of kernel per atom pair (in eV)	0.1	1.0	0.4
theta_uniform	Length scale in Gaussian kernel (in Å)	1.0	1.0	1.0
covariance_type	Form of kernel	ard_se		
sparse_method	Choice of representative points	uniform grid		
Many-body SOAP descriptor		**$GeSe_2$**	**NVP-v1**	**NVP-v2**
cutoff	Cutoff distance in the kernel (in Å)	4.5	5.0	5.0
n_max & l_max	Number of radial and angular basis functions	6 & 8	5 & 8	5 & 8
atom_sigma	Gaussian smearing width of atom density (in Å)	0.7	0.5	0.5
cutoff_transition_width	Distance over which the kernel is smoothly reduced to 0	1.0	1.0	1.0
n_sparse	Number of representative points	2500	2676	3600
delta	Scaling of kernel, per descriptor (in eV)	1.0	0.2	0.2
zeta	Power of the kernel	4	4	4
default_sigma	Default regularisation for: energy, force, virial	{0.001 0.05 0.05}	{0.01 0.02 0.02}	{0.01 0.05 0.02}
sparse_jitter	Extra diagonal regulariser	10^{-12}	10^{-10}	10^{-10}
sparse_method	Choice of representative points	cur_points		

Bibliography

[1] S.K. Sapra, J. Pati, P.K. Dwivedi, S. Basu, J.K. Chang, and R.S. Dhaka. A comprehensive review on recent advances of polyanionic cathode materials in na-ion batteries for cost effective energy storage applications. *Wiley Interdiscip. Rev.: Energy Environ.*, 10(5):e400, 2021.

[2] D. Kundu, E. Talaie, V. Duffort, and L.F. Nazar. The emerging chemistry of sodium ion batteries for electrochemical energy storage. *Angew. Chem. Int. Ed.*, 54(11):3431–3448, 2015.

[3] J.L. Bredas, J.M. Buriak, F. Caruso, K.S. Choi, B.A. Korgel, M.R. Palacin, K. Persson, E. Reichmanis, F. Schuth, R. Seshadri, et al. An electrifying choice for the 2019 chemistry Nobel Prize: Goodenough, Whittingham, and Yoshino, 2019.

[4] H. Zhang. *Polyanionic cathode materials for sodium-ion batteries*. PhD thesis, Dissertation, Karlsruhe, Karlsruher Institut für Technologie (KIT), 2018, 2019.

[5] G. Haxel. *Rare earth elements: critical resources for high technology*, volume 87. US Department of the Interior, US Geological Survey, 2002.

[6] S.P. Ong, V.L. Chevrier, G. Hautier, A. Jain, C. Moore, S. Kim, X. Ma, and G. Ceder. Voltage, stability and diffusion barrier differences between sodium-ion and lithium-ion intercalation materials. *Energy Environ. Sci.*, 4(9):3680–3688, 2011.

[7] M. Sawicki and L.L. Shaw. Advances and challenges of sodium ion batteries as post lithium ion batteries. *RSC Advances*, 5(65):53129–53154, 2015.

[8] R. Usiskin, Y. Lu, J. Popovic, M. Law, P. Balaya, Y.S. Hu, and J. Maier. Fundamentals, status and promise of sodium-based batteries. *Nat. Rev. Mater.*, 6(11):1020–1035, 2021.

[9] X. Liang, L. Wang, X. Wu, X. Feng, Q. Wu, Y. Sun, H. Xiang, and J. Wang. Solid-state electrolytes for solid-state lithium-sulfur batteries: Comparisons, advances and prospects. *J. Energy Chem.*, 73:370–386, 2022.

[10] A. Machín, C. Morant, and F. Márquez. Advancements and challenges in solid-state battery technology: An in-depth review of solid electrolytes and anode innovations. *Batteries*, 10(1):29, 2024.

[11] L. Ma, Y. Dong, N. Li, W. Yan, S. Ma, Y. Fang, Y. Li, L. Xu, C. Liu, S. Chen, et al. Current challenges and progress in anode/electrolyte interfaces of all-solid-state lithium batteries. *eTransportation*, page 100312, 2024.

[12] B. Sayahpour, H. Hirsh, S. Parab, L.H.B. Nguyen, M. Zhang, and Y.S. Meng. Perspective: Design of cathode materials for sustainable sodium-ion batteries. *MRS Energy Sustain.*, 9(2):183–197, 2022.

[13] M.S. Whittingham. Electrointercalation in transition-metal disulphides. *J. Chem. Soc., Chem. Commun.*, (9):328–329, 1974.

[14] M.S. Whittingham. Lithium batteries and cathode materials. *Chem. Rev.*, 104(10):4271–4302, 2004.

[15] M. Li, J. Lu, Z. Chen, and K. Amine. 30 years of lithium-ion batteries. *Adv. Mater.*, 30(33):1800561, 2018.

[16] C. Masquelier and L. Croguennec. Polyanionic (phosphates, silicates, sulfates) frameworks as electrode materials for rechargeable Li (or Na) batteries. *Chem. Rev.*, 113(8):6552–6591, 2013.

[17] K.J.P.C. Mizushima, P.C. Jones, P.J. Wiseman, and J.B. Goodenough. Li_xCoO_2 $(0 < x < -1)$: A new cathode material for batteries of high energy density. *Mater. Res. Bull.*, 15(6):783–789, 1980.

[18] V. Palomares, P. Serras, I. Villaluenga, K.B. Hueso, J. Carretero-Gon.zález, and T. Rojo. Na-ion batteries, recent advances and present challenges to become low cost energy storage systems. *Energy Environ. Sci.*, 5(3):5884–5901, 2012.

[19] C. Xu, J. Zhao, C. Yang, and Y.S. Hu. Polyanionic cathode materials for practical Na-ion batteries toward high energy density and long cycle life. *ACS Cent. Sci.*, 9(9):1721–1736, 2023.

[20] J. Xiao, F. Zhang, K. Tang, X. Li, D. Wang, Y. Wang, H. Liu, M. Wu, and G. Wang. Rational design of a P2-type spherical layered oxide cathode for high-performance sodium-ion batteries. *ACS Cent. Sci.*, 5(12):1937–1945, 2019.

[21] R. Liu, Z. Liang, Z. Gong, and Y. Yang. Research progress in multielectron reactions in polyanionic materials for sodium-ion batteries. *Small Methods*, 3(4):1800221, 2019.

[22] H.Y. Shi, Z. Jia, W. Wu, X. Zhang, X.X. Liu, and X. Sun. The development of vanadyl phosphate cathode materials for energy storage systems: a review. *Chem. - Eur. J.*, 26(37):8190–8204, 2020.

[23] J.B. Goodenough, H.P. Hong, and J.A. Kafalas. Fast Na^+-ion transport in skeleton structures. *Mater. Res. Bull.*, 11(2):203–220, 1976.

[24] Q. Ni, Y. Bai, F. Wu, and C. Wu. Polyanion-type electrode materials for sodium-ion batteries. *Adv. Sci.*, 4(3):1600275, 2017.

[25] H. Zhang, I. Hasa, B. Qin, T. Diemant, D. Buchholz, R.J. Behm, and S. Passerini. Excellent cycling stability and superior rate capability of $Na_3V_2(PO_4)_3$ cathodes enabled by nitrogen-doped carbon interpenetration for sodium-ion batteries. *ChemElectroChem*, 4(5):1256–1263, 2017.

[26] Q. Wang, Q. Wang, M. Zhang, B. Han, C. Zhou, Y. Chen, and G. Lv. A first-principles investigation of the influence of polyanionic boron doping on the stability and electrochemical behavior of $Na_3V_2(PO_4)_3$. *J. Mol. Model.*, 25:1–7, 2019.

[27] C. Zhu, K. Song, P.A. Van Aken, J. Maier, and Y. Yu. Carbon-coated Na_3V_2 $(PO_4)_3$ embedded in porous carbon matrix: an ultrafast Na-storage cathode with the potential of outperforming Li cathodes. *Nano Lett.*, 14(4):2175–2180, 2014.

[28] R. Tripathi, G.R. Gardiner, M.S. Islam, and L.F. Nazar. Alkali-ion conduction paths in $LiFeSO_4F$ and $NaFeSO_4F$ tavorite-type cathode materials. *Chem. Mater.*, 23(8):2278–2284, 2011.

[29] Y. Chen, Y. Zhao, F. Liu, M. Ding, J. Wang, J. Jiang, P. Boulet, and M.C. Record. Structural and electrochemical properties of Li_2O-V_2O_5-B_2O_3-Bi_2O_3 glass and glass-ceramic cathodes for lithium-ion batteries. *Molecules*, 28(1):229, 2022.

[30] H. Yamauchi, J. Ikejiri, K. Tsunoda, A. Tanaka, F. Sato, T. Honma, and T. Komatsu. Enhanced rate capabilities in a glass-ceramic-derived sodium all-solid-state battery. *Sci. Rep.*, 10(1):9453, 2020.

[31] S. Gandi, V.S.C.S. Vaddadi, S.S.S. Panda, N.K. Goona, S.R. Parne, M. Lakavat, and A. Bhaumik. Recent progress in the development of glass and glass-ceramic cathode/solid electrolyte materials for next-generation high capacity all-solid-state sodium-ion batteries: A review. *J. Power Sources*, 521:230930, 2022.

[32] J. Du, M. Montorsi, S. Barbi, and X. Lu. Rare earth and transition metal containing glasses. *Atomistic Simulations of Glasses: Fundamentals and Applications*, pages 367–438, 2022.

[33] S. Siriroj, J. Padchasri, A. Montreeuppathum, J. Lomon, N. Chanlek, Y. Poo-arporn, P. Songsiriritthigul, S. Pinitsoontorn, S. Rujirawat, and P. Kidkhunthod. New glass cathode materials for Li-ion battery: Ni-Co doping in Li-BO based glass. *Mater. Sci. Energy Technol.*, 6:554–560, 2023.

[34] N.F. Mott. Conduction in glasses containing transition metal ions. *J. Non-Cryst. Solids*, 1(1):1–17, 1968.

[35] B. Roling and K. Funke. Polaronic transport in vanadium phosphate glasses. *J. Non-Cryst. Solids*, 212(1):1–10, 1997.

[36] G. Tricot, L. Montagne, L. Delevoye, G. Palavit, and V. Kostoj. Redox and structure of sodium-vanadophosphate glasses. *J. Non-Cryst. Solids*, 345:56–60, 2004.

[37] S. Nakata, T. Togashi, T. Honma, and T. Komatsu. Cathode properties of sodium iron phosphate glass for sodium ion batteries. *J. Non-Cryst. Solids*, 450:109–115, 2016.

[38] M. Tanabe, T. Honma, and T. Komatsu. Unique crystallization behavior of sodium manganese pyrophosphate $Na_2MnP_2O_7$ glass and its electrochemical properties. *J. Asian Ceram. Soc.*, 5(2):209–215, 2017.

[39] T. Honma, T. Togashi, N. Ito, and T. Komatsu. Fabrication of Na_2FeP_{27} glass-ceramics for sodium ion battery. *J. Ceram. Soc. Jpn.*, 120(1404):344–346, 2012.

[40] T. Honma, A. Sato, N. Ito, T. Togashi, K. Shinozaki, and T. Komatsu. Crystallization behavior of sodium iron phosphate glass $Na_{2-x}Fe_{1+0.5x}P_2O_7$ for sodium ion batteries. *J. Non-Cryst. Solids*, 404:26–31, 2014.

[41] G. Suman, C.S. Rao, P.K. Ojha, M.S.S. Babu, and R.B. Rao. Mixed polyanion $NaCo_{1-x}(VO)_xPO_4$ glass–ceramic cathode: role of 'Co' on structural behaviour and electrochemical performance. *J. Mater. Sci.*, 52:5038–5047, 2017.

[42] M. Tanabe, T. Honma, and T. Komatsu. Crystallization behavior and electrochemical properties of $Na_2Fe_yMn_{1-y}P_2O_7$ glass. *J. Non-Cryst. Solids*, 501:153–158, 2018.

[43] Y. Ji, T. Honma, and T. Komatsu. Crystallization of the $Na_2Fe_xNi_{1-x}P_2O_7$ glass and ability of cathode for sodium-ion batteries. *Front. Mater.*, 7:34, 2020.

[44] S. Gandi, V.K. Katta, D.P. Dutta, and B.R. Ravuri. A mixed polyanion $NaFe_{1-x}(VO)_xPO_4$ glass-ceramic cathode system for safe and large-scale economic Na-ion battery applications. *New J. Chem.*, 44(7):2897–2906, 2020.

[45] V.K. Katta, S. Gandi, N.K. Katari, W. Mekprasart, W. Pecharapa, D.P. Dutta, and B.R. Ravuri. Mixed polyanion Na-Mn-V-P glass–ceramic cathode network: improved electrochemical performance and stability. *Energy Technol.*, 9(2):2000845, 2021.

[46] M. Sayer, A. Mansingh, J.M. Reyes, and G. Rosenblatt. Polaronic hopping conduction in vanadium phosphate glasses. *J. Appl. Phys.*, 42(7):2857–2864, 1971.

[47] G.S. Linsley, A.E. Owen, and F.M. Hayatee. Electronic conduction in vanadium phosphate glasses. *J. Non-Cryst. Solids*, 4:208–219, 1970.

[48] Monia Montorsi, Giulia Broglia, and Consuelo Mugoni. Structural insight into transition metal oxide containing glasses by molecular dynamic simulations. *Molecular Dynamics Simulations of Disordered Materials: From Network Glasses to Phase-Change Memory Alloys*, pages 181–213, 2015.

[49] R.J. Barczyński, P. Król, and L. Murawski. Ac and dc conductivities in V_2O_5–P_2O_5 glasses containing alkaline ions. *J. Non-Cryst. Solids*, 356(37-40):1965–1967, 2010.

[50] K. Nagamine, T. Honma, and T. Komatsu. Selective synthesis of Lithium Ion-Conductive β-$LiVOPO_4$ crystals via Glass–Ceramic Processing. *J. Am. Ceram. Soc.*, 91(12):3920–3925, 2008.

[51] K. Nagamine, T. Honma, and T. Komatsu. A fast synthesis of $Li_3V_2(PO_4)_3$ crystals via glass-ceramic processing and their battery performance. *Journal of Power Sources*, 196(22):9618–9624, 2011.

[52] H.I Hsiang, B.R. Cai, S.H. Chung, L.W. Chu, J.R. Tseng, and Y.M. Shen. Preparation and electrochemical properties of $Li_3V_2(PO_{43}$ glass-ceramic materials. *Ceram. Int.*, 49(21):34155–34163, 2023.

[53] U. Hoppe, N.P. Wyckoff, M.L. Schmitt, R.K. Brow, A. Schöps, and A.C. Hannon. Structure of V_2O_5–P_2O_5 glasses by X-ray and neutron diffraction. *J. Non-Cryst. Solids*, 358(2):328–336, 2012.

[54] U. Hoppe, R. Kranold, and E. Gattef. An X-ray diffraction study of the structure of vitreous V_2O_5. *Solid State Commun.*, 108(2):71–76, 1998.

[55] U. Hoppe, A. Ghosh, S. Feller, A.C. Hannon, D.A. Keen, and J. Neuefeind. Structural units of binary vanadate glasses by X-ray and neutron diffraction. *J. Non-Cryst. Solids*, 572:121120, 2021.

[56] A. Chrissanthopoulos, C. Pouchan, and G.N. Papatheodorou. Structural investigation of vanadium-sodium metaphosphate glasses. *Zeitschrift für Naturforschung A*, 56(11):773–776, 2001.

[57] G. Tricot and H. Vezin. Description of the intermediate length scale structural motifs in sodium vanado-phosphate glasses by magnetic resonance spectroscopies. *J. Phys. Chem. C*, 117(3):1421–1427, 2013.

[58] G. Tricot, L. Montagne, L. Delevoye, G. Palavit, and V. Kostoj. Redox and structure of sodium-vanadophosphate glasses. *J. Non-Cryst. Solids*, 345:56–60, 2004.

[59] X. Lu, L. Deng, S.A. Saslow, H. Liu, C.J. Benmore, B.P. Parruzot, J.T. Reiser, S.H. Kim, J.V. Ryan, J.D. Vienna, et al. Vanadium oxidation states and structural role in aluminoborosilicate glasses: an integrated experimental and molecular dynamics simulation study. *J. Phys. Chem. B*, 125(44):12365–12377, 2021.

[60] A.A. Raskovalov, N.S. Saetova, and I.S. Popov. Structural changes in V_2O_5-P_2O_5 glasses: non-constant force field molecular dynamics and IR spectroscopy. *Chim. Techno Acta*, 8(2):20218211, 2021.

[61] M. Nabavi, C. Sanchez, and J. Livage. Structure and properties of amorphous V_2O_5. *Philos. Mag. B*, 63(4):941–953, 1991.

[62] G. Giuli, E. Paris, J. Mungall, C. Romano, and D. Dingwell. V oxidation state and coordination number in silicate glasses by XAS. *Am. Mineral.*, 89(11-12):1640–1646, 2004.

[63] F. Benzi, G. Giuli, S. Della Longa, and E. Paris. Vanadium k-edge XANES in vanadium-bearing model compounds: a full multiple scattering study. *J. Synchrotron Radiat.*, 23(4):947–952, 2016.

[64] J. Kornatowski, B. Wichterlova, M. Rozwadowski, and W.H. Baur. Simultaneous occurrence of differently coordinated framework heteroatoms in one zeolite: MFI type vanadium silicalite, KVS-5. In *Studies in Surface Science and Catalysis*, volume 84, pages 117–124. Elsevier, 1994.

[65] L.D. Bogomolova, V.A. Jachkin, and N.A. Krasil'nikova. EPR study of vanadium-containing amorphous silica formed by sol–gel method. *J. Non-Cryst. Solids*, 241(1):13–26, 1998.

[66] F. Benzi, E. Paris, S. Della Longa, C. Mugoni, C. Siligardi, and G. Giuli. V K-Edge XANES Full Multiple Scattering Study of V-Bearing Phosphate Glasses. In *Synchrotron Radiation Science and Applications: Proceedings of the 2019 Meeting of the Italian Synchrotron Radiation Society—Dedicated to Carlo Lamberti*, pages 219–231. Springer, 2021.

[67] Peter Y Zavalij and M Stanley Whittingham. Structural chemistry of vanadium oxides with open frameworks. *Acta Crystallogr. B*, 55(5):627–663, 1999.

[68] M. Schindler, F.C. Hawthorne, and W.H. Baur. Crystal chemical aspects of vanadium: polyhedral geometries, characteristic bond valences, and polymerization of (VOn) polyhedra. *Chem. Mater.*, 12:1248–1259, 2000.

[69] S. Boudin, A. Guesdon, A. Leclaire, and M-M. Borel. Review on vanadium phosphates with mono and divalent metallic cations: syntheses, structural relationships and classification, properties. *Int. J. Inorg. Chem.*, 2:561–579, 2000.

[70] G. Delaizir, V. Seznec, P. Rozier, C. Surcin, P. Salles, and M. Dollé. Electrochemical performances of vitreous materials in the system Li_2O–V_2O_5–P_2O_5 as electrode for lithium batteries. *Solid State Ionics*, 237:22–27, 2013.

[71] E.D. Zanotto and J.C. Mauro. The glassy state of matter: Its definition and ultimate fate. *J. Non-Cryst. Solids*, 471:490–495, 2017.

[72] S.D. Stookey. History of the development of pyroceram. *Research Management*, 1(3):155–163, 1958.

[73] J. Deubener, M. Allix, M.J. Davis, A. Duran, T. Höche, T. Honma, T. Komatsu, S. Krüger, I. Mitra, R. Müller, et al. Updated definition of glass-ceramics. *J. Non-Cryst. Solids*, 501:3–10, 2018.

[74] R.D. Rawlings. Bioactive glasses and glass-ceramics. *Clin. Mater.*, 14(2):155–179, 1993.

[75] Y. Wang, X. Zhang, W. He, C. Wei, and Q. Cheng. A review for the synthesis methods of lithium vanadium phosphate cathode materials. *J. Mater. Sci.: Mater. Electron.*, 28:18269–18295, 2017.

[76] P. Friederich, F. Häse, J. Proppe, and A. Aspuru-Guzik. Machine-learned potentials for next-generation matter simulations. *Nat. Mater.*, 20(6):750–761, 2021.

[77] Y. S. Meng and M.E. A. Dompablo. First principles computational materials design for energy storage materials in lithium ion batteries. *Energy Environ. Sci.*, 2(6):589–609, 2009.

[78] P. Zhang, Y. Xu, F. Zheng, S.Q. Wu, Y. Yang, and Z.Z. Zhu. Ion diffusion mechanism in Pn $Na_xLi_{2-x}MnSiO_4$. *CrystEngComm*, 17(10):2123–2128, 2015.

[79] H.M. You, Y. Yoon, J. Ko, J. Back, H. Kwon, J.W. Han, and K. Kim. Atomistic scale modeling of anode/electrolyte interfaces in Li-ion batteries. *Langmuir*, 2024.

[80] G. Ori, M. Montorsi, A. Pedone, and C. Siligardi. Insight into the structure of vanadium containing glasses: a molecular dynamics study. *J. Non-Cryst. Solids*, 357(14):2571–2579, 2011.

[81] G. Broglia, C. Mugoni, J. Du, C. Siligardi, and M. Montorsi. Lithium vanadophosphate glasses: Structure and dynamics properties studied by molecular dynamics simulations. *J. Non-Cryst. Solids*, 403:53–61, 2014.

[82] L. Deng, X. Lu, J.D. Vienna, and J. Du. Structures of vanadium-containing silicate and borosilicate glasses: Vanadium potential development and MD simulations. *J. Non-Cryst. Solids*, 575:121223, 2022.

[83] Y. Xie, F. Gu, Q. Wang, M. Shui, and J. Shu. Deep insight into the defect structure, lithium diffusion kinetics and deintercalation study on β-$LiVOPO_4$ cathode material by atomistic simulation method. *J. Energy Storage*, 45:103706, 2022.

[84] A. Pedone, M. Bertani, L. Brugnoli, and A. Pallini. Interatomic potentials for oxide glasses: Past, present, and future. *J. Non-Cryst. Solids X*, page 100115, 2022.

[85] U. Hoppe and R. Kranold. A reverse monte carlo study of the structure of vitreous V_2O_5. *Solid state commun.*, 109(10):625–630, 1999.

[86] L. Deng, X. Lu, J.D. Vienna, and J. Du. Structures of vanadium-containing silicate and borosilicate glasses: Vanadium potential development and md simulations. *J. Non-Cryst. Solids*, 575:121223, 2022.

[87] A. Pedone, G. Malavasi, M.C. Menziani, A.N. Cormack, and U. Segre. A new self-consistent empirical interatomic potential model for oxides, silicates, and silica-based glasses. *J. Phys. Chem. B*, 110(24):11780–11795, 2006.

[88] G. Malavasi and A. Pedone. The effect of the incorporation of catalase mimetic activity cations on the structural, thermal and chemical durability properties of the 45S5 bioglass®. *Acta Mater.*, 229:117801, 2022.

[89] I.A. Saiko, N.S. Saetova, A.A. Raskovalov, E.A. Il'ina, N.G. Molchanova, and N.I. Kadyrova. Hopping conductivity in V_2O_5-P_2O_5 glasses: Experiment and non-constant force field molecular dynamics. *Solid State Ion.*, 345:115180, 2020.

[90] A.A. Raskovalov, N.S. Saetova, and S.V. Pershina. Nature of conductivity in $x$$Na_2O$–$(90-x)V_2O_5$–$10P_2O_5$ glasses: experimental study and computer simulation. In *J. Phys. Conf. Ser.*, volume 1967, page 012007. IOP Publishing, 2021.

[91] Y. Sakurai and J. Yamaki. V_2O_5-P_2O_5 glasses as cathode for lithium secondary battery. *J. Electrochem. Soc.;(United States)*, 132, 1985.

[92] L. Bih, L. Abbas, A. Nadiri, H. Khemakhem, and B. Elouadi. Investigations of molybdenum redox phenomenon in Li_2O–MoO_3–P_2O_5 phosphate glasses. *J. Mol. Struct.*, 872(1):1–9, 2008.

[93] M.M. El-Desoky, N.K. Wally, E. Sheha, and B.M. Kamal. Impact of sodium oxide, sulfide, and fluoride-doped vanadium phosphate glasses on the thermoelectric power and electrical properties: structure analysis and conduction mechanism. *J. Mater. Sci.: Mater. Electron.*, 32:3699–3712, 2021.

[94] K. Zhou and B. Liu. *Molecular dynamics simulation: Fundamentals and Applications*. Academic Press, 2022.

[95] B.J. Alder and T.E. Wainwright. Phase transition for a hard sphere system. *J. Chem. Phys.*, 27(5):1208–1209, 1957.

[96] A. Rahman. Correlations in the motion of atoms in liquid argon. *Phys. Rev.*, 136(2A):A405, 1964.

[97] F.H. Stillinger and A. Rahman. Improved simulation of liquid water by molecular dynamics. *J. Chem. Phys.*, 60(4):1545–1557, 1974.

[98] C.S. Peskin and T. Schlick. Molecular dynamics by the Backward-Euler method. *Commun. Pure Appl. Math.*, 42(7):1001–1031, 1989.

[99] L. Verlet. Computer" experiments" on classical fluids. I. thermodynamical properties of lennard-jones molecules. *Phys. Rev.*, 159(1):98, 1967.

[100] R.W. Pastor, B.R. Brooks, and A. Szabo. An analysis of the accuracy of langevin and molecular dynamics algorithms. *Mol. Phys.*, 65(6):1409–1419, 1988.

[101] H. Grubmüller, H. Heller, A. Windemuth, and K. Schulten. Generalized verlet algorithm for efficient molecular dynamics simulations with long-range interactions. *Mol. Simul.*, 6(1-3):121–142, 1991.

[102] W.F. Van Gunsteren and H.J.C. Berendsen. A leap-frog algorithm for stochastic dynamics. *Mol. Simul.*, 1(3):173–185, 1988.

[103] B.A. Luty and W.F. Van Gunsteren. Calculating electrostatic interactions using the particle- particle particle- mesh method with nonperiodic long-range interactions. *J. Phys. Chem.*, 100(7):2581–2587, 1996.

[104] W.C. Swope, H.C. Andersen, P.H. Berens, and K.R. Wilson. A computer simulation method for the calculation of equilibrium constants for the formation of physical clusters of molecules: Application to small water clusters. *J. Chem. Phys.*, 76(1):637–649, 1982.

[105] H.C. Andersen. Rattle: A "velocity" version of the shake algorithm for molecular dynamics calculations. *J. comput. Phys.*, 52(1):24–34, 1983.

[106] Q. Spreiter and M. Walter. Classical molecular dynamics simulation with the velocity verlet algorithm at strong external magnetic fields. *J. Comput. Phys.*, 152(1):102–119, 1999.

[107] P.M. Morse. Diatomic molecules according to the wave mechanics. II. vibrational levels. *Phys. Rev.*, 34(1):57, 1929.

[108] M. Bertani, M.C. Menziani, and A. Pedone. Improved empirical force field for multicomponent oxide glasses and crystals. *Phys. Rev. Mater.*, 5(4):045602, 2021.

[109] R.A. Buckingham. The classical equation of state of gaseous helium, neon and argon. *Proc. R. Soc. Lond. A Math. Phys. Sci.*, 168(933):264–283, 1938.

[110] H.J.C. Berendsen, J.P.M Postma, W.F. Van Gunsteren, A. DiNola, and J.R. Haak. Molecular dynamics with coupling to an external bath. *J. Chem. Phys.*, 81(8):3684–3690, 1984.

[111] H.C. Andersen. Molecular dynamics simulations at constant pressure and/or temperature. *J. Chem. Phys.*, 72(4):2384–2393, 1980.

[112] S. Nosé. A unified formulation of the constant temperature molecular dynamics methods. *J. Chem. Phys*, 81(1):511–519, 1984.

[113] W.G Hoover. Canonical dynamics: Equilibrium phase-space distributions. *Phys. Rev. A*, 31(3):1695, 1985.

[114] S. Nosé. A molecular dynamics method for simulations in the canonical ensemble. *Mol. Phys.*, 52:255–268, 1984.

[115] C. Massobrio. *The Structure of Amorphous Materials Using Molecular Dynamics*. IOP Publishing, 2022.

[116] C. Massobrio, I.A. Essomba, M. Boero, C. Diarra, M. Guerboub, K. Ishisone, A. Lambrecht, E. Martin, I. Morrot-Woisard, G. Ori, et al. On the actual difference between the Nosé and the Nosé–Hoover thermostats: A critical review of canonical temperature control by molecular dynamics. *Phys. status solidi B*, 261(1):2300209, 2024.

[117] P. Hohenberg and W. Kohn. Inhomogeneous electron gas. *Phys. Rev.*, 136:B864–B871, 1964.

[118] M. Boero, A. Bouzid, S. Le Roux, B. Ozdamar, and C. Massobrio. First-principles molecular dynamics methods: an overview. *Molecular Dynamics Simulations of Disordered Materials: From Network Glasses to Phase-Change Memory Alloys*, pages 33–55, 2015.

[119] D.R. Hamann, M. Schlüter, and C. Chiang. Norm-conserving pseudopotentials. *Phys. Rev. Lett.*, 43(20):1494, 1979.

[120] G. B. Bachelet, D. R. Hamann, and M. Schlüter. Pseudopotentials that work: From H to Pu. *Phys. Rev. B*, 26:4199–4228, 1982.

[121] N. Troullier and J.L. Martins. Efficient pseudopotentials for plane-wave calculations. *Phys. Rev. B*, 43:1993–2006, 1991.

[122] D. Vanderbilt. Soft self-consistent pseudopotentials in a generalized eigenvalue formalism. *Phys. Rev. B*, 41(11):7892, 1990.

[123] J.P. Perdew, A. Ruzsinszky, J. Tao, V.N. Staroverov, G.E. Scuseria, and G.I. Csonka. Prescription for the design and selection of density functional approximations: More constraint satisfaction with fewer fits. *J. Chem. Phys.*, 123(6), 2005.

[124] J.P. Perdew and K. Schmidt. Jacob's ladder of density functional approximations for the exchange-correlation energy. In *AIP Conference Proceedings*, volume 577, pages 1–20. American Institute of Physics, 2001.

[125] W. Kohn and L.J. Sham. Self-Consistent Equations Including Exchange and Correlation Effects. *Phys. Rev.*, 140:A1133–A1138, 1965.

[126] P. Dirac. Note on exchange phenomena in the thomas atom. *J. Comput. Nanoscience*, 26:376, 1930.

[127] D.M. Ceperley and B.J. Alder. Ground state of the electron gas by a stochastic method. *Phys. Rev. Lett.*, 45:566–569, 1980.

[128] J.P. Perdew and A. Zunger. Self-interaction correction to density-functional approximations for many-electron systems. *Phys. Rev. B*, 23:5048–5079, 1981.

[129] J.M. Seminario, M.C. Concha, and P. Politzer. Calculation of molecular geometries and energies by a local density functional approach. *Int. J. Quantum Chem.*, 40(S25):249–259, 1991.

[130] A. Bouzid. *First-principles investigation of binary and ternary amorphous chalcogenide systems*. PhD thesis, University of Strasbourg, 2014.

[131] J.P. Perdew, K. Burke, and M. Ernzerhof. Generalized gradient approximation made simple. *Phys. Rev. Lett*, 77:3865–3868, 1996.

[132] A.D. Becke. Density-functional exchange-energy approximation with correct asymptotic behavior. *Phys. Rev. A*, 38(6):3098, 1988.

[133] C. Lee, W. Yang, and R.G. Parr. Development of the colle-salvetti correlation-energy formula into a functional of the electron density. *Phys. Rev. B*, 37:785–789, 1988.

[134] P.J. Stephens, F.J. Devlin, C.F. Chabalowski, and M.J. Frisch. Ab initio calculation of vibrational absorption and circular dichroism spectra using density functional force fields. *J. Phys. Chem.*, 98(45):11623–11627, 1994.

[135] C. Adamo and V. Barone. Toward reliable density functional methods without adjustable parameters: The PBE0 model. *J. Chem. Phys.*, 110(13):6158–6170, 1999.

[136] J. Heyd, G.E. Scuseria, and M. Ernzerhof. Hybrid functionals based on a screened coulomb potential. *J. Chem. Phys.*, 118(18):8207–8215, 2003.

[137] J. Heyd and G.E. Scuseria. Efficient hybrid density functional calculations in solids: Assessment of the heyd–scuseria–ernzerhof screened coulomb hybrid functional. *J. Chem. Phys.*, 121(3):1187–1192, 2004.

[138] J. Heyd, J.E. Peralta, G.E. Scuseria, and R.L. Martin. Energy band gaps and lattice parameters evaluated with the heyd-scuseria-ernzerhof screened hybrid functional. *J. Chem. Phys.*, 123(17), 2005.

[139] A.V. Krukau, O.A. Vydrov, A.F. Izmaylov, and G.E. Scuseria. Influence of the exchange screening parameter on the performance of screened hybrid functionals. *J. Chem. Phys.*, 125(22), 2006.

[140] J.E. Peralta, J. Heyd, G.E. Scuseria, and R.L. Martin. Spin-orbit splittings and energy band gaps calculated with the Heyd-Scuseria-Ernzerhof screened hybrid functional. *Phys. Rev. B*, 74(7):073101, 2006.

[141] N. W. Ashcroft and N. D. Mermin. *Solid State Physics*. Holt-Saunders, 1976.

[142] D.J. Singh and L. Nordstrom. *Planewaves, Pseudopotentials, and the LAPW method*. Springer Science & Business Media, 2006.

[143] P. Schwerdtfeger. The pseudopotential approximation in electronic structure theory. *ChemPhysChem*, 12(17):3143–3155, 2011.

[144] J.C. Phillips and L. Kleinman. New method for calculating wave functions in crystals and molecules. *Phys. Rev.*, 116(2):287, 1959.

[145] J.D. Weeks and S.A. Rice. Use of pseudopotentials in atomic-structure calculations. *J. Chem. Phys.*, 49(6):2741–2755, 1968.

[146] P.E. Blöchl. Projector augmented-wave method. *Phys. Rev. B*, 50(24):17953, 1994.

[147] G. Kresse and D. Joubert. From ultrasoft pseudopotentials to the projector augmented-wave method. *Phys. Rev. B*, 59(3):1758, 1999.

[148] D. Vanderbilt. Soft self-consistent pseudopotentials in a generalized eigenvalue formalism. *Phys. Rev. B*, 41(11):7892, 1990.

[149] K. Laasonen, R. Car, C. Lee, and D. Vanderbilt. Implementation of ultrasoft pseudopotentials in ab initio molecular dynamics. *Phys. Rev. B*, 43(8):6796, 1991.

[150] D.R. Hamann. Generalized norm-conserving pseudopotentials. *Phys. Rev. B*, 40(5):2980, 1989.

[151] C. Herring and A.G. Hill. The theoretical constitution of metallic beryllium. *Phys. Rev.*, 58(2):132, 1940.

[152] P. Focher, A. Lastri, M. Covi, and G.B. Bachelet. Pseudopotentials and physical ions. *Phys. Rev. B*, 44(16):8486, 1991.

[153] S. Goedecker, M. Teter, and J. Hutter. Separable dual-space gaussian pseudopotentials. *Phys. Rev. B*, 54:1703–1710, 1996.

[154] Max Born and Robert Oppenheimer. On the quantum theory of molecules. In *Quantum Chemistry: Classic Scientific Papers*, pages 1–24. World Scientific, 2000.

[155] D. Marx and J. Hutter. *Ab initio molecular dynamics: basic theory and advanced methods*. Cambridge University Press, 2009.

[156] R. Car and M. Parrinello. Unified approach for molecular dynamics and density-functional theory. *Phys. Rev. Lett*, 55:2471–2474, 1985.

[157] M. Boero and A. Oshiyama. Car–parrinello molecular dynamics. *Encyc. Nanotechnol.*, pages 1–10, 2015.

[158] G. Pastore, E. Smargiassi, and F. Buda. Theory of ab initio molecular-dynamics calculations. *Phys. Rev. A*, 44(10):6334, 1991.

[159] A. Alavi, J. Kohanoff, M. Parrinello, and D. Frenkel. Ab initio molecular dynamics with excited electrons. *Phys. Rev. Lett.*, 73(19):2599, 1994.

[160] R. Resta and S. Sorella. Electron localization in the insulating state. *Phys. Rev. Lett.*, 82(2):370, 1999.

[161] N. Marzari and D. Vanderbilt. Maximally localized generalized wannier functions for composite energy bands. *Phys. Rev. B*, 56(20):12847, 1997.

[162] G.H. Wannier. The structure of electronic excitation levels in insulating crystals. *Phys. Rev.*, 52(3):191, 1937.

[163] A.I. Khan and S. Al-Habsi. Machine learning in computer vision. *Procedia Comput. Sci.*, 167:1444–1451, 2020.

[164] M.Q. Huang, J. Ninić, and Q. Zhang. Bim, machine learning and computer vision techniques in underground construction: Current status and future perspectives. *Tunn. Undergr. Space Technol.*, 108:103677, 2021.

[165] A. Le Glaz, Y. Haralambous, D.H. Kim-Dufor, P. Lenca, R. Billot, T.C. Ryan, J. Marsh, J. Devylder, M. Walter, S. Berrouiguet, et al. Machine learning and natural language processing in mental health: systematic review. *J. Med. Internet Res.*, 23(5):e15708, 2021.

[166] J.W. Goodell, S. Kumar, W.M. Lim, and D. Pattnaik. Artificial intelligence and machine learning in finance: Identifying foundations, themes, and research clusters from bibliometric analysis. *J. Behav. Exp. Finance*, 32:100577, 2021.

[167] I.Y. Chen, E. Pierson, S. Rose, S. Joshi, K. Ferryman, and M. Ghassemi. Ethical machine learning in healthcare. *Annu. Rev. Biomed. Data Sci.*, 4:123–144, 2021.

[168] T. Mueller, A.G. Kusne, and R. Ramprasad. Machine learning in materials science: Recent progress and emerging applications. *Rev. Comput. Chem.*, 29:186–273, 2016.

[169] V.L. Deringer and G. Csányi. Machine learning based interatomic potential for amorphous carbon. *Phys. Rev. B*, 95(9):094203, 2017.

[170] V.L. Deringer, M.A. Caro, and G. Csányi. Machine learning interatomic potentials as emerging tools for materials science. *Adv. Mater.*, 31(46):1902765, 2019.

[171] V.L. Deringer, M.A. Caro, and G. Csányi. A general-purpose machine-learning force field for bulk and nanostructured phosphorus. *Nat. Commun.*, 11(1):5461, 2020.

[172] J. Wei, X. Chu, X.Y. Sun, K. Xu, H.X. Deng, J. Chen, Z. Wei, and M. Lei. Machine learning in materials science. *InfoMat*, 1(3):338–358, 2019.

[173] V.L. Deringer, A.P. Bartók, N. Bernstein, D.M. Wilkins, M. Ceriotti, and G. Csányi. Gaussian process regression for materials and molecules. *Chem. Rev*, 121(16):10073–10141, 2021.

[174] Y. Mishin. Machine-learning interatomic potentials for materials science. *Acta Mater.*, 214:116980, 2021.

[175] G.E. Karniadakis, I.G. Kevrekidis, L. Lu, P. Perdikaris, S. Wang, and L. Yang. Physics-informed machine learning. *Nat. Rev. Phys.*, 3(6):422–440, 2021.

[176] M. Ceriotti, C. Clementi, and O. A. Von Lilienfeld. Machine learning meets chemical physics. *J Chem. Phys.*, 154(16), 2021.

[177] H. Doan Tran, C. Kim, L. Chen, A. Chandrasekaran, R. Batra, S. Venkatram, D. Kamal, Jo.P. Lightstone, R. Gurnani, P. Shetty, et al. Machine-learning predictions of polymer properties with Polymer Genome. *J. Appl. Phys.*, 128(17), 2020.

[178] N. Castel, D. André, C. Edwards, J.D. Evans, and F.X. Coudert. Machine learning interatomic potentials for amorphous zeolitic imidazolate frameworks. *Digital Discovery*, 2024.

[179] J. Westermayr, M. Gastegger, K.T. Schütt, and R.J. Maurer. Perspective on integrating machine learning into computational chemistry and materials science. *J. Chem. Phys.*, 154(23), 2021.

[180] P. Friederich, F. Häse, J. Proppe, and A. Aspuru-Guzik. Machine-learned potentials for next-generation matter simulations. *Nat. Mater.*, 20(6):750–761, 2021.

[181] J. Behler. First principles neural network potentials for reactive simulations of large molecular and condensed systems. *Angew. Chem. Int. Ed.*, 56(42):12828–12840, 2017.

[182] S. Klawohn, J.P. Darby, J.R. Kermode, G. Csányi, M.A. Caro, and A.P. Bartók. Gaussian approximation potentials: Theory, software implementation and application examples. *J. Chem. Phys.*, 159(17), 2023.

[183] T.B. Blank, S.D. Brown, A.W. Calhoun, and D.J. Doren. Neural network models of potential energy surfaces. *J. Chem. Phys.*, 103(10):4129–4137, 1995.

[184] K.H. Cho, K.T. No, and H.A. Scheraga. A polarizable force field for water using an artificial neural network. *J. Mol. Struct.*, 641(1):77–91, 2002.

[185] S. Lorenz, A. Groß, and M. Scheffler. Representing high-dimensional potential-energy surfaces for reactions at surfaces by neural networks. *Chem. Phys. Lett.*, 395(4-6):210–215, 2004.

[186] J. Behler and M. Parrinello. Generalized neural-network representation of high-dimensional potential-energy surfaces. *Phys. Rev. Lett.*, 98:146401, 2007.

[187] Representing potential energy surfaces by high-dimensional neural network potentials. *Phys. Condens. Matter*, 26(18):183001, 2014.

[188] J. Behler. Constructing high-dimensional neural network potentials: a tutorial review. *Int. J. Quantum Chem.*, 115(16):1032–1050, 2015.

[189] E. Kocer, T.W. Ko, and J. Behler. Neural network potentials: A concise overview of methods. *Annu. Rev. Phys. Chem.*, 73:163–186, 2022.

[190] A.P. Bartók, M.C. Payne, R. Kondor, and G. Csányi. Gaussian approximation potentials: The accuracy of quantum mechanics, without the electrons. *Phys. Rev. Lett.*, 104:136403, 2010.

[191] A.P. Bartók, R. Kondor, and G. Csányi. On representing chemical environments. *Phys. Rev. B*, 87(18):184115, 2013.

[192] A.P. Bartók and G. Csányi. Gaussian approximation potentials: A brief tutorial introduction. *Int. J. Quantum Chem.*, 115(16):1051–1057, 2015.

[193] L. Zhang, J. Han, H. Wang, R. Car, and E. Weinan. Deep potential molecular dynamics: A scalable model with the accuracy of quantum mechanics. *Phys. Rev. Lett.*, 120:143001, 2018.

[194] A. Musaelian, S. Batzner, A. Johansson, L. Sun, C.J. Owen, M. Kornbluth, and B. Kozinsky. Learning local equivariant representations for large-scale atomistic dynamics. *Nat. Commun.*, 14:579, 2023.

[195] S. Batzner, A. Musaelian, L. Sun, M. Geiger, J.P. Mailoa, M. Kornbluth, N. Molinari, T.E. Smidt, and B. Kozinsky. E (3)-equivariant graph neural networks for data-efficient and accurate interatomic potentials. *Nat. Commun.*, 13(1):2453, 2022.

[196] G. Wang, C. Wang, X. Zhang, Z. Li, J. Zhou, and Z. Sun. Machine learning interatomic potential: Bridge the gap between small-scale models and realistic device-scale simulations. *Iscience*, 27(5), 2024.

[197] A.P. Bartók, J. Kermode, N. Bernstein, and G. Csányi. Machine learning a general-purpose interatomic potential for silicon. *Phys. Rev. X*, 8(4):041048, 2018.

[198] R.Z. Khaliullin, H. Eshet, T.D. Kühne, J. Behler, and M. Parrinello. Graphite-diamond phase coexistence study employing a neural-network mapping of the ab initio potential energy surface. *Phys. Rev. B*, 81(10):100103, 2010.

[199] W. Li, Y. Ando, E. Minamitani, and S. Watanabe. Study of Li atom diffusion in amorphous Li_3PO_4 with neural network potential. *J. Chem. Phys.*, 147(21), 2017.

[200] W. Li, Y. Ando, and S. Watanabe. Cu diffusion in amorphous Ta_2O_5 studied with a simplified neural network potential. *J. Phys. Soc. Jpn.*, 86(10):104004, 2017.

[201] N. Artrith and A. Urban. An implementation of artificial neural-network potentials for atomistic materials simulations: Performance for TiO_2. *Comput. Mater. Sci.*, 114:135–150, 2016.

[202] N. Artrith, A. Urban, and G. Ceder. Constructing first-principles phase diagrams of amorphous Li_xSi using machine-learning-assisted sampling with an evolutionary algorithm. *J. Chem. Phys.*, 148(24), 2018.

[203] G.C. Sosso, D. Donadio, S. Caravati, J. Behler, and M. Bernasconi. Thermal transport in phase-change materials from atomistic simulations. *Phys. Rev. B*, 86(10):104301, 2012.

[204] D.K. Bhamare, P. Saikia, M.K. Rathod, D. Rakshit, and J. Banerjee. A machine learning and deep learning based approach to predict the thermal performance of phase change material integrated building envelope. *Building and Environment*, 199:107927, 2021.

[205] F.C. Mocanu, K. Konstantinou, T.H. Lee, N. Bernstein, V.L. Deringer, G. Csányi, and S.R. Elliott. Modeling the phase-change memory material, $Ge_2Sb_2Te_5$, with a machine-learned interatomic potential. *J Phys. Chem. B*, 122(38):8998–9006, 2018.

[206] N. Artrith and J. Behler. High-dimensional neural network potentials for metal surfaces: A prototype study for copper. *Phys. Rev. B*, 85(4):045439, 2012.

[207] K. Shakouri, J. Behler, J. Meyer, and G.J. Kroes. Accurate neural network description of surface phonons in reactive gas–surface dynamics: N_2 + Ru(0001). *J Phys. Chem. Lett.*, 8(10):2131–2136, 2017.

[208] B. Kolb, X. Luo, X. Zhou, B. Jiang, and H. Guo. High-dimensional atomistic neural network potentials for molecule–surface interactions: HCl scattering from Au (111). *J. Phys. Chem. Lett.*, 8(3):666–672, 2017.

[209] L. Zhang, D.Y. Lin, H. Wang, R. Car, and E. Weinan. Active learning of uniformly accurate interatomic potentials for materials simulation. *Phys. Rev. Mater.*, 3(2):023804, 2019.

[210] J. Vandermause, S.B. Torrisi, S. Batzner, Y. Xie, L. Sun, A.M. Kolpak, and B. Kozinsky. On-the-fly active learning of interpretable bayesian force fields for atomistic rare events. *Npj Comput. Mater.*, 6(1):20, 2020.

[211] J.D. Morrow, J.L.A. Gardner, and V.L. Deringer. How to validate machine-learned interatomic potentials. *J. Chem. Phys.*, 158(12), 2023.

[212] S.N. Pozdnyakov, M.J. Willatt, A.P. Bartók, C. Ortner, G. Csányi, and M. Ceriotti. Incompleteness of atomic structure representations. *Phys. Rev. Lett.*, 125(16):166001, 2020.

[213] J. Behler. Perspective: Machine learning potentials for atomistic simulations. *J. Chem. Phys.*, 145(17):170901, 2016.

[214] Felix Musil, Andrea Grisafi, Albert P Bartók, Christoph Ortner, Gábor Csányi, and Michele Ceriotti. Physics-inspired structural representations for molecules and materials. *Chemical Reviews*, 121(16):9759–9815, 2021.

[215] R. Drautz. Atomic cluster expansion for accurate and transferable interatomic potentials. *Phys. Rev. B*, 99(1):014104, 2019.

[216] S. Klawohn, J.R. Kermode, and A.P. Bartók. Massively parallel fitting of gaussian approximation potentials. *Mach. Learn.: Sci. Technol.*, 4(1):015020, 2023.

[217] C. Massobrio, A. Pasquarello, and R. Car. Microscopic structure of liquid $GeSe_2$: The problem of concentration fluctuations over intermediate range distances. *Phys. Rev. Lett.*, 80(11):2342, 1998.

[218] C. Massobrio, A. Pasquarello, and R. Car. Intermediate range order and bonding character in disordered network-forming systems. *J. Am. Chem. Soc.*, 121(12):2943–2944, 1999.

[219] M. Micoulaut, R. Vuilleumier, and C. Massobrio. Improved modeling of liquid $GeSe_2$: impact of the exchange-correlation functional. *Phys. Rev. B*, 79(21):214205, 2009.

[220] A.B. Bhatia and D.E. Thornton. Structural aspects of the electrical resistivity of binary alloys. *Phys. Rev. B*, 2(8):3004, 1970.

[221] T.E. Faber and J.M. Ziman. A theory of the electrical properties of liquid metals: III. the resistivity of binary alloys. *Philos. Mag.*, 11(109):153–173, 1965.

[222] E. Lampin, A. Bouzid, G. Ori, M. Boero, and C. Massobrio. Impact of dispersion forces on the atomic structure of a prototypical network-forming disordered system: The case of liquid $GeSe_2$. *J. Chem. Phys.*, 147(4), 2017.

[223] I.T. Penfold and P.S. Salmon. Structure of covalently bonded glass-forming melts: A full partial-structure-factor analysis of liquid $GeSe_2$. *Phys. Rev. Lett.*, 67(1):97, 1991.

[224] P. Vashishta, R.K. Kalia, and I. Ebbsjö. Structural correlations and vibrational spectra of molten and glassy $GeSe_2$. *Solid State Ion.*, 32-33:872–881, 1989.

[225] P. Vashishta, R.K. Kalia, and I. Ebbsjö. Structural correlations and phonon density of states in $GeSe_2$: A molecular-dynamics study of molten and amorphous states. *Phys. Rev. B*, 39:6034–6047, 1989.

[226] P. Vashishta, R.K. Kalia, G.A. Antonio, and I. Ebbsjö. Atomic correlations and intermediate-range order in molten and amorphous $GeSe_2$. *Phys. Rev. Lett.*, 62:1651–1654, 1989.

[227] B.K. Sharma and M. Wilson. Intermediate-range order in molten network-forming systems. *Phys. Rev. B*, 73(6):060201, 2006.

[228] M. Wilson, B.K. Sharma, and C. Massobrio. Ionicity in disordered $GeSe_2$: A comparison of first-principles and atomistic potential models. *J. Chem. Phys*, 128(24), 2008.

[229] P. Rajak, N. Baradwaj, K. Nomura, A. Krishnamoorthy, J.P. Rino, K. Shimamura, S. Fukushima, F. Shimojo, R. Kalia, A. Nakano, et al. Neural network quantum molecular dynamics, intermediate range order in $GeSe_2$, and neutron scattering experiments. *J. Phys. Chem. Lett.*, 12(25):6020–6028, 2021.

[230] M. Micoulaut, S. Le Roux, and C. Massobrio. Investigation of size effects on the structure of liquid $GeSe_2$ calculated via first-principles molecular dynamics. *J. Chem. Phys.*, 136(22), 2012.

[231] C. Massobrio, A. Pasquarello, and R. Car. Short-and intermediate-range structure of liquid $GeSe_2$. *Phys. Rev. B*, 64(14):144205, 2001.

[232] Car-parrinello molecular dynamics. https://github.com/CPMD-code. Accessed: 25/10/2023.

[233] R. Azoulay, H. Thibierge, and A. Brenac. Devitrification characteristics of Ge_xSe_{1-x} glasses. *J. Non-Cryst. Solids*, 18(1):33–53, 1975.

[234] A. Bouzid and C. Massobrio. Note: Accounting for pressure effects on the calculated equilibrium structure of glassy $GeSe_2$. *J. Chem. Phys.*, 137(4), 2012.

[235] S. Nosé and M.L. Klein. Constant pressure molecular dynamics for molecular systems. *Mol. Phys.*, 50(5):1055–1076, 1983.

[236] P.S. Salmon and A. Zeidler. Networks under pressure: the development of in situ high-pressure neutron diffraction for glassy and liquid materials. *J. Phys.: Condens. Matter.*, 27(13):133201, 2015.

[237] P.S. Salmon. Structure of liquids and glasses in the Ge–Se binary system. *J. Non-Cryst. Solids*, 353(32-40):2959–2974, 2007.

[238] A.C. Wright. The comparison of molecular dynamics simulations with diffraction experiments. *J. Non-Cryst. Solids*, 159(3):264–268, 1993.

[239] V.L. Deringer, C.J. Pickard, and G. Csányi. Data-driven learning of total and local energies in elemental boron. *Phys. Rev. Lett.*, 120(15):156001, 2018.

[240] J. Ruska and H. Thurn. Change of short-range order with temperature and composition in liquid Ge_xSe_{1-x} as shown by density measurements. *J. Non-Cryst. Solids*, 22(2):277–290, 1976.

[241] The quip package is open to academic users at, howpublished = https://libatoms.github.io/QUIP/. Accessed: 25/10/2023.

[242] A.P. Thompson, H.M. Aktulga, R. Berger, D.S. Bolintineanu, W.M. Brown, P.S. Crozier, P.J. In't Veld, A. Kohlmeyer, S.G. Moore, T.D. Nguyen, et al. Lammps-a flexible simulation tool for particle-based materials modeling at the atomic, meso, and continuum scales. *Comput. Phys. Commun.*, 271:108171, 2022.

[243] P.S. Salmon and I. Petri. Structure of glassy and liquid $GeSe_2$. *J. Phys.: Condens. Matter*, 15(16):S1509, 2003.

[244] Y. Liu, X. He, and Y. Mo. Discrepancies and error evaluation metrics for machine learning interatomic potentials. *Npj Comput. Mater.*, 9(1):174, 2023.

[245] D. Yoo, J. Jung, W. Jeong, and S. Han. Metadynamics sampling in atomic environment space for collecting training data for machine learning potentials. *Npj Comput. Mater.*, 7(1):131, 2021.

[246] X. Fu, Z. Wu, W. Wang, T. Xie, S. Keten, R. Gomez-Bombarelli, and T. Jaakkola. Forces are not enough: Benchmark and critical evaluation for machine learning force fields with molecular simulations. *arXiv preprint arXiv:2210.07237*, 2022.

[247] Y.-X. Zhou, H.-Y. Zhang, V.L. Deringer, and W. Zhang. Structure and dynamics of supercooled liquid ge2sb2te5 from machine-learning-driven simulations. *Phys. Status Solidi - Rapid Res. Lett.*, 15(3):2000403, 2021.

[248] M.P. Allen and D.J. Tildesley. *Computer simulation of liquids*. Oxford university press, 2017.

[249] J. Pomeau, Y.and Piasecki. The langevin equation. *Comptes Rendus. Physique*, 18(9-10):570–582, 2017.

[250] S. Stølen, T. Grande, and H.-B. Johnsen. Fragility transition in $GeSe_2$–Se liquids. *Phys. Chem. Chem. Phys.*, 4(14):3396–3399, 2002.

[251] S. D. Wansi Wendji, C. Massobrio, M. Boero, C. Tugène, E. Levchenko, F. Shuaib, R. Piotrowski, D. Hamani, G. Delaizir, P.-M. Geffroy, et al. Quantitative assessment of the structure and bonding properties of $50V_xO_y$-$50P_2O_5$ glass by classical and born-oppenheimer molecular dynamics. *J. Non-Cryst. Solids*, 634:122967, 2024.

[252] Data deposited and available at NOMAD data repository.

[253] S. Afyon, F. Krumeich, C. Mensing, A. Borgschulte, and R. Nesper. New high capacity cathode materials for rechargeable li-ion batteries: vanadate-borate glasses. *Scientific reports*, 4(1):7113, 2014.

[254] M. Kindle, Y. Cha, J.S. McCloy, and M.K. Song. Alternatives to cobalt: vanadate glass and glass-ceramic structures as cathode materials for rechargeable lithium-ion batteries. *ACS Sustain. Chem. Eng.*, 9(2):629–638, 2021.

[255] N.A. Chernova, M.F.V. Hidalgo, C. Kaplan, K. Lee, I. Buyuker, C. Siu, B. Wen, and et al. Vanadyl phosphates A_xVOPO_4 (A= Li, Na, K) as multielectron cathodes for alkali-ion batteries. *Adv. Energy Mater.*, 10(47):2002638, 2020.

[256] H. Wu, C. Yiqing, W. Tianzhuo, C. Long, P. Xiangjun, and C. Zhongxue. Polyanionic (phosphates, silicates, sulfates) frameworks as electrode materials for rechargeable li (or na) batteries. *Batteries*, 9(1):56, 2023.

[257] A. Pedone, G. Malavasi, M.C. Menziani, U. Segre, and A.N. Cormack. Molecular dynamics studies of stress- strain behavior of silica glass under a tensile load. *Chem. Mater.*, 20(13):4356–4366, 2008.

[258] A. Pedone. Properties calculations of silica-based glasses by atomistic simulations techniques: a review. *J. Phys. Chem. C*, 113(49):20773–20784, 2009.

[259] D. Gentili and G. Ori. Reversible assembly of nanoparticles: theory, strategies and computational simulations. *Nanoscale*, 14:14385–14432, 2022.

[260] I.T. Todorov, W. Smith, and U.K. Cheshire. The DL POLY 4 user manual. *STFC, STFC Daresbury Laboratory, Daresbury, Warrington, Cheshire, WA4 4AD, United Kingdom, version*, 4(0), 2011.

[261] T.D. K*ü*hne, M. Iannuzzi, M. Del Ben, V.V. Rybkin, P. Seewald, F. Stein, T. Laino, R.Z. Khaliullin, O. Sch*ü*tt, and F. Schiffmann. CP2K: An Electronic Structure and Molecular Dynamics Software Package - Quickstep: Efficient and Accurate Electronic Structure Calculations. *J. Chem. Phys.*, 152:1194103, 2020.

[262] J. VandeVondele and J. Hutter. Gaussian basis sets for accurate calculations on molecular systems in gas and condensed phases. *J. Chem. Phys.*, 127:114105, 2007.

[263] S. Goedecker, M. Teter, and J. Hutter. Separable dual-space gaussian pseudopotentials. *Phys. Rev. B*, 54:1703, 1996.

[264] M. Ernzerhof and G. Scuseria. Assessment of the Perdew.Burke.Ernzerhof exchange-correlation functional. *J. Chem. Phys.*, 110:5029, 1999.

[265] M. Seth and T. Ziegler. Range-separated exchange functionals with Slater-type functions. *J. Chem. Theory Comput.*, 8(3):901–907, 2012.

[266] A. Saúl and G. Radtke. Density functional approach for the magnetism of β-$TeVO_4$. *Phys. Rev. B*, 89(10):104414, 2014.

[267] P. Chaurand, J. Rose, V. Briois, M. Salome, O. Proux, V. Nassif, L. Olivi, J. Susini, J.-L. Hazemann, and Bottero J.-L. New methodological approach for the vanadium K-edge X-ray absorption near-edge structure interpretation: Application to the speciation of vanadium in oxide phases from steel slag. *J. Phys. Chem. B*, 111:5101–5110, 2007.

[268] G. Calas and J. Petiau. Structure of oxide glasses: spectroscopic studies of local order and crystallochemistry. geochemical implications. *Bull. Min.*, 106:33–55, 1983.

[269] R.S. Mulliken. Electronic population analysis on LCAO–MO molecular wave functions. i. *J. Chem. Phys.*, 23(10):1833–1840, 1955.

[270] R.F.W. Bader and M.E. Stephens. Spatial localization of the electronic pair and number distributions in molecules. *J. Am. Chem. Soc.*, 97(26):7391–7399, 1975.

[271] A.K. Rappe and W.A. Goddard III. Charge equilibration for molecular dynamics simulations. *J. Phys. Chem.*, 95(8):3358–3363, 1991.

[272] K. Han, C. Hwang, D. Kim, D. Gwoo, T. Kim, W. Choi, K. Kee, J. Kim, and B. Ryu. Effects of substituting B_2O_3 for P_2O_5 on the structures and properties of V_2O_5-P_2O_5 glass systems. *Electron. Mater. Lett.*, 8:655–658, 2012.

[273] V.F. Sears. Neutron scattering lengths and cross sections. *Neutron news*, 3(3):26–37, 1992.

[274] C.T. Chantler. Theoretical form factor, attenuation, and scattering tabulation for z= 1–92 from e= 1–10 ev to e= 0.4–1.0 mev. *J. Phys. Chem. Ref. Data*, 24(1):71–643, 1995.

[275] E. Boivin, J.N. Chotard, C. Masquelier, and L. Croguennec. Towards reversible high-voltage multi-electron reactions in alkali-ion batteries using vanadium phosphate positive electrode materials. *Molecules*, 26(5):1428, 2021.

[276] U. Hoppe, G.Walter, R. Kranold, and D. Stachel. Structural specifics of phosphate glasses probed by diffraction methods: a review. *J. Non-Cryst. Solids*, 264:29–47, 2000.

[277] T. Aoyagi, S. Kohara, T. Naito, Y. Onodera, M. Kodama, T. Onodera, and D. et al. Takamatsu. Controlling oxygen coordination and valence of network forming cations. *Scientific reports*, 10(1):1–12, 2020.

[278] J.R. Errington and P.G. Debenedetti. Relationship between structural order and the anomalies of liquid water. *Nature*, 409(6818):318–321, 2001.

[279] A. Bouzid, S. Le Roux, G. Ori, C. Tugène, M. Boero, and C. Massobrio. First-principles modeling of binary chalcogenides: Recent accomplishments and new achievements. In *Molecular Dynamics Simulations of Disordered Materials: From Network Glasses to Phase-Change Memory Alloys*, pages 313–344. Springer, 2015.

[280] A. Bouzid, T.L. Pham, Z. Chaker, M. Boero, C. Massobrio, Y.H. Shin, and G. Ori. Quantitative assessment of the structure of $Ge_{20}Te_{73}I_7$ chalcohalide glass by first-principles molecular dynamics. *Phys. Rev. B*, 103(9):094204, 2021.

[281] A. Bouzid, G. Ori, M. Boero, E. Lampin, and C. Massobrio. Atomic-scale structure of the glassy $Ge_2Sb_2Te_5$ phase change material: A quantitative assessment via first-principles molecular dynamics. *Phys. Rev. B*, 96:224204, 2017.

[282] M. Guerboub, S.D. Wansi Wendji, C. Massobrio, A. Bouzid, M. Boero, G. Ori, and E. Martin. Impact of the local atomic structure on the thermal conductivity of amorphous $Ge_2Sb_2Te_5$. *J. Chem. Phys.*, 158:084504, 2023.

[283] R.K. Brow. The structure of simple phosphate glasses. *J. Non-Cryst. Solids.*, 263:1–28, 2000.

[284] L. Zheng, X. Yang, J. Li, R. Yang, H. Qu, X. Guo, S. Huang, and S. Zhang. DFT calculation of structures and electronic characteristic of $VOPO_4$ polymorphs. *Phys. Scripta*, 97(10):105805, 2022.

[285] P.L. Silvestrelli, E. Martin, M. Boero, A. Bouzid, G. Ori, and C. Massobrio. Atomic structure of glassy $GeTe_4$ as a playground to assess the performances of density functional schemes accounting for dispersion forces. *J. Phys. Chem. B*, 124(49):11273–11279, 2020.

[286] N. Marzari, A.A. Mostofi, J.R. Yates, I. Souza, and D. Vanderbilt. Maximally localized wannier functions: Theory and applications. *Reviews of Modern Physics*, 84(4):1419, 2012.

[287] L. Pauling. The Nature of the Chemical Bond 3-rd ed Ithaca. *New York: Cornell Univer*, 1960.

[288] P.T. Senftle, S. Hong, M.M. Islam, S.B. Kylasa, Y. Zheng, Y.K. Shin, C. Junkermeier, R. Engel-Herbert, M. Janik, A. Hasan Metin, T. Verstraelen, A. Grama, and A.C.T Van Duin. The reaxff reactive force-field: development, applications and future directions. *Npj Comput. Mater.*, 2(1):1–14, 2016.

[289] S. Zhang, M. Makoś, R. Jadrich, E. Kraka, K. Barros, B. Nebgen, S. Tretiak, O. Isayev, N. Lubbers, R. Messerly, and J. Smith. Exploring the frontiers of chemistry with a general reactive machine learning potential. *chemrxiv*, 10.26434/chemrxiv-2022-15ct6-v3, 2023.

[290] Y. Manyi, L. Bonati, D. Polino, and M. Parrinello. Using metadynamics to build neural network potentials for reactive events: the case of urea decomposition in water. *Catalysis Today*, 387:143–149, 2022.

[291] S. D. Wansi Wendji, R. Piotrowski, C. Massobrio, M. Boero, C. Tugène, F. Shuaib, D. Hamani, P. M. Geffroy, P. Thomas, A. Bouzid, O. Masson, G. Delaizir, and G. Ori. Enhanced structural description of sodium vanadium phosphate glasses: A combined experimental and molecular dynamics study. *J. Non-Cryst. Solids*, 655:123420, 2025.

[292] F. Kong, X. Liang, L. Yi, X. Fang, Z. Yin, Y. Wang, R. Zhang, L. Liu, Q. Chen, M. Li, et al. Multi-electron reactions for the synthesis of a vanadium-based amorphous material as lithium-ion battery cathode with high specific capacity. *Energy*, 219:119513, 2021.

[293] M. Neyret, M. Lenoir, A. Grandjean, N. Massoni, B. Penelon, and M. Malki. Ionic transport of alkali in borosilicate glass. role of alkali nature on glass structure and on ionic conductivity at the glassy state. *J. Non-Cryst. Solids*, 410:74–81, 2015.

[294] N. A. Wójcik, P. Kupracz, R. J. Barczyński, B. Jonson, and S. Ali. Ion conduction in beryllium-alumino-silicate glasses doped with sodium or sodium and lithium ions. *Solid State Ion.*, 341:115055, 2019.

[295] H. Pan, Y.-S. Hu, and L. Chen. Room-temperature stationary sodium-ion batteries for large-scale electric energy storage. *Energy Environ. Sci.*, 6(8):2338–2360, 2013.

[296] ANR Project: Advanced Modelling as a Strategy to design glass and glass-ceramic materials for Energy Storage applications – AMSES. https://anr.fr/Project-ANR-20-CE08-0021.

[297] R. Piotrowski. *Private discussions within the AMSES project regarding the PhD project in progress: Synthesis and characterizations of glasses and glass-ceramics - Applications to the field of energy storage (cathode materials)*. PhD thesis, University of Limoges, 2024.

[298] M. Micoulaut, A. Piarristeguy, O. Masson, L.-M. Poitras, R. Escalier, A. Kachmar, and A. Pradel. Quantitative assessment of network depolymerization in archetypal superionic glasses and its relationship with ion conduction: A case study on Na_2S-GeS_2. *Phys. Rev. B*, 108(14):144205, 2023.

[299] O. Masson. PYTSREDX, a data reduction program to obtain the atomic pair distribution function (PDF) from X-ray total scattering data. 2022.

[300] Dabaxfiles. http://ftp.esrf.fr/pub/scisoft/xop2.3/DabaxFiles/.

[301] A. K. Soper and P.A. Egelstaff. Multiple scattering and attenuation of neutrons in concentric cylinders: I. isotropic first scattering. *Nucl. Instrum. Methods*, 178(2-3):415–425, 1980.

[302] M. A. Reddy, H. Euchner, R. Witter, and O. Clemens. Structure and electrochemical properties of $Na_{2\pm x}V_3P_2O_{13}$ (x= 0 and 1): a promising cathode material for sodium-ion batteries. *J. Mater. Chem. A*, 6(16):6947–6958, 2018.

[303] A. Haddad and T. Jouini. $Na_2V_3P_2O_{13}$: Préparation et structure cristalline. *J. Solid State Chem.*, 112(2):218–221, 1994.

[304] F. Shouib. *Private discussions within the AMSES project regarding the PhD project in progress: Atomic scale modeling via molecular dynamics and machine learning of Na_2O-V_2O_5-TeO_2 galsses (G) and glass ceramic (GC) cathodes.* PhD thesis, University of Limoges, 2024.

[305] A. Khanna, M. Fábián, A.-C. Dippel, O. Gotowski, et al. Structure of lithium tellurite and vanadium lithium tellurite glasses by high-energy X-ray and neutron diffraction. *Acta Crystallogr. B Struct. Sci. Cryst. Eng. Mater.*, 77(2):275–286, 2021.

[306] A.I. Priven. General method for calculating the properties of oxide glasses and glass forming melts from their composition and temperature. *Glass Technol.*, 45(6):244–254, 2004.

[307] SciGlass. https://github.com/epam/SciGlass/releases.

[308] S. D. Wansi Wendji, R. Piotrowski, A. Familiari, C. Massobrio, M. Boero, C. Tugene, F. E. Shuaib, D. Hamani, P.-M. Geffroy, A. Pedone, ..., and G. Ori. Structure, bonding and ionic mobility in na-vpo glasses for energy storage applications. *Chem. Commun.*, 2025.

[309] T.L. Pham, M. Guerboub, A. Bouzid, M. Boero, C. Massobrio, Y.H. Shin, and G. Ori. Unveiling the structure and ion dynamics of amorphous na 3- x oh x cl antiperovskite electrolytes by first-principles molecular dynamics. *J. Mater. Chem. A*, 2023.

[310] T.-L. Pham, M. Guerboub, S.D. Wendj, A. Bouzid, C. Tugène, M. Boero, C. Massobrio, Y.-H. Shin, and G. Ori. Structural properties of amorphous Na_3OCl electrolyte by first-principles and machine learning molecular dynamics. *arXiv preprint arXiv:2404.11442*, 2024.

[311] G. Sivaraman, A.N. Krishnamoorthy, M. Baur, C. Holm, M. Stan, G. Csányi, C. Benmore, and Á. Vázquez-Mayagoitia. Machine-learned interatomic potentials by active learning: amorphous and liquid hafnium dioxide. *Npj Comput. Mater.*, 6(1):104, 2020.

[312] I.G. Austin and N. Fr. Mott. Polarons in crystalline and non-crystalline materials. *Adv. Phys.*, 18(71):41–102, 1969.

[313] L. Murawski, R.J. Barczynski, and A. Rybicka. V_2O_5-P_2O_5 glass and its polaron transport properties derived from molecular dynamic simulations of structure. In *dielectric and related phenomena: materials physico-chemistry, spectrometric investigations, and applications*, volume 3181, pages 136–141. SPIE, 1997.

[314] J. Nikolić, L. Pavić, A. Šantić, P. Mošner, L. Koudelka, D. Pajić, and A. Moguš-Milanković. Novel insights into electrical transport mechanism in ionic-polaronic glasses. *J. Am. Ceram. Soc.*, 101(3):1221–1235, 2018.

[315] A. Moguš-Milanković, A. Šantić, S. T. Reis, K. Furić, and D. E. Day. Mixed ion–polaron transport in Na_2O–PbO–Fe_2O_3–P_2O_5 glasses. *J. Non-cryst. Solids*, 342(1-3):97–109, 2004.

[316] M.-C. Ungureanu, M. Lévy, and J.-L. Souquet. Electrical properties of glasses of the Na_2O-V_2O_2-P_2O_5 system. *Ceramics Silikáty*, 44:81–85, 2000.

[317] M. Wasiucionek, J. Garbarczyk, P. Kurek, and W. Jakubowski. Electrical properties of glasses of the Na_2O-V_2O_2-P_2O_5 system. *Solid State Ion.*, 70:346–349, 1994.

[318] A. Sharma, I. Suzuki, K. Toyooka, T. Ishiyama, J. Nishii, and T. Omata. Replacing Sodium Ions with Protons in Vanadophosphate Glass: Suppression of Electronic Conduction by Local Structural Change around Vanadium Ions. *J. Phys. Chem. C*, 2024.

[319] Z. Wang, S.-H. Luo, X. Zhang, S. Guo, P. Li, and S. Yan. Glass and glass ceramic electrodes and solid electrolyte materials for lithium ion batteries: A review. *J. Non-Cryst. Solids*, 619:122581, 2023.

[320] S. Marijan, M. Razum, T. Klaser, P. Mošner, L. Koudelka, Ž. Skoko, J. Pisk, and L. Pavić. Tailoring structure for improved sodium mobility and electrical properties in V_2O_5–Nb_2O_5–P_2O_5 glass (es)-(ceramics). *J. Phys. Chem. Solids*, 181:111461, 2023.

[321] S. Renka, L. Pavić, G. Tricot, P. Mošner, L. Koudelka, A. Moguš-Milanković, and A. Šantić. A significant enhancement of sodium ion conductivity in phosphate glasses by addition of wo 3 and moo 3: The effect of mixed conventional–conditional glass-forming oxides. *Phys. Chem. Chem. Phys.*, 23(16):9761–9772, 2021.

[322] J.C. Bazan, J.A. Duffy, M.D. Ingram, and M.R. Mallace. Conductivity anomalies in tungstate-phosphate glasses: evidence for an ion-polaron interaction? *Solid State Ion.*, 86:497–501, 1996.

[323] J.E. Garbarczyk, M. Wasiucionek, P. Machowski, and W. Jakubowski. Transition from ionic to electronic conduction in silver–vanadate–phosphate glasses. *Solid State Ion.*, 119(1-4):9–14, 1999.

[324] L. Ngamwongwan, I. Fongkaew, P. Phonsuksawang, T. Siritanon, P. Hirunsit, S. Jungthawan, and S. Suthirakun. On the origin of ion intercalation and conductivity enhancement in sn-doped V_2O_5 cathodes of Li-ion batteries: A computational study. *J. Phys. Chem. C*, 127(24):11526–11535, 2023.

[325] X. Zhang, X. Rui, D. Chen, H. Tan, D. Yang, S. Huang, and Y. Yu. $Na_3V_2(PO_4)_3$: an advanced cathode for sodium-ion batteries. *Nanoscale*, 11(6):2556–2576, 2019.

[326] K. J. Laidler. The development of the arrhenius equation. *J. Chem. Educ.*, 61(6):494, 1984.

[327] A. Pedone, G. Malavasi, A. N. Cormack, U. Segre, and M. C. Menziani. Elastic and dynamical properties of alkali-silicate glasses from computer simulations techniques. *Theor. Chem. Acc.*, 120:557–564, 2008.

[328] A.N. Cormack, J. Du, and T.R. Zeitler. Alkali ion migration mechanisms in silicate glasses probed by molecular dynamics simulations. *Phys. Chem. Chem. Phys.*, 4(14):3193–3197, 2002.

[329] J. Wiktor, F. Ambrosio, and A. Pasquarello. Role of polarons in water splitting: the case of $BiVO_4$. *ACS Energy Lett.*, 3(7):1693–1697, 2018.

[330] R. Defrance, B. Sklénard, M. Guillaumont, J. Li, and M. Freyss. Ab initio study of electron mobility in V_2O_5 via polaron hopping. *Solid State Electron.*, 198:108455, 2022.

[331] A.L. Shluger, K.P. Mckenna, P.V. Sushko, D.M. Ramo, and A.V. Kimmel. Modelling of electron and hole trapping in oxides. *Model. Simul. Mat. Sci. Eng.*, 17(8):084004, 2009.

[332] H. Seo, Y. Ping, and G. Galli. Role of point defects in enhancing the conductivity of $BiVO_4$. *Chem. Mater.*, 30(21):7793–7802, 2018.

[333] C.S. Ahart, K.M. Rosso, and J. Blumberger. Electron and hole mobilities in bulk hematite from spin-constrained density functional theory. *J. Am. Chem. Soc.*, 144(10):4623–4632, 2022.

[334] C.S. Ahart, K.M. Rosso, and J. Blumberger. Implementation and validation of constrained density functional theory forces in the CP2K package. *J. Chem. Theory Comput.*, 18(7):4438–4446, 2022.

[335] M. Razum, L. Pavić, D. Pajić, J. Pisk, P. Mošner, L. Koudelka, and A. Šantić. Structure–polaronic conductivity relationship in vanadate–phosphate glasses. . *Am. Ceram. Soc.*, 2024.

[336] B. Kaduk, T. Kowalczyk, and T. Van Voorhis. Constrained density functional theory. *Chem. Rev.*, 112(1):321–370, 2012.

[337] T.A. Young, T. Johnston-Wood, V.L. Deringer, and F. Duarte. A transferable active-learning strategy for reactive molecular force fields. *Chem. Sci.*, 12(32):10944–10955, 2021.

[338] D. Milardovich, D. Waldhoer, M. Jech, A.-M. B. El-Sayed, and T. Grasser. Building robust machine learning force fields by composite gaussian approximation potentials. *Solid State Electron.*, 200:108529, 2023.

[339] D. Milardovich, C. Wilhelmer, D. Waldhoer, L. Cvitkovich, G. Sivaraman, and T. Grasser. Machine learning interatomic potential for silicon-nitride (si_3n_4) by active learning. *J. Chem. Phys.*, 158(19), 2023.

[340] Y. Hu, J. Musielewicz, Z.W. Ulissi, and A.J. Medford. Robust and scalable uncertainty estimation with conformal prediction for machine-learned interatomic potentials. *Mach. Learn.: Sci. Technol.*, 3(4):045028, 2022.

[341] F. Shang, J. Wei, J. Xu, H. Zhang, Y. Xia, G. Zhu, K. Jiang, G. Chen, Z. Ye, and H. Xu. Boosting energy storage performance of glass ceramics via modulating defect formation during crystallization. *Adv. Sci.*, 11(7):2307011, 2024.

[342] A. Ibrahim, K. Kubo, S. Watanabe, S. Shiba, I. Khan, B. Zhang, Z. Homonnay, E. Kuzmann, L. Pavić, A. Santić, et al. Enhancement of electrical conductivity and thermal stability of iron-or tin-substituted vanadate glass and glass-ceramics nanocomposite to be applied as a high-performance cathode active material in sodium-ion batteries. *J. Alloys Compd.*, 930:167366, 2023.

Scientific productions

Scientific publications

1. **S.D. Wansi Wendji**, C. Massobrio, M. Boero, C. Tugène, E. Levchenko, F. Shuaib, R. Piotrowski, D. Hamani, G. Delaizir, P.-M. Geffroy, P. Thomas. O. Masson, A. Bouzid, G. Ori 'Quantitative Assessment of the Structure and Bonding Properties of $50V_xO_y$-$50P_2O_5$ Glass by Classical and Born-Oppenheimer Molecular Dynamics' *J. Non-Cryst. Solids*, 634, 122967, **(2024)**. DOI: 10.1016/j.jnoncrysol.2024.122967.

2. T.-L. Pham, M. Guerboub, **S.D. Wansi Wendji**, A. Bouzid, C. Tugène, M. Boero, C. Massobrio, Y.-H. Shin and G. Ori 'Structural properties of amorphous Na_3OCl electrolyte by first-principles and machine learning potential molecular dynamics' *arXiv preprint*, **(2024)**. DOI: arXiv:2404.11442.

3. C. Massobrio, I.A. Essomba, M. Boero, C. Diarra, M. Guerboub, K. Ishisone, A. Lambrecht, E. Martin, I. Morrot-Woisard, G. Ori, C. Tugène, **S.D. Wansi Wendji** 'On the actual difference between the Nosé and the Nosé-Hoover thermostats: a critical review of canonical temperature control by molecular dynamics' *Phys. Status Solids B* 261, 2300209 **(2024)**. DOI: 10.1002/pssb.202300209; HAL: hal-04280276.

4. M. Guerboub, **S.D. Wansi Wendji**, C. Massobrio, A. Bouzid, M. Boero, G. Ori, and E. Martin. 'Impact of the local atomic structure on the thermal conductivity of amorphous $Ge_2Sb_2Te_5$.' *J. Chem. Phys.* 158, 084504 **(2023)**. DOI: 10.1063/5.0139590; HAL: hal-04014339.

5. **S.D. Wansi Wendji**, R. Piotrowski, C. Massobrio, M. Boero, C. Tugène, F. Shuaib, D. Hamani, P.-M. Geffroy, P. Thomas, A. Bouzid, O. Masson, G. Delaizir, G. Ori 'Enhanced structural description of sodium vanadium phosphate glasses: A combined experimental and molecular dynamics study', *J. Non-Cryst. Solids*, 655, 123420, **(2025)**. DOI: 10.1016/j.jnoncrysol.2025.123420

6. **S.D. Wansi Wendji**, R. Piotrowski, A. Familiari, C. Massobrio, M. Boero, C. Tugène, F. Shuaib, D. Hamani, P.-M. Geffroy, P. Thomas, A. Pedone, A. Bouzid, O. Masson, G. Delaizir, G. Ori 'Structure, bonding and ionic mobility in Na-VPO glasses for energy storage applications', *Chem. Commun.*, **(2025)**.
DOI: 10.1039/D5CC00443H

7. F. Shuaib, A. Bouzid, R. Piotrowski, G. Delaizir, P.-M. Geffroy, D. Hamani, R. Raghvender, **S. D. Wansi Wendji**, C. Massobrio, M. Boero, G. Ori, P. Thomas, O. Masson 'Atomic scale structure and dynamical properties of $(TeO_2)_{1-x}$-$(Na_2O)_x$ glasses through first-principles modeling and XRD measurements' *arXiv preprint*, (2025). DOI: arXiv:2506.04137

8. **S.D. Wansi Wendji**, C. Massobrio, M. Boero, C. Tugène, A. Bouzid, G. Ori 'Structural order and dynamical properties of liquid $GeSe_2$ by molecular dynamics with

first-principles accuracy up to 1 million atoms model with a machine learning potential, *in preparation*.

Contribution at national/international conferences, workshops, and Schools

1. The 3rd Summer School on Materials Modeling (ModMat 2024). Banyuls-sur-Mer, France, August 19-23 **(2024)**.

2. **S.D. Wansi Wendji**, C. Massobrio, M. Boero, C. Tugène, E. Levchenko, A. Bouzid, G. Ori, *Structural order of liquid $GeSe_2$ by molecular dynamics with first-principles accuracy up to one million atoms model with a machine-learned potential.* Oral presentation, International Workshop on Advanced Ceramics, 9^{th} edition (IWAC 09), Limoges, France, September 26-29 **(2023)**.

3. **S.D. Wansi Wendji**, C. Massobrio, M. Boero, C. Tugène, E. Levchenko, A. Bouzid, G. Ori, *Molecular Dynamics with First-Principles Accuracy: Structural Order of Liquid $GeSe_2$ using a Machine-Learned Potential.* Poster + flash oral presentation, Paris International School on Advanced Computational Materials (PISACMS 2023). Sorbonne University, Paris, France, August 28 - September 1^{st} **(2023)**.

4. **S.D. Wansi Wendji**, C. Massobrio, M. Boero, C. Tugène, E. Levchenko, A. Bouzid, G. Ori *First-principles and Machine Learning Modelling of Complex Oxide-based Cathode Materials.* Oral presentation, Doctoral school 182 - PhD Students' Congress, University of Strasbourg, France, March 23 **(2023)**.

5. **S.D. Wansi Wendji**, C. Massobrio, M. Boero, C. Tugène, E. Levchenko, A. Bouzid, G. Ori, *First-principles and machine-learned interatomic potential molecular dynamics for $GeSe_2$ liquid and glass.* Oral presentation, European Materials Research Society (E-MRS) Fall Meeting, Symp.C: Predicting materials properties by first-principles and machine learning modeling. Warsaw, Poland, September 19-22 **(2022)**. Graduate Student, Award Prize E-MRS 2022.

6. **S.D. Wansi Wendji**, C. Massobrio, M. Boero, C. Tugène, E. Levchenko, A. Bouzid, G. Ori, *Structure and bonding of vanado-phosphate-based glasses: insights by first-principles molecular dynamics.* Poster + flash oral presentation, European Materials Research Society (E-MRS) Fall Meeting, Symp.C: Predicting materials properties by first-principles and machine learning modeling. Warsaw, Poland, September 19-22 **(2022)**.

7. **S.D. Wansi Wendji**, C. Massobrio, M. Boero, C. Tugène, E. Levchenko, A. Bouzid, G. Ori, *First-principles and machine learning interatomic potential molecular dynamics for $GeSe_2$ glass: Structural analysis.* Poster presentation, The GAP Developers & Users Meeting 2022 (GAP D&U 2022), the Otaniemi campus of Aalto University, Espoo, Finland, August 2-5 **(2022)**.

8. The 16th Conference on Physics of Non-Crystalline Solids (PNCS16). University of Kent, Canterbury, UK, July 10-15 **(2022)**.

9. **S.D. Wansi Wendji**, C. Massobrio, M. Boero, C. Tugène, E. Levchenko, A. Bouzid, G. Ori, *Machine learning interatomic potential classical molecular dynamics for $GeSe_2$ glass: Structural analysis.* Poster presentation, European Spring School in Quantum Science and Technology, Strasbourg, France, April 10-14 **(2022)**.

Résumé détaillé de la thèse en français

Introduction

La demande mondiale en énergie connaît une forte croissance, portée par son rôle central dans les activités humaines. Les combustibles fossiles, encore dominants, sont responsables de fortes émissions de CO_2, contribuant significativement au réchauffement climatique et à la dégradation environnementale. Ce constat impose une transition urgente vers des sources d'énergie renouvelables (solaire, éolienne, hydraulique), plus durables. Toutefois, leur intermittence, à la fois temporelle et géographique, limite leur intégration massive. Dans ce contexte, les systèmes de stockage d'énergie apparaissent comme des solutions clés, allant des dispositifs portables aux infrastructures de grande envergure.
Parmi les technologies de stockage, les batteries lithium-ion (LIB) se distinguent par leur densité énergétique, leur efficacité et leur durabilité (Whittingham, *Chem. Rev.*, **104**, 10, (2004)). Cependant, la rareté du lithium, sa répartition géographique inégale et l'augmentation de son coût appellent à explorer des voies complémentaires. Les batteries sodium-ion (NIB), partageant des similarités structurales et fonctionnelles avec les LIB, suscitent un intérêt croissant (Ong et al. *Energy Environ. Sci.*, **4**, 9, (2011)). Bien que les ions Na^+ soient plus lourds et volumineux que les Li^+, leur diffusion peut être facilitée dans des structures cristallines ouvertes, suggérant un fort potentiel pour les applications à grande échelle (Usiskin et al. *Nat. Rev. Mater.*, **6**, 11, (2021)).
Les avancées récentes en science des matériaux ont permis de développer des composés aux performances électrochimiques améliorées. Néanmoins, les NIB doivent encore surmonter plusieurs verrous technologiques avant une commercialisation viable. Les matériaux polyanioniques vitreux et vitrocéramiques, notamment en tant qu'électrodes, offrent des perspectives prometteuses: sécurité accrue, meilleure durabilité, procédés de fabrication simplifiés (Ni et al. *Adv. Sci.*, **4**, 3, (2017)). Toutefois, leur adoption reste freinée par un manque de compréhension fondamentale à l'échelle atomique, concernant leur structure, la nature des liaisons chimiques et les mécanismes de transport ionique.
Ce travail de recherche s'inscrit dans cette problématique et se concentre sur l'étude atomistique de verres et vitrocéramiques polyanioniques sodium-vanadium-phosphate (NVP), inspirée des performances observées pour leurs équivalents au lithium (Sapra et al. *Wiley Interdiscip. Rev.: Energy Environ.*, **10**, 5, (2021)). Le manque de données sur les systèmes vitreux NVP entrave le développement de cathodes performantes adaptées aux NIB.
L'objectif principal est d'étudier des matériaux NVP désordonnés potentiellement efficaces comme électrodes pour le stockage d'énergie. Pour ce faire, des approches de modélisation à l'échelle atomique (DFT-FPMD) et d'apprentissage automatique sont mobilisées pour concevoir et étudier des verres NVP aux propriétés structurales, chimiques et électrochimiques optimisées. En parallèle, une base de données issue des calculs DFT-FPMD (énergies, forces, ...) est construite afin de développer un potentiel interatomique basé sur l'intelligence artificielle (MLIP), permettant l'exploration efficace de modèles

réalistes de verres tout en conservant une précision de niveau quantique. Les résultats sont structurés en trois volets principaux:
(i) Evaluation des performances des champs de force empiriques pour la modélisation atomique du système binaire $50V_xO_y$–$50P_2O_5$ (VP50) et proposition d'une approche combinant la dynamique moléculaire classique (CMD) et ab-initio (BOMD).
(ii) Modélisation des systèmes ternaire αNa_2O – βV_xO_y – γP_2O_5 (NVP) par CMD et BOMD avec une analyse approfondie de leurs propriétés structurales, magnétiques, électroniques et dynamiques.
(iii) Développement d'un potentiel MLIP pour les verres NVP, basé sur les données DFT-FPMD obtenues, afin de modéliser et caractériser efficacement ces matériaux et identifier les perspectives de leur application dans les batteries à l'état solide.

Système binaire $50V_xO_y$–$50P_2O_5$ (VP50)

Ce premier volet de cette thèse, s'intéresse aux propriétés du système binaire vanadophosphate (La publication [1] présente de manière synthétique l'ensemble des résultats obtenus pour ce système). La coexistence de plusieurs états d'oxydation du vanadium (V^{5+}, V^{4+} et V^{3+}), associés à des nombres de coordination variables, engendre une structure de réseau vitreux particulièrement complexe, constituée d'un large éventail d'unités structurales. Cette complexité structurale rend la caractérisation atomique précise difficile, ce qui justifie le recours à des outils de modélisation quantitative afin d'appréhender plus finement la topologie de ces systèmes amorphes (voir également notre contribution sur les matériaux à changement de phase dans la publication [2]).
Trois champs de force classiques sélectionnés dans la littérature ont été utilisés pour réaliser des simulations de dynamique moléculaire classique (CMD) (Ori et al., *J. Non-Cryst. Solids*, **357**, 14 (2011); Bertani et al., *Phys. Rev. Mater.*, **5**, 4 (2021); Lu et al., *J. Phys. Chem. B*, **125**, 44 (2021); Malavasi et al., *Acta Mater.*, **229**, 117801 (2022)). Les simulations ont été effectuées à l'aide des codes DL-POLY et LAMMPS avec un pas d'intégration de 1 fs.
Pour chaque champ de force, quatre configurations initiales aléatoires contenant respectivement 218 et 5450 atomes ont été générées. Les tailles des cellules de simulation ont été définies de manière à reproduire la densité expérimentale du verre VP50. Les simulations ont suivi un protocole thermique impliquant des cycles de fusion et de trempe. Le contrôle de la température a été assuré par l'application du thermostat de Nosè–Hoover (voir notre contribution sur le développement des équations de Nosè dans la publication [3]).
À l'issue de chaque simulation, les 150 ps finaux d'une trajectoire de 300 ps à 300 K ont été retenus pour l'analyse. La structure finale est obtenue par la moyenne des quatre répliques associées à chaque champ de force.
La simulation *ab-initio* est réalisée à 300 K à l'aide du code CP2K à partir des configurations issues des simulations CMD. Cette approche (CMD + courte BOMD), est notée *s*-BOMD. Plus précisément, la simulation BOMD est réalisée à partir des structures extraites des configurations CMD à 300 K, pour 5 ps en utilisant la fonctionnelle d'échange-corrélation PBE, suivie de 500 fs avec la fonctionnelle hybride PBE0 (Adamo et al. *J. Chem. Phys.*, **110**, 13, (1999)). Les 3 ps finaux de la trajectoire de chaque réplique, obtenus au niveau PBE, combinés à 500 fs supplémentaires au niveau PBE0 à $T = 300$ K, ont été utilisés pour caractériser les propriétés structurales. La dernière étape de *s*-BOMD avec la fonctionnelle hybride PBE0 s'est révélée essentielle pour assurer la convergence de la localisation du spin sur les sites V. Son influence sur les propriétés structurales a cependant été négligeable. L'analyse de la structure électronique et des propriétés de liaison a été réalisée à partir de la densité d'états électronique (DOS) et des fonctions de Wannier localisées (MLWF) (Marzari et al. *Phys. Rev. B*, **56**, 20, (1997)).

Propriétés électroniques et spéciation des sites vanadium dans le verre

Le vanadium étant un métal de transition, la stabilité du verre dépends du ratio des différents états d'oxydation dans sa matrice. Du point de vue de la modélisation à l'échelle atomique, les simulations CMD utilisent un étiquetage prédéfini pour représenter les sites de vanadium (V) dans les verres, chaque état d'oxydation du V étant attribué en fonction des paramètres du champ de force considéré. En revanche, les simulations BOMD, comme toutes les approches fondées sur la DFT, ne nécessitent aucun étiquetage a priori des sites de V. La spéciation finale du vanadium est déterminée uniquement par le nombre total d'atomes d'oxygène, conformément à la composition chimique $50V_xO_y[sV_2O_5–zV_2O_4–wV_2O_3]–50P_2O_5$.
Les méthodes d'analyse de la charge électronique, telles que celles de Mulliken et Bader, n'ont pas permis de distinguer les différents sites V. Pour surmonter cette limitation et quantifier avec précision les espèces de V présentes, nous avons utilisé des projections locales de densité de spin sur les sites de vanadium, notamment lors du calcul des bandes interdites (voir Figure 1). Cette analyse a été menée à l'aide des fonctionnelles PBE et hybride PBE0. Il est important de noter qu'avec la fonctionnelle PBE, les valeurs de bandes interdites obtenues sont toutes inférieures à 0.2 eV, tandis qu'avec PBE0, une meilleure précision est atteinte avec des valeurs bien définies comprises entre 2.3 et 2.8 eV. Ces résultats indiquent que le verre VP50 se comporte comme un semi-conducteur à large bande interdite, doté d'un magnétisme faible mais mesurable, à l'instar de certaines phases cristallines de phosphates vanadyles $VOPO_4$, dont les gaps rapportés se situent entre 2.5 et 2.9 eV (Zheng et al., *Phys. Scripta*, **97**, 10 (2022)). La différence d'énergie entre les états de spin 'up' et 'down' rend compte du caractère magnétique non négligeable du verre VP50, attribuable à la présence potentielle de sites V^{4+} et V^{3+}.

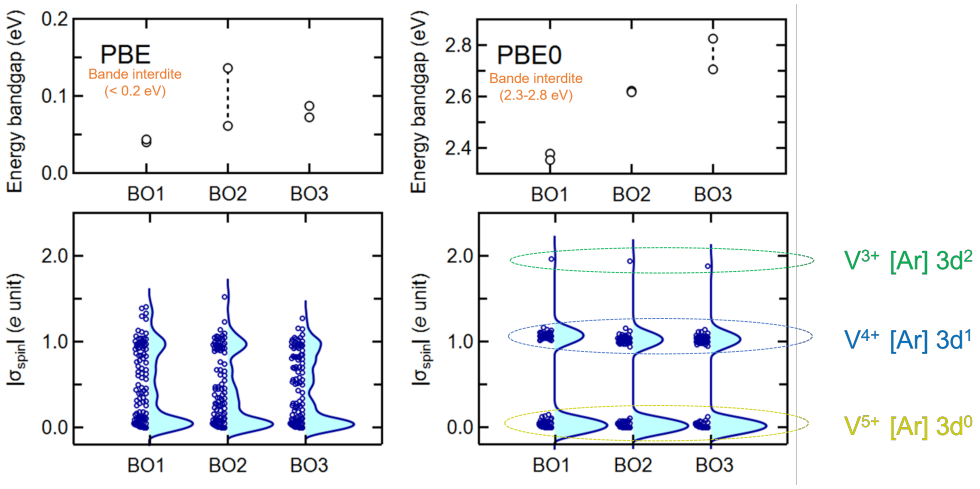

Figure 1. Valeurs moyennes de la largeur de bande interdite (en haut, en eV) et des densités de spin σ_{spin} (en bas, en unités e) calculées pour chaque site vanadium avec la fonctionnelle PBE (à gauche) et PBE0 (à droite) pour les trois modèles *s*-BOMD (BO1, BO2, BO3). Il convient de noter que les valeurs de la bande interdite pour les états de spin up et down sont indiquées en tant que moyenne des quatre configurations simulées pour chaque modèle *s*-BOMD. Les densités de spin sont indiquées sous forme de diagrammes de violon montrant la distribution des points de données individuels des quatre configurations pour chaque modèle *s*-BOMD simulé. À l'échelle PBE0, on observe une ouverture de la bande interdite (2.3–2.8 eV) ainsi qu'une organisation de la densité de spin autour des valeurs 0, 1 et 2, correspondant respectivement aux configurations des états d'oxydation V^{5+}, V^{4+} et V^{3+}.

Contrairement à la fonctionnelle PBE, où les densités de spin sont réparties aléatoirement, l'utilisation de la fonctionnelle PBE0 permet de mettre en évidence trois groupes bien définis de densités de spin σ_{spin} pour les sites de vanadium (voir Figure 1). En comparaison, tous les atomes de P et O présentent des valeurs inférieures à 0.05. Ces valeurs pour

les sites de V (∼2, ∼1, ∼0) correspondent respectivement aux états d'oxydation V^{3+}, V^{4+} et V^{5+}, en lien avec leurs configurations électroniques de valence [Ar]$3d^2$, [Ar]$3d^1$ et [Ar]$3d^0$. Cette observation est cohérente avec le caractère magnétique des ions V^{3+} et V^{4+}, et le caractère non magnétique des ions V^{5+}.
Les pourcentages assignés aux différents états d'oxydation du vanadium dans les trois modèles *s*-BOMD sont de 0.8 % pour V^{3+}, 35.9 % pour V^{4+} et 63.3 % pour V^{5+}, en excellent accord avec les données expérimentales rapportées par Hoppe et al. *J. Non-Cryst. Solids*, **358**, (2012): 35.2 % pour V^{4+}, 64.8 % pour V^{5+}, et une fraction négligeable de V^{3+}.
Sur la base de ces résultats, la composition chimique du système peut être réécrite: $50V_xO_y[31.6V_2O_5–18.0V_2O_4–0.4V_2O_3]–50P_2O_5$, indiquant clairement une teneur négligeable en V_2O_3. Cette composition contraste avec la formulation classique $50V_2O_5–50P_2O_5$ fréquemment citée dans la littérature.

Propriétés structurales du verre VP50

La Figure 2 présente la fonction de corrélation totale $T(r)$ (dans l'espace réel) ainsi que le facteur de structure $S^X(k)$ (dans l'espace réciproque), obtenu par transformation de Fourier de $T(r)$. Ces grandeurs ont été calculées à partir des simulations CMD et *s*-BOMD. Les résultats sont comparés aux données expérimentales de Hoppe *et al.*. Seules les données issues de la diffraction des rayons X sont présentées dans ce résumé, car les rayons X, contrairement aux neutrons, sont plus sensibles à l'environnement atomique complexe du vanadium. Cette sensibilité accrue s'explique par la très faible longueur de diffusion des neutrons pour le vanadium (−0.382 fm). Les résultats structuraux obtenus par diffraction des neutrons sont quant à eux détaillés dans le corps de la thèse (en Anglais).

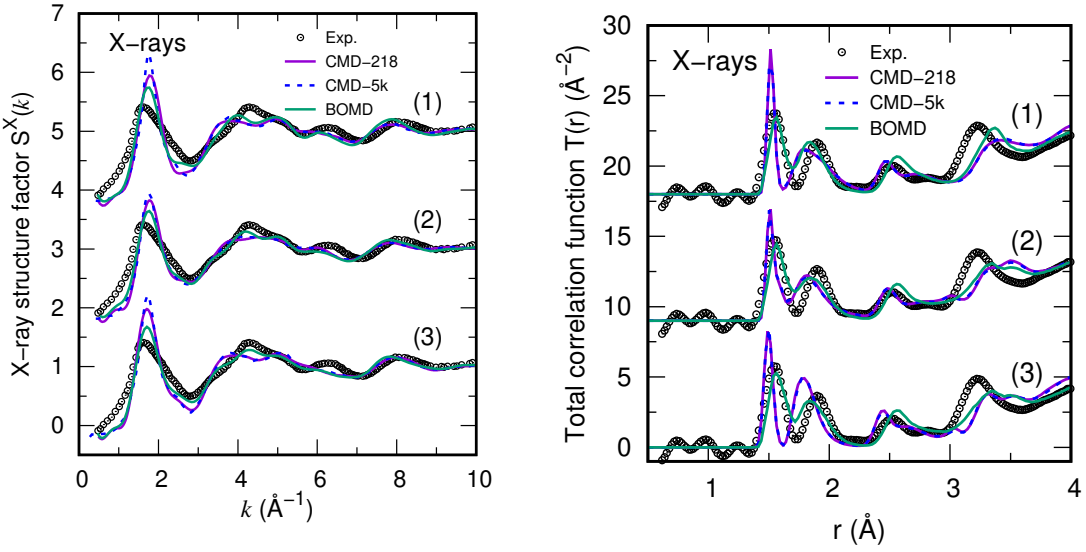

Figure 2. Facteurs de structure (à gauche) et fonctions de corrélation totale (à droite) et issus de la diffraction des rayons X pour le système VP50 simulé par CMD et *s*-BOMD, pour les trois modèles numérotés (1), (2) et (3). L'analyse est présentée pour le modèle à 218 atomes (CMD en violet et BOMD en vert), le modèle à 5450 atomes (uniquement CMD, ligne bleue en pointillés), ainsi que les données expérimentales (cercles noirs) (Hoppe et al. *J. Non-Cryst. Solids*, **358**, (2012)).

L'accord entre les résultats théoriques et expérimentaux est quantifié par le facteur de qualité R_χ, qui mesure le degré de désaccord entre la simulation et l'expérience (voir

Eq.(1)).

$$R_\chi = 100 \times \left(\frac{\sum_i \left[\mathrm{Exp}^{(i)} - \mathrm{Sim}^{(i)} \right]^2}{\sum_i \left[\mathrm{Exp}^{(i)} \right]^2} \right)^{1/2}, \quad (1)$$

Pour les trois modèles *s*-BOMD, les valeurs de R_χ associées aux données $S^X(k)$ se situent dans l'intervalle 8.4–9.8 contre 11.3–12.8 pour les modèles CMD. Ce qui met en évidence une amélioration significative des résultats obtenus par *s*-BOMD par rapport à ceux issus de CMD pour l'évaluation du facteur de structure total en rayons X indiquant une amélioration importante de la description de l'environnement local des sites V dans VP50. Concernant la fonction $T(r)$, chacun des trois modèles CMD présente une surestimation notable de l'intensité du premier pic, en comparaison avec les données issues des simulations BOMD. Néanmoins, les trois modèles *s*-BOMD montrent sans équivoque une amélioration par rapport aux modèles CMD en ce qui concerne l'intensité de ce premier pic. Il est remarquable que les résultats obtenus restent très similaires pour l'ensemble des modèles BOMD, indépendamment du schéma CMD initial utilisé. Il convient également de souligner que le modèle CMD(2) présente les plus faibles valeurs de R_χ, en comparaison avec CMD(1) et CMD(3). On note des variations négligeables entre les modèles CMD à 5450 et 218 atomes.
Cette analyse structurale est complétée et détaillée dans la thèse par: les fonctions de corrélation partielle, les nombres de coordination, l'identification des unités structurales, la distribution des angles de liaison, les paramètres d'ordre local ainsi que la connectivité du réseau. Il convient néanmoins de souligner que, concernant la fonction de corrélation partielle V−O, qui reflète les interactions chimiques entre le vanadium et l'oxygène, une différence marquée est observée entre les modèles CMD et *s*-BOMD. L'image des liaisons V−O issue de $g_{\mathrm{VO}}(r)$ diffère significativement selon la méthode de simulation. Plus précisément, les modèles CMD présentent un premier pic de $g_{\mathrm{VO}}(r)$ centré autour de 1.79–1.81 Å, tandis que les modèles *s*-BOMD montrent un comportement distinct, caractérisé par un pic principal à environ 1.83–1.84 Å, précédé d'un petit pic bien défini (voir Figure 3(Gauche)). Ce dernier témoigne de la présence de courtes liaisons de type vanadyle (V=O), caractéristiques des unités VO_n. Une analyse DFT, basée sur les fonctions localisées de Wannier, est également réalisée afin d'élucider plus en détail les interactions chimiques dans le verre VP50.

Liaisons chimiques dans le verre VP50

Afin d'approfondir la compréhension des liaisons chimiques, nous avons analysé les centres des fonctions de Wannier localisées (WFC), en mettant l'accent sur ceux situés à proximité des atomes d'oxygène. Ce choix s'explique par la forte électronégativité de l'oxygène dans le verre VP50, tandis que ni le phosphore ni le vanadium ne contribuent via des doublets non liants. Nous avons ainsi examiné la fonction de corrélation radiale $g_{\mathrm{O-W}}(r)$ calculée au niveau PBE0 et illustrée en Figure 3(Droite). La fonction de corrélation partielle $g_{\mathrm{O-W}}(r)$ révèle une bande distincte s'étendant de 0.2 à 0.5 Å, structurée autour de trois maxima principaux, accompagnés d'une contribution mineure autour de 0.23 Å. Parmi ces maxima, le plus intense se situe à 0.29 Å, tandis que les deux autres sont centrés respectivement à 0.40 Å et 0.47 Å. Les profils de $g_{\mathrm{O-W}}(r)$ issus des trois modèles *s*-BOMD sont remarquablement similaires, ne différant que par de faibles variations d'intensité des pics.
L'arrangement des WFC dans l'environnement atomique local entourant les unités PO_4 tétraédrique et $\mathrm{V0}_n$ (tétraédrique, pyramidale à base carrée, trigonale bi-pyramidale ou octaédrale) reflète la présence de trois types distincts de WFC, que l'on peut corréler aux distances identifiées par les trois maxima de $g_{\mathrm{O-WFC}}(r)$: (i) WFC associés aux doublets

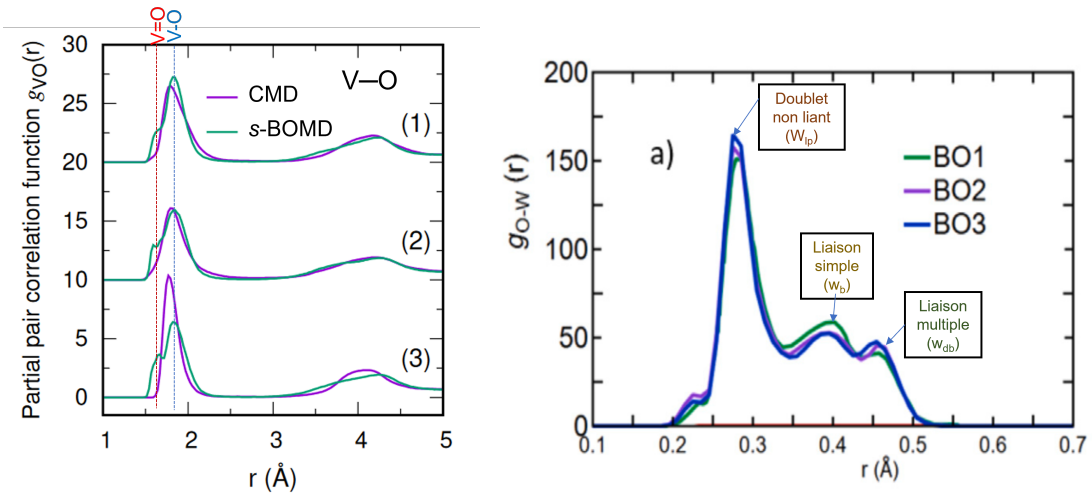

Figure 3. **Gauche**: Fonction de corrélation partielle $g_{\mathrm{VO}}(r)$ pour les modèles (1), (2) et (3), comparant les résultats obtenus par CMD et *s*-BOMD. Les positions caractéristiques des liaisons V−O et V=O sont indiquées. **Droite**: Fonction de corrélation partielle $g_{\mathrm{O-W}}(r)$ décrivant les distances entre les atomes d'oxygène et les centres de Wannier.

non liants, caractérisés par des distances O–WFC très courtes (0.29 Å); (ii) WFC individuels impliqués dans des liaisons simples de type P−O (∼1.60 Å) ou V−O (<2.4 Å) présentant une distance O–WFC intermédiaire (0.40 Å); (iii) WFC doubles ou triples, impliqués dans des liaisons plus courtes (P=O: ∼1.49–1.54 Å; V=O: ∼1.60–1.72 Å), et se situant à O–WFC plus longue (0.48 Å). L'ensemble des WFC se trouvent systématiquement plus proches des atomes d'oxygène que des atomes de phosphore ou de vanadium, ce qui témoigne du caractère iono-covalent fortement polarisé des liaisons P−O et V−O. La densité électronique de valence y est localisée préférentiellement au voisinage des sites oxygène.

Les longueurs de liaison simples et de type vanadyle obtenues par l'analyse des WFC présentent une meilleure concordance avec les valeurs expérimentales rapportées que celles extraites de la fonction de corrélation $g_{\mathrm{V-O}}(r)$. Ces distances augmentent avec le degré de coordination du vanadium, par exemple pour le V^{5+}: ∼1.86 Å (VO_4)< ∼1.92 Å (VO_5)< ∼2.00 Å (VO_6), en accord avec les observations expérimentales (Hoppe et al.; Boivin et al., *Molecules*, **26**, 5 (2021)).

Ce premier volet de la thèse met en évidence les limites des champs de force empiriques testés, qui s'avèrent insuffisamment précis pour différencier les états d'oxydation du vanadium dans le verre VP50. En revanche, les simulations *s*-BOMD offrent une description nettement plus fiable et quantitative de la spéciation chimique, des liaisons et de l'organisation structurale de ce système.

Systèmes ternaires $\alpha\mathbf{Na_2O} - \beta\mathbf{V}_x\mathbf{O}_y - \gamma\mathbf{P_2O_5}$ (NVP)

Dans ce deuxième volet de la thèse, différentes concentrations du modificateur Na_2O ont été introduites dans des matrices VP afin de produire quatre compositions de verres NVP. Ces systèmes ont été sélectionnés en concertation avec nos collaborateurs expérimentaux dans le cadre du projet ANR AMSES (entre l'IPCMS et l'IRCER), qui ont assuré leur synthèse. Les configurations atomistiques correspondantes ont été simulées par CMD, suivie d'une courte BOMD (*s*-BOMD). De plus, deux de ces compositions (NVP40) ont également été étudiées via un cycle thermique complet en BOMD (*f*-BOMD). Le Tableau 1 présente un récapitulatif des systèmes modélisés ainsi que leurs compositions chimiques.

Le facteur de structure total expérimental S(k) ainsi que les fonctions de distribution

Table 1. Composition chimique nominale (en pourcentage molaire) des verres VP50, NVP40, NVP25 et NVP43 simulés. La teneur en V_2O_4 indiquée ici est estimée à partir du nombre d'atomes d'oxygène présents dans la cellule de simulation. Le nombre d'atomes est indiqué pour les cellules de petite taille (CMD, BOMD et MLIP) ainsi que pour les cellules de grande taille (CMD et MLIP).

Systèmes	Na_2O (%)	$V_xO_y(V_2O_4 + V_2O_5)$ (%)	P_2O_5 (%)	Taille (atomes)
VP50	–	50.0 (31.3 + 18.7)	50	218/ 5450
NVP40A	10.0	40.0 (0.0 + 40.0)	50.0	396 / 3168
NVP40B	10.0	40.0 (13.3 + 26.7)	50.0	388/ 3104
NVP25	37.5	25.0 (2.7 + 22.3)	37.5	394 / 3152
NVP43	28.5	43.0 (6.5 + 36.5)	28.5	405 / 3240

radiale réduites G(r) de nos systèmes NVP ont été déterminés par diffusion totale des rayons X. Les mesures de diffusion ont été réalisées à température ambiante. Les données brutes ont ensuite été corrigées, normalisées, puis transformées de Fourier afin d'obtenir les fonctions de distribution atomique réduites G(r).
La procédure de simulation utilisée précédemment pour le système VP50 a été reprise pour les simulations CMD et s-BOMD. Une analyse des propriétés électroniques et structurales des verres NVP, similaire à celle menée pour le verre VP50, a été effectuée.
Ayant établi la supériorité des simulations s-BOMD pour la description de l'environnement local V−O, l'analyse de l'ensemble des fonctions de corrélation partielle s'appuie uniquement sur les données issues de s-BOMD, au détriment de celles obtenues par CMD.
La figure 4(Gauche) présente La décomposition de la corrélation $g_{VO}(r)$ en contributions spécifiques $g_{V^{4+}O}(r)$, $g_{V^{5+}O}(r)$ ainsi que les fonctions $g_{OO}(r)$, $g_{NaO}(r)$, et $g_{PO}(r)$ dans les verres NVP25 et NVP43 (voir la publication [4]).
Dans le cas du système NVP25, la corrélation P−O présente un pic principal à 1.50 Å, accompagné d'une "épaule" à 1,62 Å. Les corrélations V^{5+}–O révèlent deux pics situés à 1.62 Å et 1.84 Å, correspondant respectivement aux liaisons vanadyles (V=O) et aux liaisons simples V−O. La corrélation V^{4+}−O montre quant à elle un pic principal à 1.89 Å, avec une faible épaule autour de 1.62 Å. Pour le système NVP43, la corrélation P−O

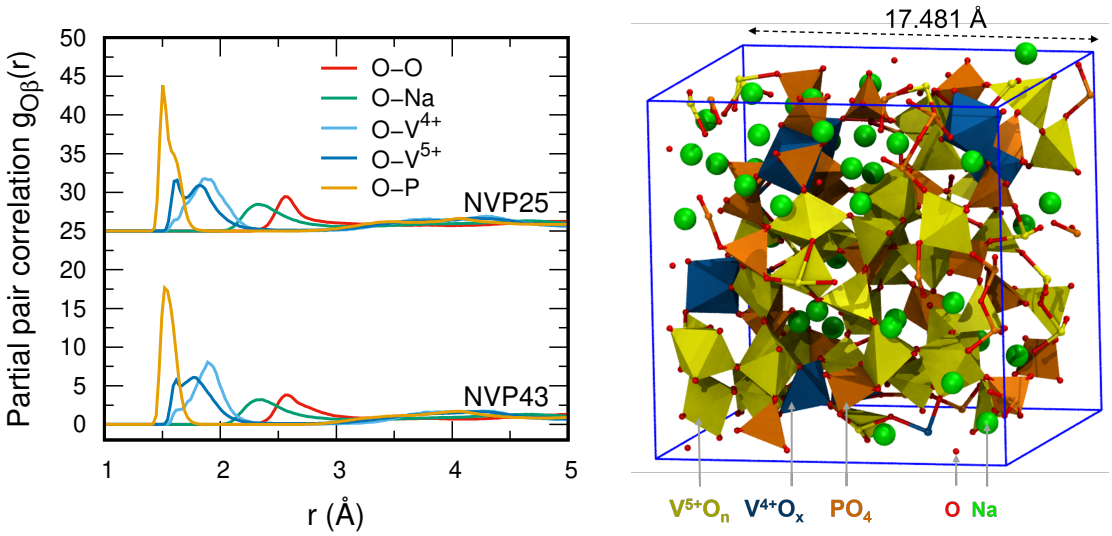

Figure 4. Gauche: Fonctions de corrélation partielle pour les verres NVP25 (haut) et NVP43 (bas), montrant les résultats des simulations s-BOMD pour $g_{OO}(r)$, $g_{NaO}(r)$ et $g_{PO}(r)$, ainsi que la décomposition de $g_{V^{5+}O}(r)$ et $g_{V^{4+}O}(r)$. Droite: Modèles atomistiques du verre NVP43 obtenu par s-BOMD.

présente un pic unique à 1.53 Å. La corrélation $V^{5+}-O$ affiche un premier pic moins défini à 1.62 Å (V=O), suivi d'un second pic à 1.75 Å, plus court que celui observé dans NVP25 (1.84 Å).
Aucune différence notable n'est observée entre les deux systèmes en ce qui concerne les corrélations O−O et $Na^{+}-O$ (avec un pic centré autour de 2.4 Å justifiant ainsi l'absence de liaison chimique et le rôle de modificateur dans le verre). Le fait que les distances $V^{5+}-O$ soient plus courtes que celles des liaisons $V^{4+}-O$ est en accord avec une tendance bien documentée dans les phases cristallines de vanadophosphates, où la longueur de la liaison V−O augmente à mesure que l'état d'oxydation du vanadium diminue (Schindler et al. *Chem. Mater.*, **12**, (2000)).
Les simulations *s*-BOMD reproduisent fidèlement ce schéma de liaison non trivial au sein des polyèdres VO_n, en accord avec les tendances expérimentales: elles capturent simultanément les courtes liaisons vanadyles et les liaisons simples V−O, avec des longueurs de liaison caractéristiques selon l'état d'oxydation du vanadium, soit: $V^{5+}-O < V^{4+}-O$. Les distances correspondantes sont de 1.75–1.84 Å pour V^{5+}–O, et de 1.89–1.90 Å pour $V^{4+}-O$ dans les systèmes NVP25 et NVP43.
Ces résultats représentent une amélioration significative par rapport aux travaux antérieurs basés uniquement sur des simulations CMD avec champs de force empiriques, tels que ceux rapportés pour les systèmes LiVP (Broglia et al. *J. Non-Cryst. Solids*, **403**, (2014)), et soulignent l'importance des approches *ab initio* pour décrire avec précision les propriétés des systèmes complexe.
Bien que la teneur en vanadium soit plus élevée dans NVP43, les environnements locaux autour du vanadium et du sodium restent globalement similaires dans les deux verres.
La Figure 4(Droite) illustre la complexité du modèle atomistique des systèmes NVP (cas du NVP43), représenté dans la cellule de simulation. Cette visualisation met en évidence l'interconnexion entre les différentes unités structurales, ainsi que la structure ouverte facilitée par l'incorporation des ions Na^{+}. On observe également que le V^{5+} se distingue comme un formateur de réseau particulièrement actif, susceptible de générer des liaisons supplémentaires au sein de la matrice vitreuse. Cette analyse *s*-BOMD révèle par ailleurs une plus grande diversité des environnements locaux, en particulier autour des espèces vanadium. Cette hétérogénéité structurale joue un rôle essentiel dans la compréhension du comportement du verre dans divers contextes, notamment en ce qui concerne son interaction avec les ions lors des processus d'insertion et d'extraction dans les applications liées aux batteries.
Il convient néanmoins de souligner que certains aspects restent à approfondir, tels que le prolongement de la relaxation thermique à l'échelle BOMD. Les simulations *f*-BOMD effectuées sur deux compositions NVP40 (en parallèle à la *s*-BOMD) permettent d'apporter une description plus réaliste de ces systèmes. Les simulations *f*-BOMD permettent une relaxation complète des constituants du verre au cours des processus de fusion et de trempe, ce qui conduit à une description plus fidèle de la structure à moyenne portée. À l'inverse, les simulations *s*-BOMD ne permettent qu'une relaxation locale, conservant en grande partie l'ordre à moyenne portée hérité des modèles CMD. Il convient de souligner que les simulations ***f*-BOMD** ont été effectuées à l'aide du code CP2K, dans le cadre de la DFT-BOMD sans restriction de spin.
La Figure 5(Gauche) présente une lecture atomistique des caractéristiques de liaison propres aux polyèdres VO_n, fondée sur l'analyse des centres de fonctions de Wannier permettant d'identifier différentes natures de liaisons. Elle présente aussi (Figure 5(Droite)) une analyse de la topologie de spin du modèle NVP40 obtenu par simulation *f*-BOMD. Celle-ci met en évidence une localisation du spin sur certains sites de vanadium correspondant aux espèces paramagnétiques V^{4+}, permettant ainsi une spéciation précise entre les états d'oxydation V^{5+} et V^{4+}.

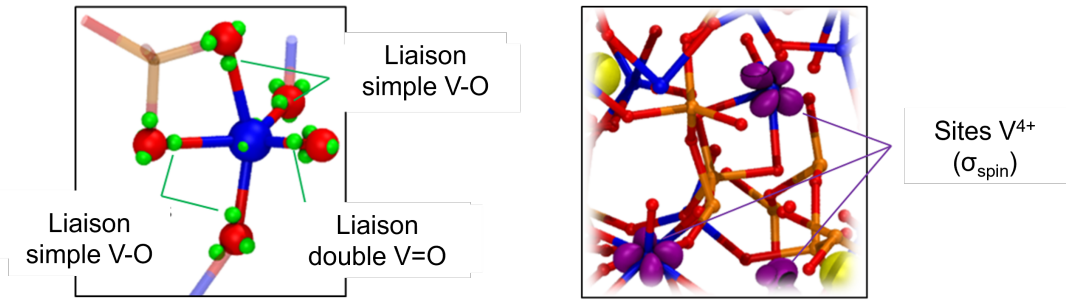

Figure 5. Modèles atomistiques obtenus par f-BOMD (Na: jaune, V: bleu, P: orange et O: rouge). Gauche: centres de Wannier (vert) dans l'environnement local d'un atome de Vanadium, au sein d'un polyèdre VO_n. Droite: isosurfaces de densité de spin locale (0.05 a.u., en violet).

Une évaluation rigoureuse de l'environnement local du vanadium permet ainsi une distinction plus fine entre "bridging oxygen" (BO) et "non-bridging oxygen" (NBO) dans le réseau vitreux, un paramètre clé influençant la dynamique des ions sodium qui fera l'objet de la section suivante, en s'appuyant sur les simulations CMD réalisées à l'aide du potentiel de type machine learning développé dans le cadre de cette thèse.

Développement d'un modèle de potentiel de Machine Learning pour l'étude des systèmes NVP

Compte tenu du coût computationnel très élevé des simulations f-BOMD, et afin d'étendre significativement les échelles de temps et d'espace accessibles, nous avons pleinement exploité les trajectoires issues d'un potentiel interatomique basé sur l'apprentissage automatique (MLIP), reposant sur la méthode GAP (Gaussian Approximation Potential) (Bartók et al. *Phys. Rev. Lett.*, **104**, (2010)). Ce potentiel a été entraîné à partir des données issues des simulations f-BOMD. Cette méthodologie a également été testée sur d'autres systèmes, notamment l'oxyde Na_3OCl (voir publication [5]) et le chalcogénure $GeSe_2$. Le MLIP permet ainsi d'optimiser l'efficacité des simulations sans compromettre la précision atteinte avec les simulations f-BOMD. Ce MLIP développé pour les systèmes NVP présente d'excellentes performances globales en termes d'énergie et de forces et de viriels, avec des erreurs moyennes d'entraînement par rapport aux valeurs de référence DFT respectivement de 5.8 meV/atome, 0.4 eV/Å et 16.9 meV/atome. Des valeurs très similaires sont observés sur les données de test/validation, attestant de la robustesse du modèle.
La Figure 6 met en évidence les améliorations significatives apportées par la méthode f-BOMD par rapport aux simulations CMD et s-BOMD pour le système NVP40, tant au niveau des facteurs de structure $S(k)$ obtenus par diffusion aux rayons X que des fonctions de distribution radiale réduites $G(r)$. Ces améliorations se traduisent, pour $S(k)$ et $G(r)$ par une réduction notable du paramètre R_χ, qui quantifie l'accord entre les données calculées et expérimentales. Dans l'espace réciproque, f-BOMD permet une meilleure description de $S(k)$ en élargissant le premier pic et en révélant une contribution secondaire autour de 1 $Å^{-1}$, capturant ainsi plus fidèlement l'ordre à moyenne distance.
Dans l'espace direct, et en se référant à $G(r)$, la méthode f-BOMD reproduit bien les données expérimentales pour le premier et le second pic, révélant clairement la présence des liaisons doubles/vanadyles et simples, respectivement. Cette amélioration se maintient également pour le quatrième pic, lié aux connexions polyédriques impliquant les distances V−V et V−P.
Les performances du nouveau potentiel MLIP pour le système NVP40 sont également illustrées à la Figure 6. Ce modèle MLIP reproduit fidèlement les résultats obtenus par f-

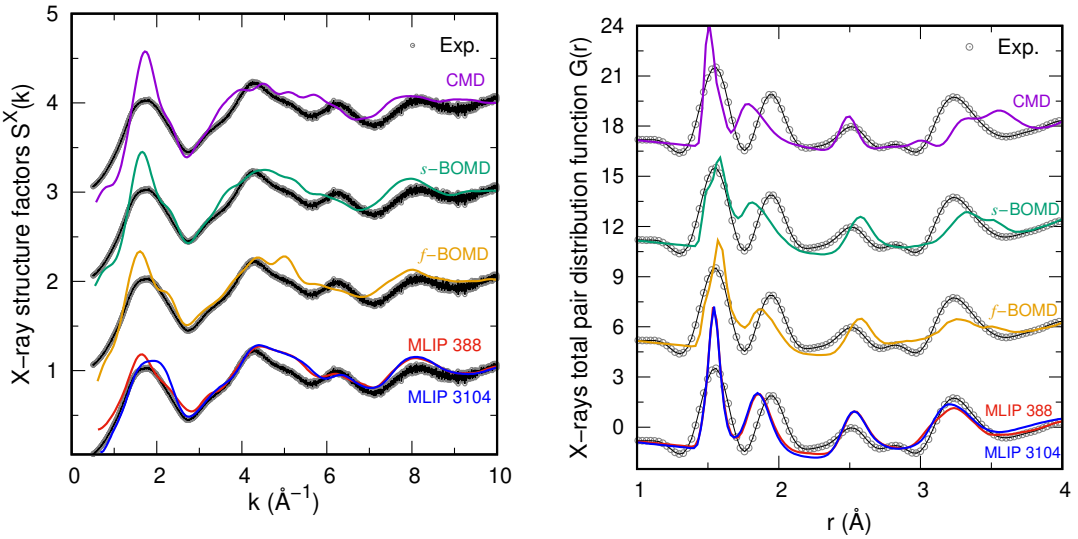

Figure 6. Facteur de structure $S(k)$ (à gauche) et fonction de corrélation total $G(r)$ (à droite) obtenues par diffraction des rayons X pour le verre NVP40. Les résultats de la modélisation atomique (CMD, s-BOMD, f-BOMD, et MLIP de différentes tailles) sont comparés aux données expérimentales.

BOMD, tant pour le facteur de structure $S(k)$ que pour la fonction de distribution radiale $G(r)$. Cette fidélité est confirmée par les valeurs similaires du paramètre R_χ obtenues avec le MLIP et le f-BOMD sur des modèles de 388 atomes. Des améliorations supplémentaires sont observées lorsqu'un système beaucoup plus grand (3104 atomes, une échelle inaccessible aux simulations BOMD pour des durées significatives) est considéré.
La Figure 7 présente de manière comparative la fonction de corrélation partielle $g_{VO}(r)$ pour les paires V–O obtenues à partir des différentes méthodes de calcul pour les systèmes VP50 (gauche) et NVP40 (droite). Le modèle s-BOMD affiche des pics bien séparés correspondant aux liaisons simples et doubles, localisés vers ∼1.6 Å (V=O) et ∼1.83 Å (V−O), et améliore ainsi la description par rapport au pic unique élargi obtenu avec CMD. Cette séparation est encore mieux marquée avec f-BOMD pour le système NVP40, qui montre un minimum bien défini entre les pics, ainsi qu'une distance de liaison V−O (∼1.88 Å) plus proche des valeurs expérimentales (∼1.92 Å).

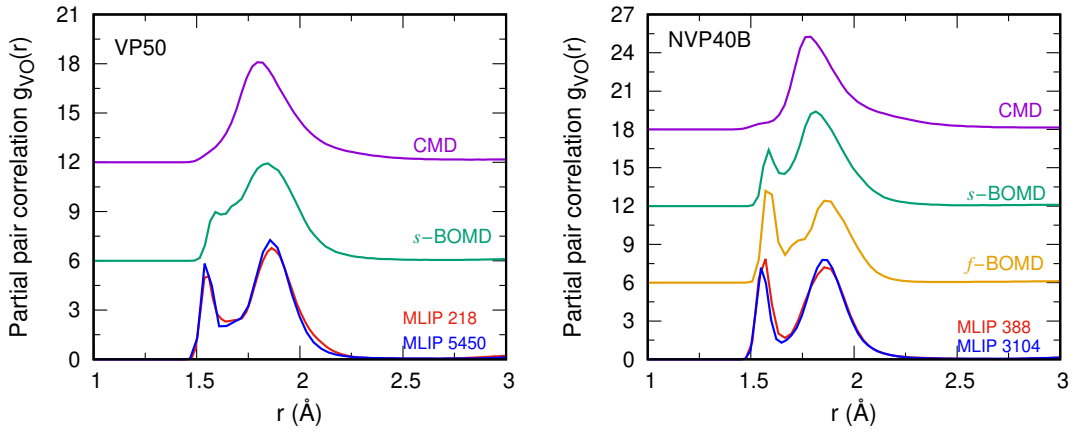

Figure 7. Fonction de corrélation partielle $g_{\mathrm{VO}}(r)$ pour les verres VP50 (gauche) et NVP40B (droite), obtenue à l'aide des méthodes CMD, s-BOMD, f-BOMD (pour NVP40B), et MLIP (avec des tailles de systèmes petites et grandes).

Le MLIP permet de reproduire avec une grande précision les pics des liaisons V=O et

V−O pour les deux systèmes comme l'illustre la Figure 7. La même précision est observée les coordinations en accord avec les données issues du f-BOMD. L'approche MLIP permet de réduire drastiquement le coût de calcul, passant d'environ 220 jours pour le f-BOMD à seulement 4 jours avec le MLIP tout en préservant la précision *ab initio*.
La description structurale précise des verres NVP obtenue grâce à notre potentiel MLIP permet une évaluation fiable de la conductivité ionique (σ_{ion}), à partir des coefficients de diffusion du sodium extraits de l'analyse des MSD. La Figure 8 présente le MSD du système NVP43 révélant une dynamique hétérogène des ions Na^+, marquée par une fraction d'ions à mobilité quasi nulle (*ions piégés*), tandis que d'autres présentent une mobilité significativement plus élevée (*ions très mobiles*) comme l'illustre la Figure 9.

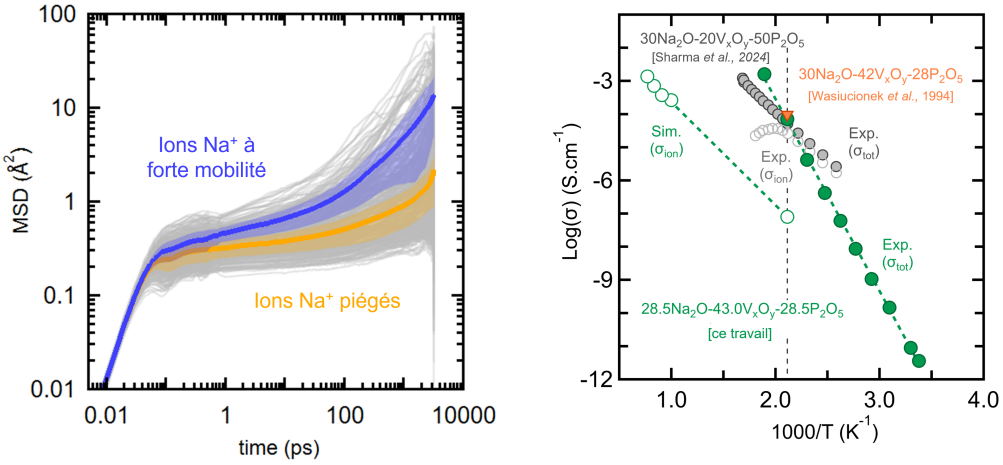

Figure 8. Gauche: déplacement quadratique moyen (MSD) des ions Na^+ dans le modèle NVP43 (3240 atomes) à 1200 K, calculé avec le potentiel MLIP, mettant en évidence les ions très mobiles en violet et piégés en orange. Droite: graphique d'Arrhenius de $\log(\sigma)$ en fonction de $1000/T$, comparant les résultats de ce travail (en vert, simulation et expérience) à ceux d'autres verres NVP (gris: (Sharma et al., *J. Phys. Chem. C*, **128**, (2024)) et orange: (Wasiucionek et al. *Solid State Ion.*,**70-71**, 1994)).

À 473 K, le verre NVP43 présente une conductivité expérimentale totale de 3.3×10^{-5} S/cm (voir Figure 8 et la publication [6]), mesurée par spectroscopie d'impédance électrochimique (EIS). Le diagramme de Nyquist présente un demi-cercle presque idéal, légèrement déprimé ce qui indique une conduction mixte, dominée par une conduction électronique (due au mécanisme de *small polaron hopping* entre les sites V^{4+} et V^{5+}), avec une contribution mineure de la conduction ionique via Na^+. Cette dernière, estimée à environ 5% à l'aide des simulations MLIP (Figure 8), reste faible. Des données pour deux autres verres NVP présentant des teneurs similaires en Na_2O, mais différant par leur rapport V/P et la spéciation du vanadium sont également indiquées. Pour ces systèmes, une conduction mixte ionique/électronique a été observée, avec une contribution ionique pouvant atteindre jusqu'à 50% (Sharma et al., *J. Phys. Chem. C*, **128**, (2024); Wasiucionek et al. *Solid State Ion.*,**70-71**, 1994))
Cette étude propose ainsi une compréhension approfondie des propriétés structurales et dynamiques des verres NVP, en s'appuyant sur une approche innovante combinant données expérimentales, simulations *ab initio* et dynamique moléculaire par MLIP. Elle offre des perspectives inédites sur l'ordre à moyenne distance, la spéciation du vanadium, les mécanismes de transport ionique du sodium et la modélisation des interfaces verre/cristal, posant ainsi les bases de la conception de matériaux vitreux et vitrocéramiques performants pour le stockage d'énergie. La précision démontrée et la montée en échelle permise par l'approche MLIP ouvrent également la voie à son application à d'autres systèmes amorphes complexes, accélérant ainsi l'innovation dans les domaines de la science des verres et des technologies énergétiques.

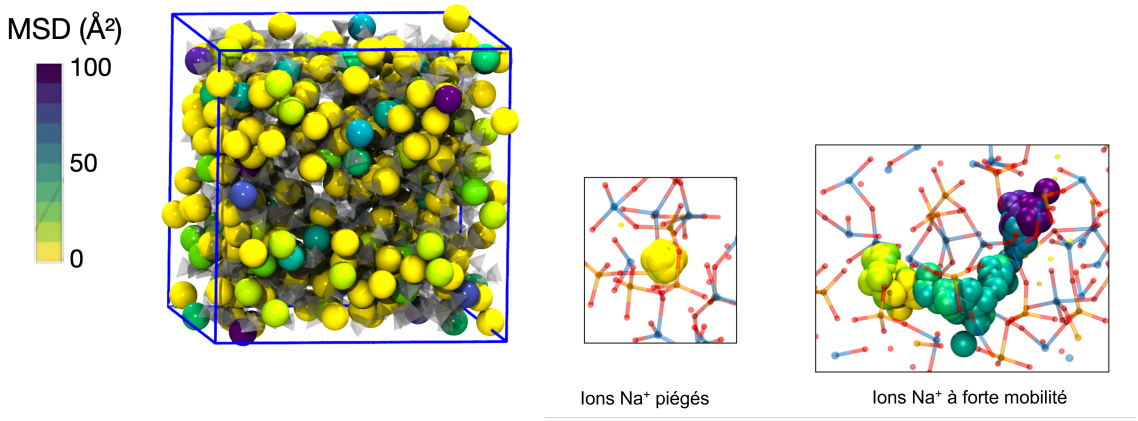

Figure 9. Gauche: Aperçu de la structure dans la cellule de simulation (3240 atomes) du système NVP43 à 1200 K, avec les ions Na^+ colorés selon la valeur de leur MSD; les unités PO_n et VO_n sont représentées par des polyèdres transparents. Centre: trajectoire d'un ion Na^+ piégé et colorée selon sa MSD avec une valeur finale de ∼2 $Å^2$. Droite: trajectoire d'un ion Na^+ très mobile, colorée selon la MSD atteignant une valeur finale de ∼85 $Å^2$.

Il convient de souligner que cette thèse s'inscrit dans le cadre du projet collaboratif ANR AMSES (Conception de verres et de matériaux vitrocéramiques pour des applications dans le stockage d'énergie par modélisation à haute performance). Ce projet associe l'équipe expérimentale dirigée par O. Masson à l'Institut de Recherche sur les Céramiques (IRCER) et l'équipe de modélisation atomique de l'Institut de Physique et Chimie des Matériaux de Strasbourg (IPCMS). Les informations ayant guidé le choix des systèmes modélisés dans cette étude, les conditions expérimentales appliquées lors de leur élaboration, ainsi que les résultats issus de leur synthèse et de leur caractérisation, notamment pour les systèmes de type NVP, sont le fruit de cette collaboration étroite entre les deux équipes.

L'ensemble des simulations réalisées dans le cadre de cette thèse a été effectué sur plusieurs infrastructures de calcul haute performance. D'une part, la plateforme régionale CAIUS (Cluster de Calcul Intensif de l'Université de Strasbourg), du mésocentre de l'Université de Strasbourg, a été largement sollicitée. D'autre part, des ressources nationales ont été mobilisées via le Grand Équipement National de Calcul Intensif (GENCI), en particulier les centres IDRIS (Institut du Développement et des Ressources en Informatique Scientifique), CINES (Centre Informatique National de l'Enseignement Supérieur) et TGCC (Très Grand Centre de Calcul).

Liste des publications

[1] **S.D. Wansi Wendji**, C. Massobrio, M. Boero, C. Tugène, E. Levchenko, F. Shuaib, R. Piotrowski, D. Hamani, G. Delaizir, P.-M. Geffroy, P. Thomas. O. Masson, A. Bouzid, G. Ori *J. Non-Cryst. Solids*, **(2024)**. DOI

[2] M. Guerboub, **S.D. Wansi Wendji**, C. Massobrio, A. Bouzid, M. Boero, G. Ori, and E. Martin. *J. Chem. Phys.* 158, 084504 **(2023)**. DOI

[3] C. Massobrio, I.A. Essomba, M. Boero, C. Diarra, M. Guerboub, K. Ishisone, A. Lambrecht, E. Martin, I. Morrot-Woisard, G. Ori, C. Tugène, **S.D. Wansi Wendji** *Phys. Status Solidi B Basic Res.* **(2023)**. DOI

[4] **S.D. Wansi Wendji**, R. Piotrowski, C. Massobrio, M. Boero, C. Tugène, F.

Shuaib, D. Hamani, P.-M. Geffroy, P. Thomas, A. Bouzid, O. Masson, G. Delaizir, G. Ori *J. Non-Cryst. Solids*, 655, 123420, **(2025)**. DOI

[5] T.-L. Pham, M. Guerboub, **S.D. Wansi Wendji**, A. Bouzid, C. Tugène, M. Boero, C. Massobrio, Y.-H. Shin and G. Ori *arXiv preprint*, **(2024)**. DOI

[6] **S.D. Wansi Wendji**, R. Piotrowski, A. Familiari, C. Massobrio, M. Boero, C. Tugène, F. Shuaib, D. Hamani, P.-M. Geffroy, P. Thomas, A. Pedone, A. Bouzid, O. Masson, G. Delaizir, G. Ori *Chem. Commun.*, **(2025)**. DOI

Steve Dave WANSI WENDJI

First-principles and machine learning atomistic modeling of disordered systems for energy applications

Résumé

Cette thèse porte sur la modélisation atomique des verres et vitrocéramiques polyanioniques sodium-vanadium-phosphate (NVP), matériaux prometteurs en tant que cathodes pour les batteries rechargeables de seconde génération. Les propriétés structurelles, magnétiques, électroniques et dynamiques de cette famille complexe de matériaux sont explorées à l'aide de simulations de dynamique moléculaire classique (CMD) et de dynamique moléculaire ab initio (FPMD). Dans un premier temps, la performance des champs de force empiriques est évaluée par comparaison avec les données expérimentales. Une approche hybride, peu coûteuse en ressources de calcul, est ensuite proposée. Elle combine la CMD suivie d'un raffinement par FPMD, permettant une description structurelle et électronique plus précise pour différentes compositions de verres binaires VP et ternaires NVP. Pour valider cette méthodologie, des simulations FPMD sont réalisées sur plusieurs compositions de verres NVP, et les résultats sont comparés à ceux obtenus via l'approche hybride. Afin de réduire davantage le coût computationnel sans compromettre la précision des simulations ab initio, un potentiel interatomique basé sur l'apprentissage automatique (MLIP) est développé à partir de données issues de calculs DFT/FPMD. Cette approche par apprentissage automatique est d'abord testée puis validée sur d'autres systèmes modèles, notamment l'oxyde Na_3OCl et le chalcogénure $GeSe_2$. En fin le ML est appliqué aux verres VP et NVP, permettant la prédiction fiable de leurs propriétés structurales et dynamiques, ainsi que la modélisation de l'interface verre/cristal.

Mots clés: Verres, vitrocéramiques, NVP, chalcogénures, CMD, FPMD, MLIP

Résumé en anglais

This thesis focuses on the atomic-scale modeling of polyanionic sodium-vanadium-phosphate (NVP) glasses and glass-ceramics, which are promising cathode materials for next-generation rechargeable batteries. The structural, magnetic, electronic, and dynamic properties of this complex family of materials are investigated using both classical molecular dynamics (CMD) and ab initio molecular dynamics (FPMD) simulations. First, the accuracy of empirical force fields is assessed by comparison with experimental data. Based on this evaluation, a low-cost hybrid approach is proposed, combining CMD with subsequent refinement via FPMD. This method offers improved structural and electronic descriptions across a range of binary VP and ternary NVP glass compositions. To validate this approach, FPMD simulations are conducted on various NVP glass compositions, and the results are benchmarked against those obtained with the hybrid method. In order to further reduce computational costs while maintaining the accuracy of FPMD simulations, a machine-learning interatomic potential (MLIP) is developed using data derived from DFT/FPMD calculations. This ML-based approach is first tested and validated on other oxide (Na_3OCl) and chalcogenide ($GeSe_2$) systems and then applied to VP and NVP glasses, enabling accurate prediction of their complex properties and facilitating the modeling of the glass/crystal interface.

Keywords: Glass, glass-ceramic, NVP, chalcogenides, CMD, BOMD, MLIP